Attenuation of volcanic seismic signals

Patrick John Smith

Submitted in accordance with the requirements for the degree of Doctor of Philosophy

The University of Leeds

School of Earth and Environment

August 2010

Acknowledgements

Studying for a PhD is inevitably a uniquely personal and individual endeavour, yet this research could not have happened without the help and support of many people.

Firstly, I am indebted to my supervisor Professor Jürgen 'Locko' Neuberg for helping me to develop as a researcher, and extend my knowledge of volcano-seismology. You have given me generous support and guidance with every aspect of my research, many fantastic travel opportunities and wonderful dinners, all of which I have greatly appreciated. I also thank Professor Greg Houseman for being part of my Research Support Group, and everyone in IGT for creating a friendly and supportive research atmosphere. I am particularly grateful to all members, past and present, of the Volcanology Research Group for lots of useful discussions about my research and many other aspects of volcanology, as well as for accompanying me on various fieldwork and conference trips.

I would also like to thank Dr. Mare Yamamoto, whose visit to Leeds in January 2008 made me think in new ways about several aspects of my research, and helped to calibrate the finite-difference model. Thanks also to Dr. Roger Clark and Dr. Brian Baptie for finding time to be my examiners, particularly at such short notice!

I also thank everyone at MVO for making me feel extremely welcome during my numerous trips to Montserrat, especially those I had the privilege of sharing a house with at Sea Dreams during my three month stay in 2009. I'm very much looking forward to spending some more time with you all in the next few years!

The funding for this research was provided by NERC studentship NER/S/A/2006/14150, for which I am very grateful. The collection and archiving by MVO staff of the seismic data used in Chapter 5 is fully acknowledged.

I wish to thank to everyone I have shared an office with during the course of my PhD, throughout the various changes of building! I cannot thank you all individually, so apologies if I miss anyone out. I particularly acknowledge (in no particular order), the members of 'The Unit': Tom for being generally super awesome and helping with my many Q-related problems, Ian for his cider skills and for sharing in some good adventures in Iceland and San Francisco, Matt for appreciating good music and good beer, Carl for the annual Canada Day fireworks display and Ben for his shell scripts and keeping office life entertaining. I also thank Chris for sharing in the trinity of joys that are TMS, Tool and guitars, and lastly Dan Tang for continually inspiring me to think critically and for kick-starting the home brewing! Special thanks must also go to everyone who's had the dubious pleasure of living with me in Leeds these past four years, in particular: Dan, Ian, Matt, Tom, Seamus and Emma.

Thanks also to all my friends back in Leicester who were always there for me whenever I needed a break or to escape from Leeds for a few days. Finally, I must thank my family: my parents and my sister, for all their love, support and encouragement over the last few years, and without whom none of this would have been possible.

Abstract

Low frequency volcanic earthquakes, characterised by slowly decaying harmonic codas of 0.5-5Hz, have been observed on many volcanoes and are considered key tools in monitoring and eruption forecasting. The common element in a variety of models proposed for the origin of these earthquakes is resonance of a fluid body within a volcanic edifice. The source of the resonance is believed to consist of dispersive interface waves, trapped at the fluid-solid boundaries. The amplitude decay or attenuation of these earthquake signals can be decomposed into radiative and intrinsic components, and in this way yield information about both the geometry and fluid properties of the resonating source body.

This thesis presents a study of the attenuation of low-frequency volcanic earthquakes, with particular emphasis on quantitatively linking seismic signals to magmatic processes and properties. The effect of the intrinsic attenuation of the fluid on the amplitude decay of low-frequency volcanic earthquakes is examined using a viscoelastic finite-difference model of seismic wave propagation. It is shown that the viscosity of the fluid contributes $23.6 \pm 2.26\%$ less than previously thought to the apparent attenuation, and that its effect may have been substantially overestimated in previous studies. A physical explanation for this lies in understanding the fundamental differences between acoustic and interface waves. An analytical approach demonstrates that, for a set of realistic volcanic parameters, interface waves can be attenuated less than acoustic waves in a pure melt, if the longitudinal viscosity is at least 10^7 Pas. These results widen the set of possible resonators and imply that resonating volcanic conduits filled with high viscosity magma are viable sources for low-frequency seismicity.

An automated method to measure the apparent attenuation of seismic signals is developed, tested, and applied to a dataset of low-frequency earthquakes from Soufrière Hills Volcano, Montserrat. Temporal trends in attenuation are observed and quantitatively interpreted as changes in magma viscosity. An estimate of the magma shear viscosity of $2.3 \pm 2 \times 10^5$ Pas is obtained, demonstrating the ability of seismological data to place constraints on the magma properties.

Contents

List of Figures **vi**

List of Tables **xii**

Symbol conventions **xiii**

1 Introduction **1**

1.1 Monitoring active volcanoes 1

1.2 Volcanic seismicity 2

1.3 Low-frequency volcanic seismicity 3

1.3.1 Characteristics 4

1.3.2 Correlation with deformation and cyclic activity 5

1.4 Origin of low-frequency seismicity 6

1.4.1 Resonance of fluid-filled bodies 7

1.4.2 Crack models 8

1.4.3 Conduit resonance 10

1.4.4 Trigger mechanism 11

1.5 Soufrière Hills Volcano, Montserrat 12

1.5.1 Geological background and history of the current eruption 12

1.5.2 Seismicity at Soufrière Hills Volcano, Montserrat 14

1.6 Seismic attenuation 17

1.6.1 Definitions of attenuation 17

1.6.2 Uses of attenuation 18

1.6.3 Application to volcanoes 19

1.7 Motivation 22

1.7.1 Linking seismic signals to magma properties: the wider context . . 22

1.7.2 Aims 23

1.7.3 Outline of thesis 24

2 Modelling attenuated low-frequency volcanic earthquakes 26

2.1 Introduction to the finite-difference model 27

2.1.1 The finite-difference method 27

2.1.2 Models of elastic wave propagation 27

2.1.3 Viscoelasticity 32

2.1.4 Modelling the intrinsic attenuation 34

2.1.5 Wave propagation in a linear viscoelastic medium 36

2.2 Testing and development of the model 40

2.2.1 Seismic amplitudes: towards a quantitative magma flow meter . . 40

2.2.2 Source implementation 41

2.3 Resonance dynamics and radiation of energy: the radiative part 47

2.3.1 Geometrical dependence of the amplitude spectra 47

2.3.2 Geometrical dependence of the radiative attenuation 55

2.4 Testing the effect of the intrinsic attenuation: the intrinsic part 58

2.4.1 Description of model runs 58

2.4.2 Results 60

2.4.3 Calibration of the model 67

2.5 Discussion and Conclusions 76

3 Attenuation of interface waves: an analytical approach 79

3.1 Interface waves 79

3.2 Motivation for quantifying their attenuation 82

3.3 Derivation 83

3.3.1 The attenuation of interface waves 83

3.3.2 The attenuation of acoustic waves 86

3.4 Comparison of interface and acoustic wave attenuation 91

3.4.1 The ratio of interface to acoustic wave attenuation 91

3.4.2 Shear and volume viscosities 91

3.5 Rheology: the link between attenuation and viscosity 94

3.5.1 SLS and Kelvin-Voight rheologies 94

3.5.2 Modifying the rheology of the finite-difference model 95

3.5.3 Results of the Kelvin-Voight finite-difference model 105

3.5.4 Comparison between the model and analytical results 111

3.6 Discussion and Conclusions 113

4 Measuring the attenuation 116

4.1 Review and evolution of methods . . . 118
4.1.1 Neighbouring peaks . . . 118
4.1.2 Logarithms . . . 122
4.2 Frequency dependence and the effects of filtering . . . 124
4.3 Automated methods . . . 128
4.3.1 Description of the methods . . . 128
4.3.2 Testing using synthetic signals . . . 136
4.4 Discussion and Conclusions . . . 148

5 Attenuation of low-frequency earthquakes at Soufrière Hills Volcano 150
5.1 Choice of dataset . . . 151
5.1.1 23rd to 28th June 1997 . . . 151
5.1.2 Family A . . . 156
5.2 Measurements of attenuation . . . 161
5.2.1 Pre-dome collapse: 23rd to 25th June . . . 161
5.2.2 Post-dome collapse: 25th to 28th June . . . 176
5.3 Linking attenuation and viscosity . . . 186
5.3.1 Interpreting temporal variations . . . 186
5.3.2 Explaining the changes in intrinsic attenuation . . . 186
5.3.3 Seismological constraints on the magma . . . 188
5.4 Discussion and Conclusions . . . 192
5.4.1 Comparison with Q_a at other volcanoes . . . 192
5.4.2 Conclusions . . . 193

6 Discussion 196
6.1 Interface and acoustic waves . . . 196
6.2 Resonance, attenuation, and low-frequency earthquakes . . . 198
6.3 Decomposing the attenuation . . . 199
6.4 Seismological constraints on the magma properties . . . 201

7 Conclusions 203
7.1 Summary of conclusions and contributions . . . 203
7.2 Future work . . . 205

A Seismic station information 208

References 209

List of Figures

1.1 Example low-frequency earthquake with characteristic decaying coda and peaked amplitude spectrum 5

1.2 Schematic diagram to highlight the differences between the crack and conduit model geometries 9

1.3 Map showing the location of Soufrière Hills Volcano, Montserrat. 13

1.4 Example waveforms of VT, Hybrid and rockfall seismic signals at SHV. . 15

1.5 Decomposition of the amplitude decay 21

2.1 Mechanical models for a Burgers body and a Standard Linear Solid (SLS) 34

2.2 Variation of displacement amplitude with timestep 43

2.3 Variation of displacement amplitude with grid spacing 44

2.4 Setup of the numerical experiment to test amplitude calibration. 45

2.5 Comparison of numerical amplitudes with analytical solutions 46

2.6 Schematic diagram showing the setup of the finite-difference model grid and recording arrays 48

2.7 0.5 and 2Hz Küpper wavelets and their amplitude spectra. 50

2.8 Amplitude spectra for two vertical arrays of stations inside the conduit (upper), and 100m from the wall (lower). 51

2.9 Corresponding waveforms for the amplitude spectra shown in Figure 2.8 . 51

2.10 Amplitude spectra for two arrays of stations: a vertical array 2km from the conduit wall (upper), and a horizontal array at the free surface (lower). 52

2.11 Corresponding waveforms for the amplitude spectra shown in Figure 2.10 52

2.12 Amplitude spectra for two vertical arrays of stations inside the conduit (upper), and 100m from the wall (lower) using a 0.5Hz Küpper source wavelet. 53

2.13 Corresponding waveforms for the amplitude spectra shown in Figure 2.12 53

2.14 Amplitude spectra for two vertical arrays of stations inside the conduit (upper), and 100m from the wall (lower), for a source at the conduit centre. 54

2.15 Corresponding waveforms for the amplitude spectra shown in Figure 2.14 54

2.16 Variation of the horizontal component quality factor with the source-receiver geometry. 56

2.17 Variation of the vertical component quality factor with the source-receiver geometry. 56

2.18 Variation of the horizontal component attenuation with the source-receiver geometry. 57

2.19 Variation of the vertical component attenuation with the source-receiver geometry. 57

2.20 Schematic diagram showing the setup of the finite-difference model grid. . 59

2.21 Smoothed Sinc function source wavelet and its amplitude spectrum. . . . 60

2.22 Synthetic seismograms produced for the same model setup using two different source wavelets 61

2.23 Synthetic waveforms and amplitude spectra from the finite-difference model, for a range of intrinsic attenuations. 63

2.24 Apparent quality factor as a function of intrinsic quality factor. 64

2.25 Apparent attenuation as a function of intrinsic attenuation. 64

2.26 Linear fits to the apparent-intrinsic attenuation relationship using a variable number of datapoints. 65

2.27 Fits to the apparent-intrinsic quality factor relationship using a variable number of datapoints. 66

2.28 Q_{i} as a function of frequency in the finite-difference model for increasing numbers of SLS 68

2.29 Q_{i} as a function of frequency in the finite-difference model for varying bandwidths. 69

2.30 Frequency dependence of the attenuation in the finite-difference model. . 71

2.31 Quality factor as a function of frequency, recovered from a half-space using spectral ratios, for a constant $Q = 100$ using a 10Hz Ricker wavelet. . . . 72

2.32 Quality factor as a function of frequency, recovered from a half-space using spectral ratios, for a constant $Q = 100$ using a 10Hz Sinc function. 73

2.33 Quality factor as a function of frequency, recovered from a half-space using spectral ratios, for a constant $Q = 100$ using a 1Hz Küpper wavelet 74

2.34 Percentage error in the recovered intrinsic quality factor. 75

3.1 Dispersion relations of Ferrazzini & Aki (1987) for an infinite fluid layer. . 82

3.2 Geometry and properties of the viscous fluid layer in the analytical problem. 84

3.3 Interface wave phase velocity as a function of frequency and shear viscosity. 85

3.4 Interface wave attenuation as a function of frequency and shear viscosity. 87

3.5 Interface wave Quality factor as a function of frequency and shear viscosity. 88

3.6 Acoustic wave attenuation as a function of frequency and longitudinal viscosity. 89

3.7 Acoustic wave Quality factor as a function of frequency and longitudinal viscosity. 90

3.8 Ratio of interface to acoustic wave attenuation for a pure liquid (melt). . 92

3.9 Ratio of interface to acoustic wave attenuation for a three-phase fluid (magma) 93

3.10 Schematic diagram showing the mechanical representations of (a) a Kelvin-Voight body and (b) a Standard Linear Solid (SLS). 95

3.11 Minimum $\tau_\sigma/\tau_\epsilon$ ratio as a function of the temporal discretization. 97

3.12 Modelled and Kelvin-Voight attenuation, for a timestep of $dt = 10^{-3}$s. . . 98

3.13 Modelled and Kelvin-Voight attenuation, for a timestep of $dt = 10^{-4}$s. . . 99

3.14 Modelled and Kelvin-Voight attenuation, for a timestep of $dt = 10^{-5}$s. . . 99

3.15 Modelled and Kelvin-Voight attenuation, for a timestep of $dt = 10^{-6}$s. . . 100

3.16 RMS misfit between modelled and Kelvin-Voight attenuation as a function of the timestep. 101

3.17 RMS misfit between modelled and Kelvin-Voight attenuation as a function of the computation time. 102

3.18 Q_i and attenuation functions recovered from a half-space using spectral ratios. 103

3.19 Attenuation coefficient functions recovered from a half-space using spectral ratios. 104

3.20 Schematic diagram showing the setup of the Kelvin-Voight finite-difference model grid. 106

3.21 Acoustic wave quality factor for a longitudinal viscosity of 10^8 Pas. 107

3.22 Synthetic waveforms and amplitude spectra from the Kelvin-Voight finite-difference model, for a range of viscosities. 108

3.23 Apparent quality factor, Q_a, as a function of the viscosity for the Kelvin-Voight finite-difference model. 109

3.24 Apparent attenuation as a function of the viscosity for the Kelvin-Voight finite-difference model. 109

3.25 Apparent quality factor, Q_a, as a function of the intrinsic acoustic wave quality factor. 110

3.26 Apparent attenuation as a function of the intrinsic acoustic wave attenuation. 110

3.27 Comparison between the analytical expressions and the finite-difference model modified to use a Kelvin-Voight rheology. 112

4.1 Attenuation: amplitude decay of a wave at a fixed fraction per cycle . . . 117

4.2 Measuring the apparent Quality factor, Q_a, using the 'neighbouring peaks' method. 120

4.3 Measuring the apparent Quality factor, Q_a, using the 'neighbouring peaks' method with band-pass filters. 121

4.4 Comparison of the 'neighbouring peaks' and logarithm methods of measuring the apparent Quality factor, Q_a. 123

4.5 Example of the analytical envelope and instantaneous phase of a signal . . 124

4.6 Example low-frequency earthquake with characteristic peaked amplitude spectrum 125

4.7 Transfer function and impulse response of Butterworth bandpass filters . 126

4.8 Calculating the apparent attenuation using the logarithm of the signal amplitude. 127

4.9 Example of the fixed regression window length method 129

4.10 Example of the fixed regression window length method failing 129

4.11 Apparent Q_a calculated using a fixed length and manually selected regression window 129

4.12 Smoothed gradient function of the signal envelope 132

4.13 Dependence of the number of segments on the amount of smoothing . . . 133

4.14 Unsmoothed gradient function and the second derivative 133

4.15 Variable-window S-transform compared to 1-pole band-pass filters 136

4.16 Variable-window S-transform compared to 2-pole band-pass filters 137

4.17 Synthetic signal created by superposition of damped sinusoids 138

4.18 Recovery of attenuation from synthetic signals with a linear Q_a distribution. 140

4.19 Recovery of attenuation from synthetic signals with a logarithmic Q_a distribution. 142

4.20 Recovery of attenuation from synthetic signals with an exponential Q_a distribution. 142

4.21 Recovery of attenuation from synthetic signals with a random Q_a distribution. 143

4.22 Recovery of attenuation from synthetic signals with a constant Q_a distribution. 143

4.23 Comparison between band-pass filtering and the S-transform for a linear Q_a distribution. 144

4.24 Comparison between band-pass filtering and the S-transform for an exponential Q_a distribution. 145

4.25 Comparison between band-pass filtering and the S-transform for a logarithmic Q_a distribution. 145

4.26 Comparison between band-pass filtering and the S-transform for a random Q_a distribution. 146

4.27 Comparison between band-pass filtering and the S-transform for a constant Q_a distribution. 146

5.1 Map showing the locations of the seismic station MBGA and the tiltmeter at Chances Peak. 152

5.2 (a) Families of seismicity together with tilt and its time derivative. (b) Waveform families and tilt at SHV during 23rd-28th June 1997. 154

5.3 Inter-event times and event rate of earthquakes swarms preceding a dome collapse at SHV. 155

5.4 Occurrence of waveform families at SHV between 23rd and 28th June. . . 155

5.5 Stacked waveforms and spectra for the seven swarms preceding dome collapse. 157

5.6 Amplitude spectra for all family A events, as a function of event number. 158

5.7 Amplitude spectra for all family A events preceding the dome collapse, plotted as a function of absolute time 159

5.8 Variation of the spectral peaks of all family A events preceding the dome collapse, as a function of event number. 159

5.9 Variation of the spectral peaks of all family A events preceding the dome collapse, as a function of absolute time. 160

5.10 Apparent Q_a as a function of the event number. 162

5.11 Apparent Q_a as a function of time. 163

5.12 Apparent attenuation, Q_a^{-1}, as a function of the event number. 164

5.13 Apparent attenuation, Q_a^{-1} as a function of time. 165

5.14 Box plot displaying the apparent Q_a distribution for each swarm. 166

5.15 Box plot displaying the apparent attenuation, Q_a^{-1}, distribution for each swarm. 167

5.16 Comparison of Q_a^{-1} kurtosis excess in each swarm for each measurement method. 167

5.17 Apparent Q_a values calculated for 20 minute bins, using an automated method. 168

5.18 Apparent attenuation, Q_a^{-1}, calculated for 20 minute bins, using an automated method. 169

5.19 Temporally averaged frequency dependence of apparent Q_a and attenuation. 170

5.20 Ratio of apparent Q_a at different frequencies. 171

5.21 Ratio of apparent attenuation at different frequencies. 172

5.22 Temporal variation of apparent Q_a and attenuation at 1.39Hz for the final four swarms preceding the dome collapse. 174

5.23 Correlation between the mean attenuation and event rate of each bin. . . 175

5.24 Amplitude spectra for post-dome collapse Family A events, as a function of event number. 178

5.25 Stacked waveforms and spectra for the six swarms of Family A earthquakes following the dome collapse. 179

5.26 Apparent Q_a and attenuation as a function of the event number for post-dome collapse Family A events. 180

5.27 Apparent Q_a and attenuation as a function of time for post-dome collapse Family A events. 180

5.28 Box plots displaying the apparent Q_a and attenuation distributions for each post-dome collapse Family A swarm. 181

5.29 Box plot displaying the apparent Q_a and attenuation distributions for *all* Family A swarms. 181

5.30 Stacked waveforms and spectra for the five swarms of Family C earthquakes following the dome collapse. 183

5.31 Amplitude spectra for post-dome collapse Family C events, as a function of event number. 184

5.32 Variation of the spectral peaks of for Family C events, as a function of event number. 184

5.33 Apparent Q_a and attenuation as a function of time for Family C events. . 185

5.34 Physical model to explain the temporal changes in attenuation. 188

5.35 Interface wave attenuation as a function of the shear viscosity. 189

5.36 Apparent attenuation at 1.39 and 2.16Hz during Swarm 6 190

5.37 Gradient of intrinsic attenuation with respect to viscosity. 191

6.1 Distance a 1-3 Hz acoustic wave could travel within a magma-filled conduit.199

List of Tables

2.1 The first four spectral peaks measured from the amplitude spectra of the synthetic signals, as a function of the intrinsic attenuation of the fluid. . . 62

2.2 Modelling results: Apparent quality factor as a function of the intrinsic quality factor. 62

2.3 Calculated gradients and Q_{r} (intercept) values from the Q_{a}^{-1} vs. Q_{i}^{-1} results. 65

4.1 Comparison of the RMS residuals for five different methods of measuring the attenuation. 141

4.2 Filter parameters used in the comparison between band-pass filtering and the S-transform 144

4.3 Comparison of the RMS residuals for the band-pass filtering and S-transform methods. 147

4.4 Averaged comparison of the RMS residuals for the different methods. . . . 148

5.1 Results of t-tests comparing the mean Q_{a} at different frequencies. 170

5.2 Measured apparent Q_{a} values from various volcanoes. 193

A.1 MBGA: seismometer location and instrument type 208

Symbol conventions

Symbols

α – attenuation factor or, P-wave velocity
β – S-wave velocity
γ – shear-to-compressional wave velocity ratio
δ – phase lag
ϵ – strain or, regression error
ζ – longitudinal viscosity
η – shear viscosity
κ – scale factor between acoustic and interface wave attenuation
Λ – longitudinal relaxation function
λ – wavelength or, 1$^{\text{st}}$ Lamé parameter
μ – shear modulus (rigidity)
ξ – volume viscosity
ρ – density
σ – stress
τ – relaxation time
ϕ – slope angle or, phase angle
Φ – phase angle of complex phase velocity
ω – (angular) frequency

A – Fault area or, Amplitude or Amplitude spectrum
B – Volume Modulus
C – Crack stiffness factor
C_d^{-1} – data covariance matrix
c – intercept
c_{p} – acoustic velocity
d – data vector
dx – horizontal grid spacing
dz – vertical grid spacing
dt – temporal discretization (timestep)
e – added noise
f – frequency
G – stress relaxation function or, condition matrix
H – Heaviside step function or, Hilbert transform
h – width/thickness
J – geometrical spreading factor

k – wavenumber or, integer smoothing parameter
L – crack length or, number of SLS
ℓ – integer weighting parameter
M – Seismic moment function or, Shear relaxation function
M_0 – Seismic moment
M_c – Complex modulus
M_R – Relaxation modulus
m – gradient
N – Event rate
$\mathbf{n}$ – normal vector
p – model parameters (polynomial coefficients)
Q – Seismic quality factor
Q^{-1} – Seismic attenuation (inverse of the quality factor)
r – source-receiver distance
T – traction
t – time
u – displacement
$\bar{u}$ – average fault slip
V_{f} – complex interface wave phase velocity
V_{p} – P-wave velocity
V_{s} – S-wave velocity
v – velocity
v_{ph} – phase velocity
x – horizontal coordinate
w – weighting factor
z – vertical coordinate

Subscripts and superscripts

$_{\mathrm{a}}$ – apparent
$_{\mathrm{acoustic}}$ – pertaining to acoustic waves
$_{\mathrm{f}}$ – fluid
$_{\mathrm{i}}$ – intrinsic
$_{\mathrm{interface}}$ – pertaining to interface waves
$_{\mathrm{max}}$ – maximum
$_{\mathrm{r}}$ – radiative
$_{\mathrm{s}}$ – solid
$_{w}$ – weighted mean
$\tilde{}$ – denotes a complex quantity

Abbreviations

CFL – Courant-Friedrichs-Lewy (stability condition for the finite-difference method)
CLVD – Compensated linear vector dipole
MVO – Montserrat Volcano Observatory
RMS – Root mean square
SHV – Soufrière Hills Volcano
SLS – Standard Linear Solid
VT – Volcano-tectonic

Chapter 1

Introduction

Understanding the attenuation of volcanic seismic signals is an important part of the wider process of quantitatively linking volcanic seismic signals to magmatic processes and properties. This process is crucial for understanding the dynamical behaviour of volcanoes, and therefore critical to volcano monitoring, hazard assessment and mitigation. In this introduction a review of the relevant background is presented, followed by the motivation and aims of this thesis.

1.1 Monitoring active volcanoes

> *Only* [sic] volcano-monitoring can provide a diagnosis of a volcano's current behaviour, which in turn constitutes the *only* scientific basis for short-term (hours to months in advance) forecasts or "predictions" of impending eruption, or of mid-course changes of an ongoing eruption. (Tilling, 2005)

Monitoring of active volcanoes is focused on risk assessment and hazard mitigation, and is accomplished using a wide variety of geophysical techniques to measure different physical parameters of a volcanic system. However, monitoring of precursory seismicity at active volcanoes is one of the most reliable and widely used volcano monitoring techniques (Chouet, 2003), although because patterns of earthquakes can differ greatly between volcanoes and even between eruptions at the same volcano, it remains a somewhat elusive precursor (Scarpa & Gasparini, 1996). One benefit that seismology offers over other techniques is its ability to indicate the state of a volcano at depth. Other techniques such as monitoring gas output or ground deformation quite literally only scratch the surface, whereas seismicity is often related to processes occurring deep within the volcano.

1.2 Volcanic seismicity

Some of the key goals of volcano seismology suggested by Chouet (1996a;b; 2003) are to understand the dynamics and physical properties of magmatic systems, while McNutt (2005) suggests that quantifying magma movement and evolution is also a long term goal of the science. All of these are important steps in the process of successfully understanding, assessing and mitigating volcanic hazards. An important role of the volcano-seismologist is firstly to be able to distinguish local, regional and teleseismic sources from volcanic seismic sources for any signals recorded by an instrument or network on a volcano (McNutt, 2002). Once signals have been determined to be of volcanic origin, classifying these signals, based on certain criteria, has proved to be a valuable tool, allowing the observed seismicity to be interpreted in terms of volcanic processes.

Volcanoes possess a wide variety of potential seismic sources and as such are capable of producing a large range of seismic signal types. Volcanic signals are often classified by a combination of their spectral content and waveform, rather than simply the waveform alone, as this provides insight into their origin and source process and is therefore more useful from a monitoring point of view (see for example the 1989-1990 eruption of Redoubt volcano, Alaska in Chouet et al. (1994); Lahr et al. (1994); Power et al. (1994)). Early attempts to classify volcanic earthquakes were based only on the appearance of the waveforms (e.g. Minakami, 1974) leading to some confusion in nomenclature, and conflicting terminology still remains a problem in volcano-seismology (McNutt, 2005). This is particularly apparent with regard to low-frequency or long-period earthquakes (Chouet, 1996a), whom McNutt (2005) describes as the 'troublemakers'. However, the two main categories of seismic signal identified by Lahr et al. (1994) and others, and in common use today are:

(1) Volcano-Tectonic (VT) sometimes also termed high-frequency (HF) earthquakes, which are local earthquakes with clear impulsive P and S-phases and significant energy above 5Hz (Miller et al., 1998). They are usually simply interpreted as resulting from brittle failure, indistinguishable from ordinary double-couple tectonic earthquakes, although full moment-tensor analysis has revealed large non-couple components in some instances (e.g Miller et al., 1998a;b). VT earthquakes are often regarded as one of the earliest precursors to increased volcanic activity (Roman & Cashman, 2006).

(2) Low-frequency (LF) or long-period (LP) seismicity, categorised by its characteristic

harmonic frequency content typically between 0.5 and 5Hz (Chouet, 1996a; Neuberg et al., 1998), whose origin has been linked to processes involving volcanic fluids. This link to internal fluid processes offers the possibility of quantifying magma movement and low-frequency seismicity is therefore seen by some as the 'holy grail' of volcano-seismology (McNutt, 2005). Volcanic tremor is also included in this category (as a superposition of discrete earthquakes) distinguished by its longer (continuous) duration, although some authors treat this as a separate category entirely. The relationship between low-frequency earthquakes and tremor is discussed in more detail in Section 1.3.1.

This is the terminology that will be used throughout this thesis, as it is consistent with the terminology used by many authors in the literature. This is by no means an exhaustive list and other types of seismic signals seen on volcanoes include: rockfalls and surface flow signals (e.g pyroclastic flows and lahars) which are emergent signals with a broad spectral content (Miller et al., 1998) and often associated with active dome growth at silicic volcanoes; very-long period (VLP) events with periods in the range 3-100s or longer (McNutt, 2005), seen for example at Stromboli volcano or Aso volcano, Japan and attributed to gas slugs (Neuberg et al., 1994) or hydrothermal processes (Yamamoto et al., 1999) and explosion signals, often with accompanying visual observations or infrasonic (acoustic) signals (e.g. Hagerty et al., 2000; Green & Neuberg, 2005).

Analysis of the fault-plane solutions of VT earthquakes has been used to determine local stress conditions at many volcanoes (e.g. Moran, 2003; Sánchez et al., 2004; Roman et al., 2006; 2008) and the distribution of VT events is sometimes used to give a crude estimate of the extent of the magmatic plumbing system. Yet this on its own does not provide much information about the precise geometry and dynamics of the system (Chouet, 1996b), and this is where the analysis of low-frequency events and their source mechanism comes into its own.

1.3 Low-frequency volcanic seismicity

Low-frequency or long-period volcanic earthquakes have been claimed to have immense forecasting potential (Chouet, 1996a), yet have also proved one of the most challenging signals to understand since they have their origin in fluid processes that are still not fully understood (McNutt, 2005). Low-frequency seismicity has long been known as a precursory indicator of eruptive activity, having sometimes been seen to precede eruptions at

many volcanoes such as: Soufrière Hills Volcano, Montserrat (Miller et al., 1998; Neuberg et al., 1998); Galeras volcano, Columbia (Fischer et al., 1994; Gil Cruz & Chouet, 1997); Redoubt volcano, Alaska (Chouet et al., 1994; Stephens et al., 1994); Mount Pinatubo, Philippines (Ramos et al., 1999) and Asama volcano, Japan (Minakami, 1974; Sawada, 1994). Despite this, their full significance and potential as a forecasting tool has only been appreciated since a more theoretical understanding of their origin has evolved, that links these signals and their source to processes in volcanic fluids (Chouet, 1996a).

1.3.1 Characteristics

With the advent of better quality volcano monitoring networks being deployed on an increasing number of volcanoes, low-frequency seismicity, including both discrete events and continuous tremor, has been observed in many locations worldwide. It does not seem to be confined to volcanism in a particular tectonic setting, and although seen at many volcanoes its characteristics do show subtle variations.

In basaltic systems, low frequency seismicity is often manifested as tremor, seismic energy concentrated in narrow frequency bands lasting from minutes to days (e.g. Piton de la Fournaise, La Réunion (Battaglia et al., 2005) or Kilauea, Hawai'i (Goldstein & Chouet, 1994)), and has been linked to unsteady magma or fluid transport in the shallow plumbing system (Chouet, 1996b). If a tremor signal has a peaked spectrum of integer harmonics it is often referred to as *harmonic tremor*, and peaked spectra such as this can be produced in two ways: by repetitive triggering of identical wavelets where the fundamental frequency is determined by the repeat interval, or, the spectral peaks represent the eigenfrequencies of a resonating system (Neuberg, 2000). These frequencies can sometimes systematically shift over a few minutes or hours (e.g. Benoit & McNutt, 1997; Neuberg et al., 1998) producing what are termed 'gliding lines' in a spectrogram of the data. The explanation for these rapid temporal changes in spectral peaks depends on the choice of model, and requires changes in either the triggering frequency of discrete events (Powell & Neuberg, 2003) or changes in the physical parameters that control the eigenoscillations (Benoit & McNutt, 1997).

On silicic volcanoes, low-frequency seismicity is more typically characterised not by continuous tremor, but by discrete events with distinctive slowly decaying harmonic codas and peaked frequency spectra (e.g. Soufrière Hills Volcano (SHV), Montserrat (Neuberg et al., 1998) - see Figure 1.1; Galeras volcano, Columbia (Gil Cruz & Chouet, 1997)

or at Redoubt volcano, Alaska (Chouet et al., 1994)). However, low-frequency events are often observed as *swarms*, large numbers of events occurring in the space of hours, seen for example at SHV (Miller et al., 1998) or Redoubt Volcano, Alaska (Lahr et al., 1994; Stephens et al., 1994). Individual events within a swarm often exhibit a high degree of waveform similarity, indicative of a stationary source process (Green & Neuberg, 2006). Such swarms may also show structure related to dynamical processes, and can accelerate and merge into continuous tremor as the inter-event time reduces (e.g. SHV, Hammer & Neuberg, 2009). The often common spectral content between tremor and low-frequency events, suggests that, at least for certain volcanoes, a common source process is responsible for both (Chouet, 1996a).

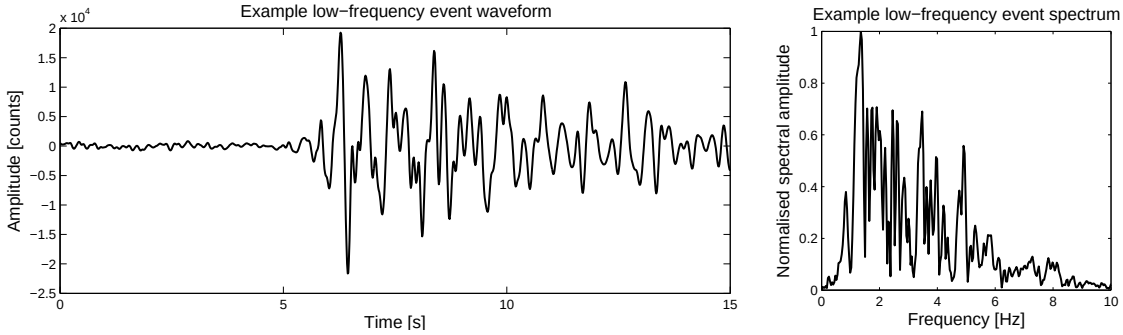

Figure 1.1: Low-frequency earthquake waveform with characteristic decaying coda and peaked amplitude spectrum. This example shows a 15-second vertical component velocity seismogram recorded at station MBGA, SHV, Montserrat on 23rd June 1997.

1.3.2 Correlation with deformation and cyclic activity

Active volcanoes, and silicic volcanoes in particular, often exhibit cyclic behaviour on a variety of timescales, from a few minutes or hours up to decadal timescales and beyond. This cyclic behaviour can manifest itself as episodic changes in eruptive style or quasi-periodic perturbations in a number of measurable geophysical parameters such as seismicity, volatile output, petrology, erupted volume and ground deformation. This suggests a multi-disciplinary approach is required to model such behaviour. Understanding this cyclicity, and in particular what the controls on this behaviour are, is one of the outstanding questions in volcanology, with direct implications in terms of prediction and hazard mitigation.

At Soufrière Hills Volcano low-frequency seismicity has not only been precursory, but has also been observed to occur in cycles, with periods of 8-12 hours (Neuberg, 2000), which Voight et al. (1998) showed to correlate well with measurements of ground deformation,

and in particular with similar cycles in tilt observed very close to the volcanic edifice. Green et al. (2006) suggested these tilt cycles can be explained by a shear force exerted by the traction of magma on the conduit wall, whereas the cycles in seismicity are associated with a relaxation process in the volcano (Green & Neuberg, 2006). This is important because it not only provides some clues as to the source mechanism for low-frequency seismicity, but also begins to provide a quantitative link between the seismicity and shallow magma-movement and ascent rates. The connection between the cyclic behaviour of the seismicity and deformation and a model for the seismic trigger is discussed further in Section 1.4.4, and with particular reference to SHV in Section 1.5.2.

1.4 Origin of low-frequency seismicity

Despite long being recognised as an important monitoring tool, and shown to correlate well with ground deformation observations, the precise origin of low-frequency volcanic seismicity has proved to be somewhat elusive, with no single model able to encompass the characteristics observed at all volcanoes. Some authors have argued that, at least in some cases, the low-frequency nature of these signals is due to path rather than source effects; such as Harrington & Brodsky (2007) who suggested that low-frequency earthquakes observed at Mount St. Helens volcano are brittle failure events with slow rupture velocities and complicated paths. On the other hand, the consensus amongst many authors is that the low-frequency content of most observed signals must be due to a source effect, since spectral characteristics are often common across several stations within a seismic network (e.g. Fehler & Chouet, 1982; Gómez & Torres, 1997). In fact, understanding the source process has proved to be the key to unlocking the potential of low-frequency events. Chouet (1996b) suggests that a low-frequency event can be thought of as a combination of a 'trigger', which provides the initial seismic energy, and a 'resonator', which sustains the low-frequency coda of the signal. In the next sections, models for both of these two key components are discussed, with resonance of a fluid-filled body being the favourite candidate for the resonator and brittle fracturing of volcanic melt in glass transition being one model for the trigger mechanism.

1.4.1 Resonance of fluid-filled bodies

Much research over the last few decades has been focused on resonance of a fluid-filled body as a source of low frequency signals. In some of the earliest models for the source of low-frequency seismicity and tremor, such as the fluid-driven crack model of Aki et al. (1977), Ferrazzini & Aki (1987) noted that "the fluid did not support acoustic waves and simply behaved like a cushion to the vibration of the crack walls. Therefore the observed long duration of the long-period events could not be simulated because of the weak resonance and strong radiation loss." Connected to this was the problem that using the acoustic velocity of the fluid to determine the resonant period or frequency of the crack, required a very large magma reservoir as the resonator to explain the length of the periods seen on volcanoes such as Mount Aso in Japan. The key to solving this puzzle proved to be the discovery of the significance of interface waves (also termed 'slow waves' or 'crack waves') in a series of modelling works (Chouet & Julian, 1985; Chouet, 1986; 1988), in which the coupling between the fluid and surrounding solid was fully analysed. Waves of this type were first detected close to and within fluid-filled boreholes, as what Biot (1952) termed 'tube waves'. Alongside these numerical studies, in a seminal contribution, Ferrazzini & Aki (1987) studied an inviscid fluid layer sandwiched between two elastic half-spaces and derived an analytical expression for the phase velocity of interface waves confined to the fluid-solid boundaries. They recognised that one mode of these highly dispersive waves has phase velocities lower than the acoustic velocity of the fluid. This important finding, together with the numerical work of Chouet (1986; 1988), demonstrated that low-frequency resonance could be generated from comparatively small source bodies. It is worth reinforcing here that this form of resonance is a fundamentally different process from harmonic standing waves, whose resonant eigenfrequencies (so called 'organ pipe modes') would depend only on the acoustic velocity of the fluid and the length of the resonator (Neuberg et al., 2000). The exact nature of the resonating source body for low-frequency events has, however, been the subject of some debate, and ideas for model geometries at various volcanoes have broadly fallen into one of two different camps: crack models or conduit models, the nature of which are described in the following sections.

1.4.2 Crack models

The first approach was to model the events as being produced by the resonant excitation of a fluid-driven crack. The origin of this crack geometry is a work by Aki et al. (1977) who proposed a model for volcanic tremor on Kilauea volcano, Hawaii, of magma transport in a narrow fluid-filled crack driven by excess pressure of the fluid. This fluid-driven crack model was further developed by Chouet (1986; 1988), who used finite-difference models to examine the seismic wavefield associated with resonance in narrow fluid-filled cracks. He showed that the dynamics and resonant frequencies of the crack depend on both the geometry and the contrast in elastic parameters across the fluid-solid boundary, summarised by the 'crack stiffness factor', first defined by Aki et al. (1977) as:

$$C = \begin{cases} \dfrac{B\lambda}{\mu h} & \text{for an infinitely long crack} \\ \\ \dfrac{BL}{\mu h} & \text{for a finite length crack} \end{cases} \tag{1.1}$$

where B is the volume modulus of the fluid in the crack, μ is the rigidity or shear modulus of the surrounding elastic solid, h is the crack width and for the case of an infinitely long crack λ is the wavelength of the propagating wave, which for a crack of finite length is replaced by the crack length L. Smith (2006) showed that this stiffness factor is not adequate to describe fully the resonance characteristics and frequencies in all cases, and that the material property ratio B/μ should be broken down further into separate ratios of density and seismic velocities.

Similar crack-like source bodies containing highly compressible fluids (e.g. ash-H_2O, H_2O-CO_2 or H_2O-SO_2 mixtures (Morrissey & Chouet, 2001)), with aspect ratios in the range $100 \leq L/h \leq 10^4$, have been suggested by many authors since these early pioneering works. In one such example, Chouet et al. (1994) quantitatively analysed the precursory low-frequency seismicity on Redoubt Volcano, Alaska in 1989 and proposed a $280 - 380\text{m} \times 14 - 190\text{m} \times 0.05 - 0.2\text{m}$ crack containing water and steam as the source body, based on a forward model which matched the observed spectral characteristics.

As well as by forward modelling, the source mechanism for low-frequency earthquakes has also been studied by waveform inversion of low-frequency earthquake codas to obtain the seismic moment tensor components, assuming a point-source for the event (e.g. Kumagai et al., 2002) or an extended set of several points sources by inverting in the frequency domain (e.g. Nakano et al., 2007). The result of these studies has often been

a particular form of the moment tensor, known as a Compensated Linear-Vector Dipole (CLVD) (Knopoff & Randall, 1970), with the interpretation being resonance in shallow vertical or sub-horizontal crack-like structures within or below the volcanic edifice. However, there is an inherent ambiguity in the interpretation of the source mechanism since various geometries can be responsible for such a CLVD mechanism (Chouet, 1996b). This approach, of inverting waveforms for the source mechanism, has been tried for low-frequency seismicity at various volcanoes in recent years such as: Kusatsu-Shirane Volcano, Japan (Kumagai et al., 2002; Nakano et al., 2003; Nakano & Kumagai, 2005a), Kilauea Volcano, Hawai'i (Kumagai et al., 2005) and Cotopaxi Volcano, Ecuador (Molina et al., 2008). This type of crack geometry has also recently been proposed as a source of long-period earthquakes at Mount St. Helens, with the specific orientation of a gently NNW-dipping, steam-filled crack derived from waveform inversion for the source mechanism (Waite et al., 2008).

(a) (b)

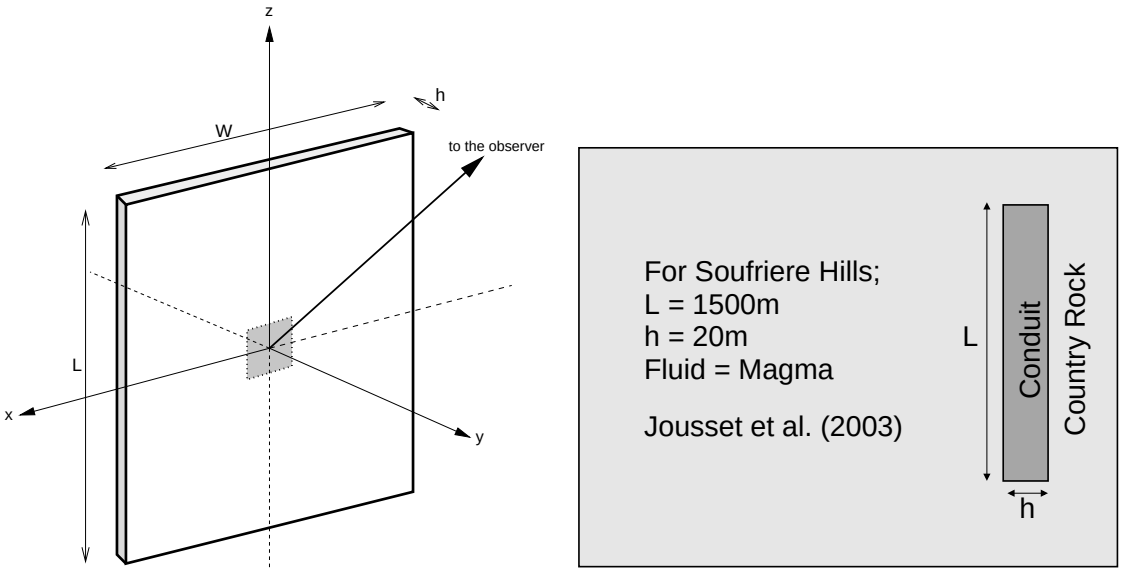

Figure 1.2: Schematic diagram that highlights the differences between the crack and conduit model geometries. (a) The 'crack' model, in 3-D with large aspect ratios (L/h) and containing compressible, low viscosity, and often low density fluids, such as gas or ash-gas mixtures. (b) The 'conduit' model in 2-D, with comparatively small aspect ratios (L/h) containing higher viscosity fluids with lower compressibilities, such as magma. Figure (a) Modified from Collier (2005), after Chouet et al. (1994) and (b) modified from Green (2005).

1.4.3 Conduit resonance

In contrast to the crack model geometry, a number of authors such as Neuberg et al. (2000), Jousset et al. (2003; 2004) and Sturton & Neuberg (2006) have proposed resonance of a magma-filled conduit or dyke as a low-frequency seismic source. The key differences between this and the crack model are the lower aspect ratios, $L/h < 100$, along with a higher density and a lower compressibility of the fluid contained (Figure 1.2). The model proposed by Jousset et al. (2003) for example employed a 2-D conduit or dyke section of around 1000m long $\times$ 20m wide, and was filled with a three-phase mixture of gas, crystals and melt (e.g Neuberg & O'Gorman, 2002) to simulate the characteristics of low-frequency events at SHV.

Due to the trade-off between geometry and fluid parameters, contained in the 'Stiffness Factor' in Equation 1.1, both models can, in fact, explain the frequency content of the observed signals. However, there are other considerations which may determine how appropriate both geometries are. A criticism of the crack-model could be the geological plausibility of such structures, on the scale of a few hundred metres and with high aspect ratios, existing in a likely highly fractured and heterogeneous volcanic edifice (Green, 2005). Dykes and conduit systems with widths of a few metres and lengths of a few hundred metres are, by contrast, observed in nature as a feature of magma transport and storage at silicic volcanoes (Eichelberger, 1995). On the other hand, one of the criticisms levelled at the conduit resonance model has been that if the source body contains high viscosity, bubble-rich magma such as andesite, typical of subduction zone volcanic arcs, then the attenuation of the fluid would be too high to support resonance and seismic energy would be too rapidly damped (Chouet, 1996b). This argument would suggest that such a model cannot produce events with slowly decaying codas, yet these are evidently observed at andesitic volcanoes (e.g. Galeras (Fischer et al., 1994) or SHV (Neuberg et al., 1998)). There are two ways out of this apparent paradox; either you reject the conduit model and instead favour a lower density, less attenuating material such as ash-laden gas, or, you show that the attenuation mechanism of highly viscous magma on low-frequency earthquakes is weaker than previously assumed. This is discussed in more detail in Section 1.6.3 and the latter approach is, in fact, one of the possibilities that will be examined in Chapters 2 and 3.

1.4.4 Trigger mechanism

Rowe et al. (2004), Green & Neuberg (2006) and Ottemöller (2008) have all used cross-correlation techniques to show the existence of families of low frequency events at SHV which exhibit a high degree of waveform similarity. This behaviour of repeating, almost identical events is far from unique to SHV, and has been both observed and analysed at other volcanoes, such as Shishaldin Volcano, Alaska (Petersen et al., 2006), Unzen Volcano, Japan, (Umakoshi et al., 2008) and Volcán de Colima, Mexico (Varley et al., in press; 2010). The fact that these repeating events occur implies a small source volume for their location and requires a stable, non-destructive and repeatable source mechanism. This observation, together with the apparent correlation of the seismicity with short-term deformation cycles at SHV (Green & Neuberg, 2006) and fluid-dynamical models of magma flow in the conduit (Collier & Neuberg, 2006), led Neuberg et al. (2006) to propose a model where brittle fracturing of the magma in a narrow depth range acts as the seismic 'trigger', which then excites the resonance responsible for the coda part of low-frequency earthquake signals.

A high lateral viscosity gradient exists at the conduit walls, controlled by gas and heat loss through the boundary (Collier & Neuberg, 2006). This can lead to a build up of shear stress (the product of the viscosity and the shear strain rate) near the conduit wall, and if a critical value is exceeded, this can cause a brittle rupturing of the magma (e.g. Tuffen et al., 2008); providing the seismic energy for the conduit resonance that generates the low-frequency seismic signals (Neuberg et al., 2006). The results of this study suggest that resonance in the conduit can occur within a 'seismogenic window', between the bubble nucleation level at the base and the trigger or source depth at the top, above which the magma movement is no longer ductile flow but aseismic friction-controlled slip.

Other possible source mechanisms for triggering the resonance responsible for low-frequency seismicity have been suggested, including: periodic interaction of super-heated water with magma (Zimanowski, 1998), fluid dynamical instabilities during ash venting (Julian, 1994) and, at Mount St. Helens, stick-slip motion of ascending magma (Iverson et al., 2006).

1.5 Soufrière Hills Volcano, Montserrat

This study potentially has implications for low-frequency events observed on many volcanoes worldwide, but will focus on Soufrière Hills Volcano, Montserrat, as a case study, due to the well monitored nature of the volcano and the availability of a variety of datasets to test out ideas. The modelling parameters used, such as the conduit width, the magma density and the range of magma viscosities, are based on values determined for SHV in the scientific literature. The attenuation of low-frequency earthquake signals at SHV has never been studied before, although it has been attempted at many other volcanoes (e.g. Kumagai & Chouet, 1999; 2000; De Angelis & McNutt, 2005). This presents a unique and interesting opportunity to explore the similarities and differences between SHV and other silicic volcanoes, to add to the breadth of knowledge and material about the current eruption and to feed results directly into the risk assessment process.

1.5.1 Geological background and history of the current eruption

Soufrière Hills Volcano is an andesitic, dome-building volcano occupying the southern portion of the island of Montserrat in the Leeward Islands, in the northern part of the Lesser Antilles volcanic arc. The arc is a result of subduction of the North American plate beneath the Caribbean plate and runs for around 800km in length (Le Friant et al., 2004). The island of Montserrat itself is made up of at least three volcanic complexes, getting progressively younger from the oldest in the north (c.2.6 Ma) to the youngest in the south (c.170 Ka) (Harford et al., 2002). SHV is the youngest of these volcanic centres and comprises of a core of at least four andesitic domes and associated pyroclastic aprons (Rea, 1974).

The current eruption of SHV began in July 1995, starting with phreatic activity that followed a period of three years of heightened seismic activity (Young et al., 1998). Activity escalated through 1996 and mid to late 1997, culminating in the lateral sector collapse event on 26 December (Boxing Day) 1997. A series of Vulcanian explosions occurred in June 1997, with a significant collapse event on June 25th 1997, whose associated pyroclastic flows and surges led to 19 deaths, the only known fatalities of the eruption (Robertson et al., 2000). Since this time volcanic activity has consisted of extrusive dome building alternating with distinct 1.5-2 year long pauses or periods of relative quiescence (Wadge et al., 2010), with the extrusion occurring in three major episodes lasting 2-3.5

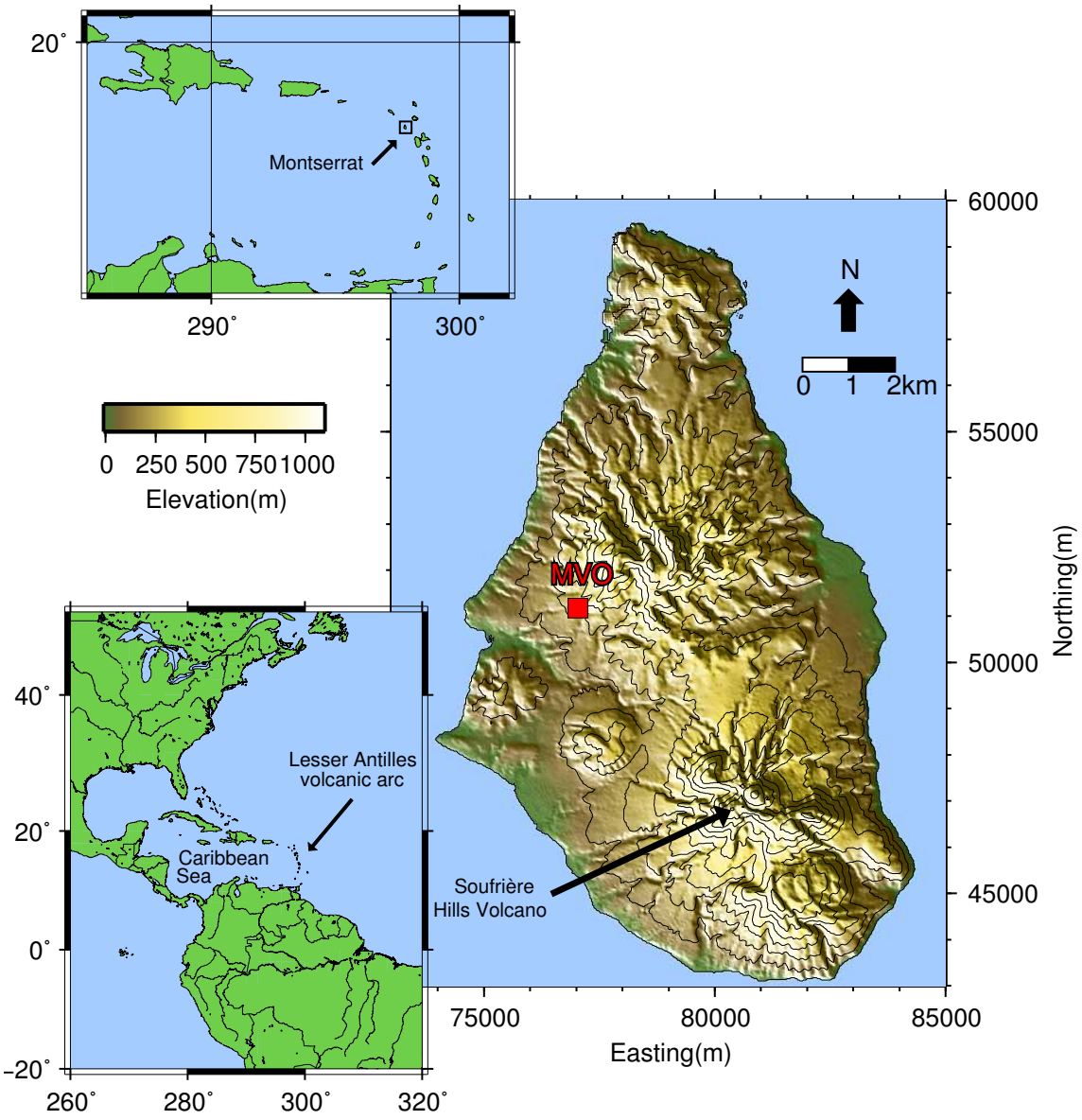

Figure 1.3: Map showing the position of Montserrat within the Lesser Antilles volcanic arc and the locations of the Soufrière Hills Volcano and the Montserrat Volcano Observatory (MVO). At the time of writing the elevation of the summit of the current dome is approximately 1170m (Cole et al., 2010) and is the highest point on the island.

years each (including 1995-1998 as the first). These alternating eruptive periods have been punctuated by several major dome or sector collapse events, notably in December 1997 (Voight et al., 2002), March 2000 (Carn et al., 2004), July 2003 (Herd et al., 2005), May 2006 (Loughlin et al., 2007) and February 2010 (Cole et al., 2010).

1.5.2 Seismicity at Soufrière Hills Volcano, Montserrat

Volcano-Tectonic earthquakes

As discussed earlier, volcano-tectonic (VT) earthquakes are a category of volcanic seismic signal, observed at Soufrière Hills Volcano, Montserrat (SHV) as well as many other volcanoes worldwide. They are thought to be a result of brittle failure, often have impulsive P and S-wave onsets, and contain significant energy above 5Hz (Miller et al., 1998). They have been observed, in varying numbers, since 1995 and throughout the entire eruptive history of SHV, mostly occurring at shallow depths ($<$ 5km) below the volcano. Analysis of VT earthquakes has been used to examine changes in local stress conditions; with changes in the dominant azimuth of the P-axis of VT fault-plane solutions linked to the intrusion of magma in a dyke below the edifice, e.g. Roman et al. (2006; 2008), who proposed the existence of a NE-SW trending dyke at SHV. However, a recent model of the ground deformation resulting from the pressurisation of a dyke-conduit system by Hautmann et al. (2009) found a NNW-SSE trending dyke feeding into a shallower conduit to be the best fit to the geodetic data at SHV.

Rockfall and surface flow signals

Rockfall and pyroclastic flow signals, associated with active dome growth, have been one of the most common seismic signals seen at SHV during the current eruption, with more than 27,000 seismic events of this type recorded between 1996 and 1998 alone (Calder et al., 2002). Individual seismic events are characterised by an emergent signal without clear P or S-wave arrivals (Miller et al., 1998) that waxes and wanes with a cigar-shaped envelope (see the example in Figure 1.4). Changes in the character of rockfall activity at SHV (in terms of the number of events, dominant direction, repose times or durations) have been well correlated with temporal changes in the extrusion of dome growth lobes (Watts et al., 2002) as well as eruption style (Calder et al., 2002) and extrusion rate (Calder et al., 2005). Rockfall signals at SHV have also been used to constrain models of extrusion rates and dome and talus slope evolution (e.g. Hale et al., 2009). Because the seismic signals produced by rockfalls lack distinct phases, they cannot be located using conventional travel time methods. Jolly et al. (2002) showed that locating rockfall signals based on the relative signal amplitudes at several stations can be a useful monitoring and research tool, providing invaluable information on the direction of pyroclastic flows.

Low-frequency and Hybrid earthquakes

Low-frequency seismicity at SHV has been primarily observed as what have been termed 'hybrid' events by several authors, as they were initially seen as a hybrid between Volcano-Tectonic (VT) and long-period events (e.g. Lahr et al. (1994) at Redoubt volcano, Alaska or White et al. (1998) at SHV). They are characterised by their high-frequency onset and slowly decaying harmonic codas, allowing them to be distinguished from other volcanic seismic signals such as VT events or rockfalls (Fig. 1.4). Their higher-

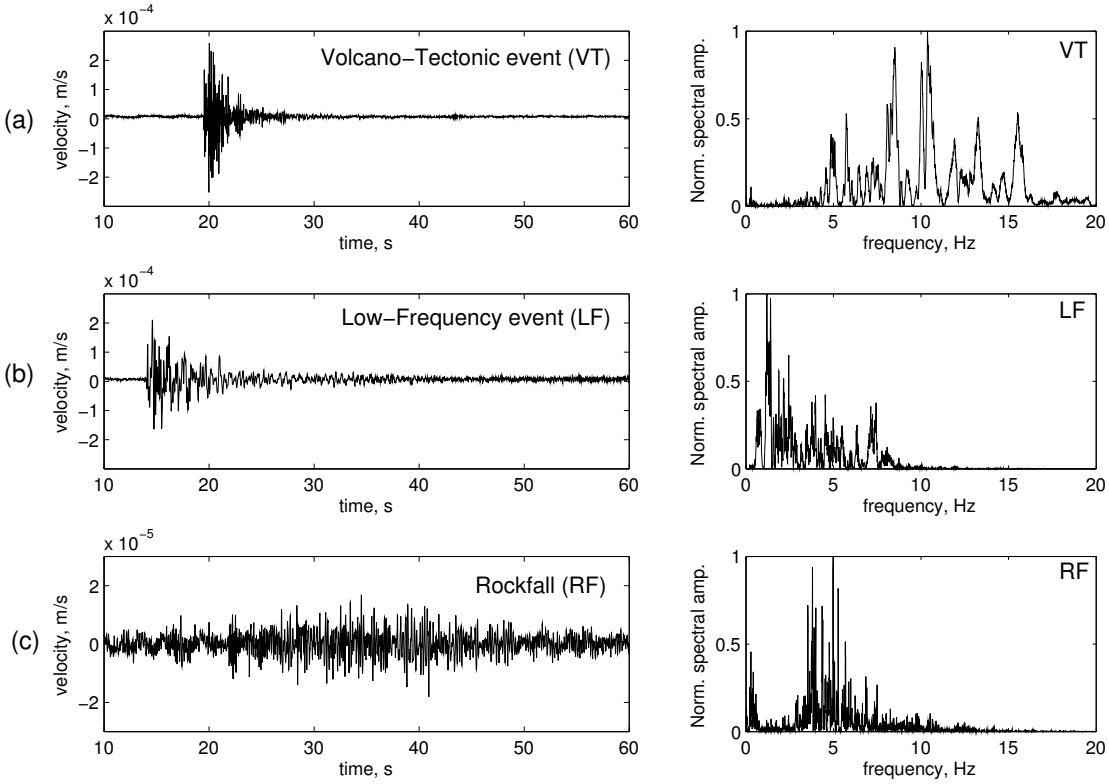

Figure 1.4: Example waveforms and spectra for different types of seismic signals observed on Soufrière Hills Volcano, Montserrat (all are vertical components). (a) A typical volcano-tectonic or VT event with a sharp high-frequency onset and short signal duration. (b) Low-frequency event showing high-frequency onset followed by slowly decaying harmonic coda. (c) This example shows the cigar shaped envelope and emergent signal which is typical of rockfall events.

frequency onset is not always observed, leading to some confusion in nomenclature, with events lacking this termed low-frequency or long-period and not hybrid. However, Neuberg et al. (2000) assert that hybrids and low-frequency events are in fact end-members of a continuum of low-frequency seismicity at SHV, and should be regarded as a result

of the same source processes. Hybrid events at SHV have been extensively studied and were recorded in large numbers throughout the earlier stages of the eruption in 1995-1996 (White et al., 1998) and 1997-1998 (Neuberg et al., 1998) as well as up to 2003 (Ottemöller, 2008). Since this time the number of hybrid earthquakes has declined, even during periods of relatively rapid extrusion, an observation noted by Luckett et al. (2008). However, in July 2008 a hybrid swarm of 1588 hybrid and long-period events between July 26 and July 28 preceded the large explosion which occurred on July 29 (Stewart et al., 2008), one of the largest seismic swarms since the beginning of the eruption in 1995. Low-frequency seismicity also occurred during the burst of rapid extrusion that took place at the volcano from December 2008 to January 2009, with numbers steadily increasing over the month long period (Stewart et al., 2009).

This illustrates one key feature of low-frequency events at SHV: that they occur in swarms with distinct periodicities which have sometimes preceded the major dome collapses or explosions (e.g. Neuberg et al., 1998), and that the dynamics of these swarms can be related to the magma ascent rate (Hammer & Neuberg, 2009). Other key features are their occurrence in families with similar waveforms, and their correlation with cyclic deformation signals. A study which examined low-frequency events from Soufrière Hills volcano in June 1997 led to a classification system being developed to group these similar events into families or multiplets based on their particular waveforms (Green & Neuberg, 2006). Previous use of these multiplets, which have been observed at several different volcanic locations, has been to improve relative source relocation of events (e.g. Got et al., 1994). These different multiplets or families of events with similar waveforms correlate with the deformation and tilt of the volcanic edifice. The occurrences of the different families of events were plotted against tilt and were seen to be well ordered, with the events first occurring at the maximum positive derivative of the tilt. The families of events evolved throughout the swarm (as the tilt increases) and then stopped occurring when the derivative of the tilt reached a minimum. Green & Neuberg (2006) suggest that if the derivative of tilt is taken as a proxy for the rate of pressurisation in the volcano, it can be concluded that low-frequency events are in some respect, either as a consequence or as a trigger, directly related to depressurisation or relaxation within the edifice or conduit system.

1.6 Seismic attenuation

1.6.1 Definitions of attenuation

A seismic wave propagating in an elastic medium will lose amplitude due to geometric spreading as energy spreads out from the source. However, the total energy of the propagating wavefront, integrated over the medium, will remain constant. But if, as in most physical materials, the wave amplitude is damped due to various small-scale processes which can be summarised as the macroscopic process of internal friction (Aki & Richards, 2002), then the material is said to be anelastic. Anelasticity is different to other forms of wave amplitude loss, such as geometric spreading, scattering and multipathing, because seismic energy is actually lost (dissipated as heat) rather than just redistributed throughout the wavefield (Stein & Wysession, 2003).

Q in terms of energy

This anelastic or intrinsic attenuation is often quantified in seismology by a dimensionless quality factor, Q, which has been defined in the literature in different ways depending on the application. In one of the most common definitions it is considered to be the inverse of the internal friction and defined as:

$$\frac{1}{Q(\omega)} = \frac{-1}{2\pi}\frac{\Delta E}{E_{\max}} \tag{1.2}$$

where $E_{\max}$ is the peak energy stored during one cycle at a particular frequency, ω, and ΔE is the energy lost or dissipated during the cycle (Aki & Richards, 2002). Hence, because of the 2π factor, $\frac{1}{Q(\omega)}$ represents the fractional energy loss per radian. The damping of seismic energy is often observed as either (i) the temporal amplitude decay of a standing wave at fixed wavenumber, or (ii) the spatial decay of a propagating wave at a fixed frequency (Aki & Richards, 2002). Case (i) of a *temporal* Q represents how the amplitude decay or attenuation of low-frequency events is actually observed and several methods developed to measure this are fully described in Chapter 4. To use case (ii) and describe the amplitude decay in terms of a spatial decay, Equation 1.2 can be written in terms of an attenuation coefficient, α, as:

$$\frac{1}{Q(\omega)} = \frac{2v_{\text{ph}}\alpha}{\omega} \tag{1.3}$$

where v_{ph} is the phase velocity at frequency ω. Using this definition the spatial reduction of amplitude can be written as an exponential decay process:

$$A(x) = A_0 e^{-\alpha x} \tag{1.4}$$

for a wave propagating a distance x with an initial amplitude A_0. Note that this spatial exponential decay of the amplitude can be absorbed into the normal solution to the wave equation for a travelling wave by the introduction of a complex wavenumber.

An important point is that these definitions are only valid for low attenuation levels (high Q) and become impractical when the loss is large (Kjartansson, 1979). An alternative definition to Equation 1.2, also in terms of energy, and valid for all values of Q is given by O'Connell & Budiansky (1978):

$$\frac{1}{Q(\omega)} = \frac{-1}{4\pi}\frac{\Delta E}{E_{\text{ave}}} \tag{1.5}$$

where ΔE is again the energy loss, and E_{ave} is the average stored energy, during a single sinusoidal deformation cycle. This definition can also be in written terms of the attenuation coefficient as:

$$\frac{1}{Q(\omega)} = \left(\frac{\omega}{2v_{\text{ph}}\alpha} - \frac{\alpha v_{\text{ph}}}{2\omega}\right)^{-1}, \tag{1.6}$$

noting that the first term of the RHS is equivalent to Equation 1.3.

Q in terms of material properties

As well as these definitions in terms of energy, the attenuation can also be directly expressed in terms of the material properties of an anelastic medium:

$$\frac{1}{Q(\omega)} = \tan\delta = \frac{\Im(M_c(\omega))}{\Re(M_c(\omega))} \tag{1.7}$$

where δ is the phase angle or lag between applied stress and resulting strain and $M_c(\omega)$ represents the complex modulus of the material describing the viscoelastic stress-strain relationship (O'Connell & Budiansky, 1978) (see Section 2.1.4 for more discussion on this relationship).

1.6.2 Uses of attenuation

The attenuation of seismic waves is dependent upon, and can therefore provide some information about, the material properties of the medium through which the seismic wave

propagates. This ability makes it a useful measurement in many contexts: in global seismology attenuation studies have often been used alongside seismic velocity tomography to place constraints on the structure and dynamics of the mantle (e.g Roth et al., 2000) and even the core (e.g Souriau & Romanowicz, 1996), since it can be more sensitive to temperature than elastic velocity (Romanowicz, 1998); in applied seismology measuring attenuation is beginning to prove its value as an important tool for determining certain attributes of hydrocarbon reservoirs (Dasgupta & Clark, 1998), such as permeability (Best et al., 1994) or porosity, (Klimentos & McCann, 1990) as it usually linked to processes occurring in the pore-fluid of rocks (Dvorkin & Mavko, 2006). Finally, seismic attenuation has also begun to be used as tool in volcanic environments, and its main applications in this field will now be discussed.

1.6.3 Application to volcanoes

Attenuation and magma properties

Attenuation tomography has been used in regional scale studies to infer and image zones of partial melt beneath volcanic regions (e.g. Southwest Pacific, Barazangi et al. (1974) or the Central Andes, Schurr et al. (2003)) but on a more local scale the main use of seismic attenuation has been in determining the nature, composition and/or properties of volcanic fluids. In order to do this, the attenuative effect of volcanic fluids, such as magma, must be quantified. This is also a necessary step to understand and quantify the ability of a gas-charged magma to allow and support resonance.

The attenuation of seismic waves in a conduit filled with a three-phase magma depends strongly on the magma and melt viscosities as well as the gas and crystal content. Collier et al. (2006) theoretically quantified this attenuation in a gas-charged magma, including the previously neglected effects of diffusion on bubble growth. This diffusion is a process of mass transport by exsolution of volatiles from the melt into the bubble (Navon et al., 1998). The attenuation was calculated through the material properties of the magma, using the ratio of the real and imaginary parts of the complex velocity (see Sections 2.1.4 and 3.3.2 for more details on this relationship). The value of the quality factor, Q, was calculated for varying values of diffusivity and the effect of increasing diffusion was shown to decrease Q significantly, therefore increasing the attenuation. Collier et al. (2006) showed that when bubble growth by diffusion is included (rather than just by gas expansion alone, e.g. Commander & Prosperetti (1989)), the dependence of Q

on pressure and frequency is more complicated and depends on two factors: the melt viscosity and the diffusion processes. From their models, a finite region of maximum Q was identified within the conduit, where the attenuation may be low enough to support conduit resonance, and therefore it was shown that this quantitative assessment of attenuation should now be considered an essential part of any attempt to model seismic wave propagation and resonance in gas-charged magmas.

As well as for magma, intrinsic attenuation has also been estimated for various non-magmatic volcanic fluids, such as bubbly water (Chouet, 1996b; Nakano et al., 1998; Kumagai & Chouet, 2000), gas mixtures (H_2O-CO_2, H_2O-SO_2), liquid-gas mixtures (water-H_2O and basalt-H_2O), and dusty and misty gases (ash-SO_2 and water droplet-H_2O) (Kumagai & Chouet, 2000; Morrissey & Chouet, 2001).

Decomposing the attenuation of a resonating body

In a discussion on harmonic tremor and magma intrusion in the Mammoth Lakes area of California, Aki (1984) was the first to put forward the idea of decomposing the energy loss from a vibrating fluid body. He proposed that the total seismic energy loss could be represented as the sum of the radiation and viscous damping losses:

$$Q_{\mathrm{a}}^{-1} = Q_{\mathrm{i}}^{-1} + Q_{\mathrm{r}}^{-1} \tag{1.8}$$

where Q_{r}^{-1} is the attenuation corresponding to radiation loss and Q_{i}^{-1} is the intrinsic or viscous attenuation which Aki (1984) attributed to magma viscosity. Morrissey & Chouet (2001) suggest that the intrinsic term, Q_{i}^{-1}, encompasses a host of physical damping mechanisms including viscous, thermal, and acoustic damping in bubbly liquids as well as phase interactions in multi-phase fluids. Note that the radiative part, Q_{r}^{-1}, describes the amplitude decay of the resonating body for a purely elastic case, with no intrinsic damping provided by the fluid. Path effects, including further amplitude losses due to scattering, intrinsic attenuation in the edifice and geometric spreading, do not contribute to the measured *temporal* amplitude decay, since each packet of energy that is radiated from the fluid travels the *same path* between the resonator and receiver. Although the terminology is different to that used in applied seismology, in this study, the same convention as Aki (1984); Kumagai & Chouet (1999; 2000) and others who have studied volcanic signals is followed, with the value for the attenuation obtained from the temporal amplitude decay of the observed signal referred to as the *apparent* attenuation, Q_{a}^{-1}.

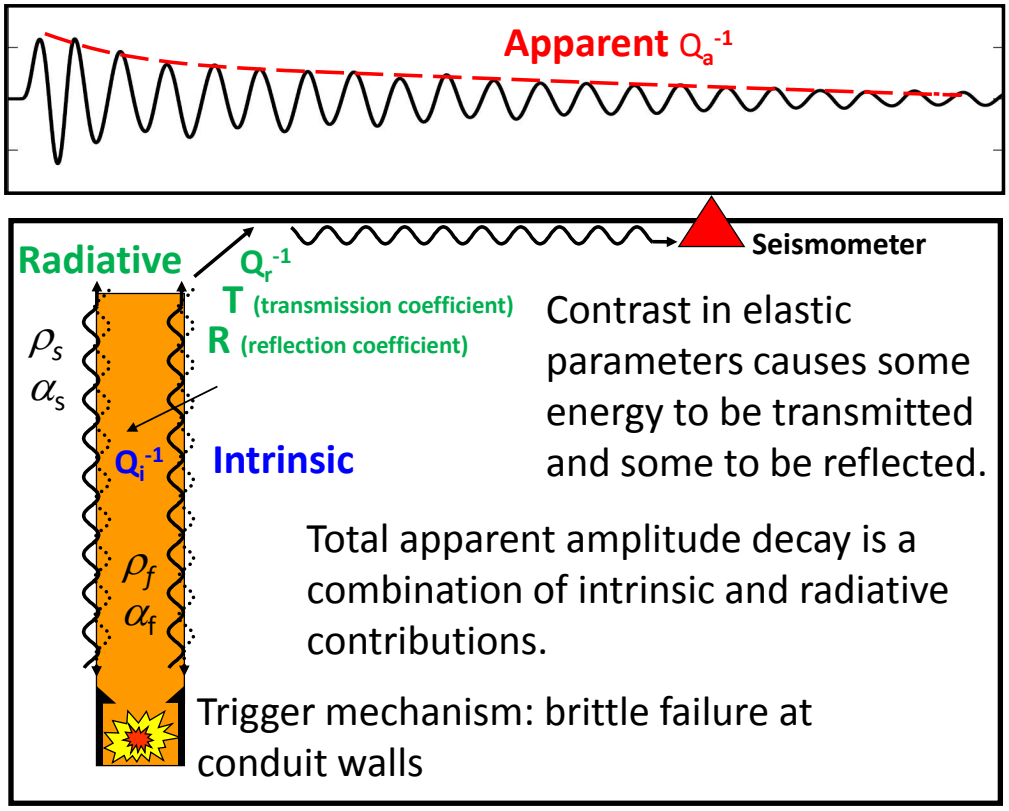

Figure 1.5: Schematic cartoon illustrating how the total amplitude decay of the recorded signal, Q_{a}^{-1}, is composed of an intrinsic part, Q_{i}^{-1}, and radiative part, Q_{r}^{-1}. The contrast in elastic parameters is described by the different densities of the fluid and solid, ρ_{f} and ρ_{s}, and the seismic velocities, α_{f} and α_{s}, respectively.

Attenuation as a probe for fluid composition

Many authors (e.g. Kumagai & Chouet, 1999; 2000) have treated the coda portion of low-frequency earthquakes as simply the superposition of decaying sinusoids of different frequencies and different Q factors, which have been argued to represent the excitation response of a resonating system (Nakano & Kumagai, 2005b). One way to describe such a waveform is via its complex frequencies, which are analogous to real damping factors for a travelling wave expressed as a complex exponential function. The preferred method of calculating the complex frequencies of the seismic waveform has been by performing spectral analysis using the parametric 'Sompi' method (Kumazawa et al., 1990), based on a homogeneous autoregressive (AR) description of a linear dynamic system. Estimation of the apparent attenuation from the complex frequencies has often accompanied waveform inversion and the 'crack model' described in Section 1.4. The intrinsic attenuation of the fluid, Q_{i}^{-1}, is either neglected (e.g Morrissey & Chouet, 2001) or treated separately (e.g Kumagai & Chouet, 2000), since these losses are 'not

included in the crack model simulations' (Nakano & Kumagai, 2005b)). The radiative process is assumed to dominate the energy loss and Kumagai & Chouet (2001) described the dependence of Q_{r}^{-1} on the aspect ratio of such cracks and on the specific mode of resonance analysed.

This approach has been used as a 'probe' for the composition of volcanic fluids by comparing the measured Q_{a}^{-1} to the Q_{r}^{-1} generated by the 'fluid-driven crack model' containing fluids of the appropriate density and compressibility to generate the required impedance contrast (Kumagai & Chouet, 1999). Because of the trade-off between geometry and fluid properties, discussed in Section 1.4, the large aspect ratio of crack-like geometries effectively forces the fluid to be a low density, highly compressible material to generate the high impedance contrast needed to sustain the resonance and produce the correct Q_{r}^{-1}. Also, with both parts of the attenuation considered separately this approach is limited in what it can achieve and not universally applicable, because not all components and effects are taken into account.

The 'Sompi' method has also been used to analyse temporal variations of the complex frequencies, and hence attenuation, of low-frequency events at Mount Spurr volcano in Alaska (De Angelis & McNutt, 2005), Cotopaxi (Molina et al., 2004) and Tungurahua volcanoes (Molina et al., 2008) in Ecuador and Kusatsu-Shirane volcano, Japan (Nakano & Kumagai, 2005a). The interpretation of the observed temporal variations has been either geometrical, compositional (Nakano & Kumagai, 2005a) or a combination of the two (De Angelis & McNutt, 2005).

1.7 Motivation

1.7.1 Linking seismic signals to magma properties: the wider context

As we have seen, both the generation and propagation of seismic waves in a volcanic environment are highly dependent on the properties of volcanic fluids. This means a multi-disciplinary approach is required if we are to have a complete picture of the system which generates low-frequency seismicity. Therefore it is necessary to combine and incorporate information on magma flow and the spatial distribution of magma properties into wavefield models of the seismicity, since these provide clues and constraints such as where the triggering and resonance may occur. However, this is a two-way process that also aims to relate the characteristics of observed seismic signals, directly to

changes in the internal conditions of the volcano. This has important implications for monitoring and understanding the dynamical behaviour of volcanoes, particularly with regard to cyclicity at silicic volcanoes. Making the link between observed seismicity and magmatic processes is also a key step in the assessment of volcanic hazards, especially if low-frequency seismicity can be used to gain quantitative constraints on key properties such as the magma ascent rate. This research therefore has applications to forecasting future eruptive behaviour and style, and this provides the ultimate motivating factor for the study.

1.7.2 Aims

In a broad sense this project aims to examine the relationship between magma properties and low-frequency seismicity at Soufrière Hills Volcano, Montserrat, and by combining modelling work, theory and data analysis, allow the seismicity to provide information and constraints on the magma properties (and vice versa).

As discussed in Section 1.6, attenuation is an important parameter to measure because it is a function of material properties. This is particularly useful on volcanoes, where constraining the properties of sub-surface fluid bodies is a key aim of monitoring and forecasting. The following inter-linked problems are some of the key questions that this study hopes to address by using the attenuation of volcanic seismic signals:

1. Resonance and the source mechanism of low-frequency earthquakes.

   Attenuation is important in understanding the source of low frequency earthquakes, in terms of both the trigger and the resonance. As previously discussed, Chouet (1996b) has criticised the idea of conduit resonance in a highly attenuating bubbly magma. The question of whether a viscous magma can support resonance in this way is still open for debate. Can quantifying the attenuation of resonating seismic waves in magma provide some new insight?

2. Acoustic and interface wave attenuation.

   As Collier et al. (2006) point out, estimations of Q_i^{-1} for magma and other volcanic fluids have all assumed that the seismic energy propagates as a simple acoustic wave. Yet we know that low-frequency resonance is a result of interface waves trapped in a narrow conduit, dyke or crack, and that these waves are fundamentally different in terms of velocity and dispersion to acoustic waves (Ferrazzini & Aki,

1987; Chouet, 1986; 1988; Neuberg et al., 2000). This raises several questions: How are interface waves different to acoustic waves in terms of their attenuation? Can we use the attenuation of the fluid as a parameter for discriminating between crack and conduit models for resonator source bodies?

3. Decomposition of attenuation.

   As already discussed in Section 1.6.3, previous efforts have assumed the amplitude decay from a resonating body to be made up of two components, the radiative part related to the geometry and elastic parameters contrast and an intrinsic part related to fluid viscosity. It is really possible to decompose linearly the intrinsic and radiative components?

4. Constraints on magma properties.

   What information can be gleaned from the two components in terms of constraining the geometry and fluid properties of the resonating system? Through the appropriate choice of rheological model can we obtain useful constraints on the viscosity? Appropriate quantitative understanding of amplitude losses is also essential if the ascent rate of magma is to be constrained by a combination of event rate and signal amplitudes.

1.7.3 Outline of thesis

Chapter 2 describes the modelling of attenuated low-frequency volcanic earthquakes. Section 2.1 contains a summary of the methodology and theory behind the model and a review of previous implementations of attenuation through viscoelasticity. New modifications to the model and amplitude calibration are then described in Section 2.2. Section 2.3 uses the model to explore the dynamics of resonance, how energy is radiated from a conduit or dyke, and hence the radiative part of the amplitude decay. Finally, in Section 2.4, the effect of the intrinsic attenuation of the fluid on the overall amplitude decay of the signal is examined through forward modelling of low-frequency earthquakes in a viscoelastic medium. Parts of this chapter have been presented at several international conferences including Smith & Neuberg (2007a;b; 2008; 2010).

In Chapter 3 an expression for the phase velocity and hence the attenuation of interface waves is derived, for a viscous fluid layer with realistic volcanic parameters. This is then compared to the attenuation of acoustic waves in the fluid. The key results of this

chapter were presented in Smith & Neuberg (2010).

Chapter 4 describes the development, testing and refinement of an automated time-domain method to calculate the apparent attenuation of a signal at a given frequency.

Chapter 5 presents measurements of attenuation from datasets of low-frequency earthquakes at SHV, and tries to link the measured attenuation to viscosity. In this chapter the results of the numerical and analytical approaches are brought together, and the constraints on the properties of the magma provided by the seismological trends and observations are discussed. Some of the preliminary results used in this chapter were presented in Smith & Neuberg (2008).

Finally, a wider discussion on the significance and implications of this research, the main conclusions and suggestions for future work are presented in Chapters 6 and 7.

Chapter 2

Modelling attenuated low-frequency volcanic earthquakes

Forward modelling of seismic wave propagation allows insight to be gained into the processes which control the character of low-frequency earthquakes. The effects of both temporal and spatial variations in the properties of the magma or volcanic edifice on low-frequency earthquakes can be quantified using numerical models. This is something which cannot easily be achieved analytically. Since attenuation is a seismic attribute that can be linked directly to material properties, modelling the propagation of seismic waves in an anelastic medium allows the magma viscosity and rheology to be constrained, through their impact on the amplitude decay of such signals.

This chapter aims to resolve some of the key questions posed in Section 1.7.2, such as: Can a fluid body filled with highly viscous magma support resonance of seismic energy; and, what are the contributions to the observed amplitude decay of the radiative and intrinsic components? It begins with a theoretical description of the finite-difference method for modelling both elastic and viscoelastic wave propagation, and summarises previous applications of such models to volcanic environments. These models are then used to examine both the radiative and intrinsic components of the apparent attenuation, and their effects on the observed amplitude decay. The methods for measuring the attenuation (from synthetic signals or data) are fully described in Chapter 4.

2.1 Introduction to the finite-difference model

The models used in this thesis simulate the propagation of seismic waves in a volcanic environment, and build on the work of many previous efforts in this field. It is therefore necessary to summarise here (Section 2.1) the history, evolution and characteristics of these models and fully acknowledge the contributions of others to this research. The relative merits of the *crack* and *conduit* models, were discussed in Section 1.4 and so will not be repeated here. This chapter follows in the footsteps of many authors (e.g. Neuberg et al., 2000; Jousset et al., 2003; 2004; Sturton & Neuberg, 2006) and develops the models that simulate low-frequency volcanic earthquakes generated in a resonating conduit.

2.1.1 The finite-difference method

The finite-difference method is a numerical method of solving differential equations. The basic approach of the method is to use a grid to cover a solution domain and then to consider the differential equation to be solved at every node of the grid, replacing the derivatives in the differential equation by the differences between values at neighbouring points. As a result of this discretization process, the differential equation is converted to a set of algebraic expressions at every node of the grid. Solving the algebraic equations at all the nodes in the solution domain, together with appropriate boundary and initial conditions, gives the numerical solution to the differential equation under investigation. Here we are concerned with the propagation of seismic waves through both elastic and viscoelastic media, so the differential equations to be solved are the equations of motion for the medium, coupled to a constitutive relationship between stress and strain.

2.1.2 Models of elastic wave propagation

The model of Jousset et al. (2004), and that used in this thesis, simulates wave propagation in a *viscoelastic* medium, but uses much of the same formulation for the underlying finite-difference scheme as earlier models of wave propagation through an *elastic* medium (e.g. Neuberg et al., 2000). Hence these earlier elastic models will be described first, before then, in Section 2.1.3, examining how the attenuation is introduced into the later model.

Neuberg et al. (2000) were one of the first to model a resonating conduit of magma as a potential source of low-frequency earthquakes. The finite-difference code used in their wavefield model used a 2-D staggered grid stress-velocity formulation based on the work of Virieux (1986), expressed at the 4^{th}-order in space and 2^{nd}-order in time (Levander, 1988), to solve the 2-D elastic equations of motion. Rather than using the wave equation which is a 2^{nd}-order hyperbolic system, Virieux (1986) formulated the problem in terms of the elastodynamic equations, simply derived from Newton's 2^{nd} Law:

$$\begin{aligned} \rho\frac{\partial^2 u_x}{\partial t^2} &= \frac{\partial \sigma_{xx}}{\partial x} + \frac{\partial \sigma_{xz}}{\partial z} \\ \rho\frac{\partial^2 u_z}{\partial t^2} &= \frac{\partial \sigma_{xz}}{\partial x} + \frac{\partial \sigma_{zz}}{\partial z} \end{aligned} \tag{2.1}$$

where ρ is the density of the medium, u_x and u_z are the horizontal and vertical components of displacement and σ_{xx}, σ_{zz}, σ_{xz} are the normal and tangential components of the stress tensor.

By replacing the 2^{nd} derivatives of the displacements with the 1^{st} derivatives of the velocity with respect to time, these equations can easily be reformulated in a form which Levander (1988) and Jousset et al. (2004) term the *P-SV* equations of motion:

$$\begin{aligned} \rho\frac{\partial v_x}{\partial t} &= \frac{\partial \sigma_{xx}}{\partial x} + \frac{\partial \sigma_{xz}}{\partial z}, \\ \rho\frac{\partial v_z}{\partial t} &= \frac{\partial \sigma_{xz}}{\partial x} + \frac{\partial \sigma_{zz}}{\partial z} \end{aligned} \tag{2.2}$$

where v_x and v_z are the horizontal and vertical components of the velocity. The reason for this terminology is that only *SV*-waves, whose displacements are perpendicular to the direction of propagation and in the *vertical* plane, can be modelled in 2-D. The implementation of the model used here contains one vertical and one horizontal dimension, hence *SH*-waves are not considered.

The constitutive relationship for a linearly elastic, isotropic and homogeneous medium, commonly known as Hooke's law, relates the stress to the strain for assumed infinitesimal strains, and in summation notation is given by

$$\sigma_{ij} = \lambda\epsilon_{kk}\delta_{ij} + 2\mu\epsilon_{ij}, \tag{2.3}$$

where σ_{ij} are the components of the stress tensor, ϵ_{ij} are the components of the strain tensor, and δ_{ij} is the Kronecker delta. The symbols λ and μ denote the 1^{st} and 2^{nd} Lamé parameters.

Together the coupled *P-SV* equations of motion (Equation 2.2) and the constitutive law (Equation 2.3) can be transformed into a 1^{st}-order hyperbolic system of equations in

terms of velocities and stress (Virieux, 1986):

$$\begin{gathered}\frac{\partial v_x}{\partial t} = \frac{1}{\rho}\left(\frac{\partial \sigma_{xx}}{\partial x} + \frac{\partial \sigma_{xz}}{\partial z}\right), \quad \frac{\partial v_z}{\partial t} = \frac{1}{\rho}\left(\frac{\partial \sigma_{zx}}{\partial x} + \frac{\partial \sigma_{zz}}{\partial z}\right) \\ \frac{\partial \sigma_{xx}}{\partial t} = (\lambda + 2\mu)\frac{\partial v_x}{\partial x} + \lambda\frac{\partial v_z}{\partial z}, \quad \frac{\partial \sigma_{zz}}{\partial t} = (\lambda + 2\mu)\frac{\partial v_z}{\partial z} + \lambda\frac{\partial v_x}{\partial x}. \\ \frac{\partial \sigma_{xz}}{\partial t} = \mu\left(\frac{\partial v_z}{\partial x} + \frac{\partial v_x}{\partial z}\right)\end{gathered} \tag{2.4}$$

This set of five equations is then discretized and solved numerically with the finite-difference method, using the explicit scheme of Levander (1988).

The derivatives are discretized using centred finite-differences, and assuming the equations are verified at nodes, this leads to a unique staggered grid; with the difference from usual finite-difference schemes being that the two separate components of the velocity are not known at the same node (Virieux, 1986). The scheme is explicit, in that the numerical values for the velocity and stress components at a particular time level are computed explicitly from the values at the previous timestep, and therefore a stability condition must be satisfied. This numerical condition imposes a computational limit on the choice of discretization. The explicit stability criterion for the $O\left(dx^4, dt^2\right)$ scheme used, with equal x and z grid spacing, is given by

$$dt < 0.606\frac{dx}{\alpha} \tag{2.5}$$

where dt is the timestep in seconds, dx is the grid spacing in metres and α is the P-wave velocity of the medium (Levander, 1988). This type of constraint is often seen written in the general form:

$$v\frac{dt}{dx} < C \tag{2.6}$$

for an arbitrary velocity v, and is often called the Courant-Friedrichs-Lewy or *CFL condition*, with the quantity C termed the *Courant Number* (Courant et al., 1928). In this case the factor 0.606 arises from a purely geometrical constraint and comes from the numerical constants used to approximate the 4^{th}-order derivative in the staggered grid scheme. This explicit formulation also introduces a degree of numerical dispersion, the amount of which is controlled by how close you push the model to the stability criterion limit and also the frequency or wavelength of the propagating wave. Therefore an inherent trade-off exists between accuracy and computation time. Levander (1988) suggest that the shortest shear-wavelength (highest frequency) in the grid needs to be sampled at at least 5 grid-points per wavelength to minimise the effects of grid dispersion and anisotropy.

Virieux (1986) demonstrated that for the finite-difference scheme described here, the same formulation can be used to solve the system of equations for any liquid areas introduced within the medium, without the complex problem of connecting the liquid and solid areas along an interface with explicit boundary conditions. This makes the scheme a particularly suitable choice for numerical modelling of magma-filled bodies in a volcanic environment.

Absorbing boundary conditions were applied on the bottom and sides of the solution domain to reduce reflections of the seismic energy from these boundaries, by employing an attenuative zone on each of these three boundaries. The absorbing conditions were implemented by using a one-way approximation to the wave equation at the boundaries (Clayton & Engquist, 1977) and also by exponential damping of the amplitudes in this zone (Cerjan et al., 1985).

Neuberg et al. (2000) firstly compared the wavefield in and around a fluid-filled conduit embedded in an elastic half-space to that of a point source in a purely fluid medium. The fluid medium example demonstrated circular wavefronts propagating with the expected acoustic velocity of the fluid. The model with the conduit present by contrast, shows that most of the energy remains trapped inside the conduit, and whilst the waves inside the conduit again propagate with the acoustic velocity, interface waves form and propagate along the boundaries with a much lower velocity. The velocity of the interface waves in the numerical simulations was found by Neuberg et al. (2000) and Sturton & Neuberg (2006) to match the phase velocity predicted by the analytical work of Ferrazzini & Aki (1987). After the wavefronts detach from the interface they then propagate through the surrounding medium, and due to further interaction with the free-surface, form a complicated interference pattern. It was shown that, in agreement with observed data, the fundamental frequency of the low-frequency seismic signal was not dependent on which virtual recording station the signal was observed at on the free surface, but the amplitude of the spectral peaks did change with each station due to this complex interference pattern. This observation will have important implications for the determination of attenuation from the amplitude decay.

For an open system scenario, with the conduit top directly at the free surface, the seismic energy leaks away faster and the resonance is only sustained for a short period (Neuberg et al., 2000).

Depth-dependence

The effect of varying gas content in the magma with depth was modelled by Neuberg et al. (2000) by introducing depth-dependent acoustic velocity into the fluid-filled container simulating the volcanic conduit. Neuberg et al. (2000) varied the gas content, firstly as a constant and then as a function of depth, within the fluid to produce corresponding acoustic velocity profiles within the conduit and compared the results of the simulated wavefield to a constant acoustic velocity model. A change in the gas content was observed to change the spectral lines observed at virtual recording stations on the free surface, since the corresponding velocity change affects the fundamental wavelength of the resonance. More realistic parameter gradients at the conduit walls and depth-dependent magma properties, based on the work of Sturton & Neuberg (2003), were also taken into account in the models of the low-frequency seismic wavefield by Jousset et al. (2003; 2004). The main effects of a transition zone in the properties at conduit walls were to delay the travel-times and also to modify the frequency dependence of the dispersion. Jousset et al. (2003) concluded that vertical gradients in magma properties in the conduit allow more energy to be released in areas where the impedance contrast is low, but are not the key parameters that control the character or the occurrence of the low-frequency resonance.

Time-dependence

Gliding spectral lines have been observed on Montserrat and many other volcanoes and have been modelled by repeated triggering of identical low-frequency seismic events (Powell & Neuberg, 2003). The shifting of the spectral lines is indicative of a change in either the value of the frequency spacing $\Delta\omega$ or the time between events Δt, and therefore implies a rapid change in the interface wave speed in the conduit. This change in wave speed reflects changes in magma properties, in particular changes in the pressure causing a change in the gas volume fraction and therefore the seismic velocity. Importantly this means that through modelling the time-dependent effects of these properties on the seismic wavefield, observed changes in $\Delta\omega$ and Δt can now be directly related to changes in magma pressure and the gas volume fraction within the conduit. The finite-difference conduit resonance models of Neuberg et al. (2000) were further developed by Jousset et al. (2003) to include the effects of this time-dependence of the magma properties controlling seismic wave propagation, with the aim of explaining the changing frequency

content of the spectrograms. This was achieved by re-evaluating both the elastic parameters and the densities used at each node for every time interval within the finite-difference code, thus computing the changing magma properties and the seismic wavefield simultaneously. The numerical values for the changing parameters used were adapted from the work of Sturton & Neuberg (2003) and the seismograms were restricted to lengths of 60 seconds to avoid numerical instabilities and to ensure reasonable computation times.

Conduit geometry

The effects of conduit length and acoustic velocity on conduit resonance were examined by Sturton & Neuberg (2006) who used numerical models to compare synthetic results to observed signals and spectrograms from Montserrat. Short-windowed spectrograms were used to examine the time and frequency relationships within particular events in detail and the numerical results were compared to the observed seismic data from Montserrat. The numerical and observed spectrograms shared similar features and showed that low-frequency events from Montserrat are composed of distinct subevents, with the spacing of subevents being dependent on the conduit length. Increasing the conduit length was shown to increase the spacing between subevents because the wave has to travel further along the conduit, whilst decreasing the conduit length brought the subevents closer together, eventually merging to produce a tornillo-like event (Sturton & Neuberg, 2006).

2.1.3 Viscoelasticity

It is clear that in order to model the attenuation of seismic waves we need to move away from a purely elastic medium where all strain energy is recovered and choose some appropriate rheological model that describes the dissipation of the energy of the propagating wave. In the following sections (2.1.3-2.1.5) the basic principles of linear viscoelastic theory are reviewed, before discussing how the intrinsic attenuation is implemented into the finite-difference model, following the method of Jousset et al. (2004). New modifications, source implementation and amplitude calibration of the model are described in Section 2.2, before the model is then used to study the radiative and intrinsic parts of the amplitude decay, in Sections 2.3 and 2.4, respectively.

Linear viscoelastic theory and the Standard Linear Solid

The theory of linear viscoelasticity relates stresses to strains for a given material and is valid for small changes in the stress and strain. The general differential equation of 1-D viscoelasticity is given by:

$$\left(1 + \alpha_1 \frac{\partial}{\partial t} + \alpha_2 \frac{\partial^2}{\partial t^2} + \ldots \alpha_n \frac{\partial^n}{\partial t^n}\right) \sigma(t) = \left(\beta_0 + \beta_1 \frac{\partial}{\partial t} + \beta_2 \frac{\partial^2}{\partial t^2} + \ldots \beta_m \frac{\partial^m}{\partial t^m}\right) \epsilon(t) \tag{2.7}$$

where σ and ϵ are the stress and strain, and α and β are the parameters that define the rheological behaviour of the material (Jousset et al., 2004).

Two fundamental end-members can be derived from this equation (Barnes et al., 1989). Firstly if β_0 is the only non-zero parameter we have Hooke's Law for an elastic material, the mechanical analogue of which is a spring with rigidity $\mu = \beta_0$. For the case where β_1 is the only non-zero parameter, we have Newton's viscous law where the stress is proportional to the strain rate, with the mechanical representation of the material being a dashpot with viscosity $\eta = \beta_1$.

A viscoelastic material is defined by a superposition of these two cases, such that the stress depends on both the strain and rate of strain. The mechanical analogue of this system can be considered as a combination of a spring (elastic behaviour) and a dashpot (viscous behaviour). Using more parameters α and β produces a wide range of viscoelastic models, with a given material behaving like a solid or a viscous fluid depending on the timescale of the deformation processes. Hence, more complex material behaviours have mechanical analogues involving combinations of springs and dashpots in series and in parallel (Barnes et al., 1989). Two simple and widely used examples are the Maxwell body, consisting of a spring and dashpot in series, and the Kelvin-Voight body, consisting of a spring and dashpot in parallel.

The Standard Linear Solid as an appropriate magma rheology

Jousset et al. (2004) looked at previous studies modelling the rheology of volcanic media and considered two models: (1) a bubble- and crystal-free melt behaving like a Maxwell body (Dingwell, 1995) and (2) a rhyolitic foam best approximated by a so-called Burger's body (Figure 2.1), and in three-phase magmas (melt, crystals and gas) having two viscoelastic behaviours that can be distinguished, depending on the crystal

content (Bagdassarov et al., 1994). The Standard Linear Solid (SLS), sometimes called a

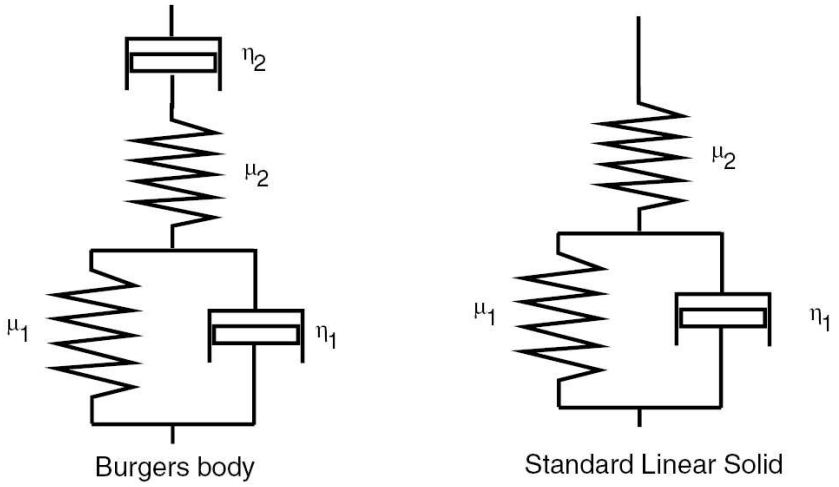

Figure 2.1: Mechanical models for (a) Burgers body and (b) Standard Linear Solid (SLS). The μ_n and η_n values represent the rigidities of the springs and the shear viscosities of the dashpots used in the mechanical analogues. At seismic frequencies the viscosity controlling the long timescale vanishes and the two models are equivalent. (Figure taken from Jousset et al. (2004)).

Zener model (Zener, 1948), is a rheological body whose mechanical analogue is a spring (rigidity μ_1) and a dash-pot (viscosity η_1) in parallel, in series with a second spring (rigidity μ_2) (see Figure 2.1). The presence of crystals in the melt causes the material behave more elastically than a viscous Maxwell body, leaving the Burger's Body as the more realistic choice. Jousset et al. (2004) argue that at seismic frequencies above 2 Hz its long-timescale process vanishes, equivalent to a frozen dashpot, and it is therefore equivalent to an SLS. Hence, they argue, an SLS can approximate a rhyolitic foam at seismic frequencies.

2.1.4 Modelling the intrinsic attenuation

Relating the Quality factor, Q, and material properties

Jousset et al. (2004) show that by taking the Fourier Transform of the 1-D differential equation of linear viscoelasticity (Equation 2.7), the quality factor can be related to the phase-lag between stress and strain, and the properties of the material via the relaxation functions. Taking the Fourier transform of Equation 2.7 gives:

$$\tilde{\sigma}(\omega) = \frac{\beta_0 + \beta_1(i\omega) + \beta_2(i\omega)^2 + \ldots + \beta_n(i\omega)^n}{1 + \alpha_1(i\omega) + \alpha_2(i\omega)^2 + \ldots + \alpha_n(i\omega)^n}\tilde{\epsilon}(\omega) = M_c(\omega)\tilde{\epsilon}(\omega) \tag{2.8}$$

where $\tilde{\sigma}(\omega)$ and $\tilde{\epsilon}(\omega)$ are the Fourier transforms of the stress and strain, and $M_c(\omega)$ is the complex relaxation modulus for an angular frequency ω.

If the input strain is harmonic, i.e. $\epsilon(t) = \epsilon_0 e^{i\omega t}$, with a stress response $\sigma(t) = \sigma_0 e^{i(\omega t+\delta)}$, using Equation 2.8, Jousset et al. (2004) show that the phase lag between stress and strain can be related to the complex relaxation modulus through:

$$\tan\delta = \frac{\Im(M_c(\omega))}{\Re(M_c(\omega))}. \tag{2.9}$$

As δ represents the lag of stress behind applied strain, a measure of the attenuation is given via the quality factor, Q, and defined as a function of frequency by O'Connell & Budiansky (1978) as:

$$\frac{1}{Q(\omega)} = \tan\delta = \frac{\Im(M_c(\omega))}{\Re(M_c(\omega))}. \tag{2.10}$$

Q and the Standard Linear Solid

In one dimension, the Standard Linear Solid is governed by the constitutive equation:

$$\sigma + \tau_\sigma \frac{\partial\sigma}{\partial t} = M_R \left(\epsilon + \tau_\epsilon \frac{\partial\epsilon}{\partial t}\right) \tag{2.11}$$

where σ and ϵ are the stress and strain, and the relaxation modulus of the medium, M_R is

$$M_R = \frac{\mu_1\mu_2}{(\mu_1+\mu_2)}. \tag{2.12}$$

The stress relaxation time (under constant strain) is $\tau_\sigma = \eta_1/(\mu_1+\mu_2)$ and the strain relaxation time (under constant stress) is $\tau_\epsilon = \eta_1/\mu_1$. The solution of Equation 2.11 for $\epsilon = \epsilon_0 H(t)$ is $\sigma(t) = \epsilon_0 G_1(t)$ where $G_1(t)$ is the stress relaxation function and $H(t)$ is the Heaviside step function. For a single SLS, Jousset et al. (2004) give the stress relaxation function as:

$$G_1(t) = M_R \left(1 - \left(1 - \frac{\tau_\epsilon}{\tau_\sigma}\right) e^{\frac{-t}{\tau_\sigma}}\right) H(t) \tag{2.13}$$

where M_R is the relaxation modulus and τ_σ and τ_ϵ represent the stress and strain relaxation times.

One SLS or relaxation mechanism is not usually sufficient to describe fully the anelastic behaviour of a material, so an array of several SLS in parallel is used to model the particular rheology (Jousset et al., 2004). By using an array of L SLS it is possible to get a macroscopic model of the anelasticity (Ben-Menahem & Singh, 2000), sometimes

referred to as a Generalised Zener model in the literature (e.g. Carcione, 2001). To implement this, the definition given by Blanch et al. (1995) for the stress relaxation function for an array of L Standard Linear Solids is used:

$$G_L(t) = M_R \left(1 - \sum_{\ell=1}^{L} \left(1 - \frac{\tau_{\epsilon\ell}}{\tau_{\sigma\ell}} \right) e^{\frac{-t}{\tau_{\sigma\ell}}} \right) H(t) \tag{2.14}$$

where M_R is the relaxation modulus and $\tau_{\sigma\ell}$ and $\tau_{\epsilon\ell}$ represent the stress and strain relaxation times for the ℓth SLS. Hence, for an array of L SLS, Equations 2.10 and 2.14 yield:

$$Q(\omega) = \frac{1 - L + \sum_{\ell=1}^{L} \frac{1 + \omega^2 \tau_{\epsilon\ell} \tau_{\sigma\ell}}{1 + \omega^2 \tau_{\sigma\ell}^2}}{\sum_{\ell=1}^{L} \frac{\omega(\tau_{\epsilon\ell} - \tau_{\sigma\ell})}{1 + \omega^2 \tau_{\sigma\ell}^2}}. \tag{2.15}$$

Using this expression, it is possible to model many attenuative frequency behaviours by adjusting the relaxation times for the L mechanisms. Attenuation is in general frequency dependent (Aki, 1980), but since McDonal et al. (1958) argued that Q is approximately constant in the seismic frequency range (1-200Hz), this assumption has often been applied, particularly in exploration seismology (e.g. Robertsson et al., 1994; Blanch et al., 1995). Equation 2.15 can be used to yield a constant Q in a desired frequency band using the method of Blanch et al. (1995), which, in essence, inverts for the relaxation times or tau parameters ($\tau_{\sigma\ell}$ and $\tau_{\epsilon\ell}$ are functions of the SLS rigidities and viscosities $\mu_{1,2\ell}$ and η_ℓ) that minimise, in a least-squares sense, the difference between the attenuation of the array of SLS at each frequency and a constant value. This constant Q assumption is the approach used by Jousset et al. (2004) and in the remainder of this chapter. In Chapter 3 a Kelvin-Voight rheology is implemented within the finite-difference model, with a linear frequency dependence of the attenuation, to allow direct comparison with analytical results.

2.1.5 Wave propagation in a linear viscoelastic medium

This section briefly describes the equations of motion solved for in the models of Jousset et al. (2004), using the SLS as their rheological model for a volcanic medium. A more complete description can be found in their paper.

Constitutive relationship

The basis of linear viscoelastic theory is that the value of the stress tensor σ_{ij} depends on the time history of the strain tensor $\epsilon_{k\ell}$, and the general constitutive relationship reinforces the idea that viscoelastic media have a 'memory' of previous stress conditions:

$$\sigma_{ij} = G_{ijk\ell} * \frac{\partial \epsilon_{k\ell}}{\partial t} = \frac{\partial G_{ijk\ell}}{\partial t} * \epsilon_{k\ell} \tag{2.16}$$

where $*$ denotes convolution, and $G_{ijk\ell}$ represents the components of a fourth-order tensor of stress relaxation functions, analogous to the elasticity tensor. This equation in fact represents a generalisation of the 1-D stress-strain relationship in Equation 2.7 to an arbitrary viscoelastic medium in three spatial dimensions. However, given some assumptions this expression can be simplified somewhat and for an isotropic, homogeneous medium this tensor $\mathbf{G}$ collapses to two independent functions Λ and M, such that:

$$\sigma_{ij} = \frac{\partial \Lambda}{\partial t} * \epsilon_{kk}\delta_{ij} + 2\frac{\partial M}{\partial t} * \epsilon_{ij} \tag{2.17}$$

where δ_{ij} is the Kronecker delta, Λ is the longitudinal relaxation function and M is the shear relaxation function.

Together, the equations of motion, Equation 2.2, and the constitutive relationship, Equation 2.17, describe viscoelastic wave propagation in an isotropic, homogeneous, viscoelastic medium; where the Λ and M functions used to describe the rheology are taken from the expression for an array of SLS in Equation 2.14 (Blanch et al., 1995; Jousset et al., 2004). In summary, the viscoelastic finite-difference model uses the same equations of motion as the elastic models, but with a new constitutive stress-strain relationship based on a SLS rheology.

The viscoelastic finite-difference scheme

The viscoelastic finite-difference model builds on the elastic models, but differs in the following important ways:

- Viscoelastic dissipation of the seismic energy in the medium introduces physical (in addition to the numerical) dispersion and implies that seismic energy propagates with a phase velocity. This means we need a new stability criterion that is somehow frequency (or timescale) dependent, such that a sufficiently small enough timestep

is employed in order to accommodate the highest phase velocity in the model. Hence, the stability criterion of the viscoelastic scheme depends on the relaxation times of the SLS used, with the velocity used to define the Courant Number, $v_{max}dt/dx$, given by

$$v_{max} = \sqrt{\frac{\tau_\epsilon M_R}{\tau_\sigma \rho}} \tag{2.18}$$

where M_R is the relaxation modulus, with τ_σ and τ_ϵ the stress and strain relaxation times for the SLS (see Equation 2.12), with this maximum phase velocity occurring at infinite frequency (Jousset et al., 2004). Contrast this with Equation 2.5 for the elastic finite-difference scheme, which is only dependent on the choice of discretization.

- The absorbing boundary conditions at the domain edges are applied in the same way (non-reflecting boundaries (Clayton & Engquist, 1977) and exponential damping (Cerjan et al., 1985)), plus an additional damping factor introduced by setting a very high level of attenuation in the damped zone.

- The implementation of the free surface boundary condition varies between the elastic and viscoelastic models. The elastic medium model of Neuberg et al. (2000) implements the stress-free boundary condition by simply setting all components of the stress tensor to zero above the free-surface, following Xu (1995). The viscoelastic model of Jousset et al. (2004) instead sets only the traction vector, with components T_j, to zero:

$$T_j = \sigma_{ij} n_i = 0 \tag{2.19}$$

for the components of the stress tensor σ_{ij} and normal vector to the local surface n_i. This formulation also allows the free-surface condition to be implemented for non-flat topography, through the definition of the normal vector:

$$\mathbf{n} = \begin{pmatrix} -\tan\phi \\ 1 \end{pmatrix} \tag{2.20}$$

for a slope angle of the local topography ϕ.

Topography

The effect of a more realistic topographical surface on the seismic signals observed at virtual recording stations for conduit resonance models of low-frequency events has also been explored. Even for simple cases such as an open or buried conduit and a free

surface, the conduit walls act as a waveguide, concentrating the wavefield in the upward and downward directions and increasing the amplitude of the vertical ground motion observed at the surface directly above the conduit (Neuberg et al., 2000). A simple cone or dome-shaped topography above the conduit was also shown by Neuberg et al. (2000) to further increase the amplitudes through focusing effects.

More recently seismic wave propagation has been modelled by Jousset et al. (2004), in and around a magma-filled conduit embedded in a surrounding medium, including the effects of realistic surface topography on the wavefield propagation in the medium surrounding the conduit. This is based on the work of Hestholm & Ruud (2000) who used finite-difference methods to model seismic scattering from free surface topography through mapping of a rectangular computational grid onto a 2-D curved topographic grid system (Tessmer et al., 1992).

Topography has been shown to affect strongly the particle motion and hence waveforms of seismic signals (Ohminato & Chouet, 1997; Neuberg & Pointer, 2000). Low-frequency seismic events are particularly affected by topography, due to the ruggedness of the volcanic topography and the shallow nature of the top end of the conduit (Jousset et al., 2004). The combined effects of topography and conduit resonance were investigated by Jousset et al. (2004) who computed several examples of the wavefield propagation using cross-sections of the Montserrat topography, and in all cases topographic scattering resulted in more complex waveforms. Including the topographic free surface was shown to modify the travel-times and waveforms of low-frequency earthquake signals. For steep volcanic topography, e.g. Montserrat, the frequency content of low-frequency events is a superposition of both the resonance and topographic scattering effects (Jousset et al., 2004), and it was therefore concluded that observed single frequency peaks should not be directly interpreted as resulting from source processes.

Jousset et al. (2004) showed that the amplitude decay of the coda of low-frequency signals is affected by the scattering due to steep volcanic topography. Hence for this reason, and in order to fully understand the effects of the intrinsic attenuation alone on the amplitude decay of the waveforms, topography was ignored and not implemented in any of the models used in this thesis, with a simple flat free-surface preferred instead.

2.2 Testing and development of the model

2.2.1 Seismic amplitudes: towards a quantitative magma flow meter

The need for amplitude calibration

Research into seismic phenomena on active volcanoes aims to interpret the seismic signals recorded in terms of internal volcanic processes. In particular the source process for low-frequency events may prove a useful tool in understanding the volcano's behaviour and in assessing the hazard posed (Chouet, 2003).

The trigger mechanism for low-frequency events on Soufrière Hills volcano, Montserrat, proposed by Neuberg et al. (2006) can be viewed in terms of a seismic source as either: brittle failure on a single fault plane, or, the superposition of several elementary fault planes simulating failure in a dyke or conduit. A general aim of volcano seismology is to be able to quantify magma movement (McNutt, 2005) and a specific goal of the research here is to use the seismic moment and the seismic amplitudes of the initial P-wave arrivals to determine the amount of slip on these surfaces, and hence ultimately a quantitative estimate of the ascent rate of magma within a conduit. Assuming the event rate times the amount of slip per event gives the ascent rate, this can be related to the seismic moment since

$$M_0 = \mu A \bar{u} \tag{2.21}$$

where M_0 is the seismic moment, μ is the shear modulus or rigidity, A is the area of fault rupture and $\bar{u}$ is the average amount of slip (Aki & Richards, 2002). Therefore, making some assumptions about the fault area and rigidity, we obtain a relation of the form:

$$v = N\bar{u} = \frac{NM_0}{\mu A} \tag{2.22}$$

where v is the magma ascent rate or velocity, N is the event rate and $\bar{u}$ is the average amount of slip per event. It is important to note however that this simple relationship is only valid for a simple double-couple mechanism in the centre of a single fault plane, and the exact source properties of several superimposed double couples still needs to be fully investigated. The possibility of using low-frequency seismicity to place quantitative constraints on the ascent rate of magma within the conduit has grown out of the development of the idea of brittle failure of the melt in glass transition as a model for the trigger mechanism (Neuberg et al., 2006). It is also motivated by observations of the rate of low-frequency events rapidly increasing to merge to tremor preceding a dome

collapse (Neuberg et al., 1998; Hammer & Neuberg, 2009).

It is clear that to apply this idea, a fuller understanding of the source process that triggers low frequency-events is needed, particularly its seismic characteristics and radiation pattern. But initially, if a numerical model is to be used to explore the feasibility of this method of determining the ascent rate, a clear definition of how the seismic source is implemented within the finite-difference code and proper calibration of the amplitudes of the synthetic waveforms is essential. There is a definite need to calibrate the finite-difference model fully in order to relate the slip at the source (for a particular mechanism) to the amplitude of events at the surface. For this a good understanding of energy losses in the resonating system is needed, which needs to be examined using the seismic wavefield model. Previous studies using numerical models of low-frequency events on Montserrat, (e.g Neuberg et al., 2000; Sturton & Neuberg, 2006) have so far neglected the issue of absolute amplitudes for the two-dimensional problem, instead focusing more on the waveform characteristics and frequency content of the signals.

2.2.2 Source implementation

Source time function

Historically for earthquake seismology, the term *source time function* has been used to refer to the *moment rate function*, corresponding to the time derivative of the seismic moment function:

$$\dot{M}(t) = \frac{\partial}{\partial t} M(t) = \mu \frac{\partial}{\partial t} \left(A(t) u(t) \right), \tag{2.23}$$

where $\dot{M}(t)$ is the source time function and $M(t)$ is the moment history or seismic moment function, varying with the time-dependent area $A(t)$ and slip history $u(t)$ (Stein & Wysession, 2003).

The reason for this is that, in the far-field, the displacement waveforms are equivalent in shape to the time derivative of the moment history, i.e. the source time function (Stein & Wysession, 2003). Because the finite-difference code for an elastic medium used in this research was originally developed from this perspective (modelling of non-volcanic earthquakes generated by fault rupturing), this definition of the source is used as input to the model. The outputs produced are therefore velocity seismograms which can be easily numerically integrated (since the transfer function is constant with frequency) to obtain the ground motion signal.

Grid independence

As described in Section 2.2.2, the finite-difference code requires the time derivative of the moment history as the input source signal. For an explosive or isotropic source signal, the source is implemented within the finite-difference code by adding the source time function to a single stress node within the grid. However, to ensure that the amplitude of the synthetic waveforms is independent of both the grid size and time-step within the numerical model, scaling by these factors is required. A series of model runs were performed to confirm that the amplitude of the synthetic waveforms was invariant with both the chosen spatial and temporal discretization. The source function used was a Küpper (1958) wavelet, whose analytical expression is given by:

$$f(t) = A\left[\sin\left(m\frac{\pi t}{T}\right) - \frac{m}{m+2}\sin\left((m+2)\frac{\pi t}{T}\right)\right] \tag{2.24}$$

for $f(t)$ the wavelet as a function of time, where A is the amplitude, T is the duration and m controls the number of half-cycles or 'lobes' (Küpper, 1958; Müller, 1970; Fuchs & Müller, 1971). Two examples of such a wavelet and its spectrum are shown in Figure 2.7. In this instance a 1 second long, 1Hz, one-lobe Küpper wavelet was used, following Neuberg et al. (2000). The source was introduced at a depth of 500m, with a single receiver placed 250m away laterally at the free surface. All parameters were fixed except either the timestep (Fig 2.2) or the grid spacing (Fig 2.3) used in the finite difference model, whilst ensuring the stability criterion was still satisfied.

Figure 2.2 shows that to ensure consistent amplitude values with different timesteps, the source signal must be multiplied by the timestep, dt, within the time loop of the program. This is effectively a numerical integration to convert the source to the seismic moment from its time derivative. The results in Figure 2.3 demonstrate that the source term must also be divided by the grid spacing squared, dx^2, in order to produce amplitudes that do not vary with the grid spacing. The grid setup used to compute the results in both figures comprised of an isotropic source, buried in a homogeneous, isotropic, elastic medium.

Verification using analytical solutions

In order to verify that the amplitudes produced by the finite-difference code were correctly calibrated, the waveforms produced by the model were compared to results from analytical solutions. The particular case chosen was a variant of the classic 'Garvin's

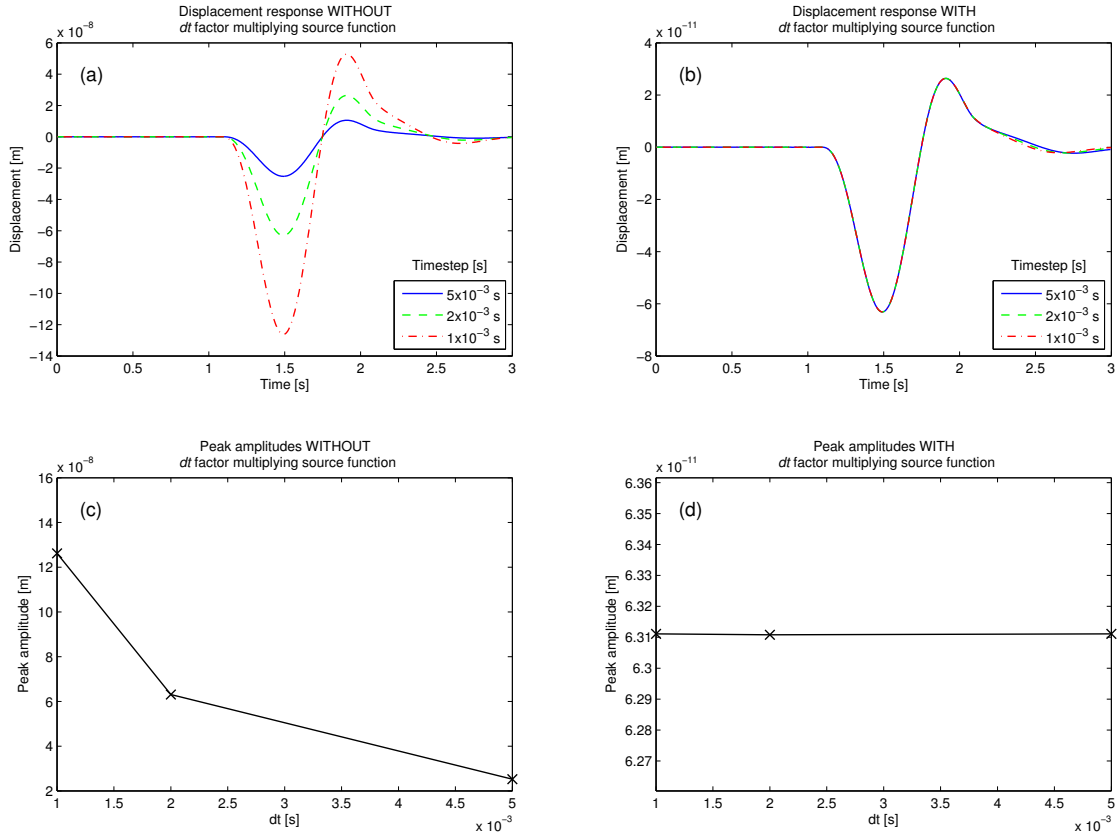

Figure 2.2: Variation of the displacement amplitudes with the timestep for two cases. Plots (a) and (c) are for the case where the source signal is not scaled by a factor dt, and shows how the displacement seismograms and their peak amplitudes vary with the timestep. Note the strong variation of amplitude with timestep and the inverse relationship. In contrast, plots (b) and (d) demonstrate that multiplying the source signal by dt produces amplitudes that do not vary with the timestep used in the code. The seismograms shown are the vertical components of the displacement and the grid spacing was fixed at $dx = 5$m for all cases.

problem', where an analytical expression for the displacement due to a buried line source was described. Here the Cagniard (1939) method, described in Garvin (1956), was used to compute the response to a step-like force and the solution was convolved with, in this case, a Ricker (1943; 1944; 1953) wavelet (a zero-phase wavelet defined as the second derivative of a Gaussian function) with a centre frequency of 2Hz. A description of the problem and numerical experiment, along with the source wavelet, is shown in Figure 2.4.

The results in Figure 2.5 show that both the waveforms and more importantly the amplitudes of the finite-difference code match very well to the analytical solutions. There are some discrepancies due to additional reflected energy from the domain boundaries that has not been damped, which can be seen towards the end of the traces. However the waveforms and amplitude of the direct P-phase match very well, and the ratios of the

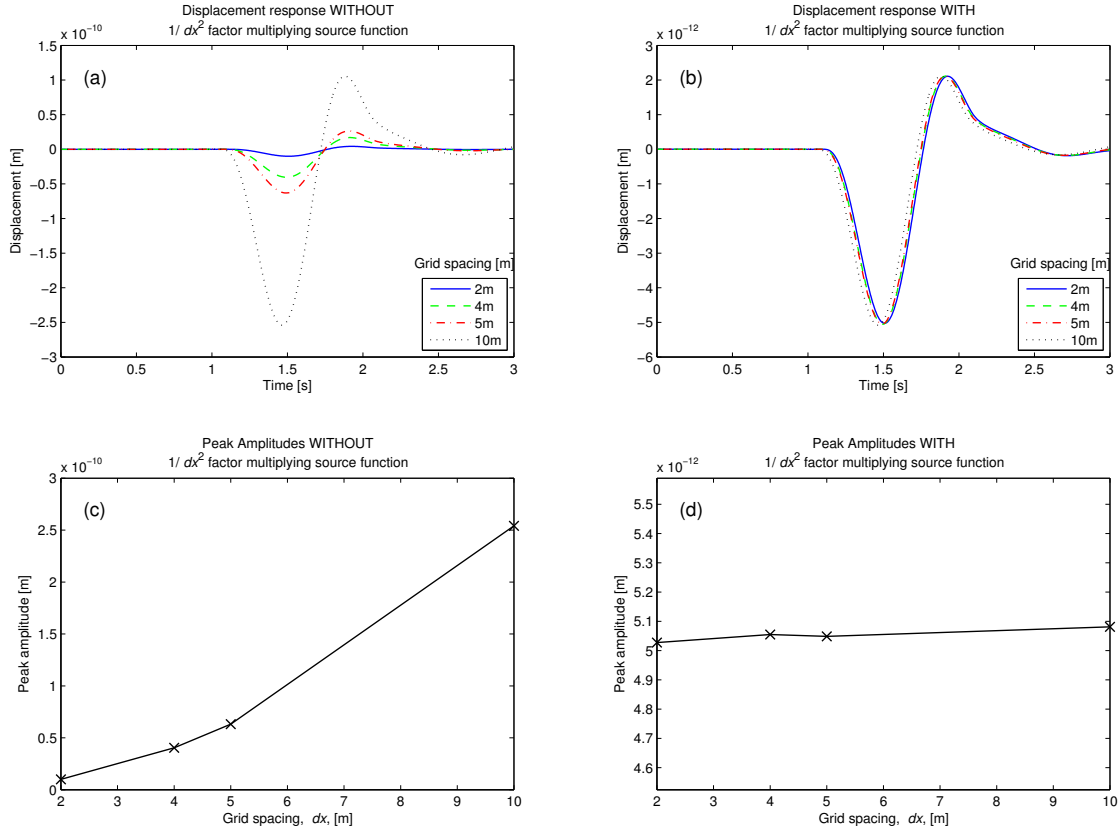

Figure 2.3: The layout of this figure is similar to that of Figure 2.2, except that now the plots show variation with the grid spacing. Plots (a) and (c) show that without multiplying the source amplitude by a factor of $1/dx^2$, the peak amplitude varies strongly with the grid spacing. However introducing this factor, as in plots (b) and (d), produces displacement responses whose amplitudes are constant and independent of the grid spacing used in the calculation. Again, vertical components are shown and the timestep was fixed at $dt = 2 \times 10^{-3}$s.

peak-to-peak amplitudes shows that the differences are all less than 3%, not systematic, and are within the numerical noise levels for the code. Note that the analytical signal for the horizontal component of the receiver directly above the source contains no energy, but due to the staggered grid implementation within the finite-difference code, the model results do show a small but visible signal.

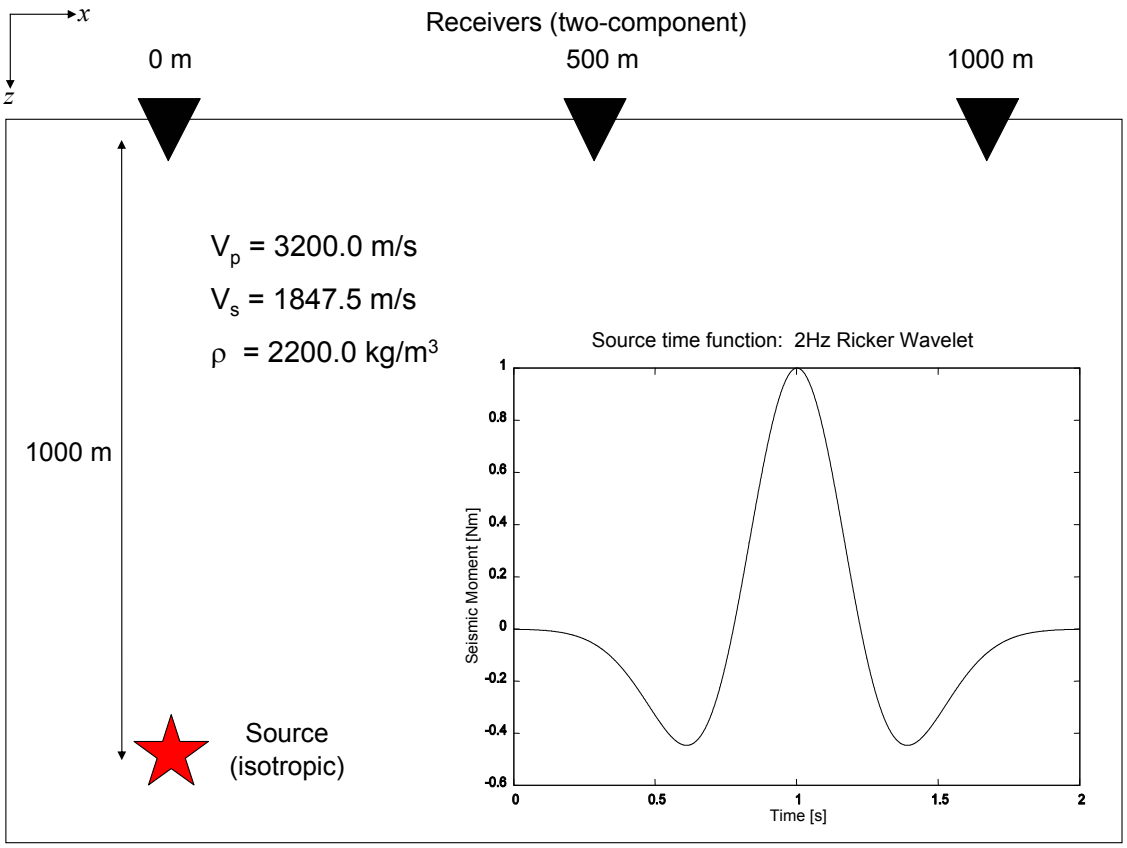

Figure 2.4: Setup of the numerical experiment to compare the numerical amplitudes with analytical solutions to Garvin's problem. The 2-D grid contains an isotropic source buried at 1km depth and three receivers at the free surface, at distances 0m, 500m and 1km respectively. The source time function used was a Ricker wavelet with a centre frequency of 2Hz. The medium is parameterised as an isotropic, homogeneous, elastic solid, with the parameters shown in the diagram.

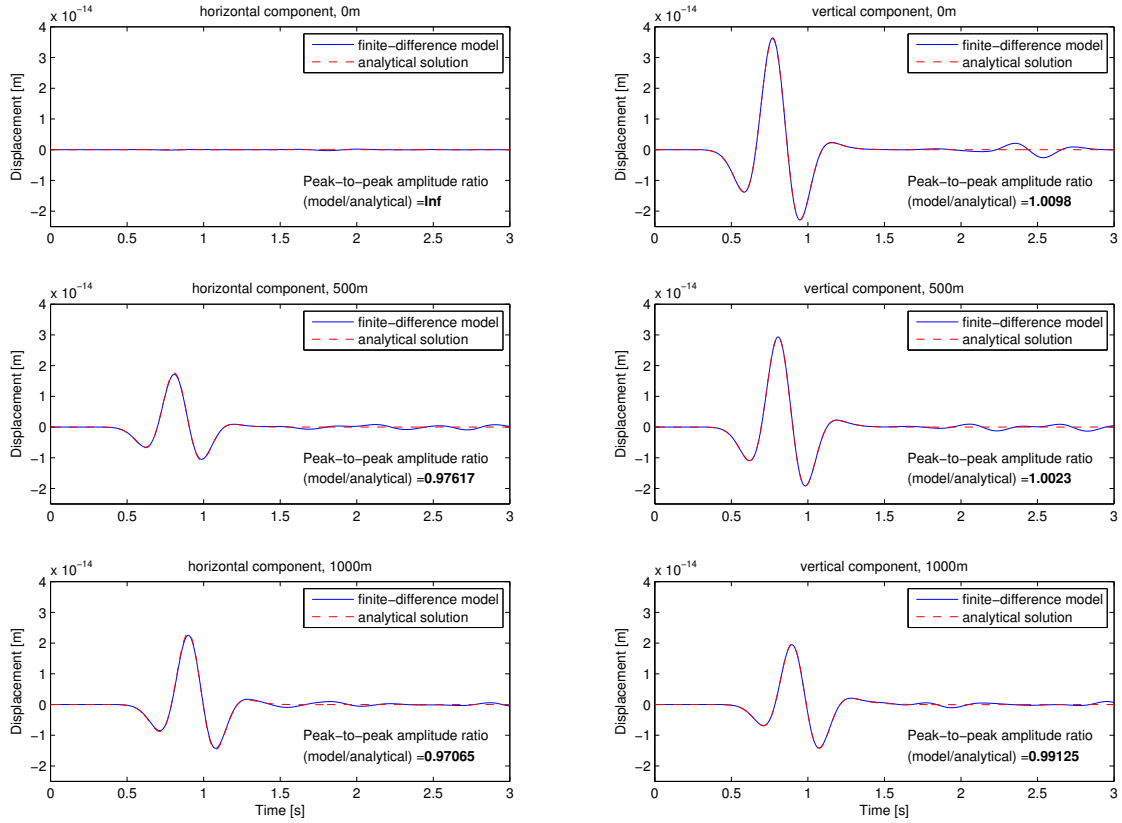

Figure 2.5: Verification of the amplitudes of the 2-D finite-difference code by comparison with analytical solutions to Garvin's problem. The separate plots show the horizontal and vertical displacement signals at the three receivers whose locations are described in Figure 2.4. The waveforms produced by the finite-difference code are shown by the solid line, and the analytical solutions to the same problem by the dashed lines. There are some discrepancies due to additional reflected energy from the domain boundaries that has not been damped, which can be seen in the coda of the traces. The ratio of the peak-to-peak amplitudes of the results is also displayed in the figure. Note the similarity in the far-field displacement and moment function waveforms, as expected.

2.3 Resonance dynamics and radiation of energy: the radiative part

Before the effect of intrinsic attenuation is examined, it is important to consider the other component of the amplitude decay: the radiative part of the attenuation. Despite much research on the dynamics and physics of crack/conduit/dyke resonance (Aki et al., 1977; Chouet & Julian, 1985; Chouet, 1986; 1988; Neuberg et al., 2000; Kumagai & Chouet, 2001), many questions are still outstanding: is the free-surface fundamentally important to the way energy is transmitted from the resonating body? Is the energy radiated from the tips of the resonator and then propagated as surface waves? Does the radiative component of the amplitude decay depend on the source-receiver geometry? Is the radiative attenuation frequency dependent?

In this section, forward models of the seismic wavefield are used to attempt to address some of these questions and better understand the dynamics of how energy is radiated or transmitted into the surrounding medium from such a resonating fluid body. Since this component of the amplitude decay is only due to the attenuating effects of the geometry and contrast in elastic parameters, the radiative attenuation was modelled with the elastic finite-difference code (equivalent to using the viscoelastic finite-difference code with $Q \rightarrow \infty$).

2.3.1 Geometrical dependence of the amplitude spectra

The fundamental frequency of the resonator and its harmonic overtones are determined by the contrast in elastic parameters between the fluid and solid, and, the geometry, particularly the aspect ratio, of the resonating fluid body (Aki et al., 1977; Ferrazzini & Aki, 1987; Sturton & Neuberg, 2006). These two factors are the fundamental controls on the dispersion characteristics of the interface wave phase velocity and hence the frequencies of the resonant excitation. The bandwidth of the source-time function which excites the resonance determines how many of the higher modes are excited by sufficient high frequency energy. But how exactly does energy leak out of a conduit with finite-length, compared to the analytical model of Ferrazzini & Aki (1987)? And how does this affect the observed frequency content of the signals? Are the same spectral peaks observed everywhere?

To investigate how the source-receiver geometry and the free surface affect the relation-

ship between the observed frequency content and the resonance, dense arrays of virtual stations were used to record the velocity throughout the solution domain, both inside and outside the fluid-filled resonator. Two examples of Küpper wavelets, with different frequency content, are also used to illustrate the effect of the source bandwidth on the excitation of the resonance. The setup of the numerical experiment and the arrays used to record the results are shown in Figure 2.6.

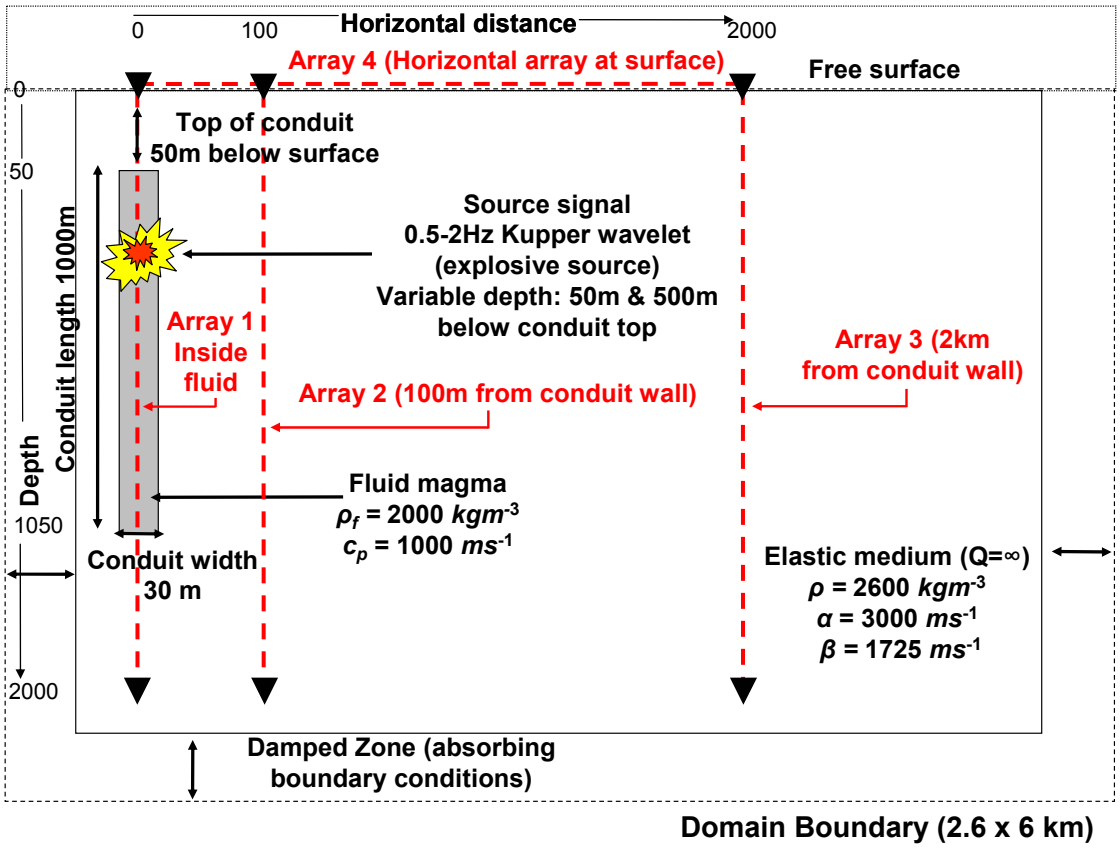

Figure 2.6: Schematic diagram showing the setup of finite-difference model grid and the recording arrays. The dimensions and properties of the conduit are based on typical Montserrat parameters, such as those used by Sturton & Neuberg (2006). The grid-spacing used was $dx = 5$m with timestep $dt = 5 \times 10^{-4}$s. The arrays are 2000m long, although only depths up to 1250m are shown in Figures 2.8- 2.13. All arrays have 50m spacing between stations.

Figures 2.8 and 2.9 show the case for a 2Hz Küpper wavelet (depicted in Figure 2.7) as the seismic source, recorded at two vertical arrays of seismometers: the first in the centre of the conduit (Array 1) and the second in the surrounding elastic medium 100m from the wall (Array 2). The amplitude spectrum of each seismogram recorded at each depth was used to create a surface plot of the frequency content with depth. The plots of these spectral surfaces of the synthetic seismograms at varying depths show a clear

resonance pattern, particularly in the horizontal components. There is a clear pattern of increasing integer modes, as larger numbers of wavelengths divide into the length of the conduit. The asymmetry in the vertical components is due to the interaction of vertically guided energy with the free surface at the top domain boundary. The frequency axis is truncated at 2Hz in the plot because above this frequency there is little energy in the spectrum. The relative amplitudes of the peaks and the highest order of modes excited is very dependent on the frequency bandwidth of the source signal, a fact illustrated in Figure 2.12 where a 0.5Hz Küpper wavelet source with a lower frequency cut-off in its spectrum only excites the first 3 modes up to around 1 Hz.

If instead the array is moved to a distance of 2km away (Array 3), the difference in the radiation pattern of energy can be seen in the upper plot of Figure 2.10. Here, the same spectral peaks representing the modes are present, but each depth level contains all frequencies and there are no nodal points where there is cancellation of energy, as seen in the cases of being in or very close to the resonator. The lower plot in Figure 2.10 shows a horizontal array of seismometers at the free surface (Array 4), the most realistic case from an observational point of view. This example shows that even in the case of a simple flat free-surface geometry with no topographic scattering, the relative amplitudes of the spectral peaks is strongly affected by the source-receiver distance, with strong interaction with the free-surface clearly visible on the vertical components to a distance of around 500m from the conduit.

Figure 2.14 shows a case where instead of being 50m from the top, the seismic source is placed in the exact centre of the conduit. In this instance complete cancellation of the even modes can be seen with only the odd modes surviving. In this example the free surface was also removed from the top domain boundary and replaced with the same absorbing boundaries as the other three sides. It is evident that removing the free surface results in much more symmetry in the vertical component compared to the previous cases, but it is also striking how much energy is still guided vertically and leaks out from the conduit ends.

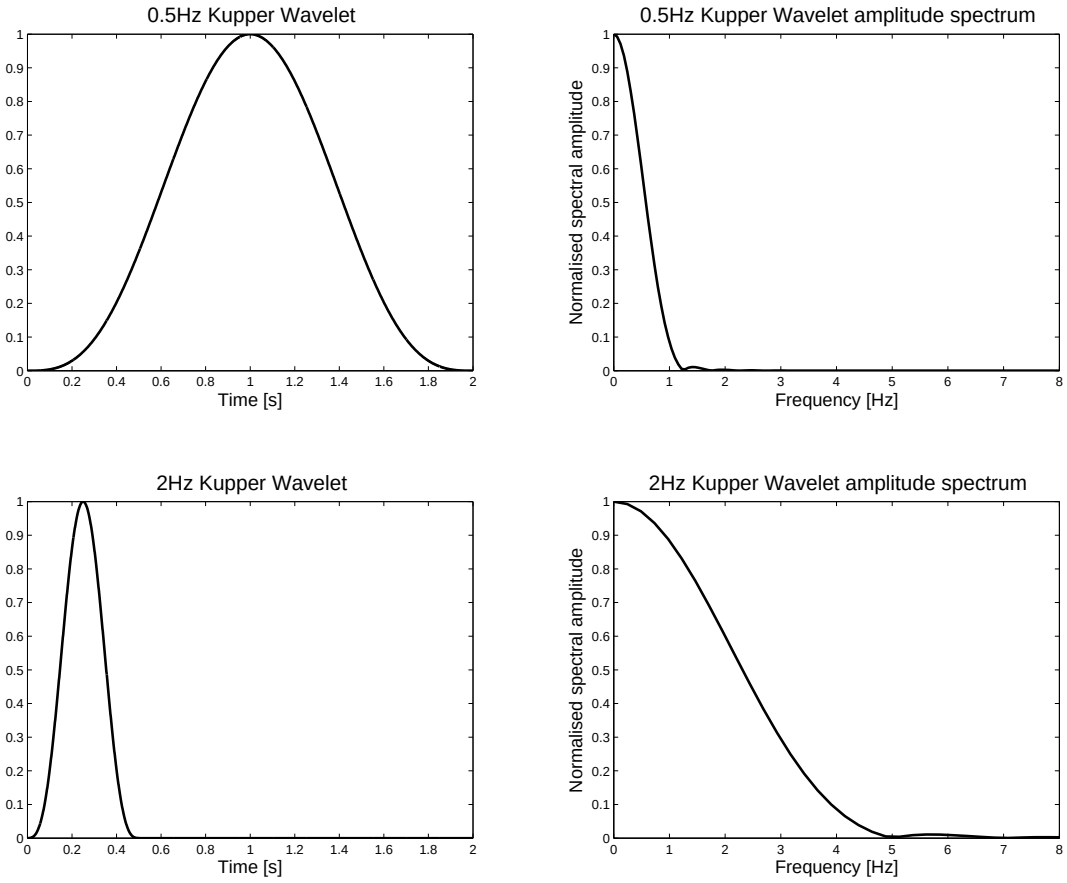

Figure 2.7: 2 seconds long 0.5 and 2Hz Küpper wavelets, used as source wavelets in the modelling, and their associated amplitude spectra. These two wavelets are used to illustrate the effect of the source bandwidth on the resonance, since this determines the number of higher modes that are excited by the source.

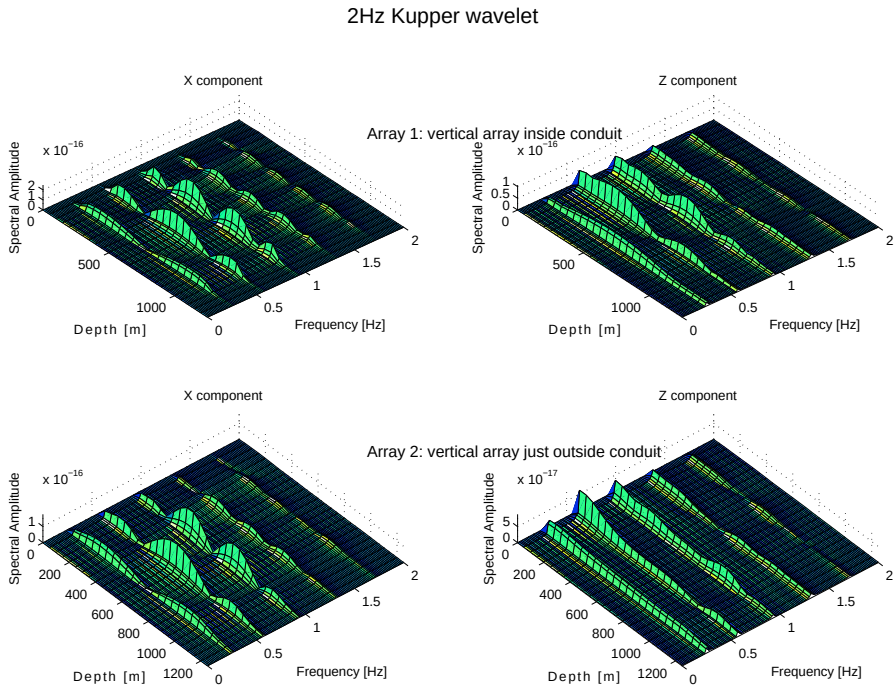

Figure 2.8: Amplitude spectra for two vertical arrays of stations inside the conduit (upper), and 100m from the wall (lower). The source used was a 2Hz Küpper wavelet 50m below the conduit top. The amplitude spectrum of each seismogram recorded at each depth was used to create a surface plot of the frequency content with depth. Note the resonance, with the integer modes seen as discrete spectral lines, particularly in the horizontal component.

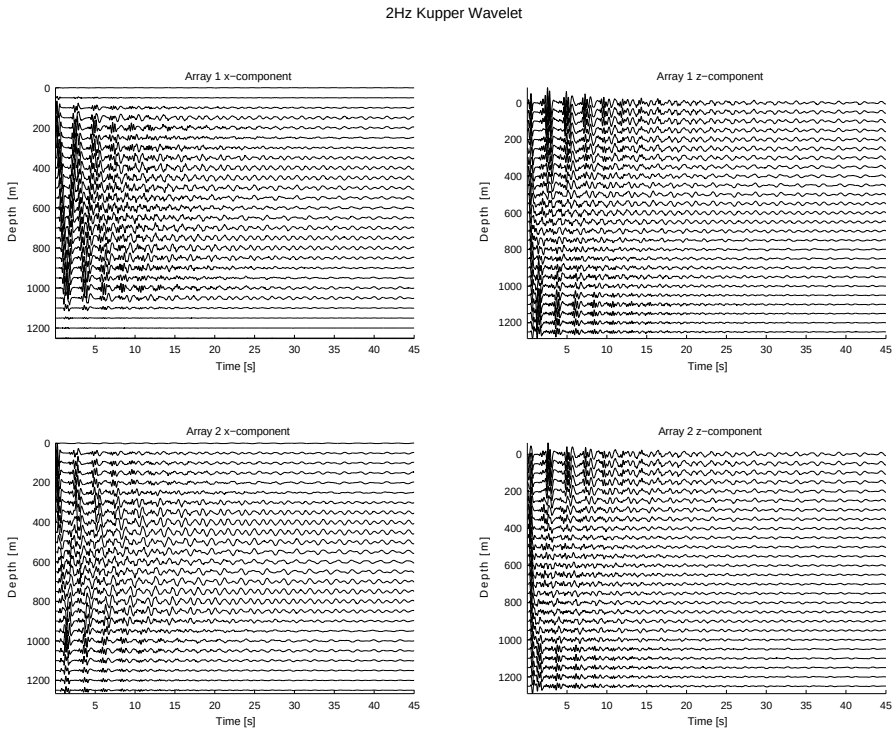

Figure 2.9: Corresponding waveforms for amplitude spectra shown in Figure 2.8, for two vertical arrays of stations inside the conduit (upper) & 100m from the wall (lower).

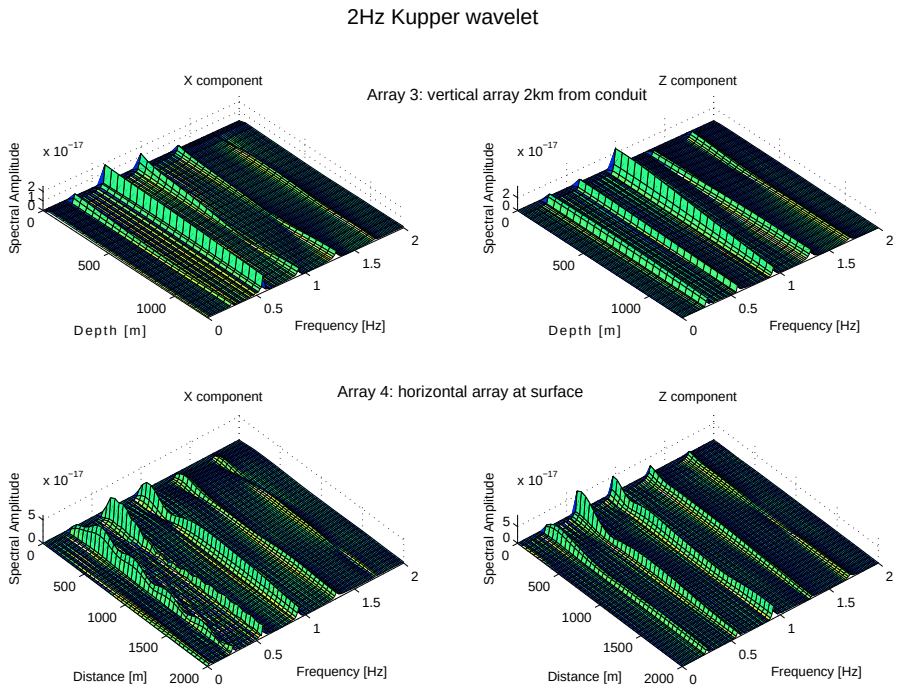

Figure 2.10: Amplitude spectra for two arrays of stations: a vertical array 2km from the conduit wall (upper), and a horizontal array at the free surface (lower). The source used was a 2Hz Küpper wavelet, 50m below the conduit top.

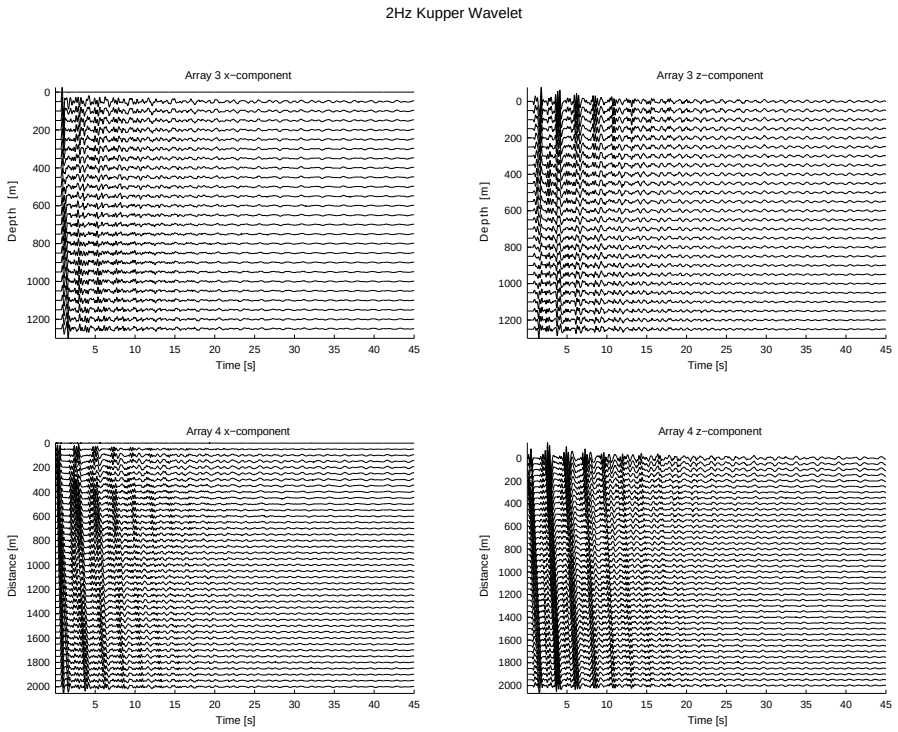

Figure 2.11: Corresponding waveforms for the amplitude spectra shown in Figure 2.10, for two arrays of stations: a vertical array 2km from the conduit wall (upper), and a horizontal array at the free surface (lower).

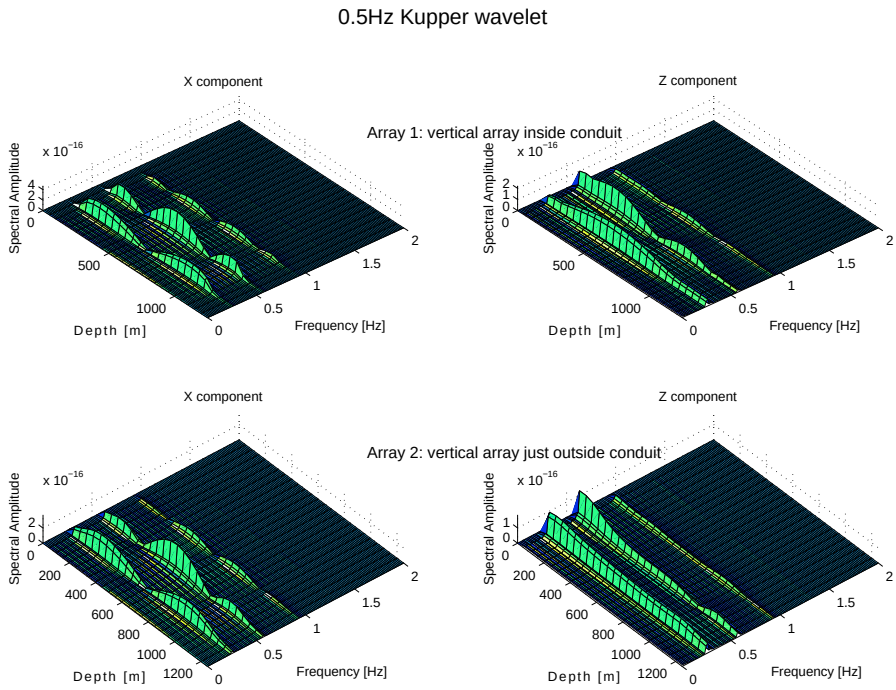

Figure 2.12: Amplitude spectra for two vertical arrays of stations inside the conduit (upper), and 100m from the wall (lower). This time the source used was a 0.5Hz Küpper wavelet, with a lower frequency bandwidth that only excites the lowest 3 modes of resonance. The source depth was again 50m below the conduit top.

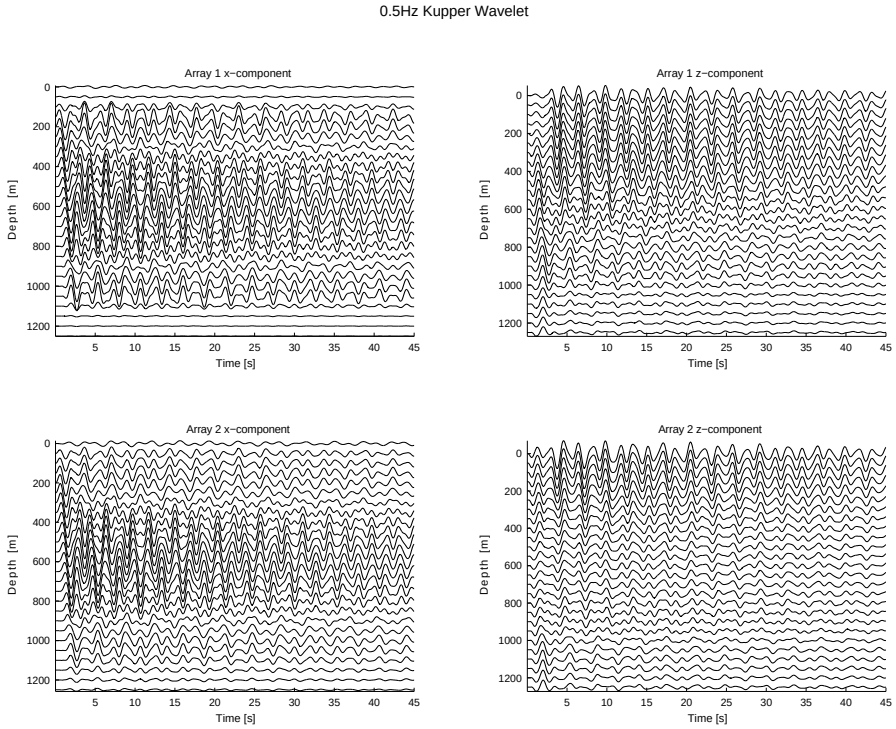

Figure 2.13: Corresponding waveforms for the amplitude spectra shown in Figure 2.12, for two vertical arrays of stations inside the conduit (upper), and 100m from the wall (lower), this time for a 0.5Hz Küpper source wavelet.

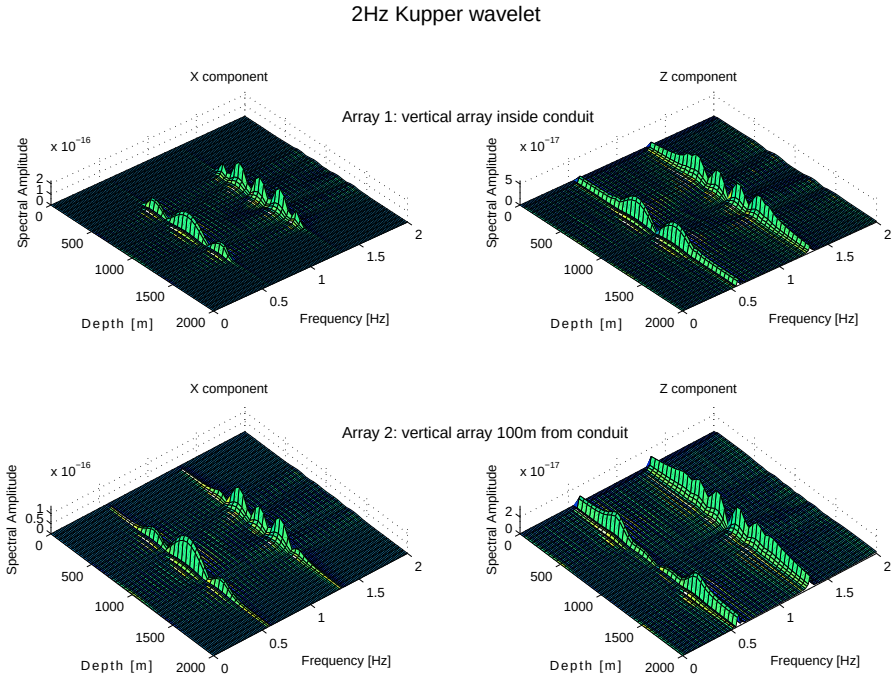

Figure 2.14: Amplitude spectra for two vertical arrays of stations inside the conduit (upper), and 100m from the wall (lower). The source used was 2Hz Küpper wavelet, but placed at the centre of the conduit (500m below the top). Note how destructive interference leads to cancellation of the even modes with only the odd modes surviving. In this example the free surface was also removed from the top domain boundary, producing increased symmetry in the vertical components.

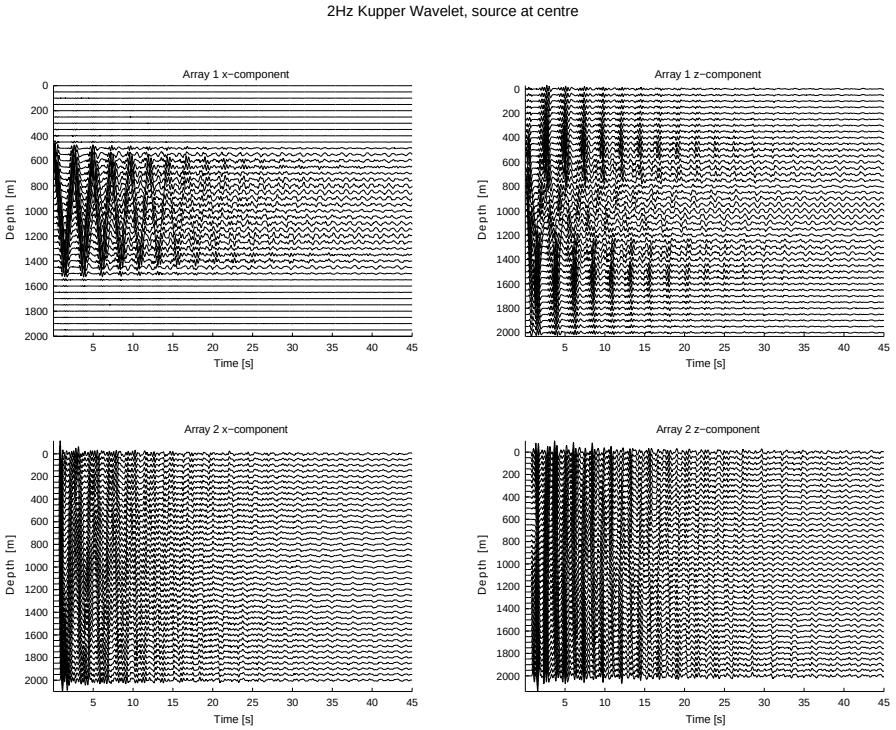

Figure 2.15: Corresponding waveforms for the amplitude spectra shown in Figure 2.14, for two vertical arrays of stations inside the conduit (upper), and 100m from the wall (lower), this time for a 2Hz Küpper wavelet placed at the centre of the conduit.

2.3.2 Geometrical dependence of the radiative attenuation

The synthetic signals from the arrays shown in Figure 2.6 were also analysed, not just in terms of their spectra, but in terms of their amplitude decay. Remember that these synthetic data were produced using the elastic finite-difference code, with no intrinsic attenuation included in the model, so the observed apparent amplitude decay is wholly due to radiative effects. Therefore, it is possible to isolate and measure the radiative component of the attenuation. This analysis allows the variation of the radiative component of attenuation with position relative to the resonator to be quantitatively examined, for a particular set of conduit parameters. Both the horizontal and vertical component seismograms were analysed to check that they produced consistent results, using the model runs which employed a 2Hz Küpper wavelet as the source.

Figures 2.16 to 2.19 show, in terms of both quality factor and attenuation, how the amplitude decay varies with position within the arrays of stations previously described (Figure 2.6). The apparent attenuation was calculated using the best of the automated methods described in Chapter 4. The first five peaks of the amplitude spectra, ranging from 0.26 to 1.71Hz, were chosen to isolate energy at the resonant frequencies and are shown as the different colours in the plots. It can be seen that there is a strong geometric and frequency dependence of the radiative attenuation. For all arrays, both horizontal and vertical components show that at low-frequencies energy is more attenuated than at higher frequencies. The two arrays within and close to the resonator show more (quasi-periodic) variation, possibly related to the nodal points seen in the earlier plots. This variation becomes more smoothed out as the distance from the resonator increases, as Array 6 does not show the same pattern.

This modulation of the radiative attenuation, together with the geometrical dependence of the spectra, will have implications regarding the separation and determination of the intrinsic attenuation in Chapters 3 and 5.

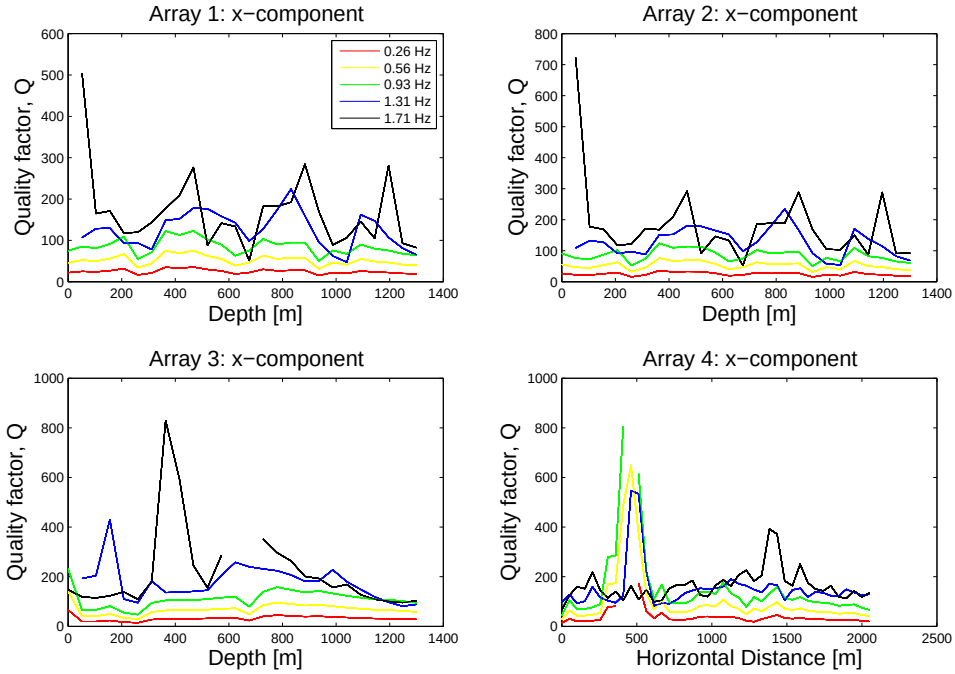

Figure 2.16: Variation of the horizontal component quality factor with the source-receiver geometry. Each of the four subplots shows the variation of Q_{a} with distance for each of the four arrays described in Figure 2.6.

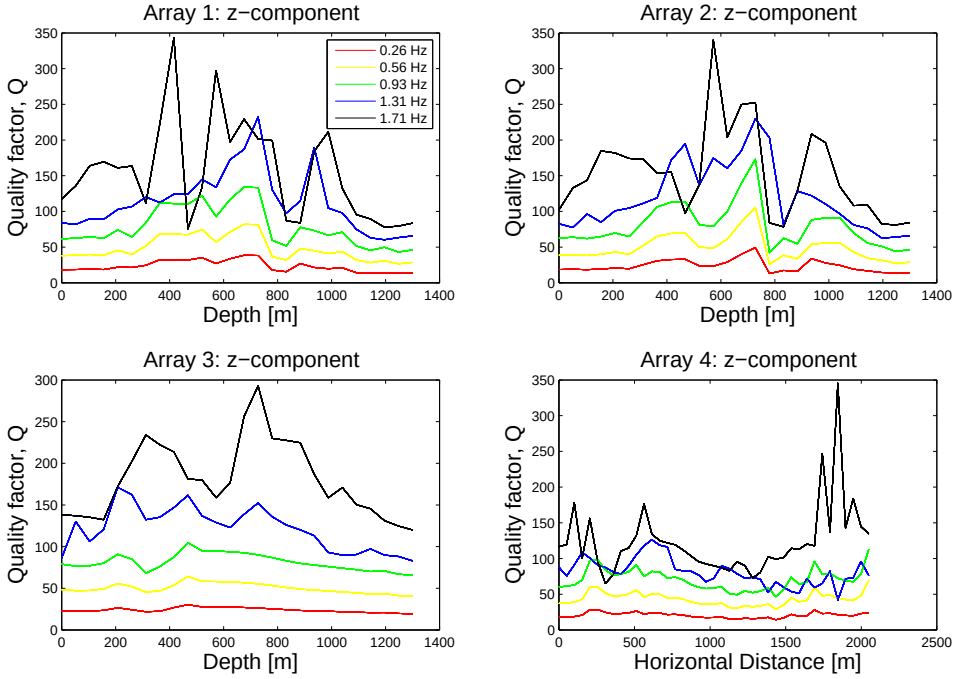

Figure 2.17: Variation of the vertical component quality factor with the source-receiver geometry.

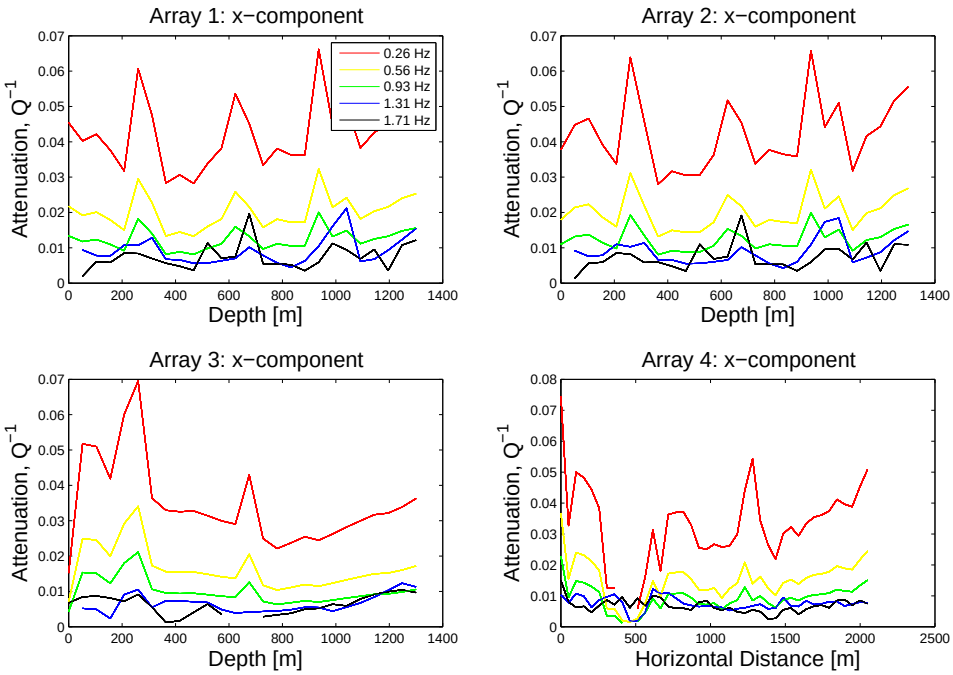

Figure 2.18: Variation of the horizontal component attenuation with the source-receiver geometry.

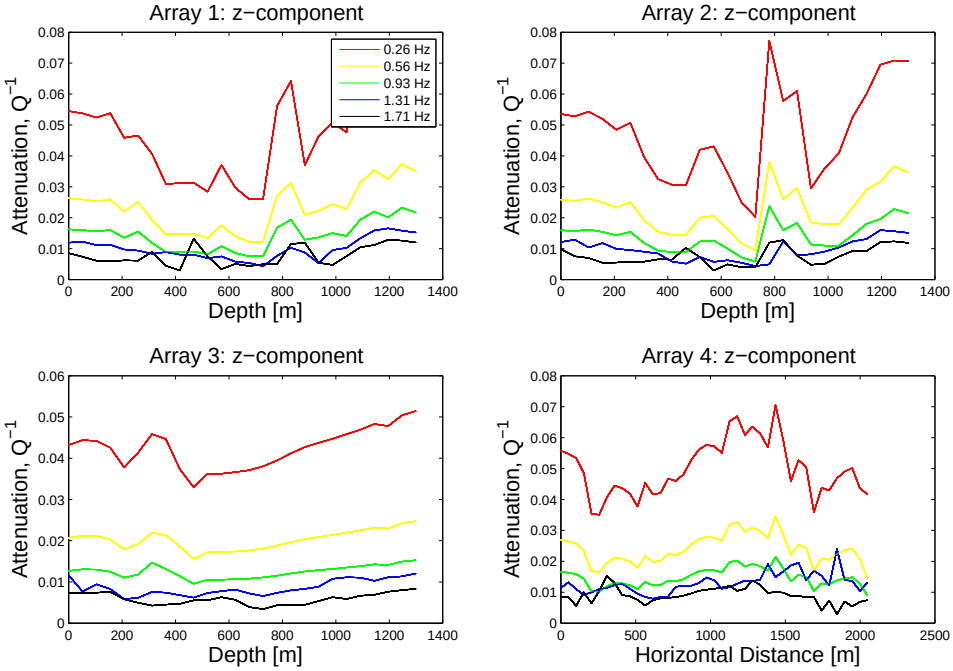

Figure 2.19: Variation of the vertical component attenuation with the source-receiver geometry.

2.4 Testing the effect of the intrinsic attenuation: the intrinsic part

The intrinsic attenuation of the fluid in the resonator can be linked directly to its properties, particularly its viscosity, if a rheological model is assumed. This provides the motivation for studying the effects of the intrinsic attenuation, with the aim of constraining the fluid properties and understanding their effect on the observed signals. Since this is an anelastic energy loss, the viscoelastic finite-difference model can be used to examine the relationship between the intrinsic attenuation of the fluid and the observed amplitude decay or apparent attenuation, measured from the coda of the synthetic signals.

2.4.1 Description of model runs

Intrinsic attenuation values corresponding to a Q_{i} of between 1 and 200 were tested using a suite of model runs. It is important to point out here that these Q_{i} values are based on the attenuation of an acoustic wave in an unbounded medium, and not interface waves at a boundary. The setup of the model used for the experiment is shown and described in Figure 2.20. All parameters (geometry and elastic properties) were fixed except the intrinsic attenuation of the fluid, with the velocity response recorded 500m horizontally away from the resonator at the free surface.

A Gaussian smoothed Sinc function, containing energy between 0 and 10Hz, was chosen as the source wavelet to excite the higher modes of resonance and to explore the frequency dependence of the attenuative behaviour (Figure 2.21). This is the same source wavelet as used by Jousset et al. (2004), and has an approximately flat spectrum within the bandwidth of interest, making it particularly suitable for use in the attenuation analysis. The impact of the source wavelet and its spectral content on the resultant waveforms is shown in Figure 2.22, which shows a comparison between a 1Hz Küpper wavelet and 10Hz Sinc function. The fundamental mode is excited for both sources and very similar values for the apparent attenuation are retrieved. However the 10Hz Sinc function, with a broader bandwidth, also excites the higher modes of the resonance.

Unlike the spectral methods of Kumagai & Chouet (1999; 2000), a time-domain approach, similar to that of Seidl & Hellweg (2003), was used to determine the apparent attenuation from the codas of the synthetic low-frequency events. Narrow band-pass filters were applied to these signals to isolate the energy at the frequency of interest, chosen

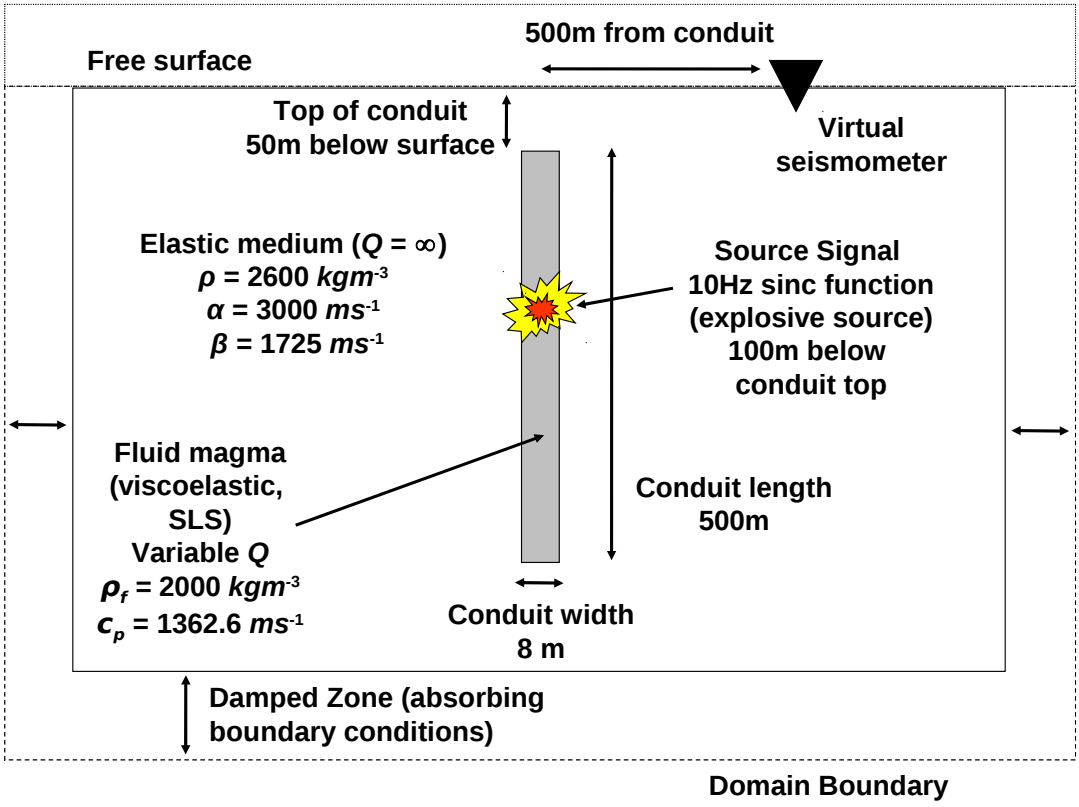

Figure 2.20: Schematic diagram showing the setup of finite-difference model grid. All parameters were fixed except the intrinsic attenuation of the fluid. Velocity seismograms were recorded 500m away at the free surface. To excite the higher modes of resonance the source wavelet was a relatively broad-band sine cardinal function with a high-frequency cut-off of 10Hz. To avoid introducing additional complexities to the waveforms no topography was included in these particular models, so a flat free surface was used.

from the dominant spectral peaks of the signal (see Table 2.1). For these examples a 2-pole Butterworth filter with a half-width of 0.3Hz was used. Once the filtered signal was obtained, the Hilbert transform was used to calculate its analytical envelope. On a logarithmic scale, the analytical envelope against time plots on a straight line, where the apparent attenuation, Q_{a}^{-1}, is a function of the slope. The apparent attenuation can be easily determined from this slope and is given by $Q_{\mathrm{a}}^{-1} = (1 - e^{m})/\pi$, where m is the gradient estimated by linear regression. The result is a single measurement of Q_{a}^{-1} at each frequency separated by filtering. This method of measuring the apparent attenuation is explained and discussed in more detail in Section 4.1.2 of Chapter 4.

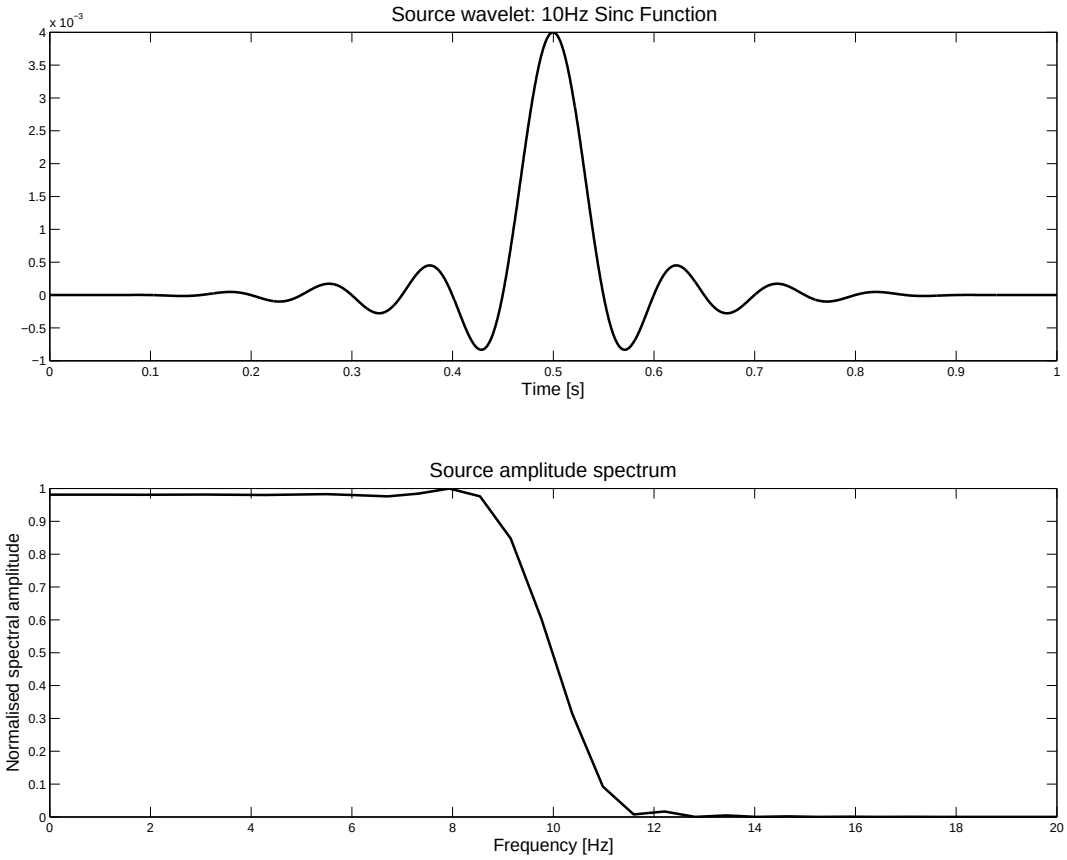

Figure 2.21: Smoothed 10Hz Sinc function source wavelet and its associated amplitude spectrum, containing energy in the spectrum up to 10Hz. The constant spectral amplitude in the chosen passband is produced by subtracting two Sinc functions at different frequencies and smoothing the result by multiplying by a Gaussian window function.

2.4.2 Results

The synthetic waveforms generated by the suite of model runs, and their associated amplitude spectra, are shown in Figure 2.23. Note the increased damping of the waveforms and widening of the spectra as the attenuation is increased (lower Q_{i}), with the values of the first four peaks in each spectrum shown in Table 2.1.

Figure 2.25 shows the apparent attenuation measured from the synthetic signals plotted against the intrinsic attenuation in the fluid. If we follow Equation 1.8 (Aki, 1984) and make the assumption that the two components are independent, the radiative part of the attenuation describes the component of the amplitude decay of the resonating body that is independent of the fluid viscosity. Hence, if the radiative part, Q_{r}^{-1}, is fixed we have a simple linear relationship between Q_{a}^{-1} and Q_{i}^{-1} of the form $y = mx + c$, where the intercept, c, should be equal to Q_{r}^{-1} and the gradient, m, should equal unity. This is

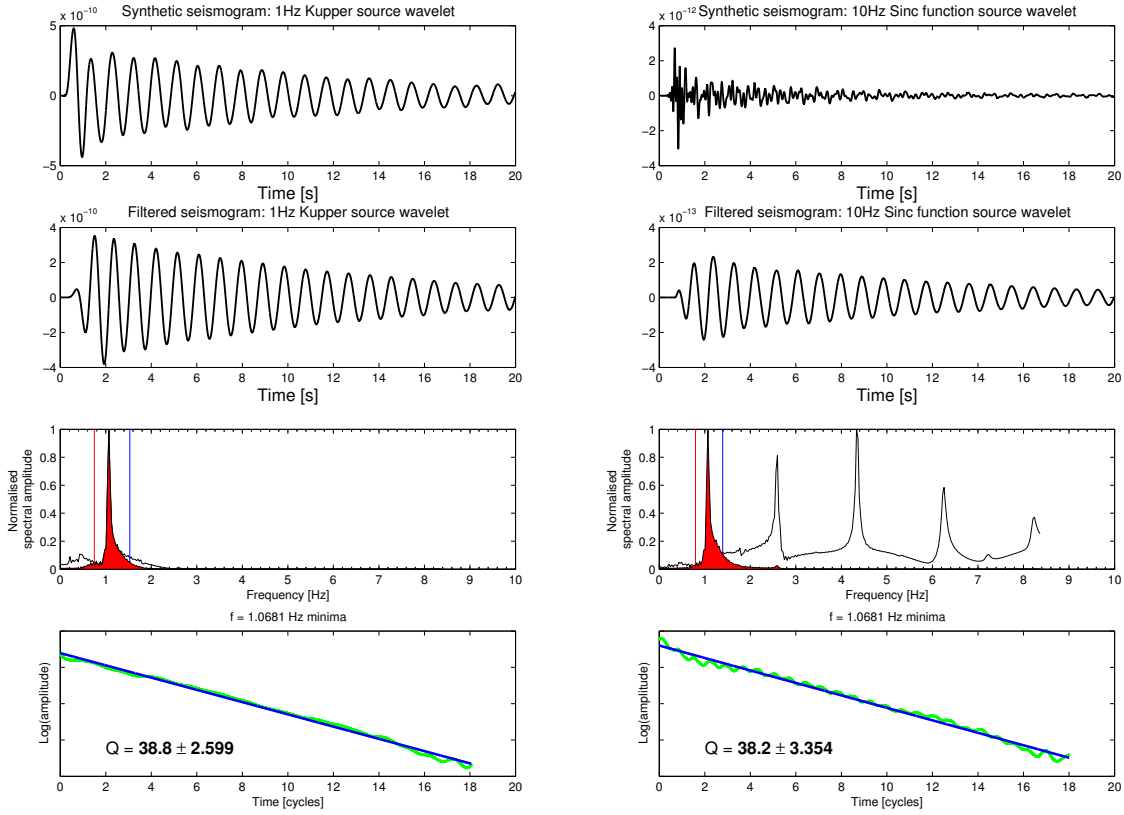

Figure 2.22: Synthetic seismograms produced for the same model setup but using two different source wavelets. The left hand side shows the results for a 1Hz Küpper source wavelet and the right side for a 10Hz Sinc function. Shown are the unfiltered synthetic seismograms, and the results after filtering around the lowest peak in the spectra (fundamental mode), with the filled areas in the spectra representing the filtered traces. Note that this peak in the spectrum is common to both examples and returns, within errors, the same value for the apparent attenuation from the amplitude decay of the filtered signals for both source wavelets.

plotted as the dashed line in Figures 2.24 and 2.25. However, it is obvious that the data have a smaller gradient than the dashed line of equality in Figure 2.25. The data show an approximate linear relationship, but clearly with a gradient of less than 1. Since Q_{i}^{-1} is based on the attenuation of acoustic waves, this is indicative that the attenuation of the interface waves may be smaller than that of the acoustic waves. The gradient and intercept (Q_{r}^{-1}) of the Q_{a}^{-1} vs. Q_{i}^{-1} relationship was calculated for each frequency, using a variable number of data points to test the robustness of the regression, with the results shown in Table 2.3 and Figure 2.27. Because the definition of Q begins to break down for $Q_i \leq 2\pi$, only attenuation values corresponding to $Q_i > 5$ are used in the regression. In the upper left plot of Figure 2.27, and the first row of Table 2.3, the two points used correspond to the *lowest* two attenuation values. Values of the measured gradients vary

slightly with each frequency analysed but taking a weighted average of the gradients, weighted by the error and excluding the fits using only two points, gives a mean gradient of $\overline{m}_{\mathrm{w}} = 0.236 \pm 0.0228$. This demonstrates that the intrinsic attenuation appears to contribute $23.6 \pm 2.28\%$ less to the measured apparent attenuation than assumed by Equation 1.8 for an acoustic wave. In other words, a key observation of the modelling is that the attenuative effect of the viscosity of the fluid on the interface waves appears to be overestimated.

	Frequencies of spectral peaks [Hz]			
Intrinsic Q_{i}	**Peak 1**	**Peak 2**	**Peak 3**	**Peak 4**
1	1.116	2.825	4.839	7.067
5	1.086	2.642	4.504	6.548
10	1.055	2.642	4.412	6.396
20	1.055	2.581	4.382	6.304
35	1.055	2.581	4.351	6.243
50	1.055	2.581	4.321	6.243
75	1.055	2.581	4.321	6.213
100	1.055	2.581	4.321	6.213
200	1.055	2.581	4.321	6.182

Table 2.1: The first four spectral peaks measured from the amplitude spectra of the synthetic signals, as a function of the intrinsic attenuation of the fluid. Note the increased dispersion and widening of the spectra as the level of attenuation increases, also illustrated in Figure 2.23. The apparent attenuation was calculated at these frequencies for each example, using narrow bandpass filters to isolate the energy in the signal.

	Apparent Q_{a}				
Intrinsic Q_{i}	**Freq. 1**		**Freq. 2**	**Freq. 3**	**Freq. 4**
	1Hz Küpper	**10Hz Sinc Function**			
1	18.51	16.13	22.38	27.42	24.02
5	21.04	21.12	24.32	29.05	26.20
10	27.17	26.24	27.93	39.98	35.36
20	34.03	32.04	34.71	56.18	49.30
35	-	36.92	42.93	74.17	62.48
50	41.5	39.09	49.51	84.93	71.61
75	-	41.37	55.12	97.04	80.55
100	44.83	41.21	58.24	104.46	86.92
200	-	53.14	59.18	121.35	97.39

Table 2.2: Modelling results: Apparent quality factor as a function of the intrinsic quality factor. The synthetic signals were bandpass filtered around the first four peaks in the spectra to give measurements of the apparent quality factor at four discrete frequencies. The results in this table are displayed graphically in Figure 2.24. Dashes indicate that no model was run for this configuration.

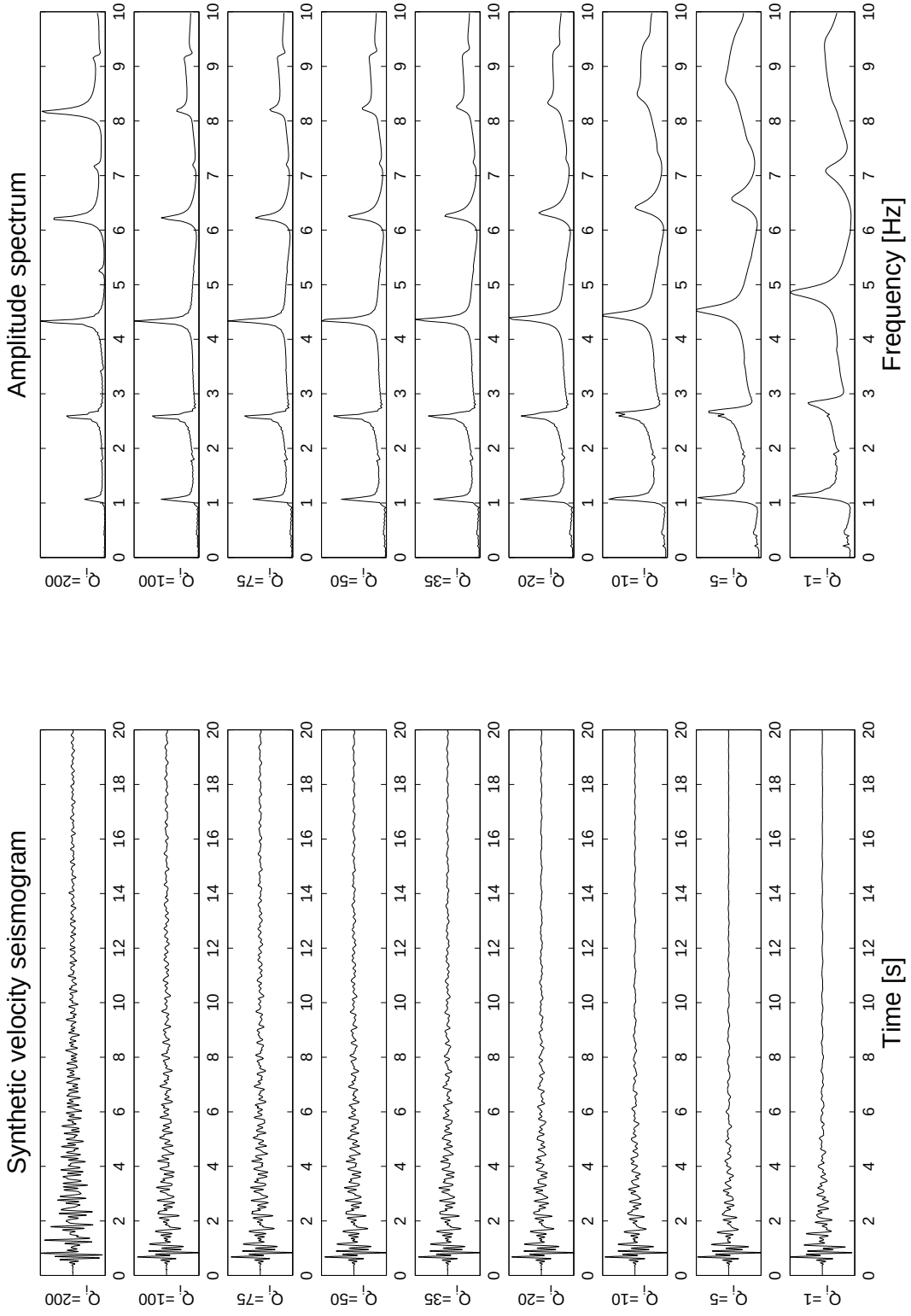

Figure 2.23: Synthetic vertical component waveforms and amplitude spectra from the finite-difference model, for a range of intrinsic attenuations. Both the velocity and spectral amplitudes have been normalised. The model geometry was a 500m long by 8m wide magma body, filled with a viscoelastic fluid, with a 10Hz Sinc function used as the source wavelet. Note the increased damping of the waveforms and widening of the spectra as the attenuation is increased.

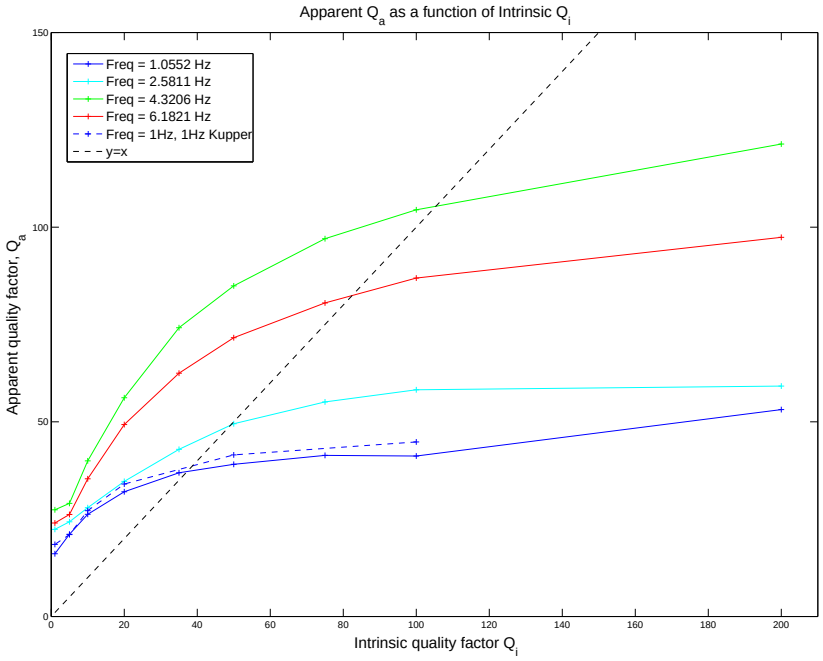

Figure 2.24: Apparent quality factor as a function of intrinsic quality factor in the range $1 \leq Q_i \leq 200$ with the frequencies analysed corresponding to the first four peaks in the spectra. The dashed blue line shows the values calculated for the lowest peak using a 1Hz Küpper wavelet, rather than a 10Hz Sinc function. The dashed line of equal apparent and intrinsic quality factor is shown for reference.

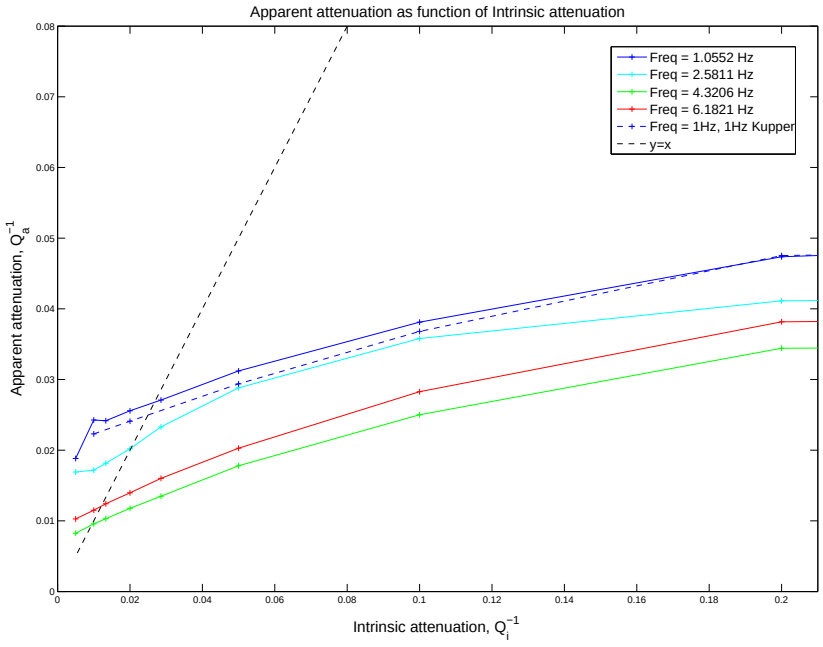

Figure 2.25: Apparent attenuation as a function of intrinsic attenuation in the range $1 \leq Q_i \leq 200$, with the frequencies analysed corresponding to the first four peaks in the spectra. The dashed blue line shows the values calculated for the lowest peak using a 1Hz Küpper wavelet for the source, rather than a 10Hz Sinc function. The dashed line of equal apparent and intrinsic attenuation is shown for reference.

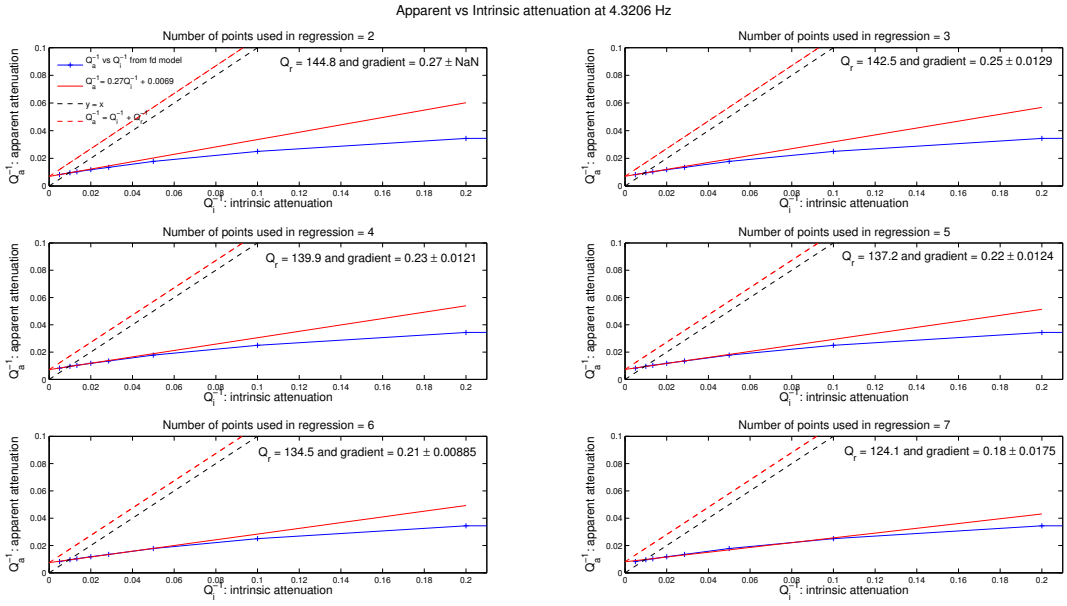

Figure 2.26: Linear fits to the apparent-intrinsic attenuation relationship using a variable number of datapoints in the linear regression. Because the definition of Q begins to break down for $Q_i \leq 2\pi$, only attenuation values corresponding to $Q_i > 5$ are used in the regression. In the upper left plot, the two points used to calculate the gradient correspond to the *lowest* two attenuation values. These results are for the third spectral peak at ≈4.3Hz. The blue solid lines indicate the measured data, with the solid red lines the linear fits to these. The plots show the radiative quality factor, Q_r, determined by the inverse of the intercept, and the gradient: the factor by which the intrinsic attenuation is less than anticipated. The plots also show the expected results as a red dashed line, i.e. a linear relationship with a gradient of 1 (parallel to $y = x$) and with the same Q_r^{-1} intercept. This process was repeated for the four frequencies analysed and the results are tabulated in Table 2.3.

Gradient and Q_r values from the Q_a^{-1} vs. Q_i^{-1} results.								
number of	**Freq. 1**		**Freq. 2**		**Freq. 3**		**Freq. 4**	
points used	**Gradient**	Q_r	**Gradient**	Q_r	**Gradient**	Q_r	**Gradient**	Q_r
2	1.09	74.8	0.05	60.2	0.27	144.8	0.25	110.7
3	0.68±0.306	62.4±27.3	0.14±0.065	62.3±12.5	0.25±0.013	142.5±19.3	0.26±0.007	111.5±9.8
4	0.41±0.240	54.8±22.9	0.23±0.066	65.2±15.5	0.23±0.012	139.9±20.9	0.25±0.007	110.5±11.4
5	0.30±0.166	51.5±19.9	0.28±0.057	67.7±17.5	0.22±0.012	137.2±23.6	0.24±0.005	110.0±11.1
6	0.23±0.092	49.3±16.8	0.28±0.029	67.5±15.1	0.21±0.009	134.5±23.6	0.22±0.012	106.7±19.7
7	0.18±0.049	47.0±15.1	0.21±0.038	62.0±20.1	0.18±0.018	124.1±38.7	0.19±0.017	100.1±28.2

Table 2.3: Calculated gradients and Q_r (intercept) values from the Q_a^{-1} vs. Q_i^{-1} results, using a variable number of points in the linear regression. For the first row, the two points used to calculate the gradient correspond to the *lowest* two attenuation values. Note that therefore these gradients have no associated regression error.

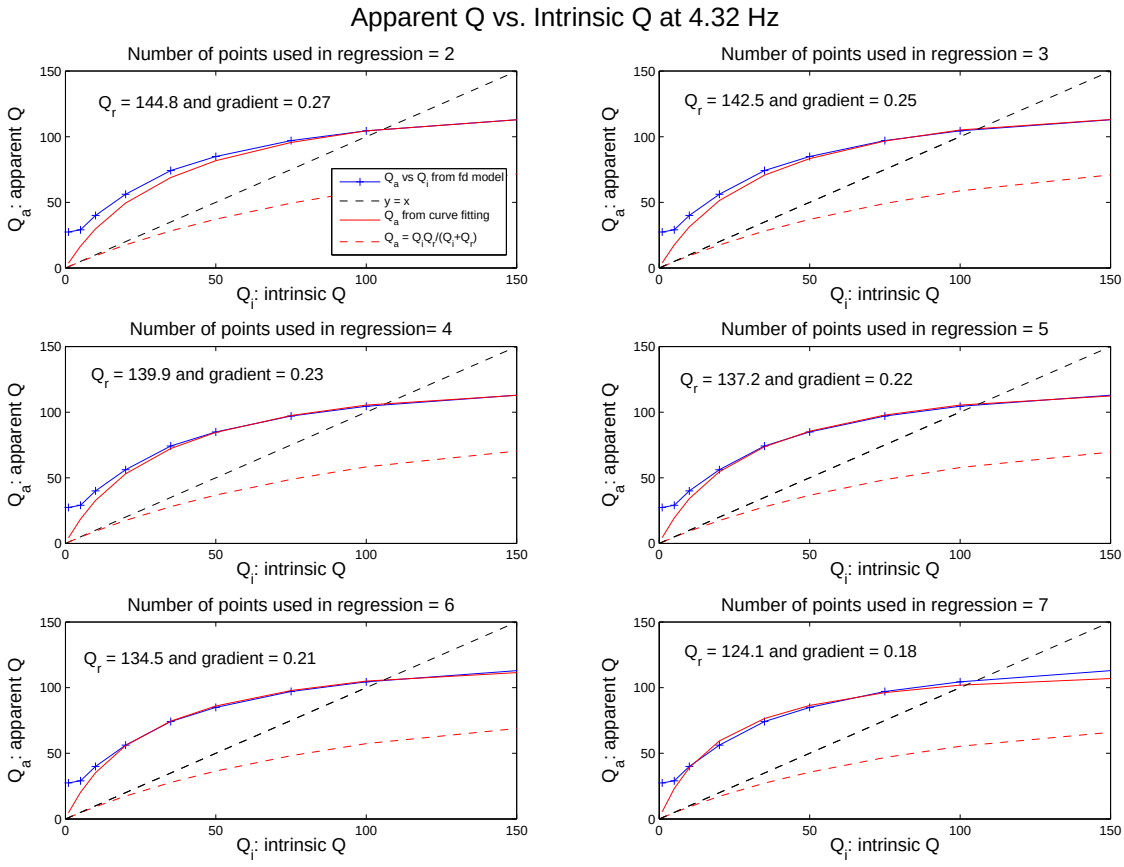

Figure 2.27: Fits to the apparent-intrinsic quality factor relationship using a variable number of datapoints. This figure contains the same information as Figure 2.26, but displayed in terms of the apparent and intrinsic quality factors, rather than the attenuation. Note that for equal intrinsic and radiative contributions (i.e. Equation 1.8), the apparent quality factor is given by $Q_{\mathrm{a}} = \dfrac{Q_i Q_r}{Q_{\mathrm{i}} + Q_{\mathrm{r}}}$, which is shown as the red dashed line in the plots.

2.4.3 Calibration of the model

Frequency dependence

To check the modelling results are not due to numerical issues with the way attenuation is implemented via the viscoelasticity in the model, it is important to test the model thoroughly. The first thing to test is the frequency dependence of Q as modelled by an array of SLS. As discussed earlier in Section 2.1.4, the model takes a value for Q_{i} and a frequency range, and inverts for the appropriate parameters to minimise the misfit to this constant attenuation level in the chosen bandwidth. Figure 2.28 shows Q_{i} as a function of frequency, between 1 and 25Hz, for increasing numbers of SLS in the array.

For a single SLS, the intrinsic quality factor as a function of frequency is given by:

$$Q(\omega) = \frac{1 + \omega^2 \tau_\epsilon \tau_\sigma}{\omega \left(\tau_\epsilon - \tau_\sigma\right)} \tag{2.25}$$

where τ_σ and τ_ϵ represent the stress and strain relaxation times (Blanch et al., 1995; Carcione et al., 2002). From this expression it is easy to see what happens as you approach low-frequencies:

$$\lim_{\omega \to 0} Q(\omega) = \infty \tag{2.26}$$

since the ω^2 term in the numerator of Equation 2.25 tends to zero faster than the ω term in the denominator. This is clearly a limitation of using the SLS rheological model as an appropriate magma rheology. Jousset et al. (2004) circumvent this problem by only considering frequencies greater than 2Hz. However, it is clear that low-frequency earthquakes contain significant energy below this frequency, and the true bandwidth of interest is more like 0.5-5Hz. Note that for increasing numbers of SLS in Figure 2.28, although in a least-squares sense the fit may be better across the whole bandwidth, in the frequency range 0-5Hz, the Q_{i} is substantially overestimated. Using 2 SLS in the array gives a suitable compromise for these particular frequency limits.

Figure 2.29 shows the Q_{i} as a function of frequency in the finite-difference model for varying bandwidths, all for 2 SLS in the array, again for a desired constant Q_{i} of 100. This plot shows the attenuative behaviour in the model between 0 and 2.5Hz, for different bandwidths passed to the model. The results highlight the importance of choosing the appropriate bandwidth, as well as the appropriate number of SLS, to ensure that the attenuation matches the desired constant value in the frequency range of interest.

In Figure 2.30, Q_{i} as a function of frequency, for input values of 10, 20, 50 and 100 are

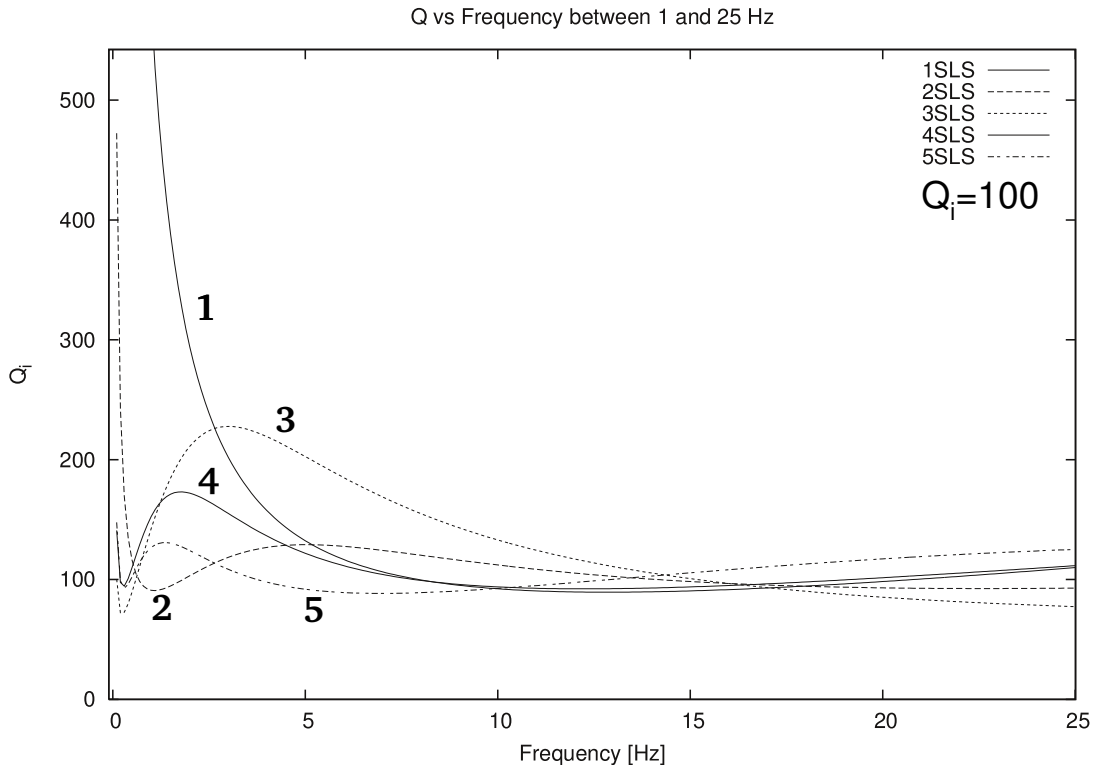

Figure 2.28: Q_i as a function of frequency, between 1 and 25Hz, for increasing numbers of SLS in the array. The desired result is a constant Q_i of 100 across the chosen bandwidth. One limitation of the Standard Linear Solid rheological model is that it forces $Q_\mathrm{i} \to \infty$ as $\omega \to 0$. Note that for increasing numbers of SLS, although in a least-squares sense the fit may be better across the whole bandwidth, in the frequency range 0-5Hz, the Q_i is substantially overestimated. Using 2 SLS in the array gives a suitable compromise.

plotted, for the cases of 1 and 2 SLS in the array. This shows that using a single SLS can substantially overestimate the Q_i at low-frequencies, meaning energy at these frequencies is not sufficiently attenuated. This demonstrates that the frequency dependence of the attenuation within the finite-difference code must be carefully considered when analysing the impact of the intrinsic attenuation on the apparent amplitude decay.

Recovery of attenuation

Now that effects of the frequency dependence have been explored, another important test is to check that the implemented attenuation can be retrieved by using spectral ratios, in a similar manner to the tests conducted by Jousset et al. (2004). The spectral ratios between stations at different distances within a homogeneous half-space are used

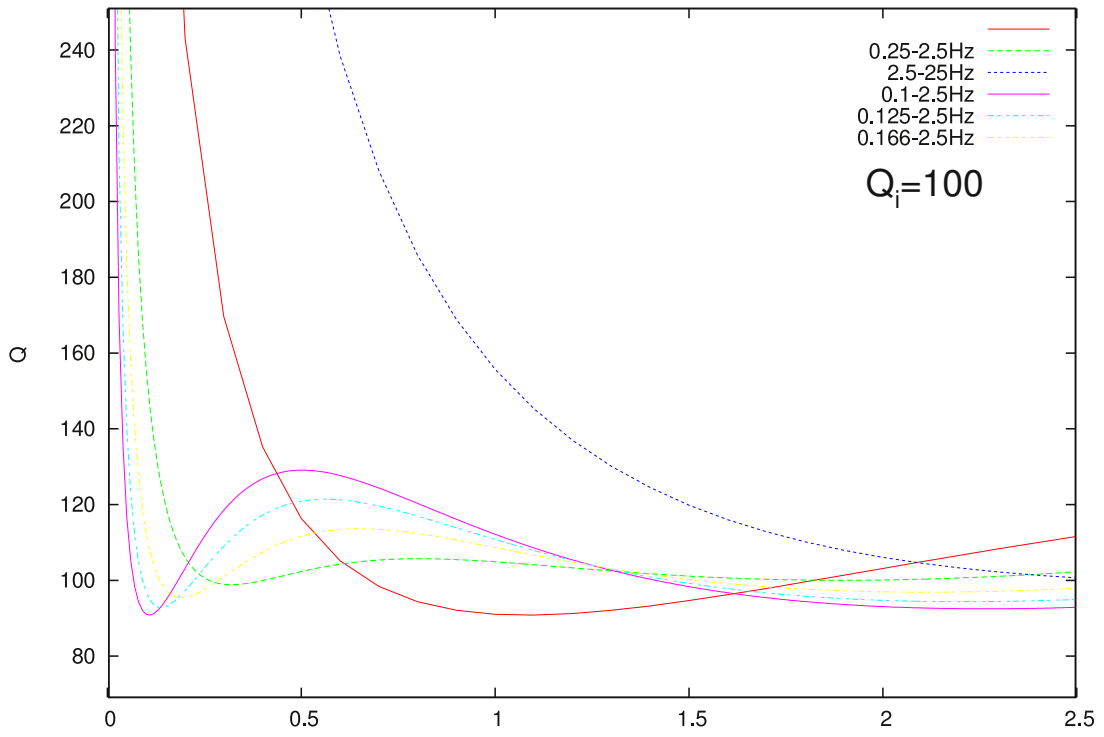

Figure 2.29: Q_i as a function of frequency in the finite-difference model for varying bandwidths, all for 2 SLS in the array, again for a desired constant Q_i of 100. This plot shows the attenuative behaviour in the model between 0 and 2.5Hz, for different bandwidths passed to the model. The results highlight the importance of choosing the appropriate bandwidth for the frequency range of interest, which for low-frequency earthquakes is between 0.5-5Hz.

to retrieve the attenuation behaviour as a function of frequency, f, using

$$Q(f) = \frac{-\pi f\,(t_2 - t_1)}{\log\left(\frac{|A_2(f)|\sqrt{r_2}}{|A_1(f)|\sqrt{r_1}}\right)} \tag{2.27}$$

for a pair of wavelets with amplitude spectra $A_1(f)$ and $A_2(f)$, recorded at distances r_1 and r_2 at times t_1 and t_2 respectively (Jousset et al., 2004). This approach to determine the frequency dependence of the attenuation is similar to that used by Jeng et al. (1999). Note that this expression is independent of the source used, and includes 2-D geometrical spreading through the $\sqrt{r}$ factor. This expression was tested for a horizontal array of stations, separated by 500m, within a homogeneous, isotropic, viscoelastic half-space, using an isotropic source.

The results show that using the whole waveform recorded at each station does not produce good results, due to the presence of reflected energy from the domain boundaries contaminating the spectra. This can be seen in three examples in Figures 2.31, 2.32

and 2.33. This approach can be improved by windowing the transmitted phases, and using these to calculate the spectral ratios. However, the resolution that can be achieved is dependent on the finite-length of the window used to isolate the transmitted phase. Using a longer time window means a higher spectral resolution, since the Q_{i} function is only evaluated at the Fourier frequencies of the amplitude spectra, but using a longer window length increases the risk of spectral contamination. Using a larger grid for the solution domain helps to reduce this effect, as reflected phases from the domain boundaries arrive at later times, allowing a longer time window to be used without contamination, although this is at the expense of increased computation time.

Despite the expression for the Q_{i} in Equation 2.27 being source independent, the frequency content of the source wavelet is still very relevant, since this determines the bandwidth of energy injected into the medium. The expression for the quality factor can only be evaluated at frequencies where there is sufficient energy for the spectral ratio to produce meaningful results. This is apparent if the results for a 1Hz Küpper source wavelet in Figure 2.32 are compared with the more broadband 10Hz Sinc function in Figure 2.32. The choice of source also has some impact on the resolution that is possible, since source wavelets with a lower frequency content or longer wavelength energy, require a longer time window for the transmitted phases.

The errors in the recovered Q_{i}, displayed in Figure 2.34, show that the recovered results do match the desired input attenuation behaviour, if the limitations of the finite-grid size and finite source bandwidth are taken into account. This indicates that any mismatch between model and theoretical Q_{i} is a function of the measurement method, and not a problem with the model implementation itself. This therefore suggests that the key result of the modelling so far, that the intrinsic attenuation contributes less than expected, has a physical explanation and is not due to calibration or numerical effects within the model. However, lessons learnt when retrieving the implemented attenuation values by using spectral ratios will have implications when real data is used in Chapter 5.

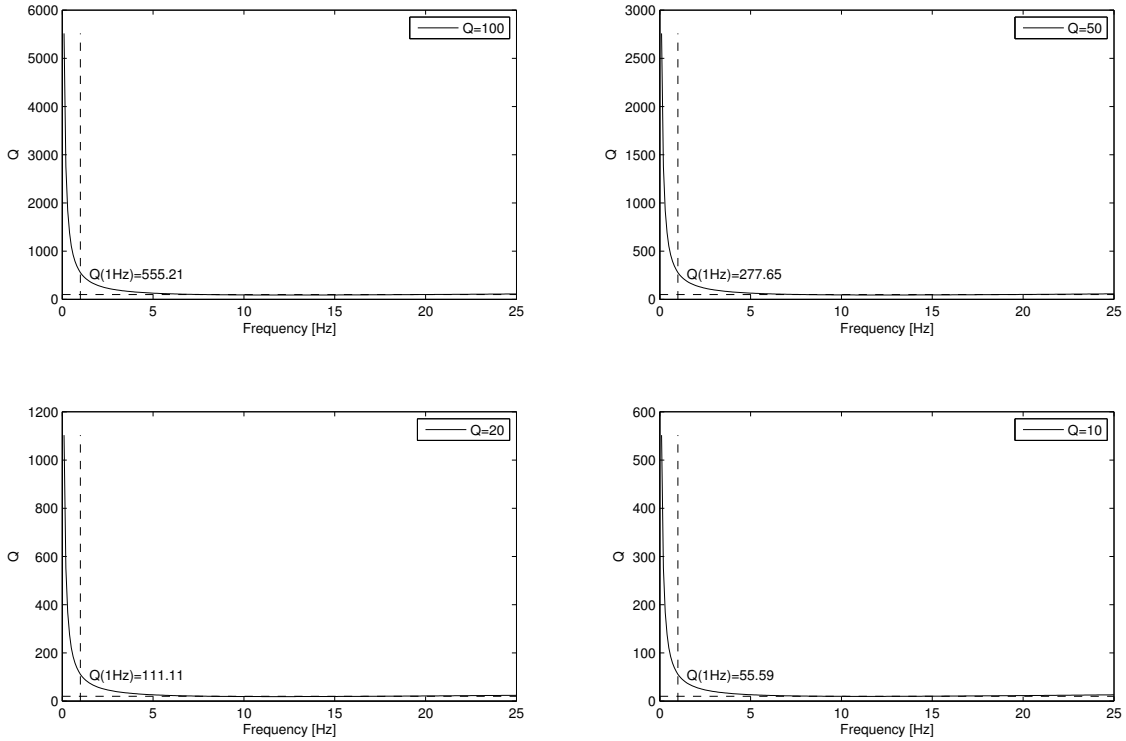

(a) 1 SLS

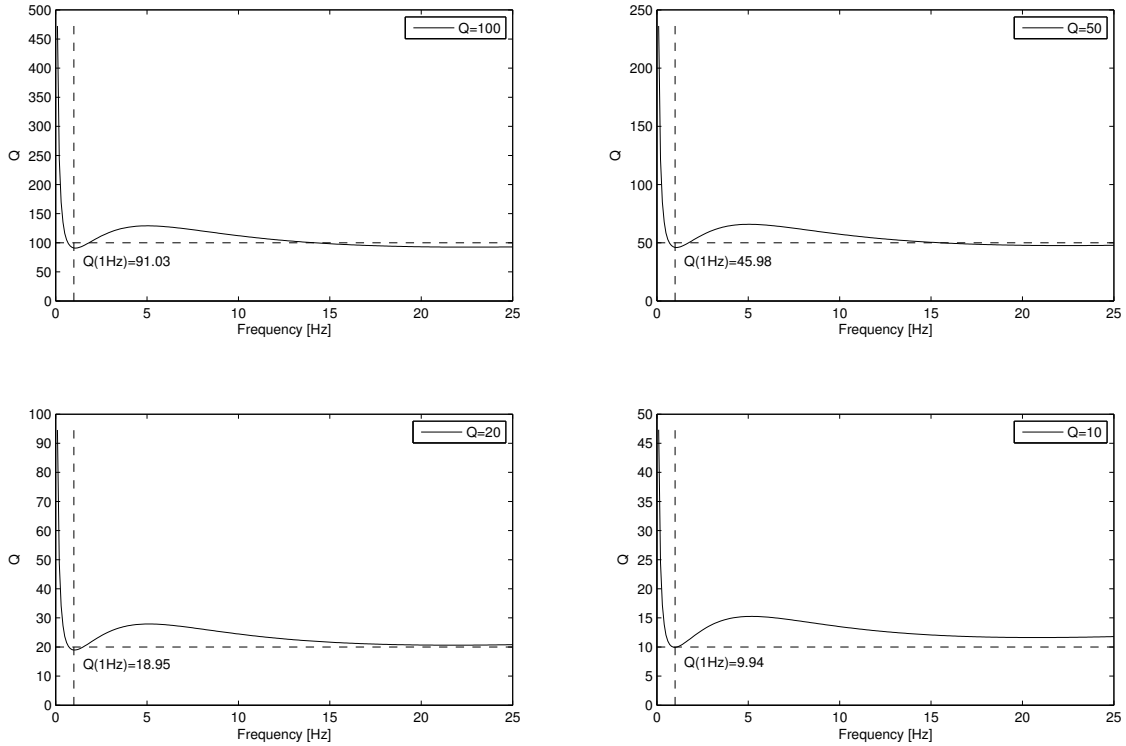

(b) 2 SLS

Figure 2.30: Quality factor as a function of frequency for intrinsic Q_{i} values of 10, 20, 50 and 100 (indicated by the dashed lines), fitted between 2 and 25Hz using (a) 1 SLS and (b) 2 SLS. The labelled values indicate the attenuation at 1Hz (the dominant frequency of the resonance) showing: (a) modelled Q_{i} values much higher than the desired input and (b) values now a better match to the desired values, especially around 1Hz.

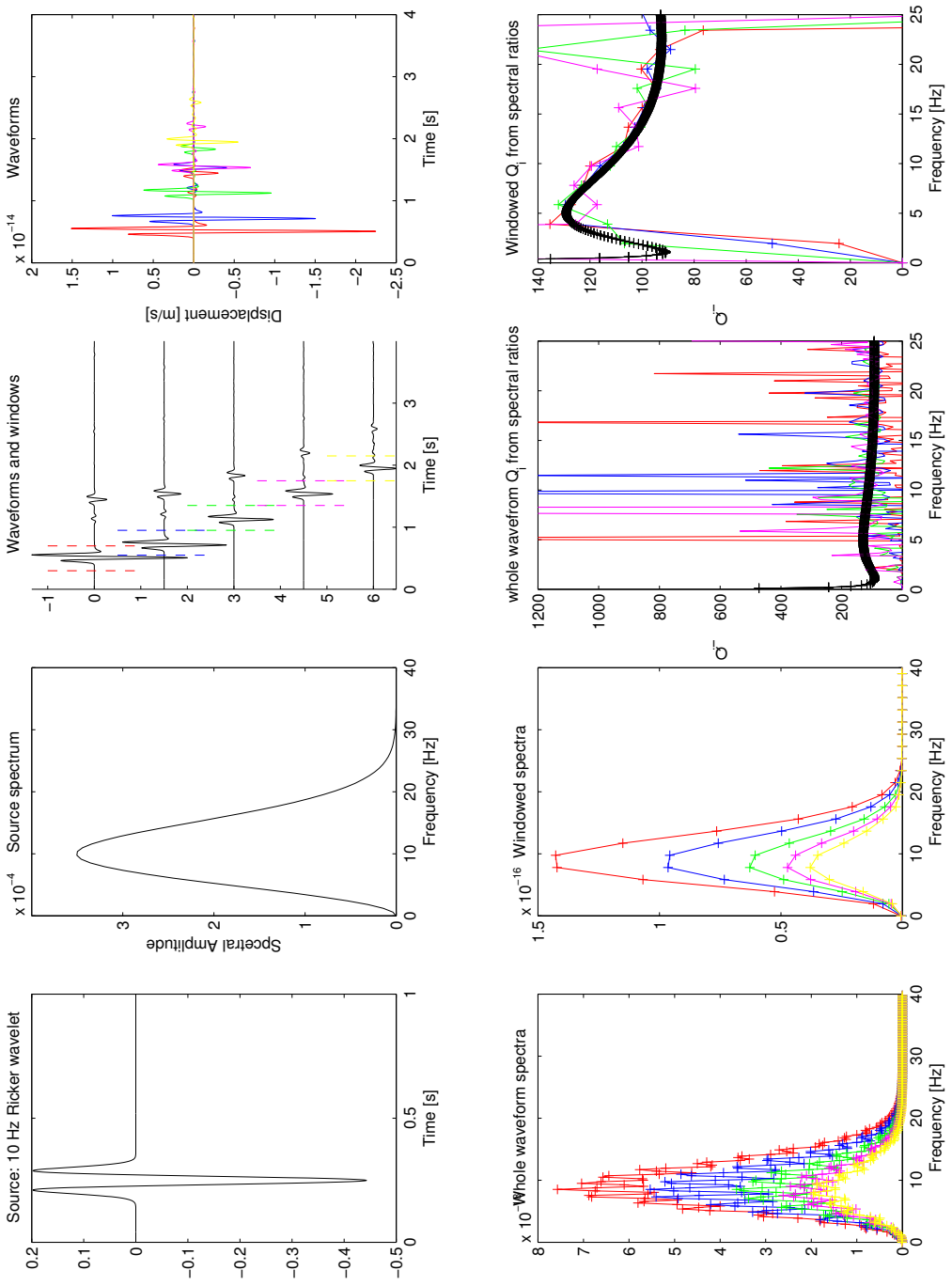

Figure 2.31: Quality factor as a function of frequency, recovered from a half-space using spectral ratios, for a constant $Q = 100$ using a 10Hz Ricker wavelet. The plot shows the source wavelet, a Ricker wavelet with centre frequency 10Hz, and its associated spectrum. The transmitted phases, recorded at stations separated horizontally by 500m, were windowed from the full waveforms and pairs used to calculate spectral ratios. The attenuation as a function of frequency was calculated, using Equation 2.27, for all possible pairs of stations and the results overlain using a different colour for each denominator in the ratio. The plots in the lower right show the recovered Q_i from both the windowed phases and the whole waveforms. This example used a 6×2km grid.

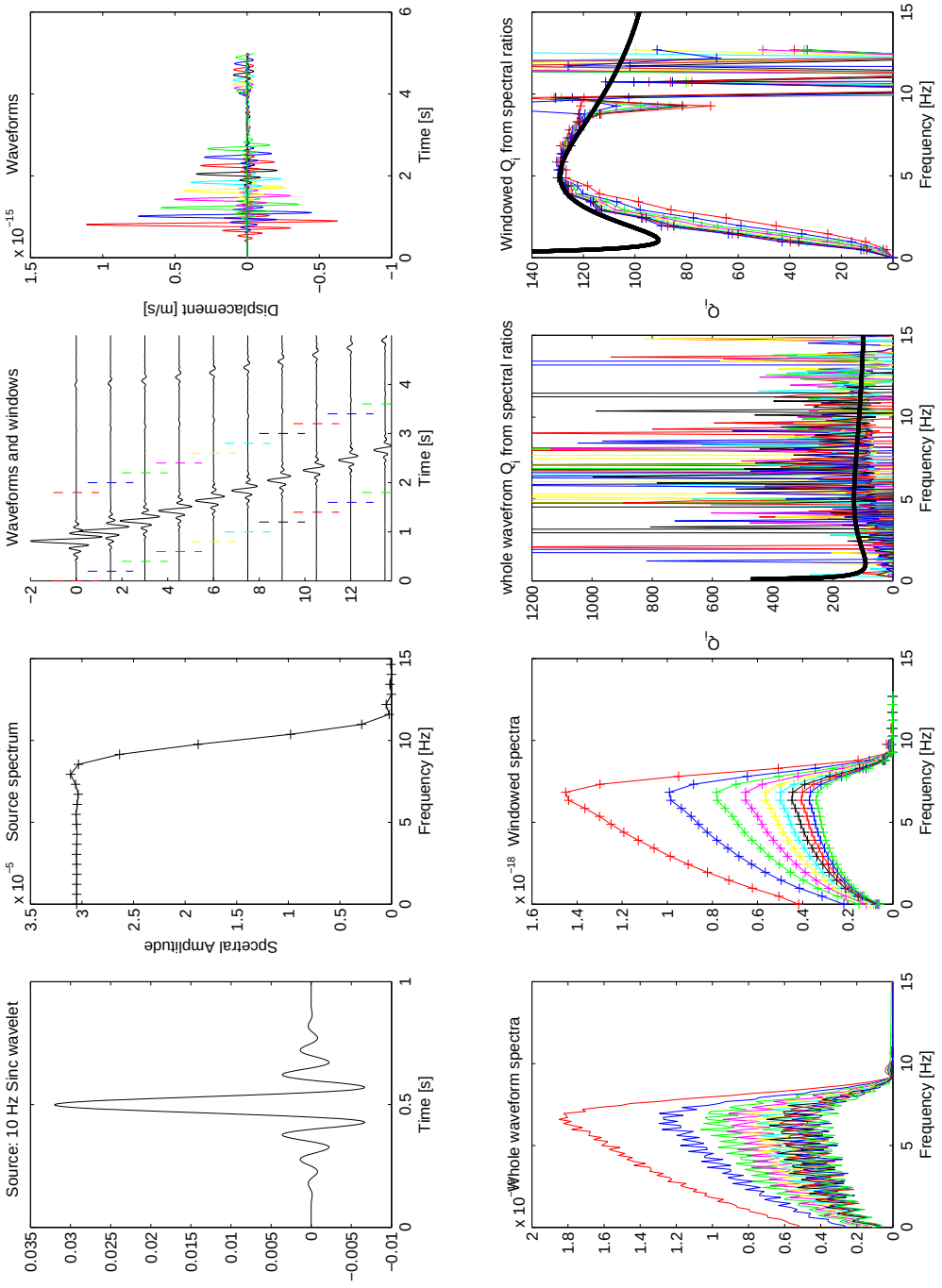

Figure 2.32: Quality factor as a function of frequency, recovered from a half-space using spectral ratios, for a constant $Q = 100$ using a 10Hz Sinc function. The format is the same as for Figure 2.31, showing a 10Hz Sinc function source wavelet and its spectrum and the windowed transmitted phases and their spectra. Note the different frequency scale, truncated at 15Hz. This example used a 18×6km grid.

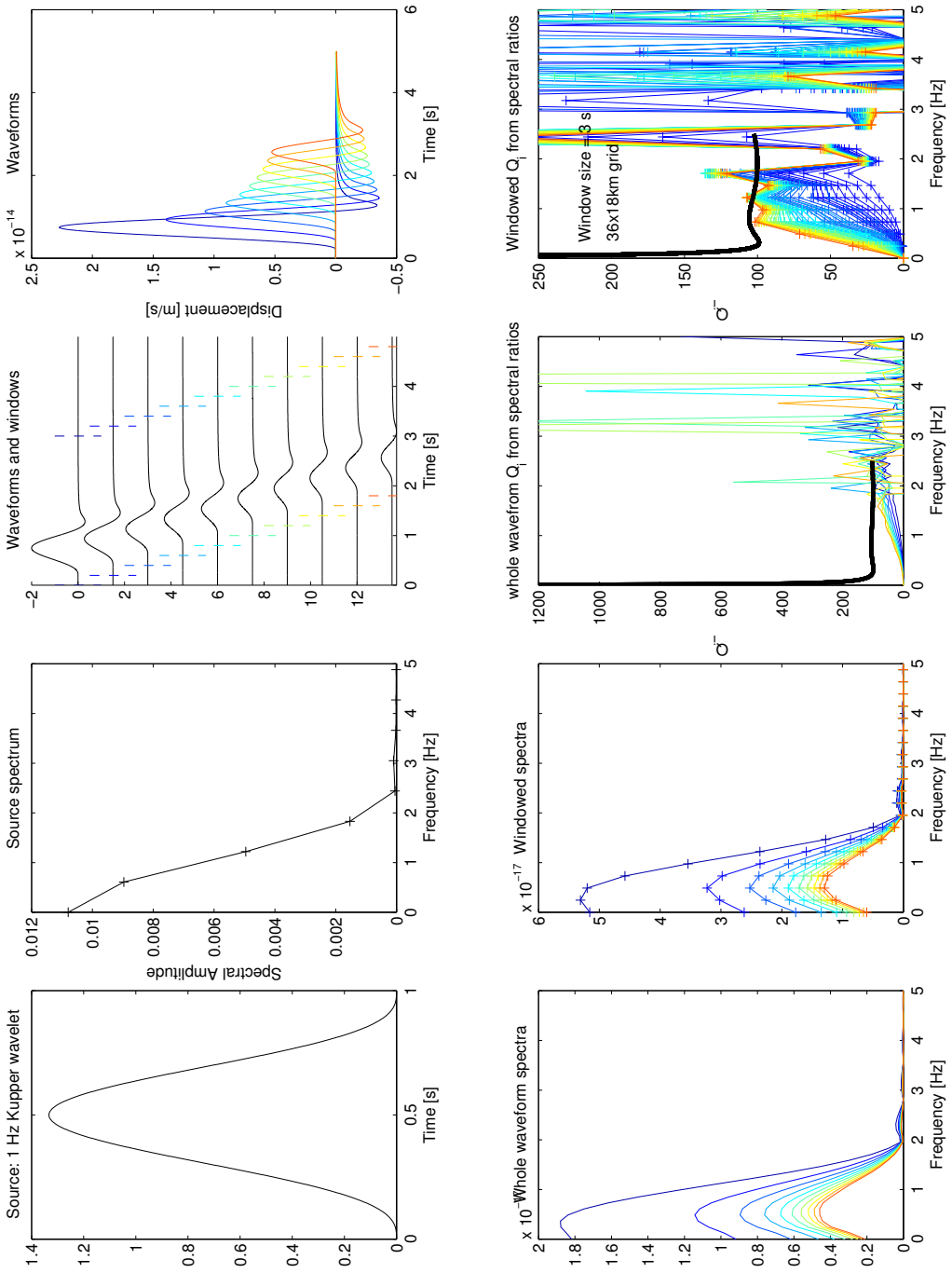

Figure 2.33: Quality factor as a function of frequency, recovered from a half-space using spectral ratios, for a constant $Q = 100$ using a 1Hz Küpper wavelet. The format is the same as for Figure 2.31, showing a 1Hz Küpper source wavelet and its spectrum and the windowed transmitted phases and their spectra. Note the different frequency scale, truncated at 5Hz. This example used a larger 36×18km grid to minimise reflections and a window length of 3 seconds.

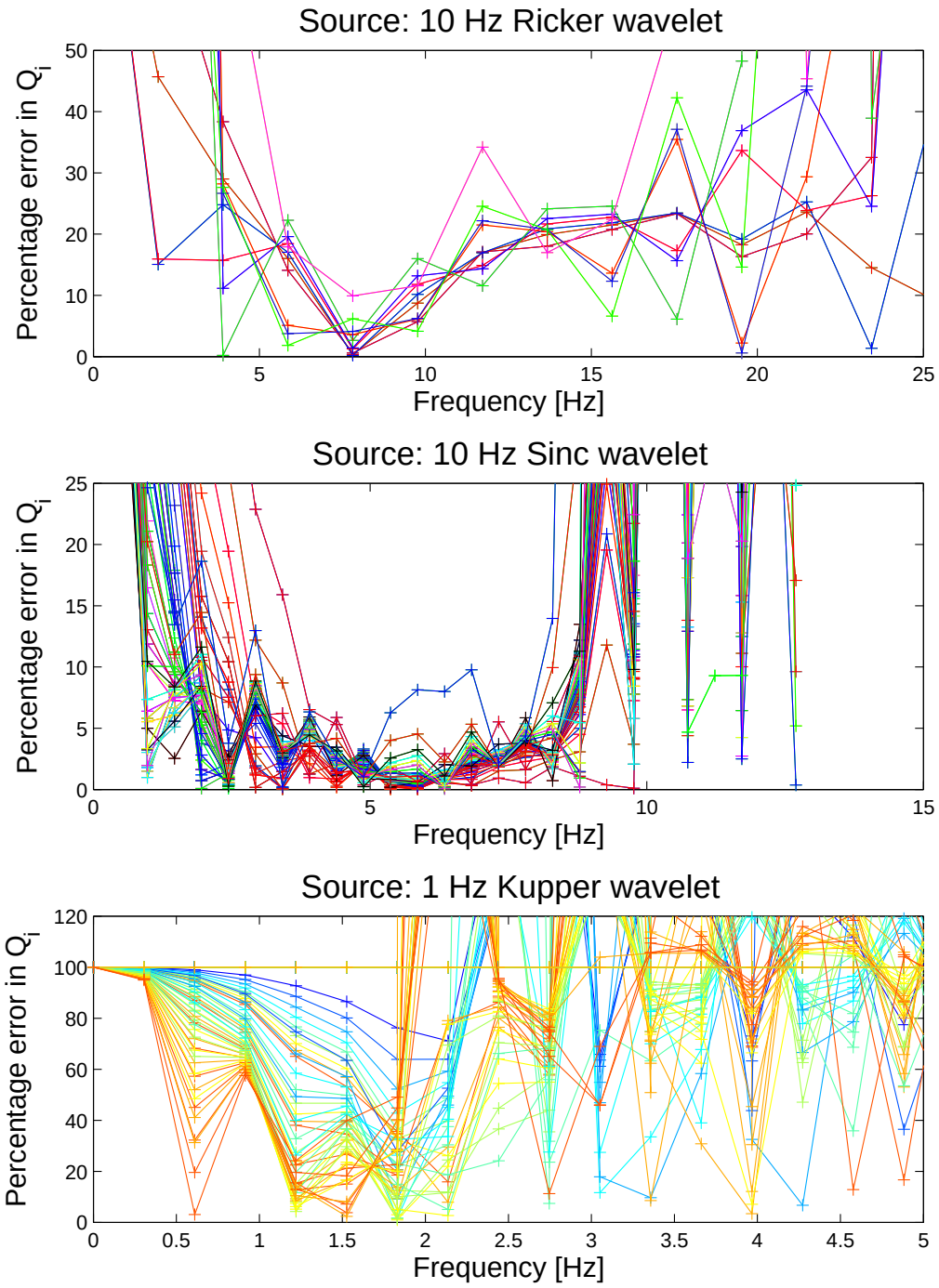

Figure 2.34: Percentage error in the recovered intrinsic quality factor as a function of frequency for three examples. The top subplot shows the error in Q_{i} for the spectral ratio results in Figure 2.31, the middle for Figure 2.32 and the lower for Figure 2.33. Note the dependence on the source bandwidth, with the lowest error in Q_{i} corresponding to the peak frequency of the source spectrum. In the 'best' example, the 10Hz Sinc wavelet source in the middle subplot, the error in Q_{i} is less than 5% for all spectral ratio pairs in the range 4-8Hz. This indicates that the recovered results do match the desired input attenuation behaviour, if the limitations of the finite-grid size and finite source bandwidth are taken into account.

2.5 Discussion and Conclusions

Both elastic and viscoelastic models of seismic wave propagation have been used to examine both the radiative and intrinsic components of the amplitude decay of low frequency earthquakes.

In Section 2.3 it was shown that the analysis of the radiative part of the amplitude decay suggests that there is significant variation in Q_{r}, with frequency and source-receiver geometry, even without the further effects of topographic scattering. For the case of a free surface, this plays an important role in determining the exact frequency content of the signals observed. In the models, with a flat free surface, the *same* spectral peaks were recorded at different arrays across the medium, which suggests that these can be attributed to source processes in the resonator (since these are also observed *within* the fluid). However the relative amplitude of these peaks is modulated by complex interference patterns, even in the case of the simplest geometry possible. This in itself is not a new result and has been shown previously by Neuberg et al. (2000). The results in Section 2.3 also suggest separation of the two parts from a combined signal may be very complex, as the specific model geometry, source receiver geometry and topography would be needed in order to model properly the radiative Q_{r}^{-1}, which needs to be subtracted from the apparent attenuation to leave the intrinsic Q_{i}^{-1}. This suggests that to get direct quantitative measurements of Q_{i}^{-1} from Q_{a}^{-1} and attribute these to viscosity values will require further study, and this problem, along with a wider discussion on the seismological constraints on magma properties, is explored in Chapter 5. *Changes* in Q_{a} however, rather than absolute measurements, may be a more appropriate tool, especially from a volcano monitoring perspective if an appropriate baseline and catalogue of measurements is developed to facilitate further analysis, and provide assistance in forecasting future behaviour. Analysis of low-frequency earthquakes at SHV and temporal changes in the apparent attenuation are the focus of Chapter 5.

In Section 2.4 it was shown that the intrinsic part of the attenuation, related to the fluid viscosity, does not contribute as much as expected to the apparent amplitude decay based on the simple relationship first suggested by Aki (1984):

$$Q_{\mathrm{a}}^{-1} = Q_{\mathrm{i}}^{-1} + Q_{\mathrm{r}}^{-1} \tag{2.28}$$

with the intrinsic part in fact contributing $23.6 \pm 2.26\%$ less than it should for this relationship to be valid. Testing of the viscoelastic finite-difference model demonstrated

that this is not a result of numerical or calibration errors within the model and must therefore have a physical explanation. The idea that this physical explanation could be differences between the way in which interface and acoustic waves are attenuated will be explored in Chapter 3.

One point that should be considered however, is the appropriateness of an array of SLS, where the attenuation is constant with frequency, as a model for the magma rheology. Jousset et al. (2004) argued that the SLS is a good approximation to the rheological behaviour of magma for frequencies above 2Hz, yet, as discussed, the bandwidth of interest for low-frequency earthquakes is closer to 0.5-5Hz. This suggests that, although extensively used, this may not be the most appropriate rheological model to parametrise the material in the model. Dingwell (1995) has suggested that a bubble and crystal free melt behaves more like a Maxwell body, even during glass transition (Dingwell & Webb, 1990), while a three-phase magma can exhibit various rheological behaviours, depending on the gas and crystal contents (e.g. Prud'Homme & Bird, 1978; Hess & Dingwell, 1996). Also, the numerical work of Collier et al. (2006), who quantified the attenuation in bubbly magma, showed that the behaviour of attenuation with frequency may be quite complex, especially if diffusion is considered, and attenuation can also vary considerably with depth. This suggests a further development of the model would be to incorporate a more realistic rheology that also includes spatial variations.

Previous studies that have used the attenuation of low-frequency events as a probe for the fluid composition have either (i) ignored Q_{i} completely (Morrissey & Chouet, 2001) or (ii) treated it separately to the radiative part (Kumagai & Chouet, 2000).

For case (i), the results in Section 2.4 suggest that this may be a valid assumption, but for different reasons. Kumagai & Chouet (2000) assumed low viscosity and therefore low attenuating fluids, whereas the results here suggest that even for a high viscosity fluid, the attenuative effect is not as much as expected based on acoustic wave propagation. For case (ii), treating both components separately relies on the assumption that the relationship of Aki (1984) (Equation 2.28) is valid, which has been shown not to be the case by the results of the modelling. This also means that any viscosity values based on the intrinsic attenuation have been substantially underestimated, suggesting the interpretation of the fluid composition or viscosities based on these values must also be reconsidered.

The key result of the modelling in Section 2.4 also has further implications for conduit resonance models of low-frequency earthquakes. The idea that the impact of the intrinsic attenuation on the overall damping is less than expected provides further evidence that as well as being an efficient energy trap through their waveguide-like properties and high acoustic impedance contrasts, fluid-filled resonators may also attenuate energy less than waves propagating in the fluid itself. This allows the prospect of high viscosity magma bodies acting as fluid-filled resonators capable of producing measurable seismic signals. This widens the set of possible plumbing systems capable of generating seismic signals, and means crack-like geometries with low-density and low viscosity fluids are not necessarily required to generate low-frequency earthquakes.

Chapter 3

Attenuation of interface waves: an analytical approach

3.1 Interface waves

As discussed in Chapter 1, resonance of seismic energy in fluid-filled bodies has been extensively studied in recent years as a potential source of low-frequency seismicity on volcanoes. One of the major advances has been the discovery of highly dispersive *interface waves* which trap energy at boundaries between fluid and solid media, and can travel more slowly than the acoustic velocity of the fluid, hence explaining the low-frequency content. In this chapter some of the terminology regarding interface waves is clarified before the motivation for studying the attenuation of such waves is discussed. An analytical approach to quantifying the attenuation of interface waves then forms the rest of the chapter.

'Stoneley waves' are inhomogeneous seismic waves that propagate along a *single* interface between two elastic media (Stoneley, 1924) or a fluid layer overlying a solid medium (Stoneley, 1926). Further investigations of coupled fluid-solid systems were carried out by Biot (1952) who considered the propagation of seismic waves in fluid-filled cylindrical boreholes. The phase and group velocity dispersion relations were derived for so-called 'tube-waves' confined to, and propagating along, the fluid-solid boundary. Two classes of waves were identified:

1. Slow waves that propagate with a velocity lower than the acoustic velocity of the fluid. At short wavelengths or high frequencies this tends towards the Stoneley wave velocity of the fluid-solid interface. For long wavelengths, the velocity tends

towards a finite asymptotic value.

2. Fast waves that propagate with a velocity intermediate between the acoustic velocity of the fluid and the S-wave velocity of the surrounding elastic solid.

Of these two classes, the first is of most interest for volcano-seismology, as it is can be used to describe the phase velocity dispersion relation for tube waves propagating in a magma-filled cylindrical conduit.

Ferrazzini & Aki (1987) followed a similar method to Biot (1952) but determined the dispersion relations for an infinite horizontal fluid layer sandwiched between two elastic half-spaces, rather than a cylindrical borehole. From a volcanological perspective this geometry represents a magma-filled sheet, crack or dyke structure. Again, two classes of wave were found:

1. What Ferrazzini & Aki (1987) term 'slow waves' which propagate with a velocity lower than the acoustic velocity of the fluid. This mode of interface wave, like the tube wave of Biot (1952), approaches the Stoneley wave velocity for the fluid-solid boundary in the high frequency or short wavelength limit. However, as the wavelength tends to infinity, the phase velocity of these waves approaches zero, unlike in the tube wave case, hence, the waves exhibit strong inverse dispersion.

2. Fast waves that propagate with a velocity intermediate between the acoustic velocity of the fluid and the S-wave velocity of the surrounding elastic solid.

The explicit dispersion relations for the modes identified by Ferrazzini & Aki (1987) are given, in terms of the ratios of phase-to-acoustic velocities $\epsilon = v_{\mathrm{ph}}/c_{\mathrm{p}}$, $\epsilon_{\mathrm{s}} = v_{\mathrm{ph}}/V_{\mathrm{s}}$, and $\epsilon_{\mathrm{c}} = v_{\mathrm{ph}}/V_{\mathrm{p}}$, by:

for $\epsilon > 1$

$$\cot\left(\sqrt{\epsilon^2-1}\frac{hk_x}{2}\right) = +\frac{\rho_{\mathrm{s}}}{\rho_{\mathrm{f}}}\frac{\sqrt{\epsilon^2-1}}{\epsilon_{\mathrm{s}}^4}\left(\frac{(2-\epsilon_{\mathrm{s}})^2}{\sqrt{1-\epsilon_{\mathrm{c}}^2}} - 4\sqrt{1-\epsilon_{\mathrm{s}}^2}\right) \tag{3.1}$$

$$\tan\left(\sqrt{\epsilon^2-1}\frac{hk_x}{2}\right) = -\frac{\rho_{\mathrm{s}}}{\rho_{\mathrm{f}}}\frac{\sqrt{\epsilon^2-1}}{\epsilon_{\mathrm{s}}^4}\left(\frac{(2-\epsilon_{\mathrm{s}})^2}{\sqrt{1-\epsilon_{\mathrm{c}}^2}} - 4\sqrt{1-\epsilon_{\mathrm{s}}^2}\right) \tag{3.2}$$

and for $\epsilon < 1$

$$\coth\left(\sqrt{1-\epsilon^2}\frac{hk_x}{2}\right) = -\frac{\rho_\mathrm{s}}{\rho_\mathrm{f}}\frac{\sqrt{1-\epsilon^2}}{\epsilon_\mathrm{s}^4}\left(\frac{(2-\epsilon_\mathrm{s})^2}{\sqrt{1-\epsilon_\mathrm{c}^2}} - 4\sqrt{1-\epsilon_\mathrm{s}^2}\right) \tag{3.3}$$

$$\tanh\left(\sqrt{1-\epsilon^2}\frac{hk_x}{2}\right) = -\frac{\rho_\mathrm{s}}{\rho_\mathrm{f}}\frac{\sqrt{1-\epsilon^2}}{\epsilon_\mathrm{s}^4}\left(\frac{(2-\epsilon_\mathrm{s})^2}{\sqrt{1-\epsilon_\mathrm{c}^2}} - 4\sqrt{1-\epsilon_\mathrm{s}^2}\right) \tag{3.4}$$

where k_x is the horizontal wavenumber and v_ph is the phase velocity of the interface waves with V_p and V_s the P-and S-wave velocities of the elastic solid. The width of the layer is h, with the fluid and solid densities given by ρ_f and ρ_s respectively. Equations 3.2 and 3.4 describe the case where the pressure perturbation is symmetric, whilst Equations 3.1 and 3.3 describe the antisymmetric case. The antisymmetric case contains all the modes that occur for a single interface between a fluid layer overlying a solid half-space, whilst the symmetric modes are specific to the case of upper and lower boundaries for the fluid layer. The four dispersion relations are displayed graphically in Figure 3.1.

The velocity behaviour of this 'slow-wave' was found to match, in terms of both velocity and amplitude, the numerical results for what Chouet (1986; 1988) termed 'crack waves', observed in finite-difference models of resonating three-dimensional fluid-filled cracks. These can be thought of as seismic waves arriving at the interface at post-critical angles, resulting in inhomogeneous waves which travel along the length the boundary. The amplitude decays rapidly away from the boundary, by a factor of around 100 in a distance equivalent to a wavelength. This means the wave is trapped at the interface, making it difficult to observe at distances greater than a wavelength from the boundary (Ferrazzini & Aki, 1987). These interface waves may have large amplitudes compared to other seismic phases and as Korneev (2008) points out, one of the distinctive features of fluid-filled fractures is their ability to trap and transport energy efficiently by acting in a waveguide-like manner. It should be noted however, that Ferrazzini & Aki (1987) consider an infinitely long fluid layer, and therefore do not treat the radiation of energy from the tips of a finite-length layer, although they suggest that this could be an important seismic source.

The finite-difference models used throughout this thesis are two-dimensional, so any fluid-filled areas embedded in the solution domain of the model represent a dyke-like structure and not a cylindrical conduit (assuming plane-strain in the 3$^{\mathrm{rd}}$ dimension). This corresponds to the fluid-filled layer solutions of Ferrazzini & Aki (1987) for interface waves trapped at the boundaries of such a layer. Hence, the remainder of this chapter

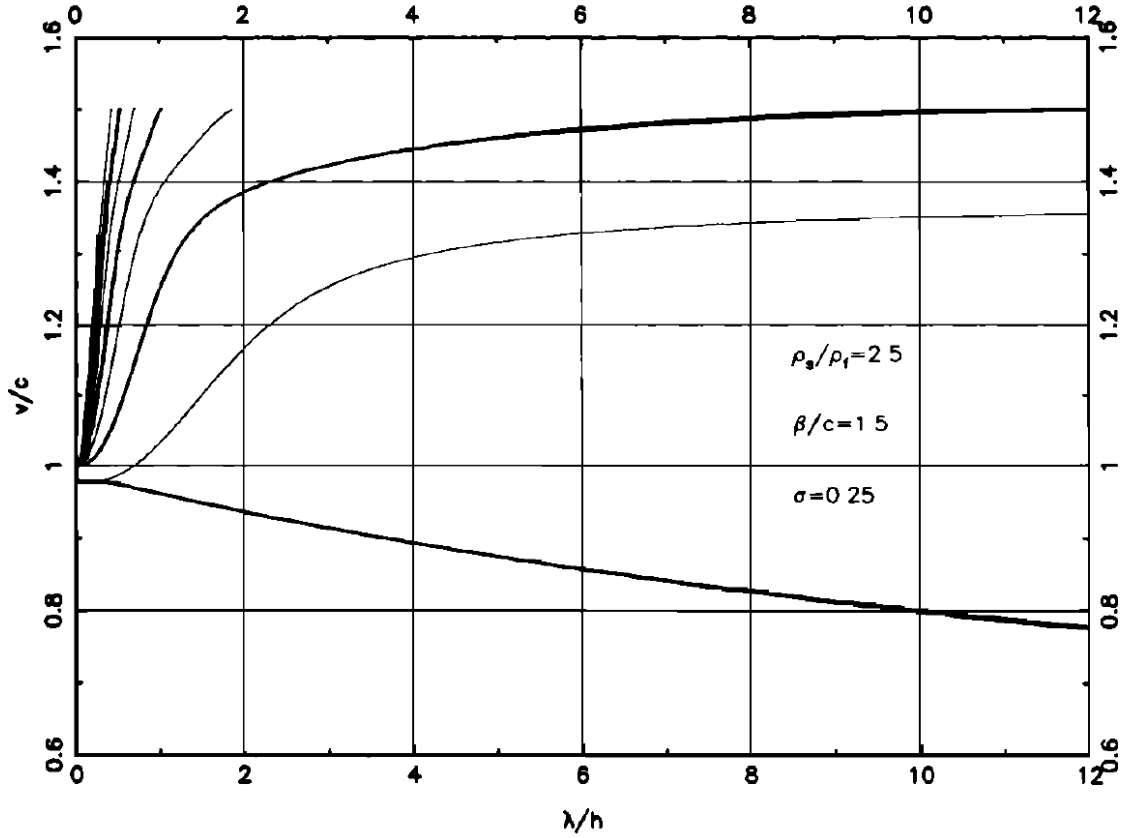

Figure 3.1: Ratio of phase velocity to acoustic velocity, $v_{\mathrm{ph}}/c_{\mathrm{p}}$, as a function of dimensionless wavelength, λ/h, for an infinite fluid layer (taken from Ferrazzini & Aki (1987)). This graph shows the different modes or branches, travelling faster or slower than the acoustic velocity. Note the 'slow wave' mode, described by the solution to Equation 3.4, which shows strong inverse dispersion. Its phase velocity is less than the acoustic velocity for all wavelengths and tends to zero as the wavelength increases. The fixed parameters used to evaluate the dispersion relations were: $\rho_{\mathrm{s}}/\rho_{\mathrm{f}} = 2.5$ and $V_s/c_{\mathrm{p}} = 1.5$ with a Poisson's ratio of $\sigma = 0.25$.

is concerned with understanding the attenuative behaviour of interface waves in this context, rather than tube waves in a cylindrical geometry, which would require three-dimensional treatment.

3.2 Motivation for quantifying their attenuation

A key observation of the modelling work in Section 2.4.2 was that the attenuative effect of the viscosity of the magma on the seismic resonance appears to be overestimated. Having ruled out calibration errors in the model in Section 2.4.3, a more exciting alternative will now be investigated, which offers a physical explanation for this result: the difference between interface and acoustic wave propagation. As Collier et al. (2006) point out,

estimations of Q_i^{-1} for magma and other volcanic fluids have all assumed that the seismic energy propagates as simple acoustic waves. Yet we know that low-frequency resonance is a result of interface waves trapped in a narrow conduit, dyke or crack, filled with fluid and that these waves are fundamentally different in terms of velocity dispersion and amplitude to acoustic waves (Ferrazzini & Aki, 1987; Chouet, 1986; 1988; Neuberg et al., 2000; Sturton & Neuberg, 2006). In particular, we know from both numerical and analytical studies that their dispersion relation is highly sensitive to the contrast in elastic parameters at the fluid-solid boundary, so one cannot assume that their attenuation is the same as that of acoustic waves in the fluid. Therefore, in the next sections an analytical approach is used to quantify the attenuation experienced by interface waves, explore how it differs from that of acoustic waves, and to prompt a discussion of the implications for resonance and low-frequency earthquakes in general.

3.3 Derivation

3.3.1 The attenuation of interface waves

The analytic expression for the phase velocity of the slow interface waves described by Ferrazzini & Aki (1987) in Equation 3.4 was derived for a purely inviscid fluid layer. To examine resonance in fluid-filled fractures in hydrocarbon reservoirs Korneev (2008) used the same method, but introduced a fluid viscosity, resulting in a complex expression for the phase velocity of these waves. Here, this work is applied to a volcanic environment and an expression for the attenuation of an interface wave at the boundaries of a horizontal viscous fluid layer sandwiched between two elastic half-spaces (see Figure 3.2) is explicitly derived.

Beginning with the general expression for the phase velocity (Equation 40 of Korneev, 2008):

$$V_{\mathrm{f}}^3 = V_{\mathrm{f0}}^3 \frac{\beta}{1 + \sqrt{\beta/3} + \beta} \tag{3.5}$$

where the parameter

$$\beta = \frac{-iS^2}{12} \tag{3.6}$$

is defined through the normalised skin factor

$$S = h\sqrt{\frac{\omega\rho_{\mathrm{f}}}{\eta}} \tag{3.7}$$

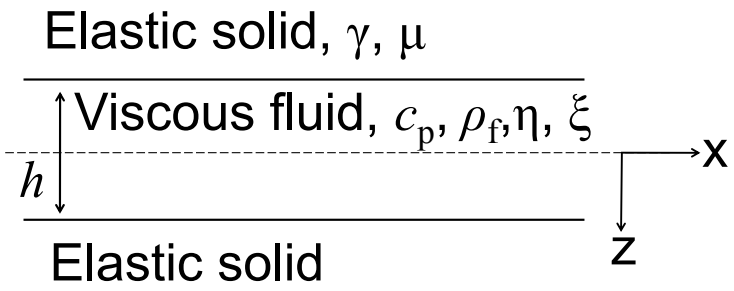

Figure 3.2: Geometry and properties of the viscous fluid layer in the analytical problem. The viscous fluid layer is of thickness h, with density ρ_f, acoustic velocity c_p and shear and volume viscosities η and ξ respectively. The fluid layer is sandwiched between two elastic half-spaces with a shear-to-compressional velocity ratio of $\gamma = V_\mathrm{s}/V_\mathrm{p}$ and rigidity μ. Solutions to the wave equation for interface waves at the boundary are of the form $u = A(k_x, z, \omega)e^{i(k_x x - \omega t)}$, which propagate along the x-axis with phase velocity V_f and wavenumber $k_x = \omega/V_\mathrm{f}$. (After Ferrazzini & Aki (1987) and Korneev (2008)).

and the low-frequency asymptote of the phase velocity is given by

$$V_{\mathrm{f}0}^3 = \frac{\omega h \mu}{\rho_\mathrm{f}} \left(1 - \gamma^2\right) \tag{3.8}$$

where h is the layer width or thickness, ρ_f the fluid density, η the fluid shear viscosity and ω the angular frequency. For the surrounding elastic solid γ represents the ratio of shear-to-compressional wave velocities with rigidity μ. The behaviour of the phase velocity with frequency is shown in Figure 3.3. Note the strong inverse dispersion, in that $|V_\mathrm{f}| \to 0$ as $\omega \to 0$.

Attenuation can be related to the material properties of a medium through the phase lag between applied stress and resulting strain (e.g. Collier et al., 2006), equivalent to the ratio of the imaginary and real parts of the complex modulus which describes the viscoelastic behaviour of a material (O'Connell & Budiansky, 1978). Since the phase-velocity of the interface waves is complex, a similar approach can be used to define the attenuation of the interface waves, $Q^{-1}_{\mathrm{interface}}$, to be the ratio of the imaginary and real parts of the complex phase velocity V_f (equivalent to using the complex wavenumber):

$$Q^{-1}_{\mathrm{interface}}(\omega) = \frac{\Im(V_\mathrm{f})}{\Re(V_\mathrm{f})}. \tag{3.9}$$

Observing that the expression for V_f^3 in Equation 3.5 is the quotient of two complex numbers, i.e. $z_1 = a + ib = \beta$ and $z_2 = c + id = 1 + \sqrt{\beta/3} + \beta$, we can write

$$V_\mathrm{f}^3 = V_{\mathrm{f}0}^3 \frac{z_1}{z_2} = V_{\mathrm{f}0}^3 \frac{a + ib}{c + id} = V_{\mathrm{f}0}^3 \frac{(ac + bd) + i(bc - ad)}{c^2 + d^2}. \tag{3.10}$$

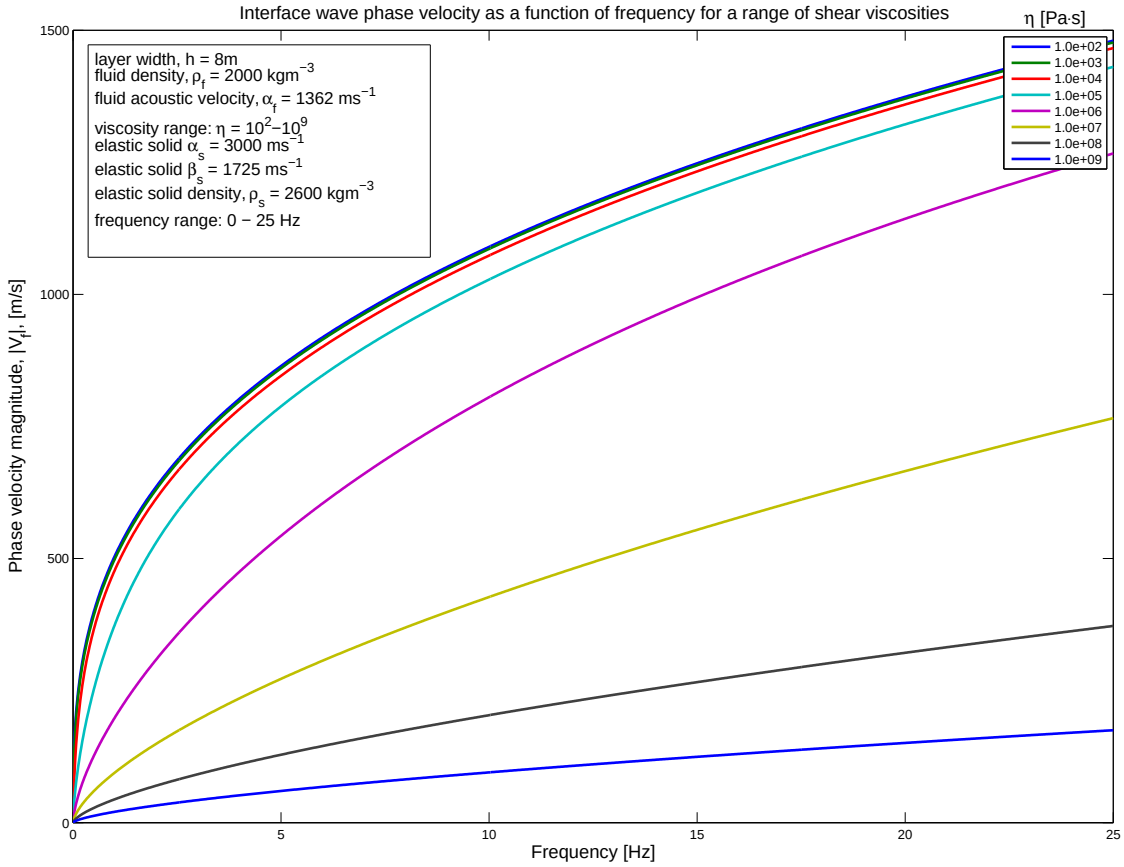

Figure 3.3: Curves showing the magnitude of the complex interface wave phase-velocity, $|V_\mathrm{f}|$, as a function of frequency. The expression in Equation 3.5 was evaluated for a set of realistic volcanic parameters (listed in the box) identical to those used in the finite-difference models in Chapter 2. Each curve represents a different shear viscosity value ranging from 10^2 to 10^9 Pas.

Since β is purely imaginary, by setting $a = \Re(z_1) = \Re(\beta) = 0$, Equation 3.10 simplifies to

$$V_\mathrm{f}^3 = V_{\mathrm{f}0}^3 \frac{bd + ibc}{c^2 + d^2}. \tag{3.11}$$

with $b = \Im(z_1) = |\beta|$, $c = \Re(z_2) = \left(1 + \sqrt{\frac{h^2\omega\rho_\mathrm{f}}{72\eta}}\right)$ and $d = \Im(z_2) = -\left(\frac{h^2\omega\rho_\mathrm{f}}{12\eta} + \sqrt{\frac{h^2\omega\rho_\mathrm{f}}{72\eta}}\right)$.

This formulation gives us the real and imaginary parts of V_f^3 from which we obtain the phase angle:

$$\phi = \tan^{-1}\left(\frac{\Im(V_\mathrm{f}^3)}{\Re(V_\mathrm{f}^3)}\right) = \tan^{-1}\left(\frac{V_{\mathrm{f}0}^3 bc}{c^2 + d^2} \Big/ \frac{V_{\mathrm{f}0}^3 bd}{c^2 + d^2}\right) = \tan^{-1}\left(\frac{c}{d}\right) \tag{3.12}$$

In order to take the cube root of Equation 3.11, we write the complex phase velocity in polar form, $V_\mathrm{f}^3 = re^{i\phi}$,

$$V_\mathrm{f} = \left(V_\mathrm{f}^3\right)^{\frac{1}{3}} = \left(re^{i\phi}\right)^{\frac{1}{3}} = r^{\frac{1}{3}} e^{i\phi/3} = Re^{i\Phi} \tag{3.13}$$

where $R = r^{\frac{1}{3}}$ and $\Phi = \phi/3$. Finally, $Q^{-1}_{\text{interface}}(\omega)$, can be directly obtained from the tangent of this new phase angle:

$$Q^{-1}_{\text{interface}}(\omega) = \frac{\Im(V_{\text{f}})}{\Re(V_{\text{f}})} = \tan\Phi = \tan\left(\phi/3\right) \tag{3.14}$$

which after substituting for ϕ from Equation 3.12 and some manipulation yields:

$$Q^{-1}_{\text{interface}}(\omega) = \tan\left(\frac{1}{3}\tan^{-1}\left(-\frac{1+\sqrt{\frac{h^2\omega\rho_{\text{f}}}{72\eta}}}{\left(\frac{h^2\omega\rho_{\text{f}}}{12\eta}+\sqrt{\frac{h^2\omega\rho_{\text{f}}}{72\eta}}\right)}\right)\right) \tag{3.15}$$

The behaviour of this expression for the interface wave attenuation with frequency is illustrated in Figure 3.4. It can be seen that low-frequencies are attenuated more than higher frequencies, with the difference more exaggerated for low viscosities. The results also show that the interface wave attenuation tends towards a fixed value of $\tan\left(\frac{1}{3}\tan^{-1}\left(\infty\right)\right) = \tan\left(\frac{\pi}{6}\right) = \frac{1}{\sqrt{3}}$ as $\omega \to 0$. The reciprocal behaviour of $Q_{\text{interface}}$ with frequency is shown in Figure 3.5.

3.3.2 The attenuation of acoustic waves

The P-wave velocity as a solution to the viscoelastic wave equation can be expressed as a complex quantity in terms of complex Lamé parameters, $\tilde{\lambda} = \lambda - i\omega\lambda_I$ and $\tilde{\mu} = \mu - i\omega\eta$, as:

$$V_{\text{p}} = \sqrt{\frac{\tilde{\lambda}+2\tilde{\mu}}{\rho_{\text{f}}}} = \sqrt{c_{\text{p}}^2 - i\frac{\omega}{\rho_{\text{f}}}\left(\xi+\frac{4\eta}{3}\right)} \tag{3.16}$$

where λ and μ are the usual elastic Lamé parameters, while λ_I and η are their viscous equivalents. The quantity

$$B = \left(\lambda + \frac{2}{3}\mu\right) \tag{3.17}$$

will be referred to as the *volume modulus* (the term *bulk modulus* being reserved for an average quantity of a multiphase mixture), and its viscous equivalent

$$\xi = \left(\lambda_I + \frac{2}{3}\eta\right) \tag{3.18}$$

as the *volume viscosity*.

In Equation 3.16, c_{p} is the real part of the velocity (the acoustic velocity in the absence of any viscosity) and ξ and η are the volume and shear viscosities respectively. Using

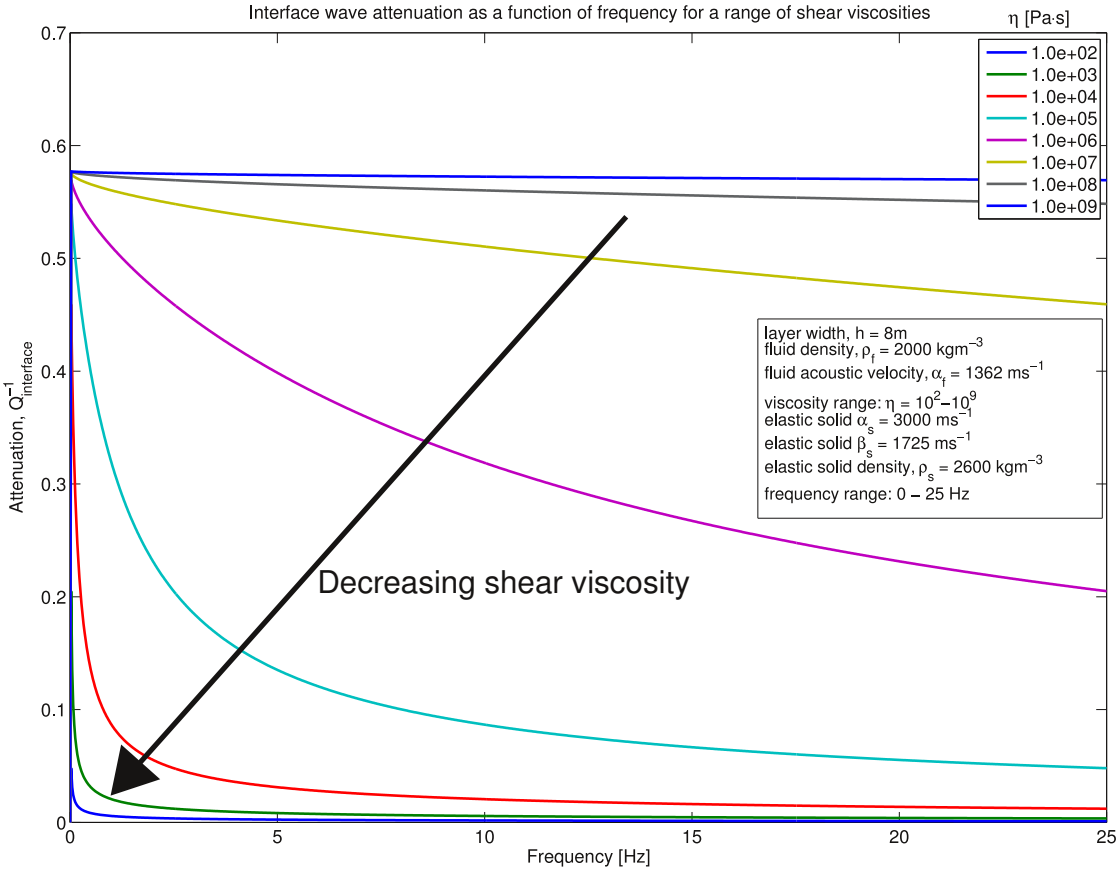

Figure 3.4: Curves showing the attenuation experienced by interface waves as a function of frequency. The expression in Equation 3.15 was evaluated for a set of realistic volcanic parameters (listed in the box). Each curve represents a different shear viscosity value ranging from 10^2 to 10^9 Pas. Note that $Q^{-1}_{\text{interface}}$ tends towards a finite asymptotic value of $1/\sqrt{3}$ at low-frequencies.

this velocity, an expression for the acoustic wave attenuation of the fluid can be obtained directly, using a similar approach to before:

$$Q^{-1}_{\text{acoustic}}(\omega) = \frac{\Im(V_{\text{p}}^2)}{\Re(V_{\text{p}}^2)} = \frac{\omega\left(\xi + \frac{4}{3}\eta\right)}{\rho_{\text{f}} c_{\text{p}}^2} = \frac{\omega\zeta}{B} \tag{3.19}$$

where ζ is defined to be the combination

$$\zeta = \left(\xi + \frac{4}{3}\eta\right) \tag{3.20}$$

equivalent to what Dingwell & Webb (1989) term the *longitudinal viscosity*.

For a fluid, B reduces to $B = \rho_{\text{f}} c_{\text{p}}^2$, since the rigidity or real part of $\tilde{\mu}$ (the now complex Lamé parameter) is $\mu = 0$. Equation 3.19 is a much simpler relationship compared to Equation 3.15 for interface waves, with the attenuation proportional to the frequency. This can be seen by the linear form of Q^{-1}_{acoustic} vs. frequency in Figure 3.6 and the inverse relationship between Q_{acoustic} and frequency shown in Figure 3.7.

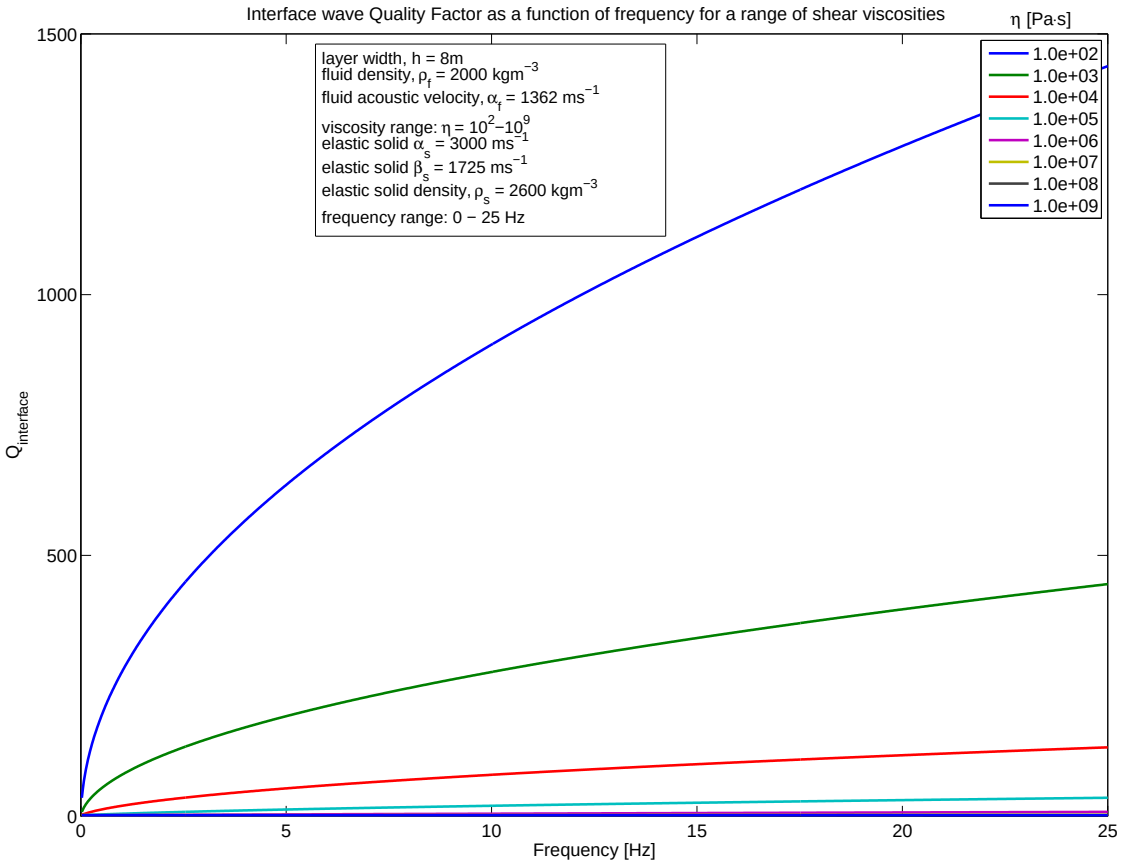

Figure 3.5: Interface wave Quality Factor (inverse of attenuation) as a function of frequency and shear viscosity. The reciprocal of Equation 3.15 was evaluated for a set of realistic volcanic parameters (listed in the box). Each curve represents a different shear viscosity value ranging from 10^2 to 10^9 Pas.

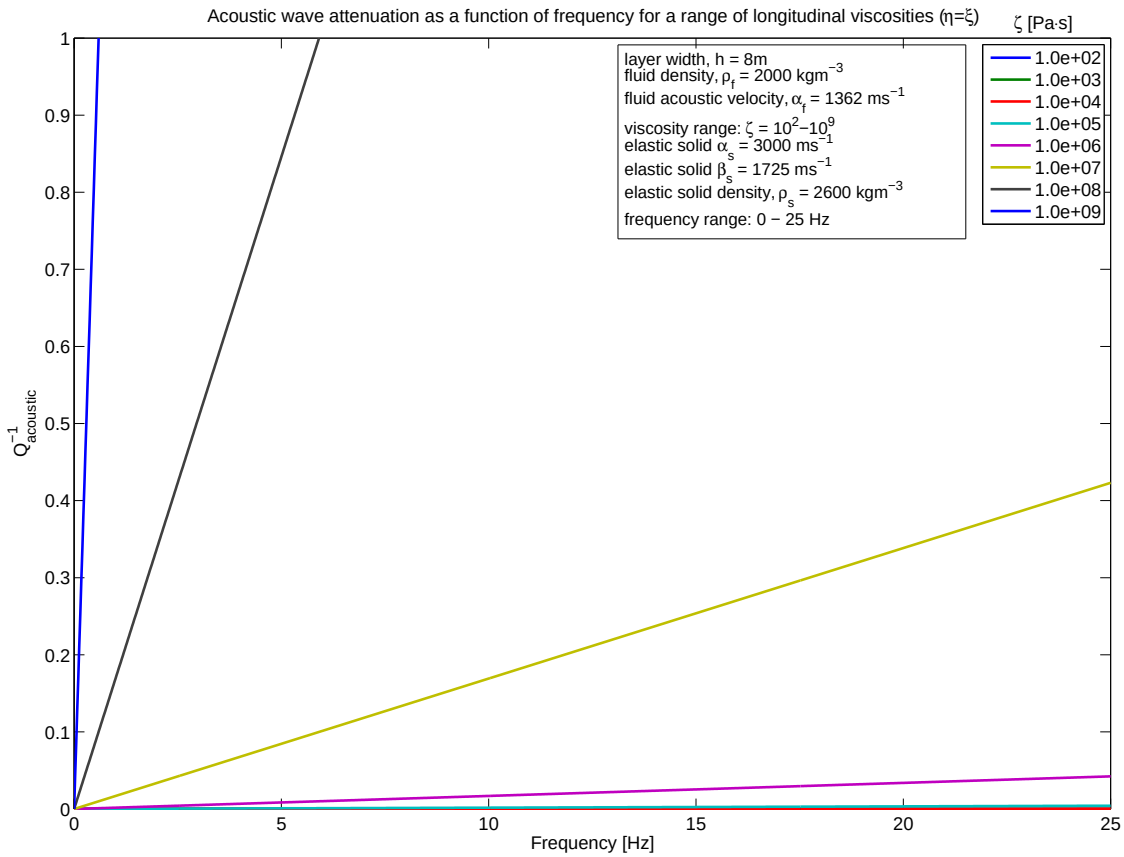

Figure 3.6: Acoustic wave attenuation as a function of frequency and longitudinal viscosity. Equation 3.19 was evaluated for a set of realistic volcanic parameters (listed in the box). Each curve represents a different longitudinal viscosity value ranging from 10^2 to 10^9 Pas. Volume and shear viscosities are assumed to be equal ($\eta = \xi$). Note the simple linear relationship.

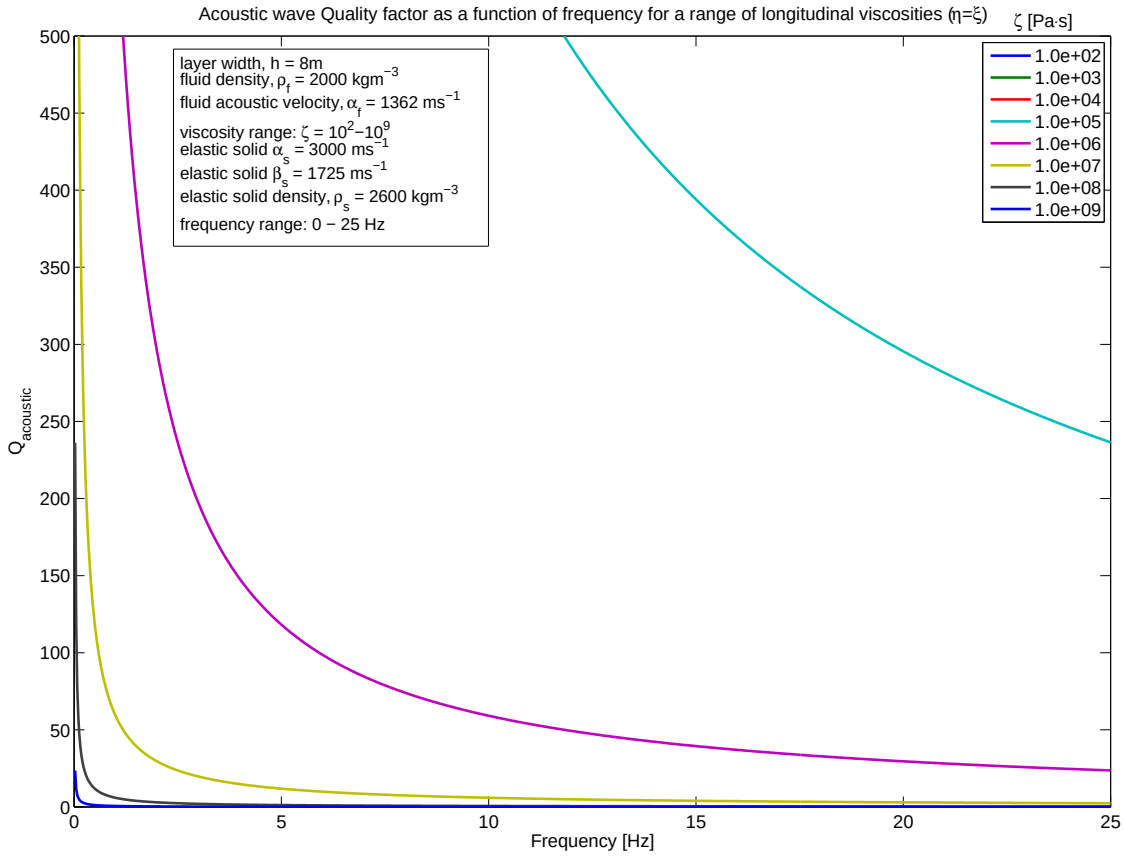

Figure 3.7: Acoustic wave Quality Factor (inverse of attenuation) as a function of frequency and longitudinal viscosity. The reciprocal of Equation 3.19 was evaluated for a set of realistic volcanic parameters (listed in the box). Each curve represents a different longitudinal viscosity value ranging from 10^2 to 10^9 Pas. Volume and shear viscosities are assumed to be equal ($\eta = \xi$). Note the simple inverse relationship and that only viscosities of $\zeta \geq 10^5$ Pas plot on these axes.

3.4 Comparison of interface and acoustic wave attenuation

Having derived explicit, analytic expressions for the attenuation experienced by interface waves at the fluid-solid boundaries and acoustic waves propagating within the fluid, respectively, the two can now be compared.

3.4.1 The ratio of interface to acoustic wave attenuation

The ratio of interface to acoustic wave attenuation was calculated using realistic parameters for a volcanic setting. The parameters used (listed in Figure 3.8) are identical to those used in Section 2.4.1 to allow comparison with the modelling results. In terms of magma viscosities, only the shear viscosity, η, appears in the expression for the interface wave attenuation in Equation 3.15. However, the acoustic wave attenuation is dependent on both the shear and volume viscosities. Hence, what appears in Equation 3.19 is the longitudinal viscosity, $\zeta = \xi + \frac{4}{3}\eta$, (combination of volume and shear) since this is the imaginary part of the velocity which represents the damping. We first assume a pure melt, with the shear and volume viscosities equal, $\xi = \eta$ (Dingwell & Webb, 1989), such that $\zeta = \frac{7}{3}\eta$.

Values of the shear viscosity were tested such that the longitudinal viscosity spans seven orders of magnitude, from 10^2 to 10^9 Pas. The value of 10^9 Pas represents an upper limit because, using the chosen fluid properties, a longitudinal viscosity higher than this corresponds to an acoustic wave attenuation of $Q_{\text{acoustic}} \ll 1$, where the wave energy is rapidly damped in less than one cycle and the definition of Q is no longer valid.

The results show that if the viscosity is sufficiently large we can arrive at a scenario where the attenuation of the interface waves is smaller than that of the acoustic waves. Figure 3.8 shows that, for the particular set of parameters chosen, a longitudinal viscosity of at least 10^7 Pas is required for interface waves to be less attenuated than acoustic waves in the seismic frequency range (0-25Hz). This is represented by the area in Figure 3.8 where the ratio of interface to acoustic wave attenuation drops below one.

3.4.2 Shear and volume viscosities

One consideration when interpreting the comparison between interface and acoustic waves is the relation between the two viscosity coefficients, ξ and η, as this depends

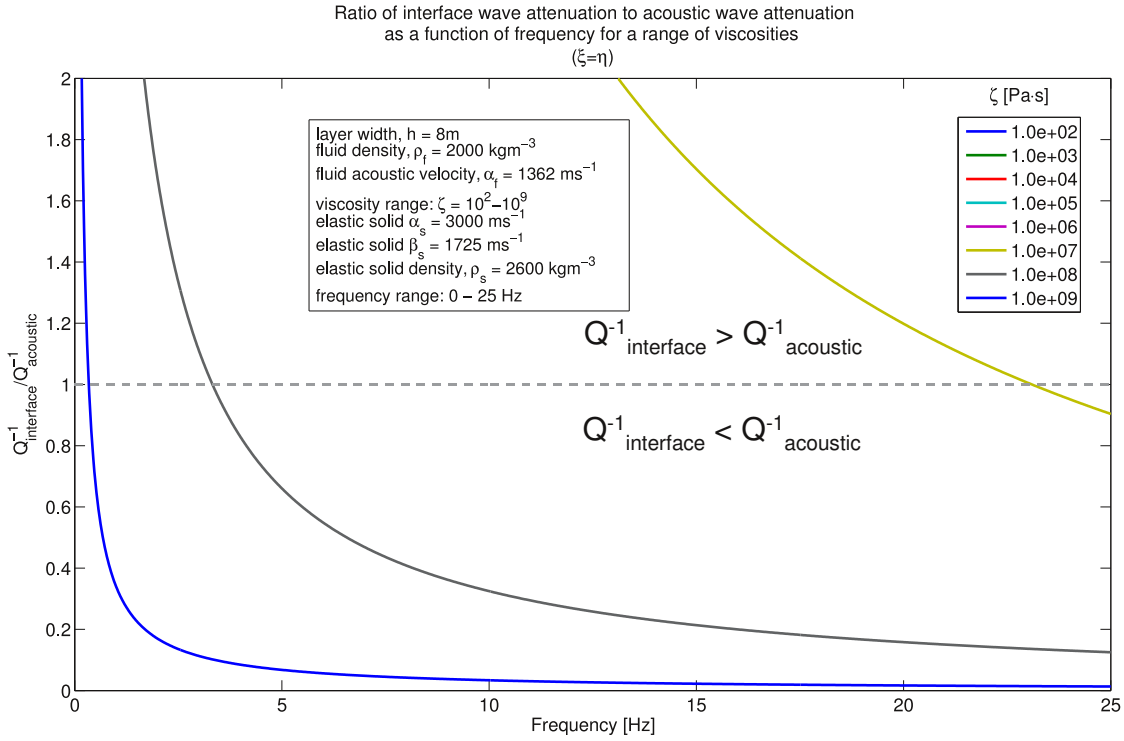

Figure 3.8: Ratio of interface to acoustic wave attenuation for longitudinal viscosities in the range $10^2 \leq \zeta \leq 10^9$ Pas. A pure melt is assumed with the shear and volume viscosities taken to be equal, $\eta = \xi$, such that $\zeta = \xi + \frac{4}{3}\eta = \frac{7}{3}\eta$. Note that only longitudinal viscosities of 10^7 and higher plot on these axes. The geometry of the body and its elastic properties are listed in the box. The dashed line where the ratio equals unity represents equal acoustic and interface wave attenuation.

on the exact nature of the fluid considered and can greatly affect the results. One of the reasons for this is that the interface wave attenuation is only dependent on the shear viscosity, whilst the acoustic wave attenuation is a function of both the volume and shear coefficients.

Having first assumed a pure melt with $\xi = \eta$ (Dingwell & Webb, 1989), a longitudinal viscosity of at least 10^7 Pas is required for interface waves to be less attenuated than acoustic waves in the seismic frequency range (0-25Hz). If a different ratio between η and ξ is used, such as $\xi/\eta = 10^4$, which is more appropriate for three-phase magma where the volume viscosity depends upon the gas volume fraction (e.g Prud'Homme & Bird, 1978), the curves plotted in Figure 3.9 show that the same conditions apply for a longitudinal viscosity of only 10^3 Pas.

This suggests that interface waves are less attenuated than acoustic waves for the given set of parameters, if we consider, (i) a pure volcanic melt, where shear and volume

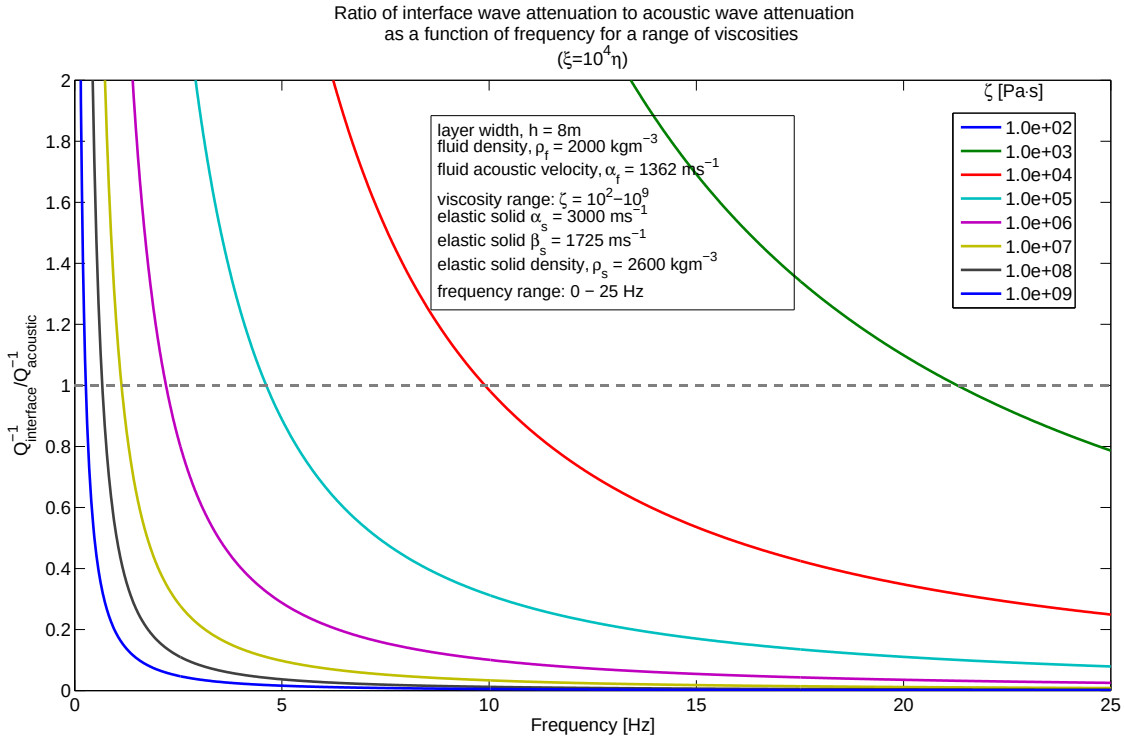

Figure 3.9: Ratio of interface to acoustic wave attenuation for viscosities in the range $10^2 \leq \zeta \leq 10^9$ Pas. Note that the curve for the lowest longitudinal viscosity of 10^2 Pas does not plot on these axes. Here a three-phase magma is considered with the relationship between shear and volume viscosities given by $\xi = 10^4\eta$.

viscosity are equal, with a longitudinal viscosity greater than 10^7 Pas, or (ii) a three-phase magma, where the volume viscosity may be several orders of magnitude larger than the shear viscosity, resulting in a longitudinal viscosity greater than 10^3 Pas. The lower shear viscosity of the melt is compensated by a higher volume viscosity due to the presence of gas and crystal phases (Figure 3.9).

3.5 Rheology: the link between attenuation and viscosity

3.5.1 SLS and Kelvin-Voight rheologies

The results of the forward modelling in Section 2.4.2 suggested that the ratio of interface to acoustic wave attenuation was as low as 0.15-0.4 for frequencies between 1 and 8Hz. A comparison of this result with Figure 3.8 shows that, for the analytical expressions, the frequency range for which the ratio slips below one is different, unless a viscosity of $\sim 10^9$ Pas is used. This difference may be partially explained by the different rheological models implicit in the analytical formulation in Equations 3.15 and 3.19, and in the modelling process in Chapter 2 where the finite-difference model parameterised the material as an array of Standard Linear Solids (SLS). In contrast, the acoustic velocity formulation (after Korneev (2008)) contains an implicit Kelvin-Voight rheological model (see Figure 3.10). The expressions for the acoustic wave velocity and attenuation in Equations 3.16 and 3.19 represent the standard Kelvin-Voight model of a spring and dashpot in parallel (e.g. Carcione, 2001, p.64-65), with a complex modulus of:

$$M_c(\omega) = M_R + i\omega\eta \tag{3.21}$$

giving an attenuation of

$$Q^{-1} = \frac{\Im(M_c(\omega))}{\Re(M_c(\omega))} = \omega\tau \tag{3.22}$$

where M_R and η are the rigidity and viscosity of the spring and dashpot respectively, and the relaxation time $\tau = \eta/M_R$. Since the complex P-wave velocity and complex modulus are related by

$$V_{\mathrm{p}} = \sqrt{\frac{M_c(\omega)}{\rho_{\mathrm{f}}}}, \tag{3.23}$$

and in this example we have

$$M_c(\omega) = \rho_{\mathrm{f}} V_{\mathrm{p}}^2 = B - i\omega\zeta, \tag{3.24}$$

hence the rigidity of the spring represents the volume modulus of the fluid, B, and the viscosity which should be used for the acoustic waves is the longitudinal viscosity, ζ. This difference in rheology means is it not possible to map a given intrinsic Q_{i} or attenuation value in the finite-difference model to a fluid viscosity in the analytical expressions. Therefore, in order to compare the results of the modelling with the analytical expressions, the finite-difference model needs to be modified to employ a Kelvin-Voight rheology.

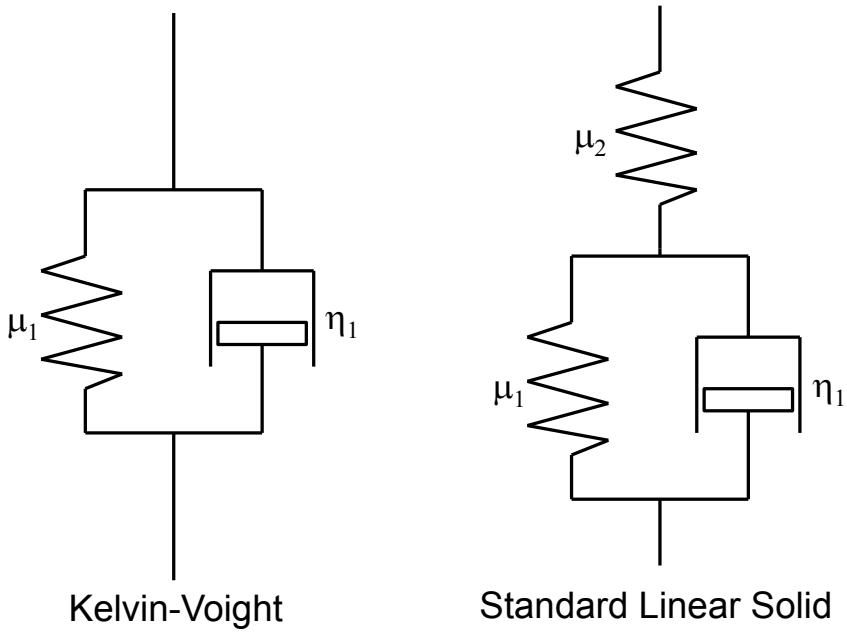

Figure 3.10: Schematic diagram showing the mechanical representations of (a) a Kelvin-Voight body and (b) a Standard Linear Solid (SLS), with the difference being the additional spring in series for the SLS, with rigidity μ_2.

3.5.2 Modifying the rheology of the finite-difference model

To convert the rheology from a SLS to Kelvin-Voight model, the rigidity of the additional spring term in the SLS (see Figure 3.10) must be forced to be infinite, $\mu_2 \rightarrow \infty$, such that the two mechanical analogues become equivalent. However, implementing this numerically presents some challenges.

As discussed in Section 2.1.4, the finite-difference code implements the SLS rheological model in terms of relaxation times, $\tau_\sigma = \eta_1/(\mu_1 + \mu_2)$ and $\tau_\epsilon = \eta_1/\mu_1$, rather than simply the rigidities and viscosities of the springs and dashpots. Allowing $\mu_2 \rightarrow \infty$, implies $\tau_\sigma \rightarrow 0$ (assuming $\mu_1 \ll \mu_2$), and setting $\tau_\sigma = 0$ introduces singularities into the computation, as τ_σ appears in the denominator of several fractions, notably the dimensionless parameter $\tau = \frac{\tau_\epsilon}{\tau_\sigma} - 1 = \frac{\tau_\epsilon - \tau_\sigma}{\tau_\sigma}$ (Blanch et al., 1995). An alternative way is forcing $\tau_\sigma \ll \tau_\epsilon$, rather than setting $\tau_\sigma = 0$, and finding a minimum ratio of $\tau_\sigma/\tau_\epsilon$ for which the formulation of the model is still numerically stable.

As described in Chapter 2 the stability or CFL criterion for the $O\left(dx^4, dt^2\right)$ formulation used in the finite-difference model is given by:

$$dt < 0.606 \frac{dx}{v_{\max}} \tag{3.25}$$

Since we are concerned with viscoelastic wave propagation, the velocity $v_{\max}$ needs to be adjusted to the maximum *phase velocity* given by:

$$v_{\max} = \sqrt{\frac{\tau_\epsilon M_R}{\tau_\sigma \rho_{\mathrm{f}}}} \tag{3.26}$$

which for a single SLS (substituting for τ_ϵ, τ_σ and $M_R = \frac{\mu_1 \mu_2}{(\mu_1+\mu_2)}$) reduces to:

$$v_{\max} = \sqrt{\frac{\mu_2}{\rho_{\mathrm{f}}}} \tag{3.27}$$

where ρ_{f} is the density of the fluid. Substituting this into the stability criterion yields:

$$dt < 0.606 \frac{dx}{\sqrt{\mu_2/\rho_{\mathrm{f}}}} \tag{3.28}$$

which can be rearranged to give the maximum value for the rigidity of the additional spring, μ_2, for which the stability criterion is still satisfied:

$$\mu_2 < \rho_{\mathrm{f}} \left(\frac{0.606 dx}{dt} \right)^2 \tag{3.29}$$

However, the viscoelasticity is implemented in terms of the three parameters, τ_ϵ, τ_σ and τ, hence writing μ_2 in terms of these relaxation times,

$$\mu_2 = \eta_1 \left(\frac{1}{\tau_\sigma} - \frac{1}{\tau_\epsilon} \right) \tag{3.30}$$

and substituting into Equation 3.29 and rearranging, gives the minimum value for this ratio whilst still maintaining numerical stability within the model:

$$\frac{\tau_\sigma}{\tau_\epsilon} > \left(1 + \left(\frac{0.606 dx}{c_{\mathrm{p}}^2 dt} \right)^2 \right)^{-1}. \tag{3.31}$$

Here the substitution $\mu_1 = \rho_{\mathrm{f}} c_{\mathrm{p}}^2$ has been made, for c_{p}^2 the ordinary acoustic velocity in the absence of any viscosity (the real part of the complex P-wave velocity).

Hence, if the choice is made to fix the spatial discretization, this minimum ratio is a function of the temporal discretization used in the model. This dependence is shown in a log-log plot in Figure 3.11, with smaller timesteps allowing a smaller ratio to be employed. The impact of the choice of ratio, in terms of the accuracy of the model at reproducing the desired attenuation behaviour, will now be explored in the next section.

Trade off: model accuracy vs. computation time.

The dependence of the minimum $\tau_\sigma/\tau_\epsilon$ ratio on the temporal discretization leads to a trade off between the accuracy of the match to the desired ideal Kelvin-Voight rheology and the computation time. Using smaller timesteps allows greater accuracy, since

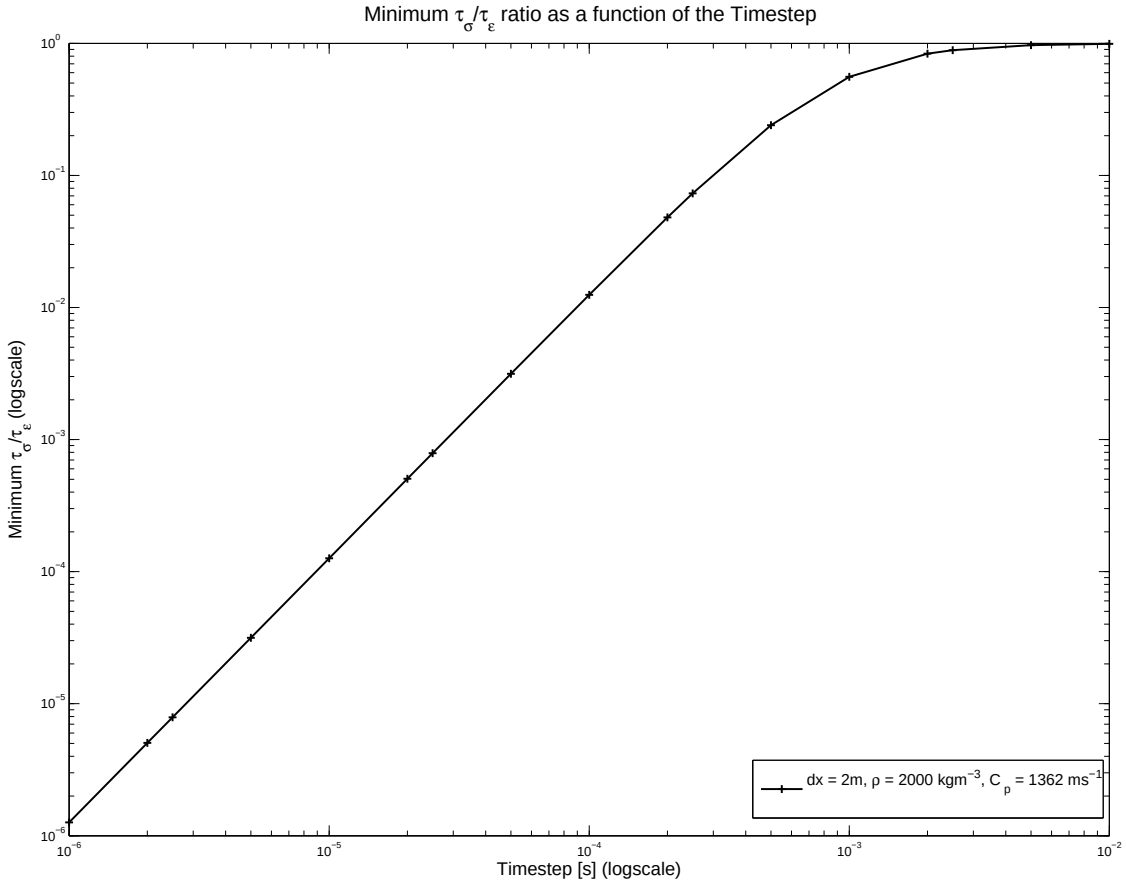

Figure 3.11: Plot of the minimum $\tau_\sigma/\tau_\epsilon$ ratio for which the model is numerically stable, as a function of the timestep on a log-log scale. The spatial discretization used was $dx = 2\text{m}$, with an acoustic velocity and density of the fluid of $c_\text{p} = 1362\text{ms}^{-1}$ and $\rho_\text{f} = 2000\text{kgm}^{-3}$ respectively.

a smaller value for the $\tau_\sigma/\tau_\epsilon$ ratio can be used, and the Kelvin-Voight rheology is more accurately approximated. However, this increase in accuracy is at the expense of computation time which will increase for finer temporal discretizations, as the model must perform more loops for the same length of synthetic seismogram.

Figures 3.12 to 3.15 show the attenuation as a function of frequency for, (a) the desired Kelvin-Voight material (linear) and, (b) the behaviour returned by the model, calculated for a finite τ_σ and determined using Equation 15 of Blanch et al. (1995). Each figure is for a different timestep value, varying from 10^{-3} to 10^{-6}s, and shows a range of viscosities from 10^2 to 10^9 Pas. For each example τ_σ was calculated using the particular minimum $\tau_\sigma/\tau_\epsilon$ ratio for the corresponding value of the timestep, while all other parameters were fixed. The comparison is made for frequencies in the seismic bandwidth from 0-25Hz. Figures 3.16 and 3.17 show the RMS misfit between the attenuation of the model and

ideal Kelvin-Voight rheology (normalised by the viscosity), plotted as a function of (a) the timestep, dt, and (b) $1/dt$, which is proportional to the computation time. The results suggest an appropriate value for the timestep of 2.5×10^{-5}s.

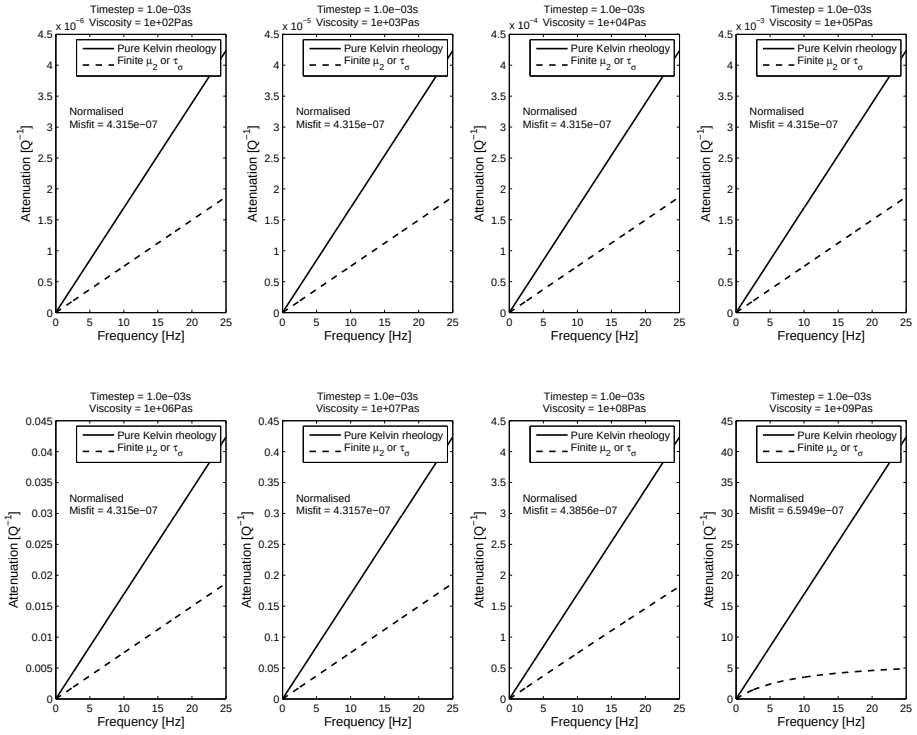

Figure 3.12: Modelled and Kelvin-Voight attenuation, for a timestep of $dt = 10^{-3}$s. The RMS misfits between the curves have been normalised by the viscosity values. Note the large discrepancies between the two curves for this large value of the timestep, with the truncation effects particularly apparent at the highest viscosities.

Testing the code: recovering Q_i distribution with spectral ratios

As an important check, to test that the modified version of the model was correctly implementing the new rheology, the input attenuation function was compared to the attenuation retrieved using spectral ratios, in a similar manner to the tests conducted in Section 2.4.3. Again, the spectral ratios between stations at different offsets within a homogeneous half-space (in this case a fluid) are used to retrieve the attenuation behaviour as a function of frequency, f, using

$$Q(f) = \frac{-\pi f\,(t_2 - t_1)}{\log\left(\frac{|A_2(f)|\sqrt{r_2}}{|A_1(f)|\sqrt{r_1}}\right)} \tag{3.32}$$

for a pair of wavelets with amplitude spectra $A_1(f)$ and $A_2(f)$, recorded at distances r_1

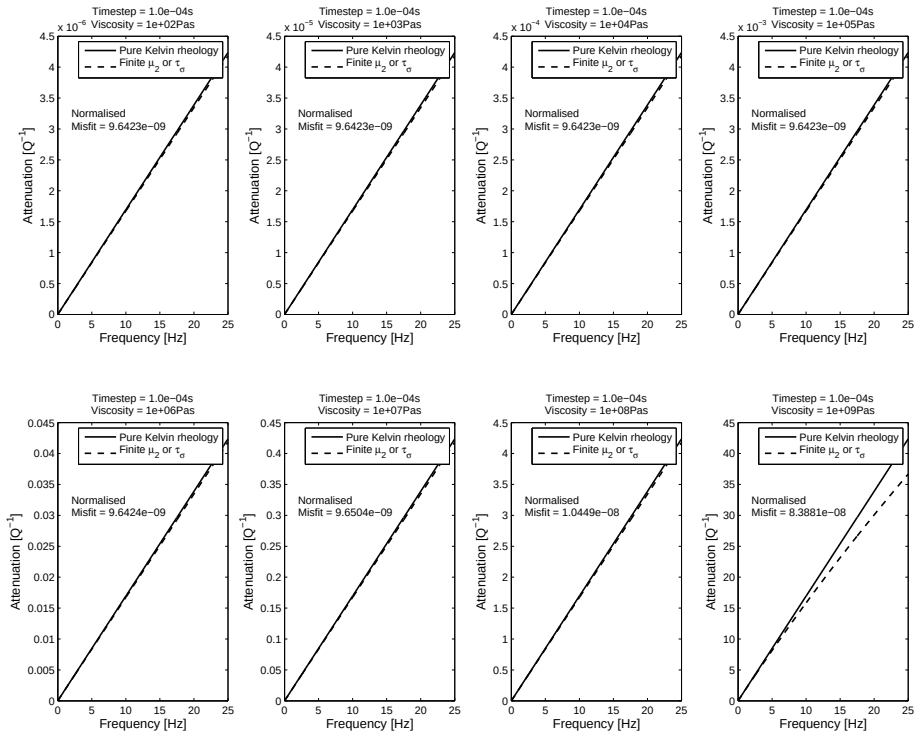

Figure 3.13: Modelled and Kelvin-Voight attenuation, for a timestep of $dt = 10^{-4}$s.

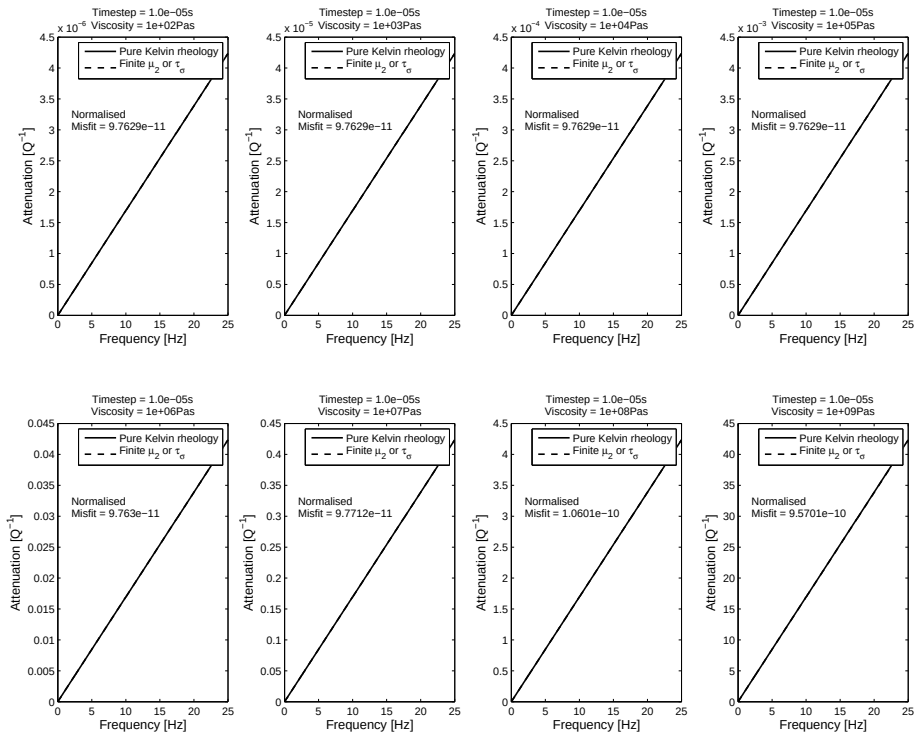

Figure 3.14: Modelled and Kelvin-Voight attenuation, for a timestep of $dt = 10^{-5}$s.

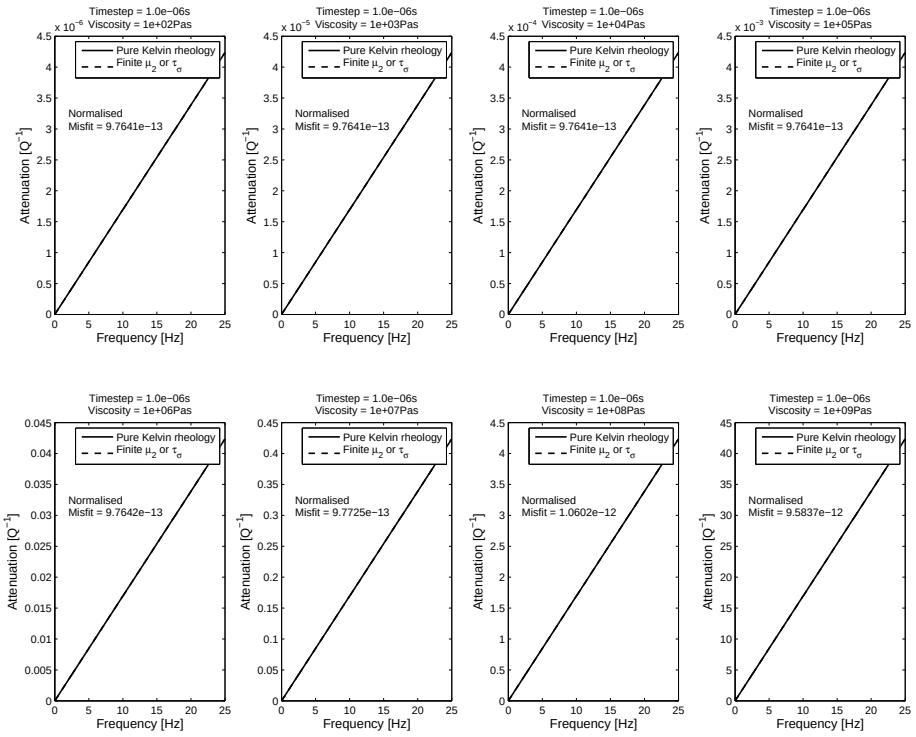

Figure 3.15: Modelled and Kelvin-Voight attenuation, for a timestep of $dt = 10^{-6}$s.

and r_2 at times t_1 and t_2 respectively (Jousset et al., 2004).

However, this formulation relies on the assumption that the intrinsic quality factor, Q_i, is constant with frequency. For a Kelvin-Voight material this is patently not the case, as we expect a linear relationship between attenuation and frequency. It can be seen in Figure 3.18 that the attenuation retrieved from the spectral ratio pairs at different stations does not match the input Kelvin-Voight behaviour at low frequencies. This is because, under the assumption of constant Q_i, the frequency term that appears in the numerator of Equation 3.32 forces $Q_\mathrm{i} \to 0$ as $f \to 0$. For a Kelvin-Voight material the behaviour is in fact opposite to this, as it is the attenuation, $Q_\mathrm{i}^{-1} \to 0$ or $Q_\mathrm{i} \to \infty$ at low frequencies.

The spatial decay of amplitude with distance can be written as an exponential decay process via the attenuation factor, α:

$$A(x) = A_0 e^{-\alpha x} \tag{3.33}$$

with

$$\alpha = \frac{\omega}{2 v_\mathrm{ph} Q_\mathrm{i}(\omega)} \tag{3.34}$$

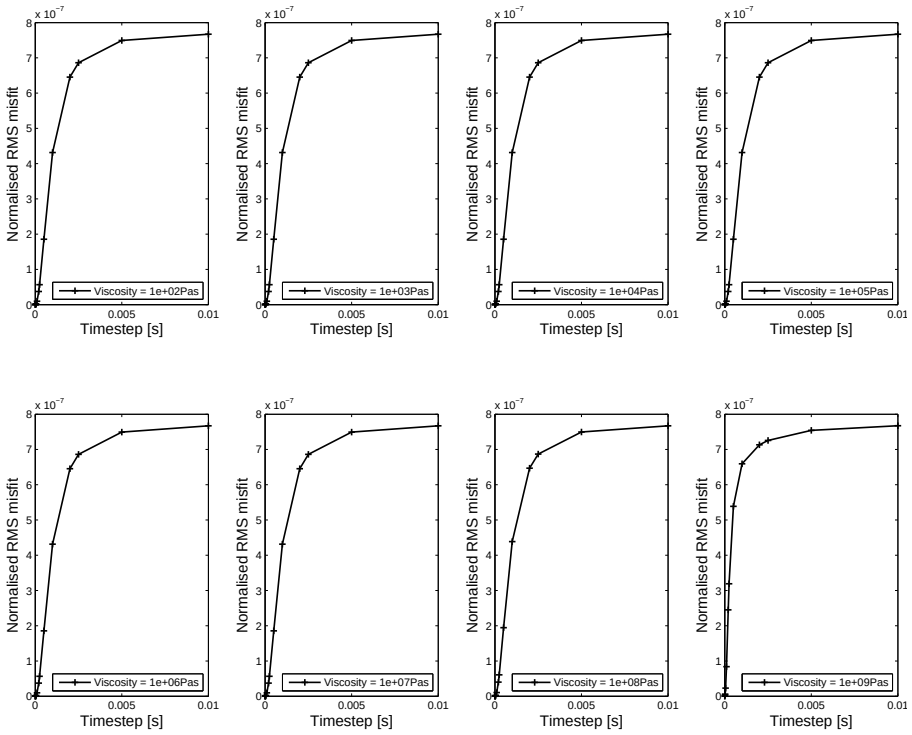

Figure 3.16: RMS misfit between the modelled and Kelvin-Voight attenuation as a function of the timestep. Note the increased discrepancy between model and theory at higher viscosities.

for phase velocity v_{ph} (Aki & Richards, 2002). For a constant (frequency independent) Q_{i} it is clear that this parameter must be linear with frequency. If the spectral ratios are used to solve for the attenuation coefficient, α, rather than the attenuation or Q_{i}, the attenuation coefficient retrieved can be compared to the theoretical value for a Kelvin-Voight material. This makes no assumptions about the frequency behaviour of the attenuation or Q_{i}.

The expression for the amplitude spectrum of a seismic wavelet at time t is given by

$$|A_t(f)| = \frac{|A_0(f)|}{J} e^{\frac{-\pi f t}{Q}} \tag{3.35}$$

where A_0 is the unattenuated source spectrum, and J is the geometrical spreading factor, which in 2-D is given by $J^{-1} = \sqrt{r}$ for a distance r from the source (Jousset et al., 2004; White, 1992). Using Equations 3.34 and 3.35 and taking the ratio of spectra at two different distances, the attenuation coefficient can be written as:

$$\alpha = \frac{-\log\left(\frac{|A_2(f)|\sqrt{r2}}{|A_1(f)|\sqrt{r1}}\right)}{v_{\mathrm{ph}}\,(t_2 - t_1)} \tag{3.36}$$

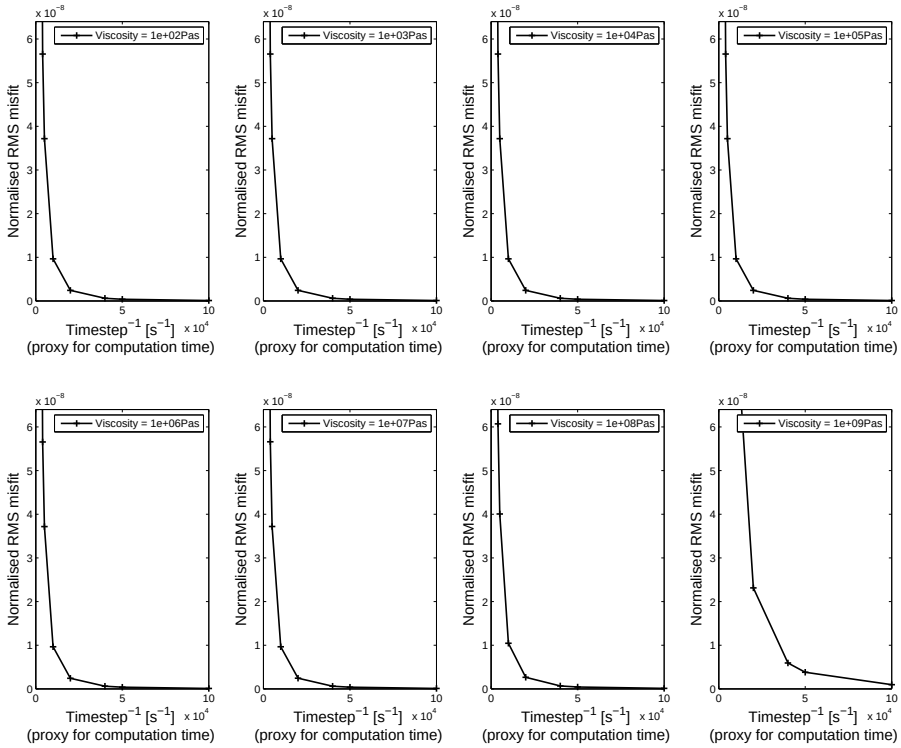

Figure 3.17: RMS misfit between modelled and Kelvin-Voight attenuation as a function of the computation time. Using $1/dt$ as a proxy for the computation time, these plots now have the form of conventional trade-off curves and can be used to pick the 'elbow', where reasonable accuracy is obtained for an acceptable computation time. The choice of timestep is obviously dependent on the viscosity used.

For an acoustic fluid with Kelvin-Voight rheology, the theoretical attenuation coefficient can be calculated from Equation 3.34, since the attenuation as a function of frequency is known (given by Equation 3.19). The results of the comparison in Figure 3.19, for a 10Hz Ricker source wavelet, show that the finite-difference code successfully models the required attenuation behaviour across the whole bandwidth of the source. By measuring the response in terms of the attenuation coefficient, it is clear that the previous mismatch between model and theoretical Q_{i} at low-frequencies is simply a function of the implicit constant-Q assumption, inherent in the measurement method, and not a problem with the model implementation itself.

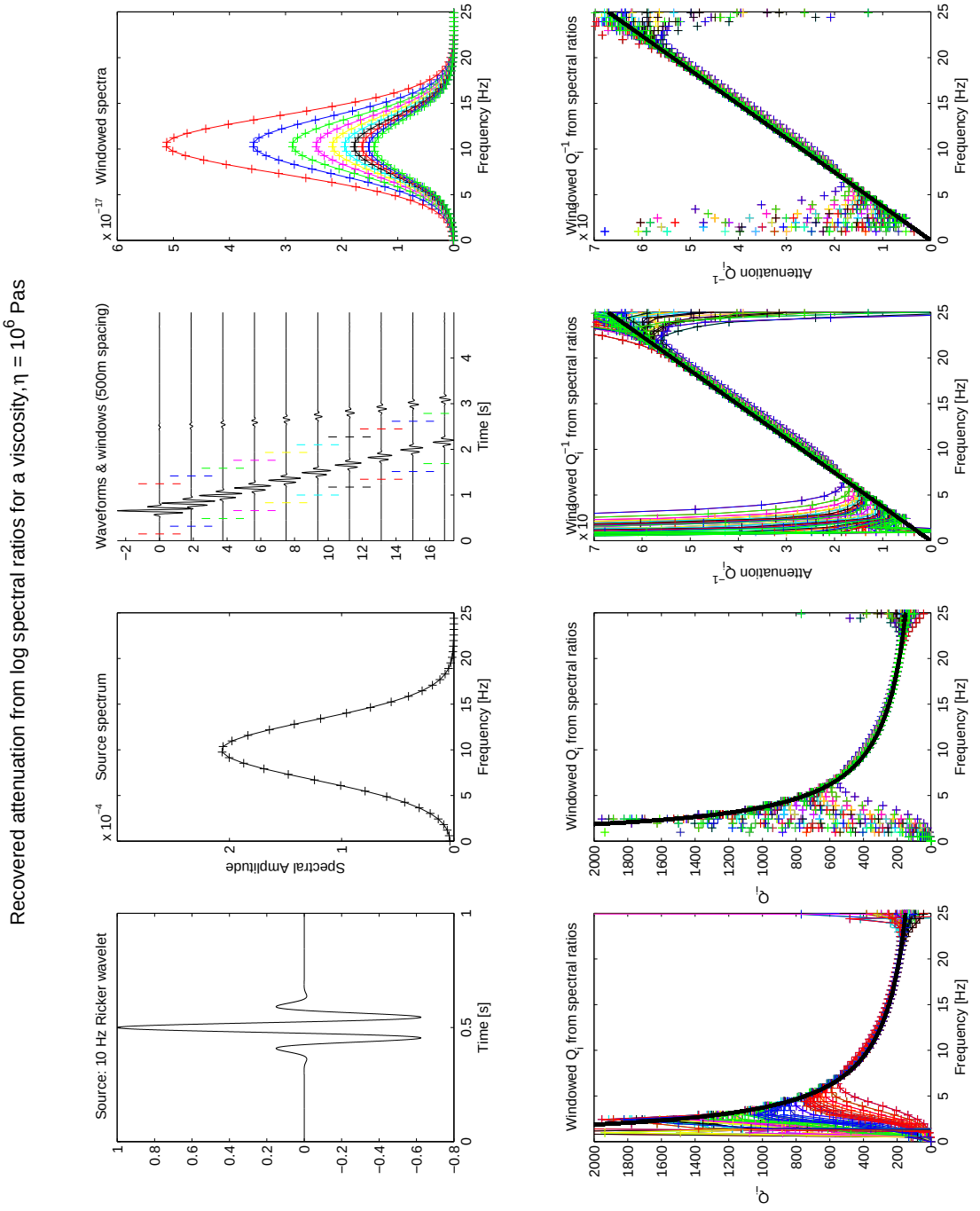

Figure 3.18: Q_i and attenuation functions recovered from a half-space using spectral ratios at different distances, for a Kelvin-Voight fluid with longitudinal viscosity $\zeta = 10^6$ Pas. The plot shows the source wavelet, a Ricker wavelet with centre frequency 10Hz, and its associated spectrum. The transmitted phases, recorded at stations separated horizontally by 500m, were windowed from the full waveforms and pairs used to calculate spectral ratios. The attenuation as a function of frequency was calculated, using Equation 3.32, for all possible pairs of stations and the results overlain using a different colour for each denominator in the ratio. Note the discrepancy between the retrieved curves and the desired response (black line) at low frequencies (below 5Hz), despite there still being energy in the spectra at these frequencies. The lower plots show both the recovered Q_i and Q_i^{-1} displayed with individual points and continuous lines.

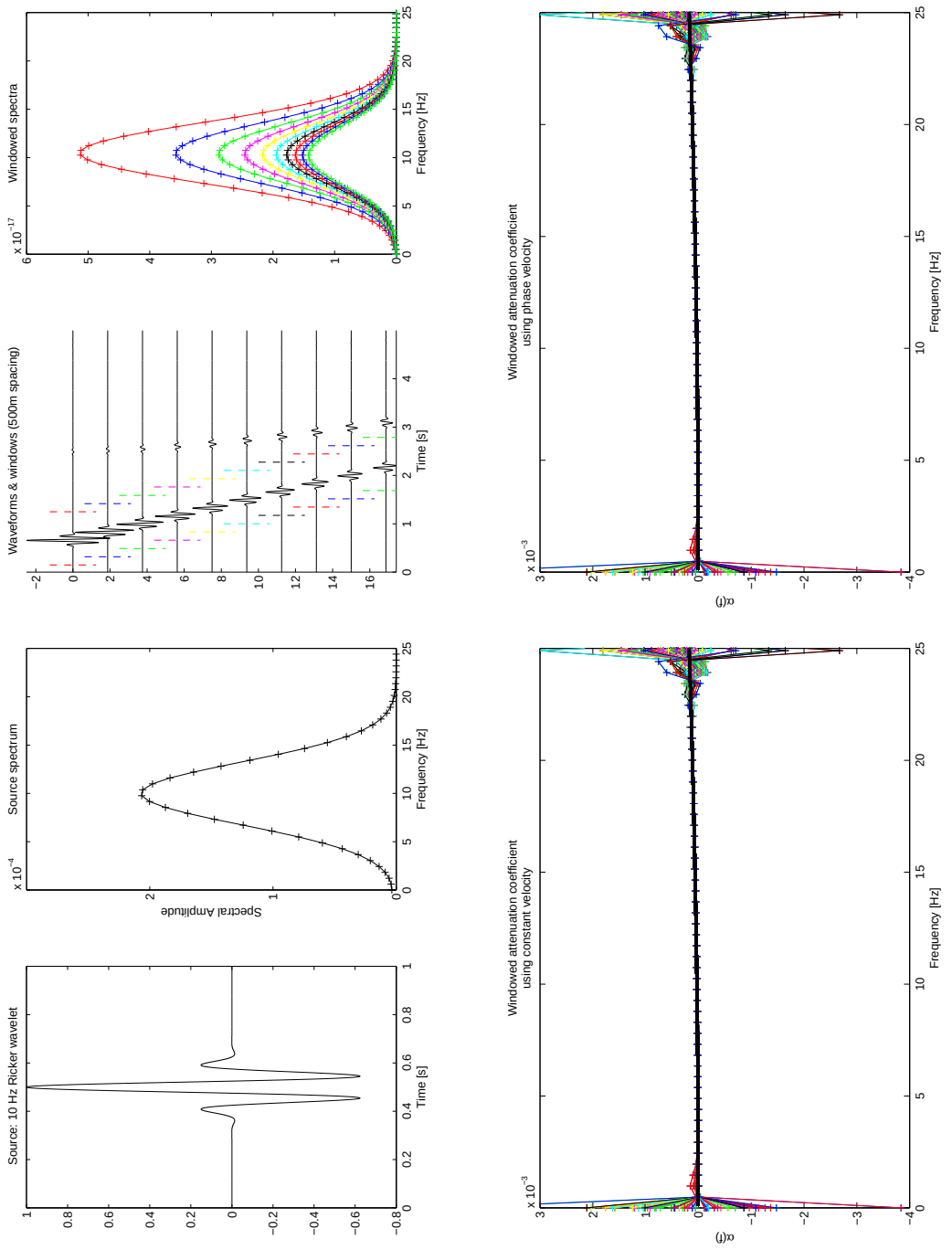

Figure 3.19: Attenuation coefficient functions recovered from a half-space using spectral ratios. The format is the same as for Figure 3.18, showing a 10Hz Ricker source wavelet and its spectrum and the windowed transmitted phases and their spectra. Here, the attenuation coefficient as a function of frequency, $\alpha(f)$, is retrieved from the spectral ratio pairs using Equation 3.36. The recovered values match the desired theoretical curves (black line) across the entire seismic bandwidth of the source, and only break down where the amplitude of energy in the spectra drops towards zero. The lower plots show that using the frequency dependent phase velocity, or a constant value for the acoustic velocity makes little difference to the results for this particular viscosity.

3.5.3 Results of the Kelvin-Voight finite-difference model

The results of repeating the model runs described in Section 2.4.1, but now for a viscoelastic fluid with Kelvin-Voight rheology, are shown in Figure 3.22. The geometry and set up of the numerical model is shown in Figure 3.20. Longitudinal viscosities in the range 10^2 to 10^8 Pas were tested, showing increased damping of the waveforms, and widening of the spectral peaks for increasing viscosity and hence attenuation. It is interesting to note that the lowest spectral peak at around 1Hz remains stable even when the viscosity is increased to 10^8 Pas. This may be due to the nature of the Kelvin-Voight rheological model, for which, as discussed in Section 3.3.2, low frequencies are less attenuated than higher frequencies. For the fluid properties chosen, this upper value of the viscosity tested corresponds to a Q_i of approximately 5 at 1Hz, falling to even lower values for higher frequencies, as Figure 3.21 shows.

The apparent attenuation was calculated from bandpass filtered versions of the waveforms shown in Figure 3.22, at frequencies corresponding to the spectral peaks, using the slope of the logarithm of the analytical envelope via the method which will be outlined in Chapter 4. This allowed the relationship between the apparent attenuation and both the fluid viscosity and the intrinsic acoustic wave attenuation to be explored.

Apparent attenuation as a function of the fluid viscosity

Figures 3.23 and 3.24 show the apparent quality factor and attenuation, respectively, as a function of the longitudinal viscosity of the fluid used in the models. In general, the plots show a smoothly varying trend of increasing apparent attenuation with increasingly higher viscosities. However, the widening and smearing out of the spectra as the viscosity increases (Figure 3.22) suggests that the higher the frequency, the less reliable the measurement of attenuation, as for the highest viscosities the higher frequency spectral peaks become far less distinct. This is due to the frequency dependence of the Kelvin-Voight rheology, meaning higher frequencies are more strongly attenuated. This effect can be seen in the red curve for the highest frequency spectral peak in Figure 3.24, which actually shows a decrease in attenuation for the highest viscosities. This effect is an artefact of the measurement process, and the attenuation is too high to be measured since the definition of Q breaks down because the energy is rapidly damped in less than a single cycle. For example, for the fluid parameters chosen, a longitudinal viscosity of

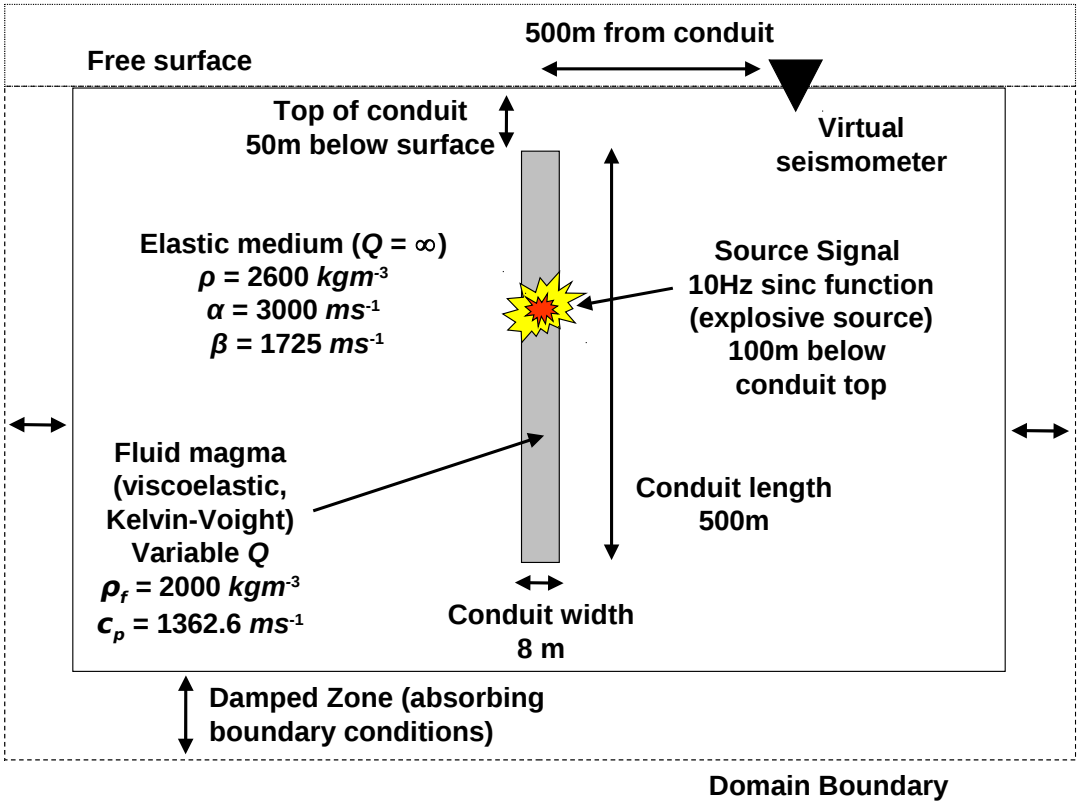

Figure 3.20: Schematic diagram showing the setup of the Kelvin finite-difference model grid. All parameters were fixed except the intrinsic attenuation of the fluid. Velocity seismograms were recorded 500m away at the free surface. To excite the higher modes of resonance the source wavelet was a relatively broad-band sine cardinal function with a high-frequency cut-off of 10Hz. To avoid introducing additional complexities to the waveforms no topography was included in these particular models, so a flat free surface was used.

10^8 Pas corresponds to $Q_\mathrm{i} \approx 0.85$ at a frequency of 7Hz, as shown in Figure 3.21.

Apparent attenuation as a function of the intrinsic acoustic wave attenuation

Since the viscosity and attenuation are quantitatively linked for the Kelvin-Voight rheology, the measurements of the apparent attenuation can also be plotted in terms of the intrinsic attenuation of the fluid. The viscosity values used in the finite-difference model were converted into the appropriate intrinsic Q_acoustic by using the relationship in Equation 3.19, at the specific frequencies identified and chosen from the spectra. Figures 3.25 and 3.26 show the apparent quality factor and attenuation, respectively, as a function of the intrinsic attenuation. When Q_a^{-1} is plotted as a function of Q_acoustic^{-1}, the results demonstrate the expected linear trend, with a gradient of less than 1, indicating

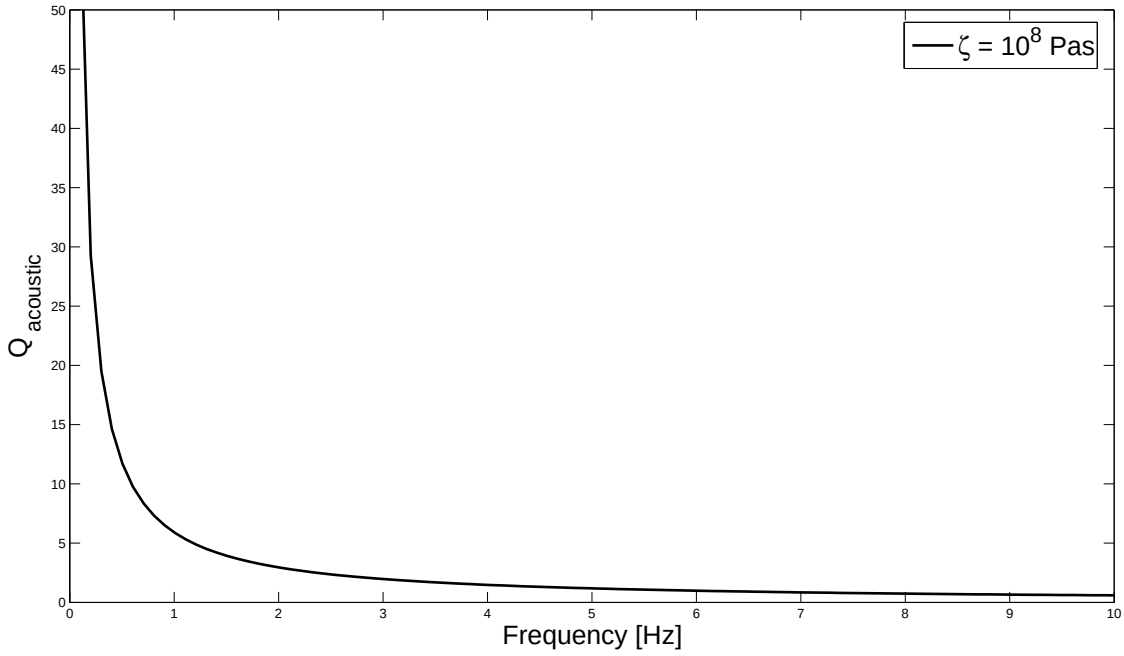

Figure 3.21: Acoustic wave quality factor as a function of frequency for the maximum longitudinal viscosity tested of 10^8 Pas. The curve was evaluated using the expression for the attenuation of a Kelvin-Voight body in Equation 3.19.

that, as for the case using a SLS, the intrinsic part contributes less than anticipated to the measured apparent attenuation. The results show values for the gradient between 0.17 and 0.37, comparable with those for the SLS finite-difference model in Section 2.4.2. The results also show a range of radiative attenuation values, determined from the intercepts, that vary with frequency. In the following section these results are compared to the analytical approach, to see if the amount by which the intrinsic part contributes less matches the $Q^{-1}_{\text{interface}}/Q^{-1}_{\text{acoustic}}$ ratio from the analytical curves.

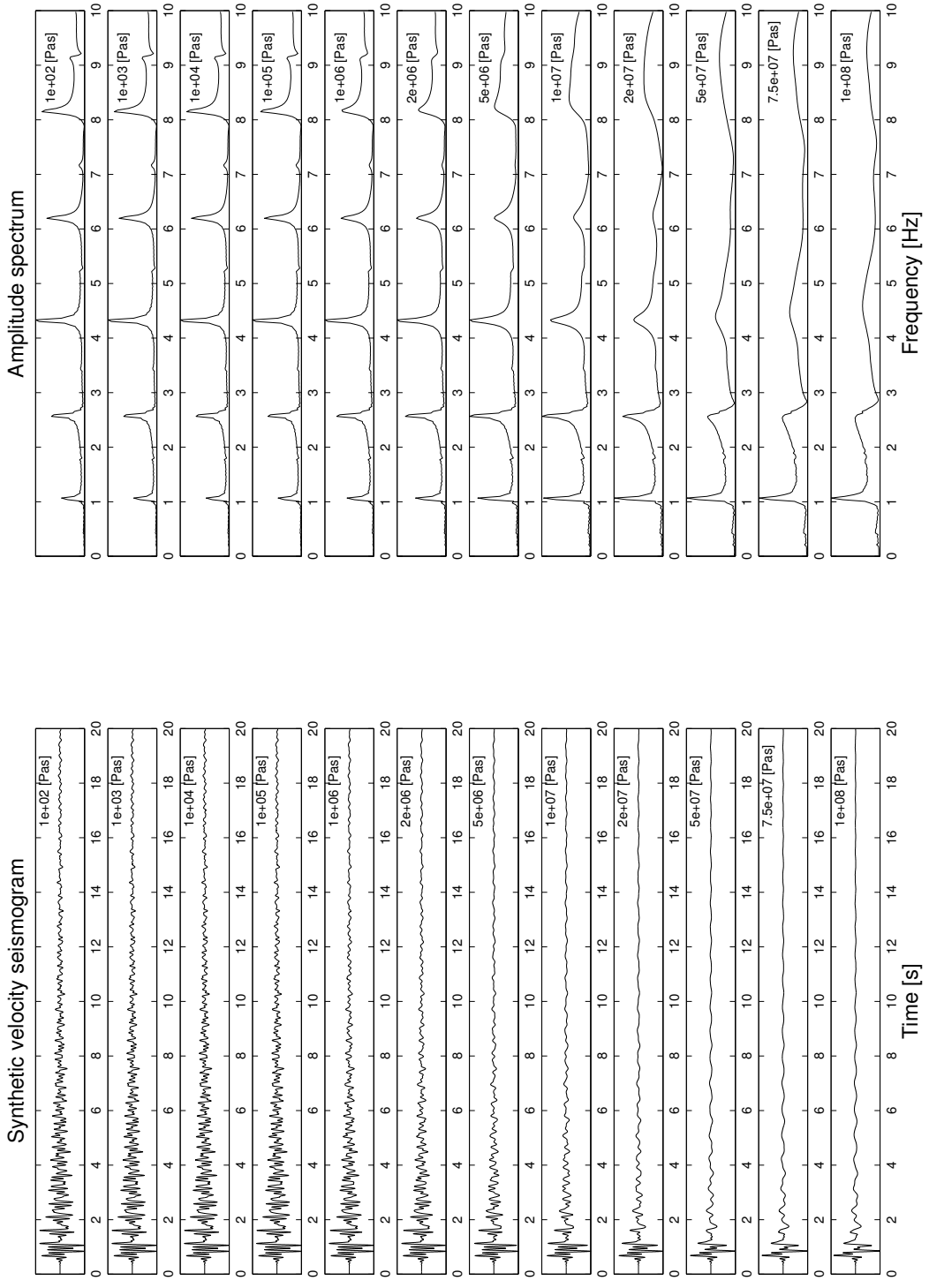

Figure 3.22: Synthetic vertical component waveforms and amplitude spectra produced by the modified Kelvin-Voight finite-difference model, for a range of longitudinal viscosities from 10^2 to 10^8 Pas. The model contains a 500m long by 8m wide magma body, filled with a viscoelastic fluid with Kelvin-Voight rheology. All geometry and elastic properties of the model are exactly the same as the case for the SLS rheology model runs in Section 2.4.1. Note the increased damping of the waveforms and the widening or smearing of the spectra as the viscosity, and hence attenuation, is increased. A 10Hz Sinc function was used as the source wavelet.

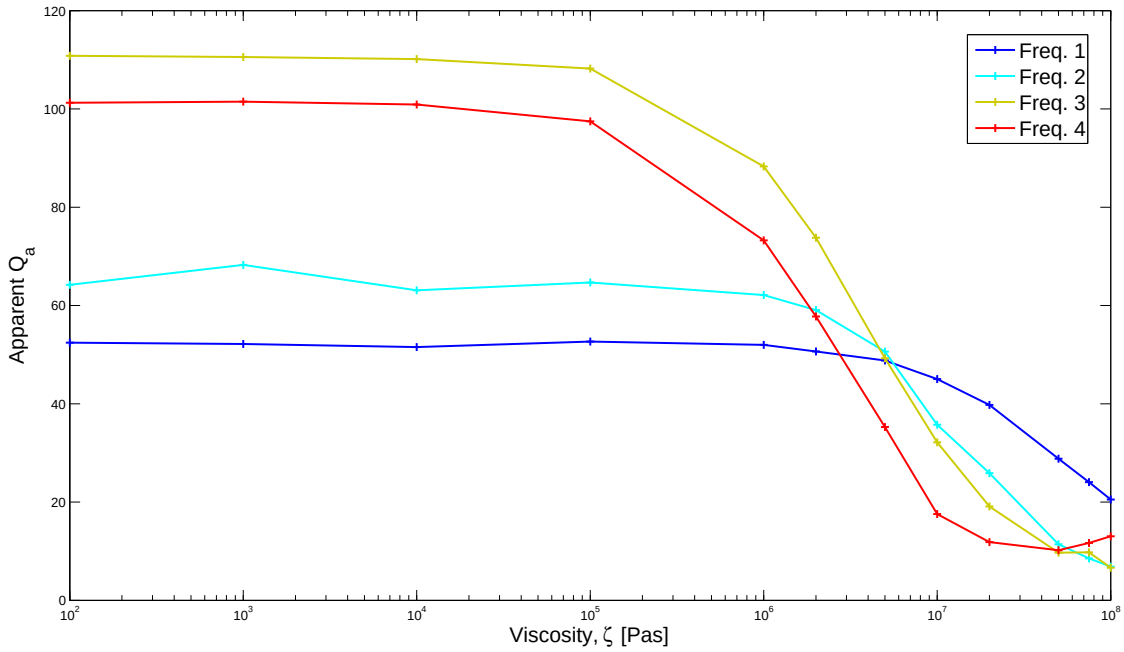

Figure 3.23: Apparent quality factor, Q_a, as a function of the fluid longitudinal viscosity (log scale) for the Kelvin-Voight finite-difference model. The apparent attenuation was calculated for each of the synthetic seismograms shown in Figure 3.22, at four frequencies identified from the spectral peaks. Note the frequency dependence of the radiative part, which corresponds to the value of Q_a for low viscosities on the left hand axis.

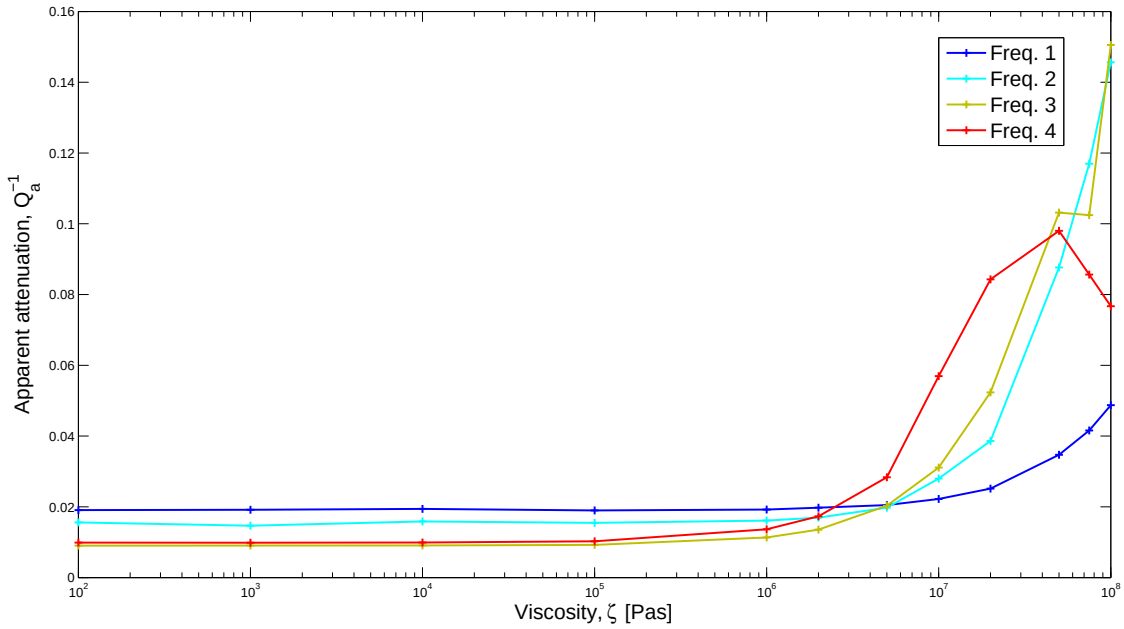

Figure 3.24: Apparent attenuation as a function of the fluid longitudinal viscosity (log scale) for the Kelvin-Voight finite-difference model. Note that for the highest frequencies and viscosity the attenuation is too high to be measured, as the definition of Q breaks down because the energy is rapidly damped in less than a single cycle, leading to the artificial decrease in attenuation of the red curve at high viscosities.

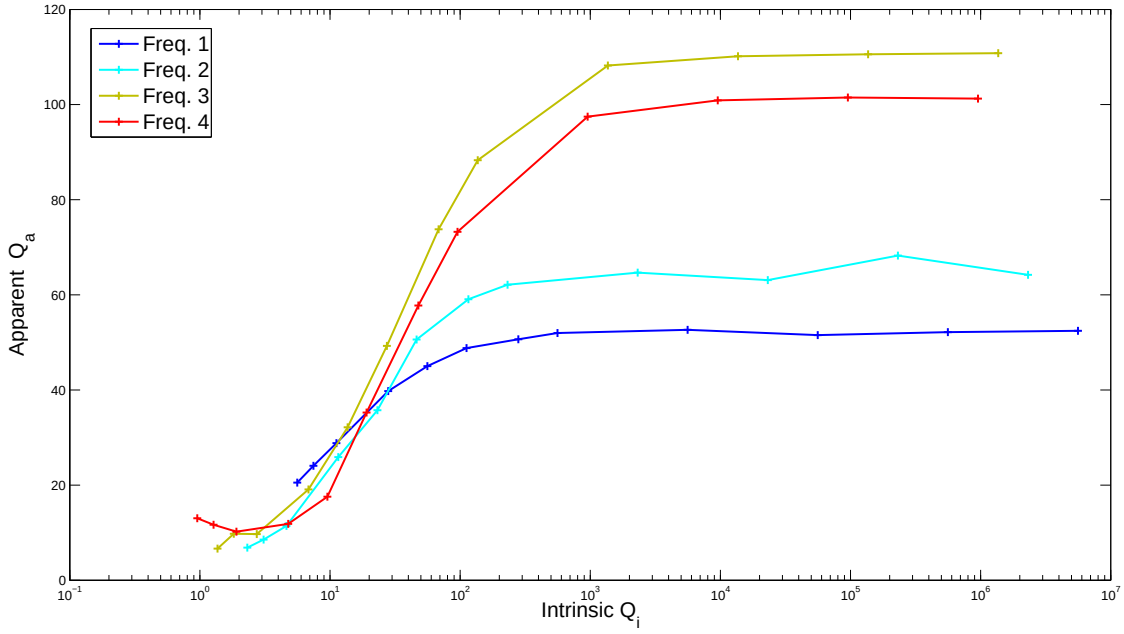

Figure 3.25: Apparent quality factor, Q_{a}, as a function of the intrinsic acoustic wave quality factor, Q_{acoustic}, for the Kelvin-Voight finite-difference model. The values of the intrinsic attenuation were determined for each frequency and viscosity value using the relationship for a Kelvin-Voight rheology in Equation 3.19, and are plotted on a logarithmic scale.

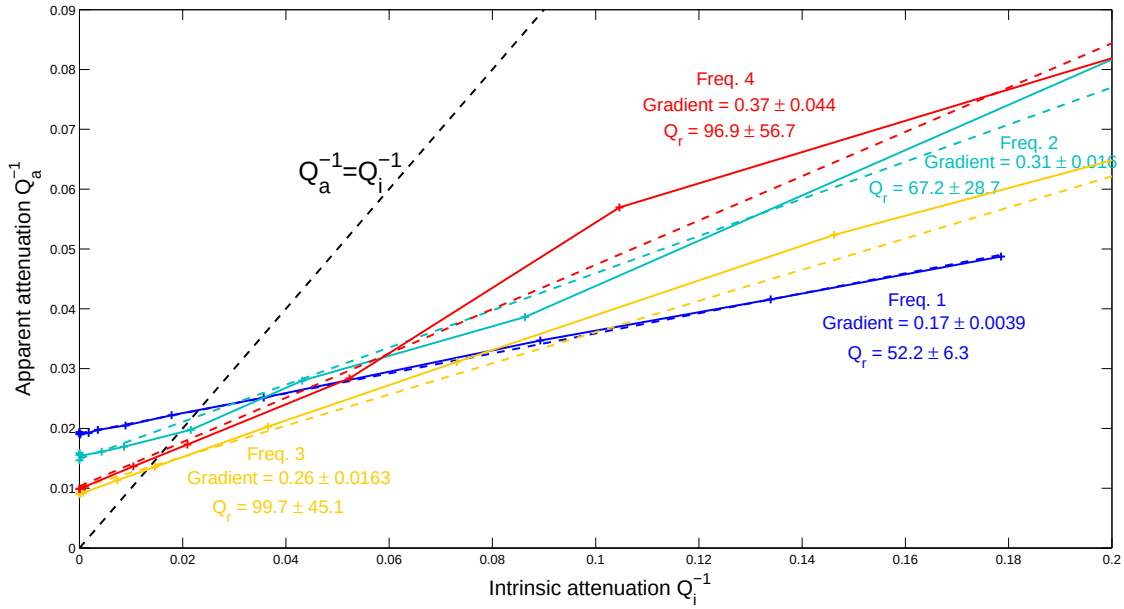

Figure 3.26: Apparent attenuation as a function of the intrinsic acoustic wave attenuation for the Kelvin-Voight finite-difference model. The gradient for the relationship was determined through linear regression for each frequency, and the gradients and intercepts (Q_{r}^{-1}), with associated errors, are displayed in the figure.

3.5.4 Comparison between the model and analytical results

Now that the modified finite-difference model has been shown to implement satisfactorily the Kelvin-Voight rheology, the model and analytical expressions can be compared in terms of the acoustic and interface wave attenuation. The key point is that with this rheological model it is possible to link attenuation and viscosity directly via the relationship in Equation 3.19, allowing direct comparison with the analytically generated curves.

Method

It is evident from the results in Section 3.4 that the factor by which the interface wave attenuation is less than the acoustic wave attenuation is a function of both viscosity *and* frequency. However, using linear fits to the data to estimate the gradient, such as in Figure 3.26, does not take account of this. If it is assumed that

$$Q_{\mathrm{a}}^{-1} = \kappa Q_{\mathrm{acoustic}}^{-1} + Q_r^{-1}, \tag{3.37}$$

with the total intrinsic contribution coming from interface waves

$$Q_{\mathrm{interface}}^{-1} = \kappa Q_{\mathrm{acoustic}}^{-1}, \tag{3.38}$$

then the ratio between interface and acoustic attenuation, κ, is a function of frequency and viscosity:

$$\kappa\left(\zeta, f\right) = \frac{Q_{\mathrm{interface}}^{-1}}{Q_{\mathrm{acoustic}}^{-1}} = \frac{Q_{\mathrm{a}}^{-1}\left(\zeta, f\right) - Q_{\mathrm{r}}^{-1}\left(f\right)}{Q_{\mathrm{acoustic}}^{-1}\left(\zeta, f\right)} \tag{3.39}$$

where it is also assumed that the radiative attenuation, Q_{r}^{-1}, is only a function of frequency and does not vary with the viscosity.

Results

The ratio between acoustic and interface wave attenuation was calculated from the synthetic signals produced by the model using the expression in Equation 3.39. These values were arranged as a function of frequency, for each viscosity, so that they could be overlaid onto the analytical curves for comparison.

A pure melt, with $\xi = \eta$ (Dingwell & Webb, 1989), was first assumed in order to compare the model results to the analytical solutions. In Figure 3.27, the results when the shear and volume viscosity are equal show a poor match between the analytical and model

results, with the modelled ratios closest to the analytical results only for the highest viscosities. However, this assumes the fluid is a pure melt. As already discussed, the relationship between the shear and volume viscosities of the fluid can greatly influence the attenuation behaviour. If a different ratio between η and ξ is used, such as $\xi/\eta = 10^4$, which is more appropriate for a three-phase magma where the volume viscosity depends upon the gas volume fraction (e.g Prud'Homme & Bird, 1978), the results in Figure 3.27 show a much better agreement between the modelled values and the analytical results. In the numerical model, however, the resonator is filled with a pure fluid (melt) of a certain longitudinal viscosity, and the model does not contain any additional physical processes to describe such a multi-phase system.

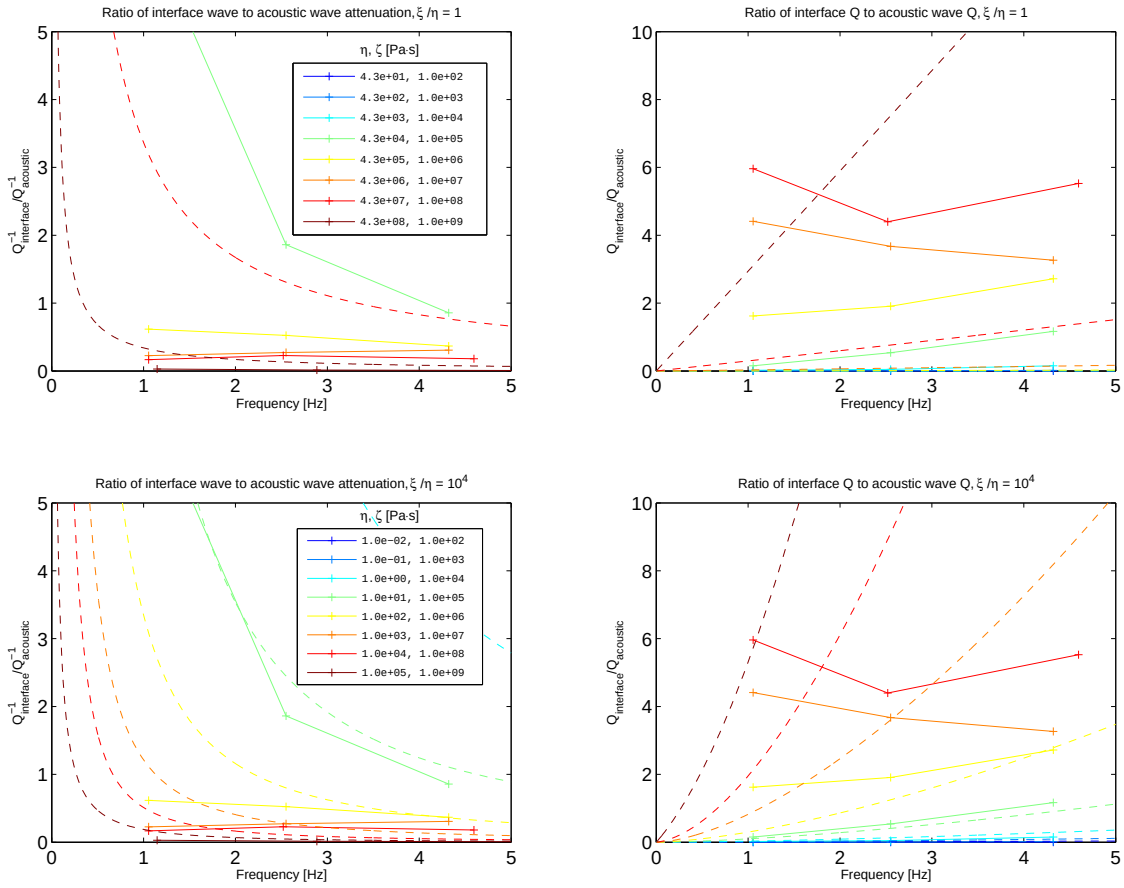

Figure 3.27: Comparison between the analytical expressions and the finite-difference model modified to use a Kelvin-Voight rheology. The plots show the ratio between interface waves and acoustic waves in terms of both attenuation and Q. The solid lines show the results derived from analysing the output of the finite-difference model and the dashed lines are those calculated using the derived analytical expressions. The top two plots are for a ratio between the two viscosities of $\xi/\eta = 1$ (pure melt), and the bottom two for $\xi/\eta = 10^4$ (three-phase magma). Only the three frequencies with the most stable measurements of the attenuation were used for the comparison.

Discussion

The comparison between the model and analytical solutions with equal shear and volume viscosities showed that, in general, the ratio of interface to acoustic attenuation derived from the synthetic signals, κ, was too small in comparison to the analytically derived results. This indicates that the intrinsic attenuation (of interface waves) does not contribute enough to the temporal decay of the signals, suggesting that there could be an additional energy trapping effect that has not been accounted for in the model.

So far, the comparison between the model and analytical results has only been made for Q_a^{-1} measured from the vertical components, at a fixed distance of 500m away at the free surface. As discussed in Section 2.3, both the frequency content and therefore the radiative attenuation are affected by the source-receiver geometry. It was shown that the relative amplitudes of the spectral peaks, corresponding to the resonant modes, are modulated by the complex interference pattern that varies with distance from the source. This is in turn leads to the significant spatial variations in the radiative component of the attenuation, as shown in Figures 2.16 to 2.19. This strong geometrical effect may go some way to explaining the mismatch between the analytical and modelling results, making absolute values of the intrinsic attenuation difficult to obtain from the observed apparent attenuation of the signal.

Another possibility is that finite-length effects may be responsible for these differences. The analytical expression for the interface wave attenuation was derived for an *infinite* fluid layer, whereas the numerical modelling employs a *finite*-length fluid body as the resonator (compare Figures 3.2 and 3.20). This suggests that radiation of energy from the tips of the fluid body and the strong geometrical dependence of the radiative component may mask direct measurements of the intrinsic component.

3.6 Discussion and Conclusions

Low frequency volcanic earthquakes are believed to originate from the resonance of interface waves which trap energy at the boundaries of a fluid-filled body. Therefore, quantifying and understanding the attenuative behaviour of such waves is critical to interpreting the attenuation of low-frequency earthquakes in terms of fluid properties.

In this chapter an analytical approach was used to quantify the attenuation of interface

waves for a horizontal layer filled with viscoelastic fluid, sandwiched between two elastic half-spaces. An explicit expression for the attenuation of interface waves in such a layer was derived via the ratio of the real and imaginary parts of their complex phase velocity. The interface wave attenuation was compared to the attenuation of acoustic waves propagating within the fluid and a key result was found: that for a particular set of parameters, interface waves are attenuated less than acoustic waves for frequencies within the seismic bandwidth of low-frequency earthquakes. This condition depends strongly on the viscosities of the fluid, requiring either, (i) a longitudinal viscosity of at least $\zeta = 10^7$ Pas, for a pure melt with equal shear and volume viscosities, or (ii) a longitudinal viscosity of at least $\zeta = 10^4$ Pas, for a three-phase magma where the volume viscosity is several orders of magnitude larger than the shear, e.g. $\xi = 10^4\eta$. The caveat to this result is that the rheology of the analytical formulation is based on an implicit Kelvin-Voight model. Therefore, to allow comparison with the results of the modelling in Chapter 2, the finite-difference model was modified to implement this new rheology, rather than that of a Standard Linear Solid (SLS). The strong geometrical modulation of the spectral peaks and radiative attenuation may account for the discrepancies between the modified finite-difference model and the analytical results.

Both the analytical and numerical research in this chapter assumed a fluid layer of constant width, with perfectly smooth planar interfaces between the fluid and surrounding elastic solid. In practice, this is unlikely to be the case. The existence of several co-existing waveform 'families' of low-frequency earthquakes at SHV (e.g. Green & Neuberg (2006), see Section 5.1) suggests the presence of several different resonators, either as separate fluid bodies or separately resonating parts of the same connected plumbing system. Constrictions in a magma filled conduit have been shown to be potential sources of increased shear stress (Key, 2007), increasing the likelihood of triggering seismicity through brittle failure of the melt in such regions (Thomas & Neuberg, 2010). Such features could affect interface wave propagation, either by acting as reflectors or secondary sources, or by scattering the energy. There are also likely to be irregularities (on various length scales) of the fluid-solid boundary at the walls, which may well disrupt and further attenuate interface waves, in a manner similar to that seen for tube waves in fluid-filled boreholes, depending on the relationship between the length scale of the irregularities and the frequency of interest.

Overall, the key outcome of this chapter lends further support to the idea that conduit

resonance of a low aspect ratio body filled with high viscosity magma is a viable source of low-frequency seismicity on volcanoes. The results confirm the idea developed in Chapter 2, that the difference between interface and acoustic waves means the attenuative effect of the viscosity of the magma on the damping of the seismic resonance has been overestimated. The analysis also demonstrates that the difference between acoustic and interface propagation must be considered in any quantitative analysis of low-frequency earthquake attenuation, particularly if this is used to infer or place constraints on the composition or properties of fluids within the resonating body.

Chapter 4

Measuring the attenuation

Low frequency volcanic earthquakes are characterised by their harmonic codas which decay with time. This chapter details the development of methods to measure and quantify the temporal amplitude decay or apparent attenuation of such a signal.

Since the energy, E, is proportional to the square of the amplitude, A^2, for a linear stress-strain relation, the Aki & Richards (2002) definition of attenuation as the fractional energy loss per cycle (Equation 1.2) can be rewritten in terms of wave amplitude as:

$$\frac{1}{Q(\omega)} = \frac{-1}{\pi}\frac{\Delta A}{A} \tag{4.1}$$

where ΔA is the amplitude loss per cycle. There is also an assumption that $Q \gg 1$, so that successive peaks have almost the same amplitude. It is worth remembering here that attenuation is generally observed as either a temporal decay of amplitude at fixed wavenumber or spatial decay at fixed frequency (see Section 1.6.1), and that it is the temporal decay of amplitude that is considered here. From Equation 4.1 it follows that this temporal amplitude decay can be written as:

$$A(t) = A_0\left(1 - \frac{\pi}{Q}\right)^n \qquad \left(\text{for } t = \frac{2n\pi}{\omega}\right) \tag{4.2}$$

given that initially $A = A_0$ and decreases by a fixed fraction π/Q at successive times $2\pi/\omega$, $4\pi/\omega$, ... $2n\pi/\omega$, where n is the number of cycles (Aki & Richards, 2002). Note that this *temporal* amplitude decay can be absorbed into the usual travelling wave solution to the wave equation by the introduction of a complex frequency, $\tilde{\omega} = \omega - i\omega/2Q$ (Aki & Richards, 2002), in an analogous way to introducing a complex wavenumber to describe the *spatial* amplitude decay (Section 1.6.1). This complex frequency therefore contains information regarding the attenuation of the signal, and, as discussed in Section 1.6.3, measuring the complex frequencies using the spectral 'Sompi' method

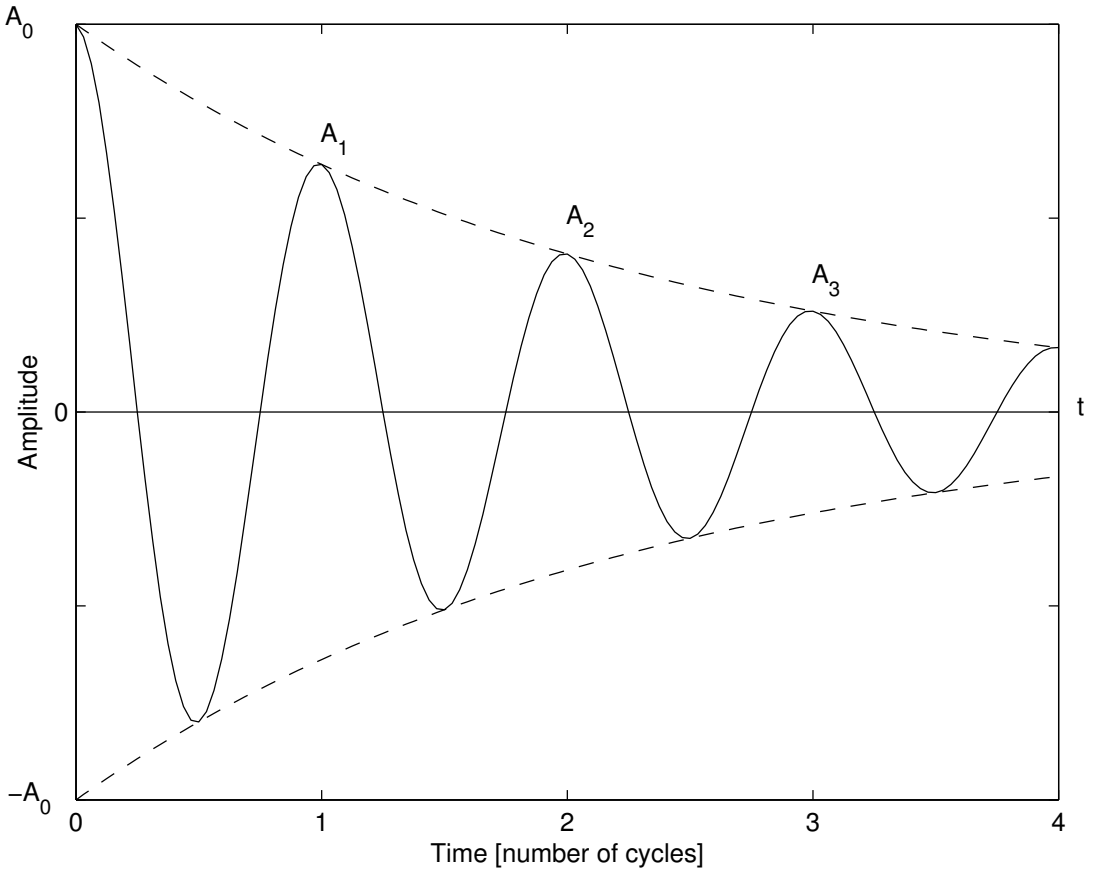

Figure 4.1: Schematic diagram illustrating how the attenuation can be described in terms of terms of temporal amplitude loss. The envelope amplitude (dashed lines) is initially A_0, but decays by a fixed factor of $(1 - \pi/Q)$ each cycle.

(Kumazawa et al., 1990) has been used to estimate the temporal attenuation of volcanic seismic signals (e.g. Nakano et al., 1998; Kumagai & Chouet, 1999; 2000). These authors define the complex frequency as $(f - ig)$, where f is the frequency and g is the imaginary part, termed the growth rate. Thus, the attenuation can be obtained from the ratio of the real and imaginary parts: $Q = -f/2g$, with the 'Sompi' analysis resolving the attenuation at spectral peaks corresponding to the dominant resonant modes (De Angelis & McNutt, 2005).

By contrast, this chapter describes time-domain methods to obtain the apparent attenuation, without the need for spectral analysis. Raikes & White (1984), who estimated Q by a waveform matching technique between synthetic and well seismic data, were among the first to use a time-domain approach. Ten different methods of measuring attenuation from VSP (Vertical Seismic Profile) data were compared by Tonn (1991), including several time-domain methods, such as using the amplitude decay or the analytical signal. Time-domain approaches to measure the attenuation of volcanic seismic

signals have been used by Seidl et al. (1999) and Seidl & Hellweg (2003), who analysed the amplitude decay of *tornillo* earthquakes at Galeras volcano, Colombia. Isolating the energy from a signal at a particular frequency, whether by filtering or other means, allows the attenuation as a function of frequency to be obtained in a similar way to the spectral analysis, since both time and frequency domain methods are based on the same fundamental assumptions.

4.1 Review and evolution of methods

This section outlines the progression of methods to measure the apparent attenuation of low-frequency earthquakes, from initial ideas to the use of logarithms and the analytical envelope. The same methods are applied throughout this thesis to both synthetically generated signals and real data from SHV to determine the apparent attenuation. A monochromatic signal is first assumed, with the frequency dependence discussed later in Section 4.2. More formalised, automated extensions to these methods are then discussed in Section 4.3.

4.1.1 Neighbouring peaks

The first approach was to calculate the apparent attenuation from the relative amplitudes of consecutive local maxima or minima (or peaks) of a monochromatic waveform. Starting from Equation 4.2 the amplitude of the peak after n cycles, or time t_n, can be defined as:

$$A(t_n) = A_0 \left(1 - \frac{\pi}{Q_\mathrm{a}}\right)^n \tag{4.3}$$

with the amplitude of the *previous* peak given by:

$$A(t_{n-1}) = A_0 \left(1 - \frac{\pi}{Q_\mathrm{a}}\right)^{n-1} \tag{4.4}$$

By taking the ratio of successive peaks an expression for the local apparent attenuation, Q_a^{-1}, at time t_n can be derived:

$$\begin{aligned} \frac{A(t_n)}{A(t_{n-1})} &= 1 - \frac{\pi}{Q_\mathrm{a}} \\ \Rightarrow \quad \frac{\pi}{Q_\mathrm{a}} &= 1 - \frac{A(t_n)}{A(t_{n-1})} = \frac{A(t_{n-1}) - A(t_n)}{A(t_{n-1})} \\ \therefore \quad Q_\mathrm{a}^{-1} &= \frac{A(t_{n-1}) - A(t_n)}{\pi A(t_{n-1})} \end{aligned} \tag{4.5}$$

Equation 4.5 can be used to calculate apparent Q_{a}^{-1} values from monochromatic seismograms with a slowly decaying coda. This was achieved by first locating the maxima and minima of the waveform by calculating the numerical gradient of the signal and finding the zeroes of this gradient function (Figure 4.1). The first few values were not used, as these correspond to the onset of the signal and not the smoothly decaying coda, which is the part of the signal that is of interest.

The method was initially tested with synthetic low-frequency events produced by the finite-difference code (Section 2.4). Attempts to calculate apparent Q_{a} values from the amplitude decay of the codas produced fluctuating results. Very large values of Q_{a} were measured, as large as $Q_{\mathrm{a}} \sim 1000$ even though an intrinsic Q_{i} of 20 was used. In some cases spurious negative Q_{a} values were generated if the amplitude of successive peaks increased with time (see Figure 4.2). This is illustrated by the $Q_{\mathrm{i}}(\omega)$ profiles in Figure 2.30(b) which show that even if an array of SLS is used to model the attenuation behaviour, the modelled intrinsic Q_{i} is forced to increase asymptotically as the frequency approaches zero. As shown in Section 2.4.3, in the low-frequency limit $Q^{-1}(\omega) \rightarrow 0$ as $\omega \rightarrow 0$, hence this method does not work for frequencies below approximately 1Hz.

Therefore, with the presence of long-period energy, smoothing of the envelopes by filtering the traces produced more stable estimates of the attenuation from the synthetic data using this neighbouring peaks method. Figure 4.2 shows the amplitude spectra of two vertical component monochromatic traces, with a single dominant spectral peak at just above 1Hz. A band-pass filter with a low-cut of 0.8 Hz and high-cut of 1.3 Hz was applied to isolate the resonant component of the signal energy. This produces a more smoothly decaying signal, and hence a more accurate estimate of the attenuation at the specific resonant frequency of the signal, seen in Figure 4.3. However, as will be discussed in Section 4.2, filtering of the data introduces additional effects on the decay of the waveform with time.

One limitation of this method is that using only neighbouring peaks gives only a local approximation to the amplitude decay at fixed times, and the method generates a series of varying Q_{a} values rather than a single value for the whole waveform. An obvious way to convert this to a single value for the apparent quality factor for each trace is to simply take the mean of the set of values. But can this be justified? This suggests an alternative approach, using all available data from the coda should be used, and this idea is described in more detail the following section.

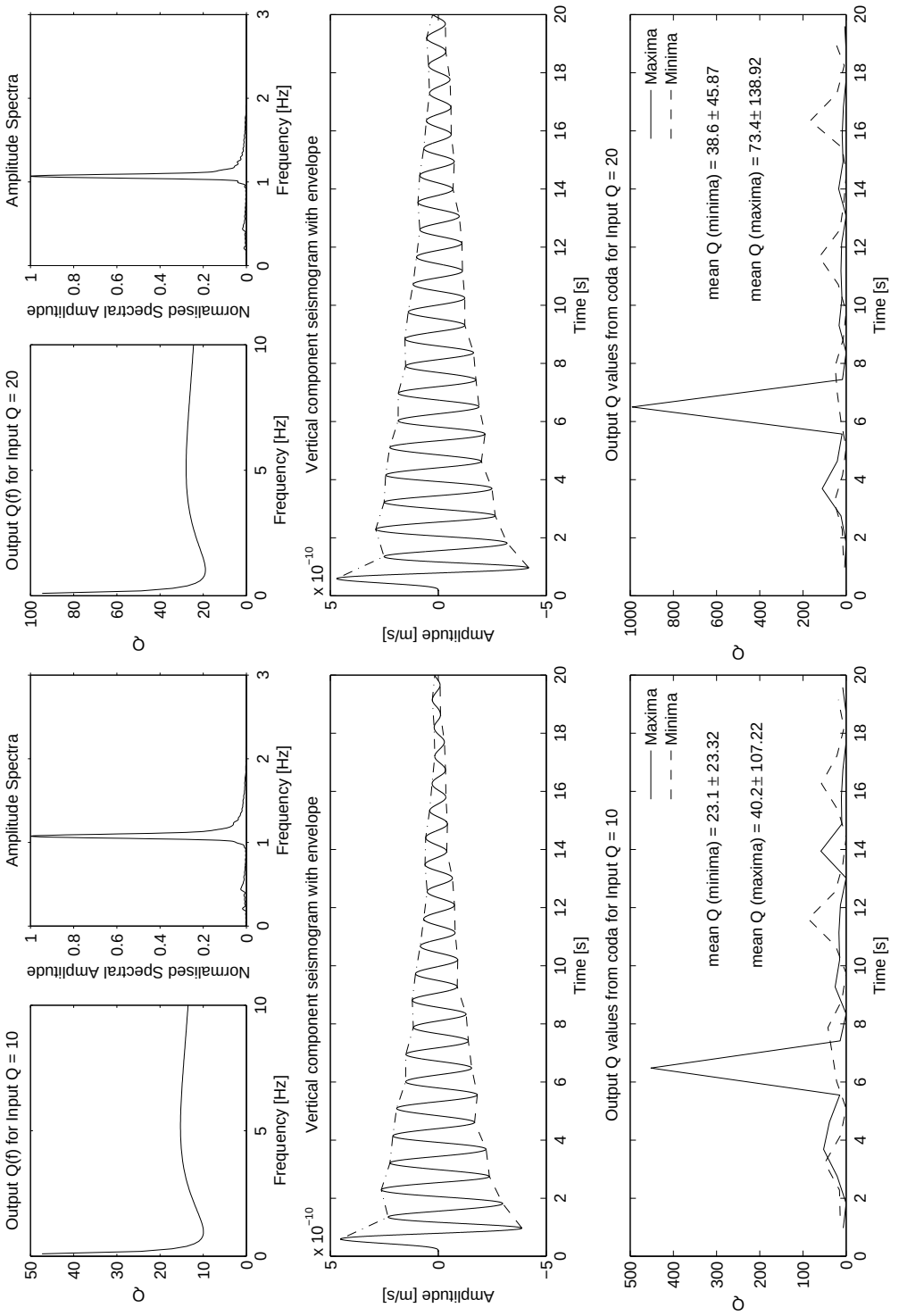

Figure 4.2: Apparent Q_a values calculated from the codas of synthetic signals with no filtering applied. The group of figures on the left are for an intrinsic Q_i of 10, and on the right for $Q_i = 20$. The top two plots represent the Q_i as a function of frequency curve modelled by the finite-difference code and the amplitude spectrum of the resultant signal respectively. The lower figures show the seismogram and its envelope, together with the apparent Q_a values calculated from the amplitude of neighbouring peaks. Negative values of Q_a were automatically discarded from the analysis.

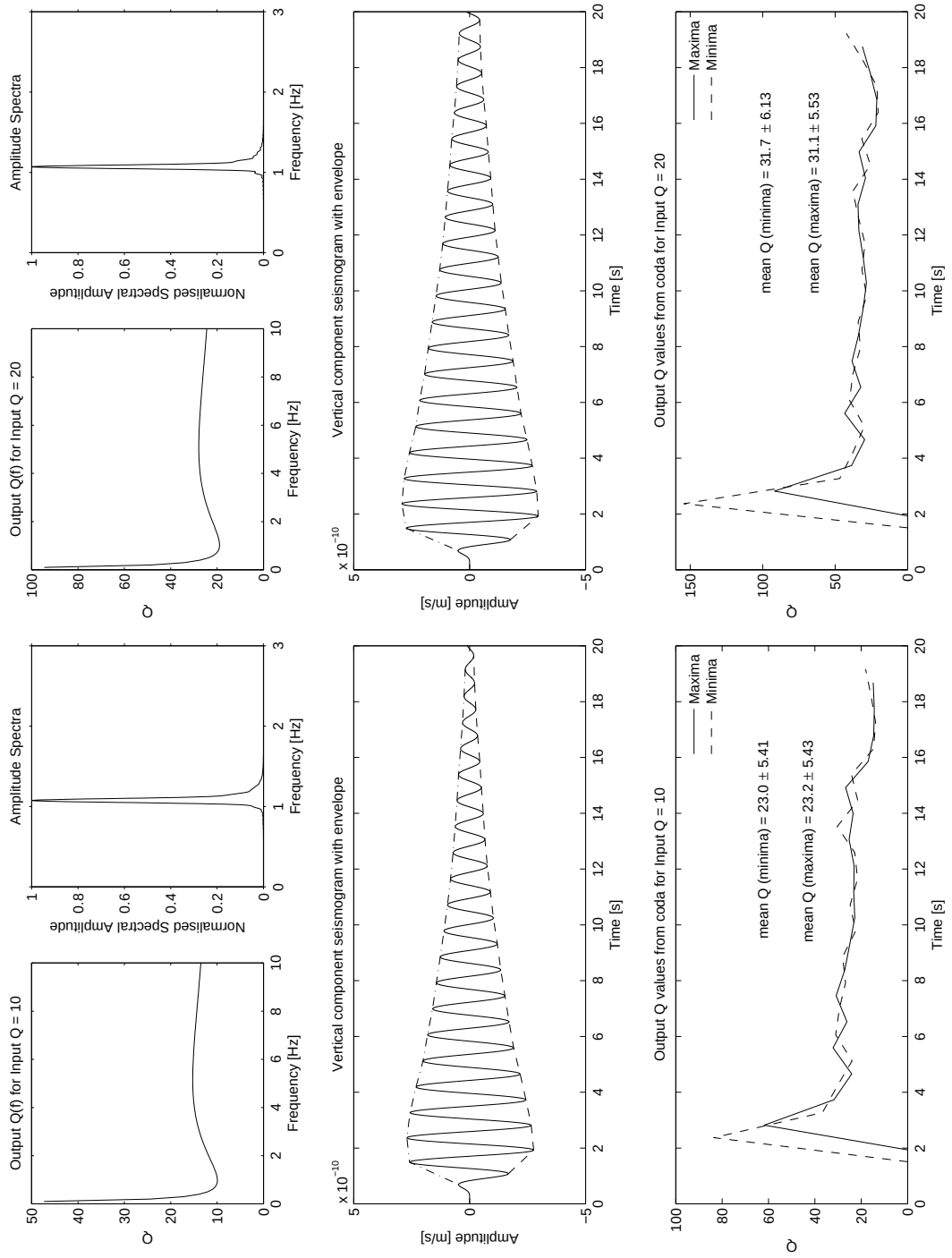

Figure 4.3: The layout is the same as for Figure 4.2. The apparent Q_a values are now calculated from the codas of the data with a band-pass filter between 0.8-1.3 Hz applied. Note that the two values obtained from the top and bottom of the envelopes are now in much better agreement than in the case with no filtering applied.

4.1.2 Logarithms

For the reasons discussed in the previous section, the 'neighbouring peaks' method for calculating the apparent Q_{a} proved somewhat problematic. Since the temporal amplitude decay can be described as an exponential decay process, the next alternative and somewhat more robust method was to use linear regression to fit a straight line to the logarithm of the signal amplitude against time (or number of cycles). Taking the logarithm of both sides of Equation 4.2 gives

$$\ln A = \ln A_0 + n \ln \left(1 - \frac{\pi}{Q_{\mathrm{a}}}\right) \tag{4.6}$$

which is of the form $f(n) = mn + c$, with gradient

$$m = \ln \left(1 - \frac{\pi}{Q_{\mathrm{a}}}\right) \tag{4.7}$$

and intercept

$$c = \ln A_0 \tag{4.8}$$

Therefore, by fitting a straight line to the logarithm of the envelope amplitudes, a value for the apparent Q_{a} can be extracted from the gradient:

$$Q_a^{-1} = \frac{(1 - \mathrm{e}^m)}{\pi} \tag{4.9}$$

This method of calculating the apparent Q_{a}^{-1} will be referred to in the following as the *logarithm* method. Note that a quasi-monochromatic is still assumed.

Determining the analytical envelope using the Hilbert Transform

Once the envelope of the signal coda has been calculated, the logarithm method of determining the apparent Q_{a}^{-1}, described in the previous section, is more robust and is easier to implement than the neighbouring peaks method. It produces accurate results without the need for filtering low frequency noise, as the results in Figure 4.4 show.

Using only the local minima and maxima to estimate the envelope and hence the apparent Q_{a} is, however, not ideal as it provides only a limited number of points which can be used in a linear regression and improved results can be obtained by using a continuous expression for the signal envelope, rather than the discrete times of the maxima and minima. One way to obtain the envelope function of a signal is by using the Hilbert

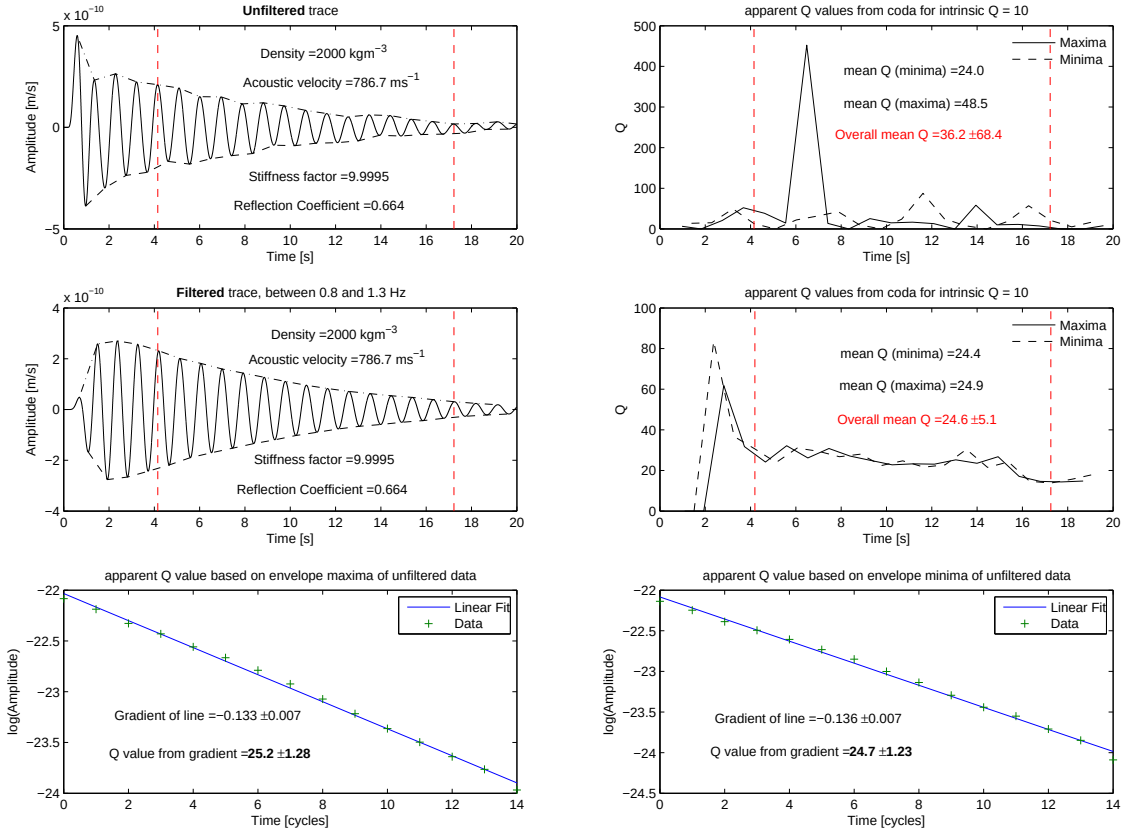

Figure 4.4: Apparent Q_{a} values calculated using the neighbouring peaks method for a raw (unfiltered) trace and a filtered trace. The bottom two plots show the Q_{a} calculated using the logarithm method for the minima and maxima envelopes of the unfiltered data. It demonstrates that the logarithm method yields results consistent with the neighbouring peaks method, without the need for filtering of the data to remove long-period noise.

Transform. The complex *analytical signal*, $x_a(t)$, of a real signal $x(t)$ can be constructed by

$$x_a(t) = x(t) + i\hat{x}(t) \tag{4.10}$$

where $i^2 = -1$ and $\hat{x}(t)$ is the Hilbert transform of $x(t)$,

$$\hat{x}(t) = H\left[x(t)\right] = \frac{1}{\pi}\ \mathrm{p.v.} \int_{-\infty}^{\infty} \frac{u(\tau)}{t-\tau} d\tau = \ \mathrm{p.v.} \frac{1}{\pi t} * x(t) \tag{4.11}$$

defined using the Cauchy principal value (p.v.) and where $*$ denotes a convolution.

Using the polar form of the analytical signal

$$x_a(t) = A(t)e^{i\phi(t)} \tag{4.12}$$

allows the *analytical envelope* to be defined as the amplitude or magnitude of the analytical signal

$$A(t) = \sqrt{x^2(t) + \hat{x}^2(t)} \tag{4.13}$$

and the *instantaneous phase* as its argument

$$\phi(t) = \arg\{x_a(t)\} = \tan^{-1}\left(\frac{\hat{x}(t)}{x(t)}\right) \tag{4.14}$$

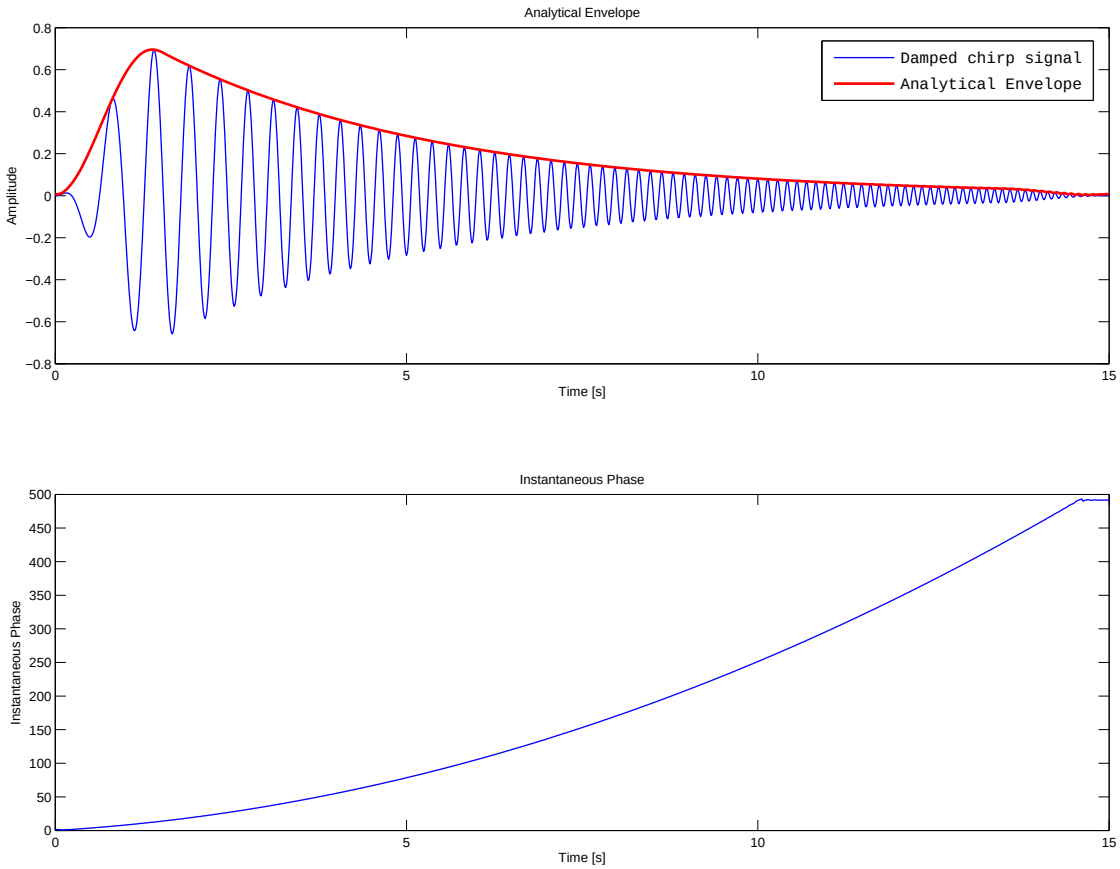

Figure 4.5: Example of a damped chirp signal, used to illustrate its associated analytical envelope (top) and instantaneous phase (bottom). The envelope and phase were calculated using the expressions in Equation 4.13 and 4.14. Note that in this example, for the purpose of illustration, the signal was tapered to remove wraparound effects.

Combining the use of the analytical envelope with the logarithm method (Section 4.1.2) provides a robust and reliable way of obtaining estimates of the apparent attenuation at a given frequency (still assuming a monochromatic signal). This approach and similar methods have been used previously to determine the attenuation of low-frequency *tornillo* earthquakes at Galeras volcano, Columbia (see e.g. Seidl et al., 1999; Seidl & Hellweg, 2003).

4.2 Frequency dependence and the effects of filtering

Since the temporal attenuation is defined to be the amplitude decay *per cycle* the apparent Q_a can only be measured in this way at a *single frequency*. However, in general

low-frequency earthquakes contain energy across a range of spectral frequencies. They are often thought of as a superposition of damped sinusoids at different frequencies corresponding to the different modes of resonance (e.g. Nakano & Kumagai, 2005b) and are hence often characterised by peaked spectra at integer harmonics.

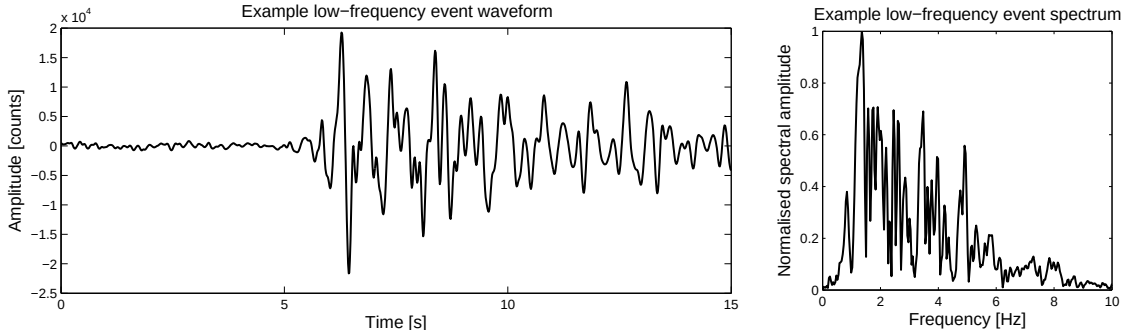

Figure 4.6: Low-frequency earthquake waveform with characteristic peaked amplitude spectrum. This example shows a 15-second vertical component velocity seismogram recorded at station MBGA, SHV, Montserrat on 23$^{\text{rd}}$ June 1997.

In order to analyse the coda of such signals and determine the apparent attenuation as a function of frequency, the energy at particular frequencies needs to be isolated. One way to achieve this is via the use of narrow band-pass filters.

One of the most widely used class of filters is the Butterworth filter, which has a transfer function defined as

$$|F_{\text{b}}(\omega)|^2 = \frac{1}{1 + [(\omega - \omega_b)/\omega_c]^{2n}} \tag{4.15}$$

for a filter centred at ω_b, with half-width ω_c and n poles (e.g. Gubbins, 2004). The number of poles is sometimes referred to as the *order* of the filter, which controls its steepness, with higher order filters rolling-off more steeply at the edges of the desired frequency passband. Ideally, a Butterworth filter with a very narrow spectral bandwidth and steep roll-off would be used to isolate energy from the spectrum of low-frequency earthquakes. However, filters such as this introduce "ringing" into the time domain (Figure 4.7). The order of the filter also affects the phase spectrum, introducing a phase shift which shifts energy to later times in the filtered signal for higher order filters. These effects are particularly important when considering temporal attenuation as they can contaminate the amplitude decay of the signal. Therefore, the effects of such filters need to be accounted for when they are used in measuring the apparent attenuation.

Figure 4.8 shows an example of combining band-pass filters with the analytical envelope and logarithm method to calculate the apparent attenuation of synthetic signal. This

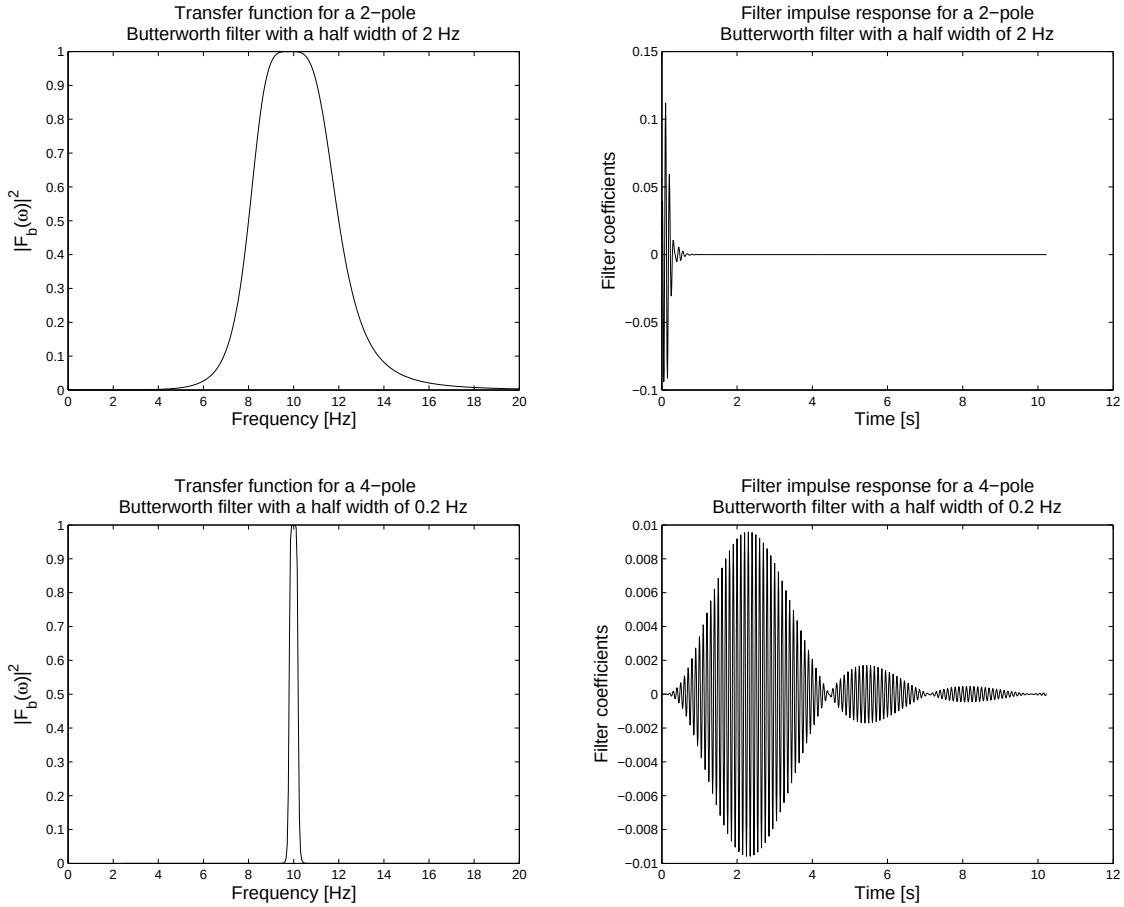

Figure 4.7: Transfer function and impulse response of Butterworth bandpass filters, showing the effect of the filter in both frequency and time domains. The top two plots are for a 2^{nd} order Butterworth bandpass filter centred at 10Hz with a half-width of 2Hz. The lower plots are for a 4^{th} order Butterworth bandpass filter, also centred at 10Hz but with a much narrower half-width of 0.2Hz.

particular signal was produced by the finite-difference model using a 10Hz Sinc function as the source wavelet to excite the higher modes of resonance and resulted in a signal whose spectrum contains several peaks.

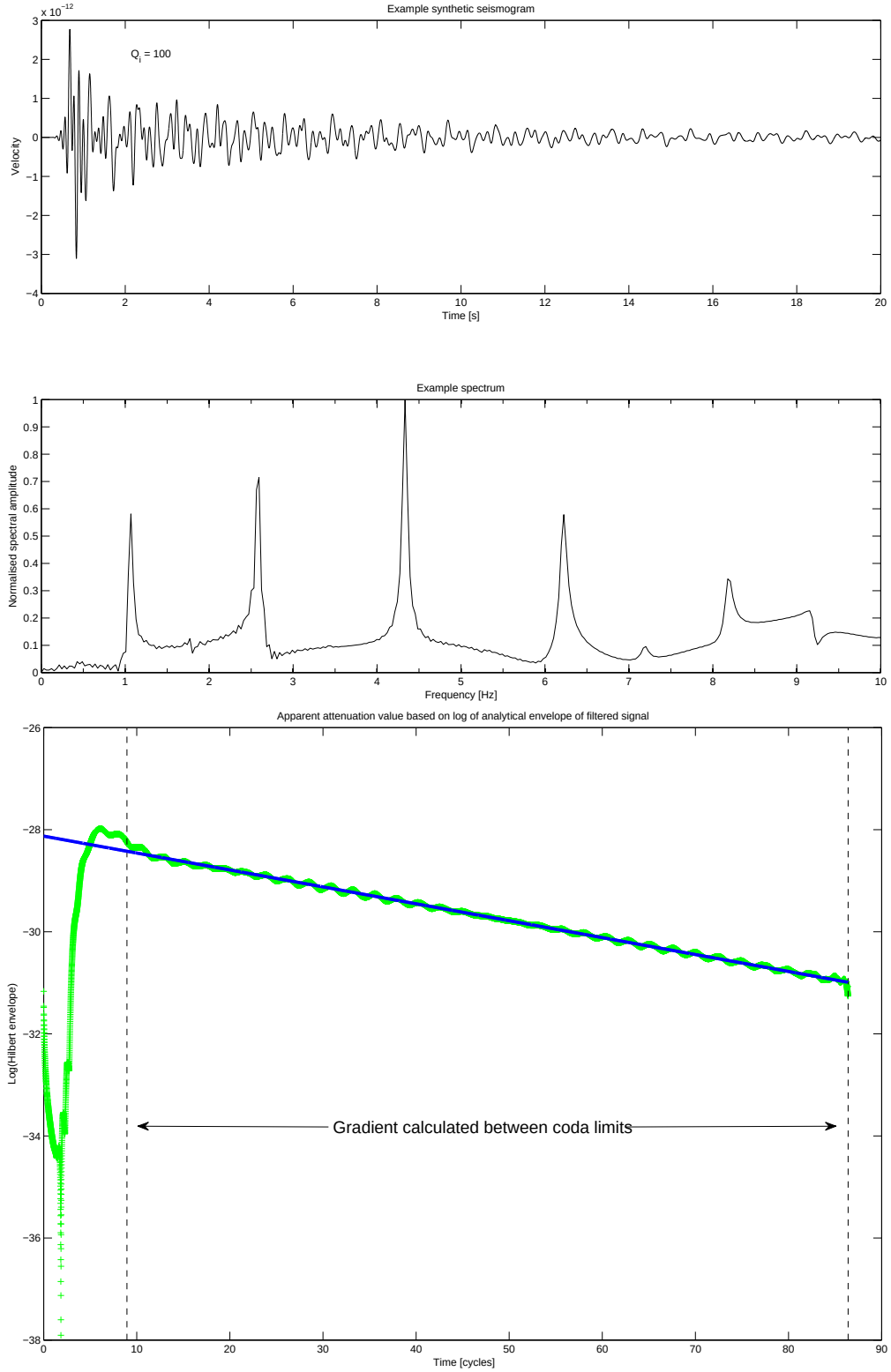

Figure 4.8: Example of a synthetic seismogram generated by the finite-difference model and its associated spectrum. The lower plot shows the logarithm of the analytical envelope of a band-pass filtered version of the signal plotted against the number of cycles ($n = \omega t/2\pi$). The apparent attenuation at a chosen frequency can be calculated from the slope of this relationship, after the appropriate portion of the coda has been selected for the linear regression.

4.3 Automated methods

4.3.1 Description of the methods

Automating the process: motivation and problems

If large numbers of events are to be processed, the process of measuring attenuation should be automated as much as possible. As well as increased efficiency and reduced computation time, this has the advantage that rigorous criteria for choosing certain parameters can be defined, reducing the possibility of user bias being introduced into the results. One of the most time consuming aspects when initially implementing the methods outlined (Section 4.1.2) was found to be manually selecting the part of the coda amplitude envelope to be used in the linear regression (see for example Figure 4.8) for each frequency component of each event. To some extent there exists a trade-off between increased accuracy (manual picking) and reduced processing time (automated). Manually selecting the regression window results in fewer spurious measurements (e.g. negative attenuation) although this can introduce some degree of user bias. The theory and development of several automated methods to measure the apparent attenuation will be discussed in the remaining sections of this chapter, followed by a comparison and discussion of the results in Section 4.3.2.

Fixed regression window length

The first approach to automating the process was to use a fixed length for the time window used to perform the linear regression as described in Section 4.1.2. The start of the window was chosen at the time of maximum amplitude, t_{max}, as illustrated in Figure 4.9.

One problem with this method is that it does not cope very well if the amplitude does not decay throughout the whole time window. This could arise if two earthquakes occur very close together in time, or if the signal is particularly noisy. The same problem may also occur if the band-pass filter applied to the data is either too, or not sufficiently, narrow. This scenario can create inappropriate values if the linear regression is applied to the whole window, and in general tends to overestimate the Q_{a} or underestimate the attenuation, as can be seen in Figures 4.10 and 4.11.

In addition, having a fixed regression window automatically introduces a bias to the

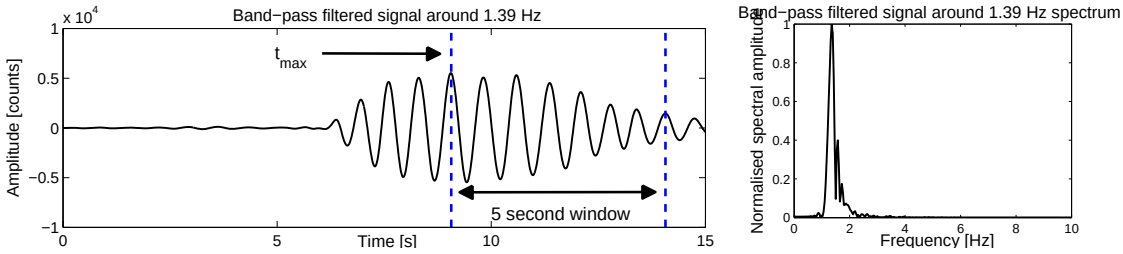

Figure 4.9: Low-frequency earthquake waveform bandpass filtered around a spectral peak at 1.39Hz. The diagram illustrates the fixed regression window length method, with the automatically generated limits shown in blue. In this example the length of the window is 5 seconds from the time of the maximum amplitude, t_{max}.

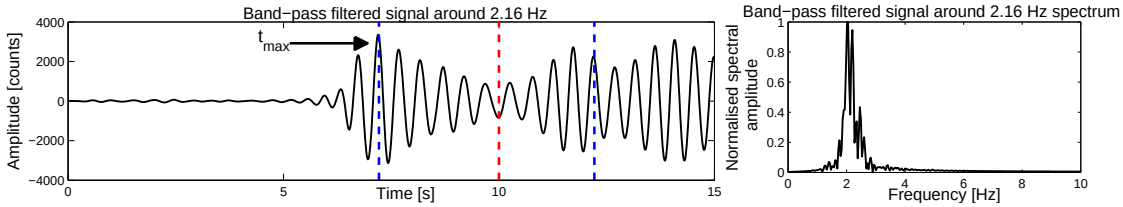

Figure 4.10: Low-frequency earthquake waveform bandpass filtered around the spectral peak at 2.19Hz. This diagram illustrates one of the problems of the fixed regression window length method, where the amplitude does not smoothly decrease throughout the entire length of the window. In this example the automatic limits are again shown in blue and the length of the window is 5 seconds. The red line shows the manually selected end of the window where the amplitude has stopped decreasing.

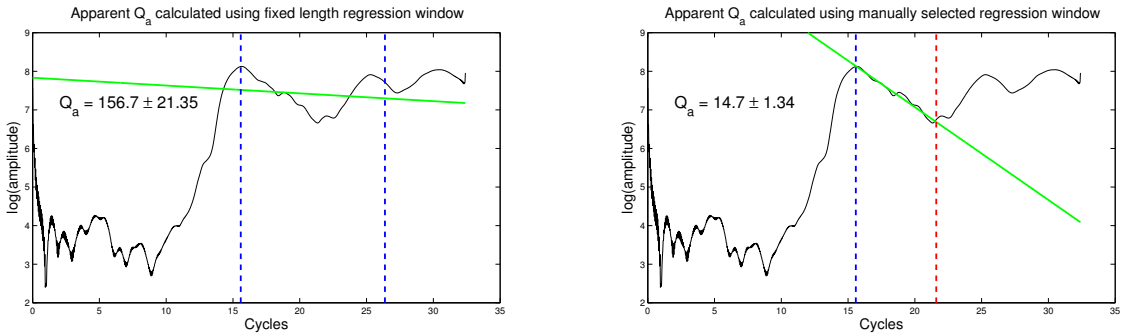

Figure 4.11: Comparison of the apparent Q_{a} calculated using a fixed length and manually selected regression window for the example in Figure 4.10. The logarithm of the analytical envelope is plotted against the number of cycles, and a linear fit to the data is calculated for the portion within the chosen regression window, with the gradient used to determine the apparent Q_{a}. Note the order of magnitude difference between the two Q_{a} values calculated, with the fixed window method significantly overestimating the Q_{a} or underestimating the attenuation, with a larger regression error.

measurements, as the use of a fixed window length puts a limit on the maximum value of Q_{a} (slowest decay with time) that can be measured. In summary, as a first order approach this method succeeds in reducing the computation time compared to manual

selection, but suffers from bias due to the fixed window length and can underestimate the attenuation. In the following section, a weighting function is introduced that suppresses noisy seismogram sections and favours portions of the coda with stable gradient.

Weighting: formalising as a least squares inversion

In order to introduce some form of weighting of the data we formalise the regression in matrix form as a linear least squares inversion:

$$d = Gp \tag{4.16}$$

where d is the data vector, in this case the set of n amplitude values $d = \begin{bmatrix} A_1 \\ A_2 \\ \vdots \\ A_n \end{bmatrix}$, and p represents the model parameters, here the polynomial coefficients $p = \begin{bmatrix} m \\ c \end{bmatrix}$, where m is the gradient of the line which is then used to calculate the apparent attenuation, and c the intercept. In this instance, the condition matrix G has the simple form $G = \begin{bmatrix} t_1 & 1 \\ t_2 & 1 \\ \vdots & \vdots \\ t_n & 1 \end{bmatrix}$ where t is the vector of times (in cycles), since we have a linear relationship of the form $A_i = mt_i + c$.

Solving for p in Equation 4.16 gives the solution to the over-determined problem:

$$p = \begin{bmatrix} m \\ c \end{bmatrix} = (G^{\mathrm{T}}G)^{-1}G^{\mathrm{T}}d \tag{4.17}$$

where pre-multiplying by G^{T} ensures the matrix $(G^{\mathrm{T}}G)$ is square for calculating its inverse.

Having formalised the problem in this way a weighting matrix can be introduced, in the form of a data covariance matrix, C_d^{-1}, to weight the points in the regression based on a criterion of our choice:

$$(G^{\mathrm{T}}C_d^{-1})d = (G^{\mathrm{T}}C_d^{-1}G)p \tag{4.18}$$

$$p = (G^{\mathrm{T}}C_d^{-1}G)^{-1}(G^{\mathrm{T}}C_d^{-1})d \tag{4.19}$$

In this case, the most stable measurement of the gradient is desired, so this criterion can be used to construct our data covariance matrix, C_d^{-1}, and weight the datapoints in the inversion appropriately.

Weighting using the second derivative

To improve the regression, we want to weight the datapoints where the gradient is most stable. The second derivative of the data (with respect to time or cycles) gives the rate of change of the gradient. We want to weight portions of the data where the gradient is most stable, which equates to small values of the second derivative (if the gradient was constant the second derivative would be zero). In this way, the data covariance matrix can be constructed to take account of this. Conventionally, for independent measurements, the data covariance is a diagonal matrix, whose diagonal elements correspond to the error on the measurements or datapoints, of the form:

$$C_d = \{\sigma_{ij}^2\} = \begin{bmatrix} \sigma_1^2 & \cdots & 0 \\ \vdots & \ddots & \vdots \\ 0 & \cdots & \sigma_N^2 \end{bmatrix} \tag{4.20}$$

where σ_{ij}^2 is the set of the variances of the measurements.

In this example we want to use the second derivative to weight the data, so instead of using the variance the second derivative can be used as the weighting parameter:

$$\sigma_i^2 = \left(\ddot{A}_i\right)^{2\ell} \tag{4.21}$$

where $\ddot{A}_i$ denotes the second derivative of the logarithm of the analytical envelope with respect to time (or cycles) and ℓ is an integer parameter. The 2 in the exponent ensures all values of the weighting are positive, and in initial trials $\ell = 1$ was chosen. The effects of introducing this weighting in comparison with the other methods is discussed in Section 4.3.2.

Selecting the regression window: segments of negative gradient

We want to determine the portion of the data where the gradient is *negative* and most *stable* with time, corresponding to manually selecting the limits of the regression time window. To automate this process, the data can be weighted based on the sign of the gradient, thus only including segments with a negative gradient in the inversion. A smoothed gradient function for the logarithm of the envelope is calculated numerically and used to select 'segments' of the amplitude envelope that have a negative gradient. To avoid using segments produced by wraparound effects when calculating the gradient numerically, the gradient function is truncated, and only the portion after the time of the

maximum amplitude of the original band-passed trace (t_{max}) is used (see Figures 4.12-4.14). This also discards the onset part of the signal, ensuring only the decaying coda is used in determining the attenuation, in the same way as for the fixed regression window method.

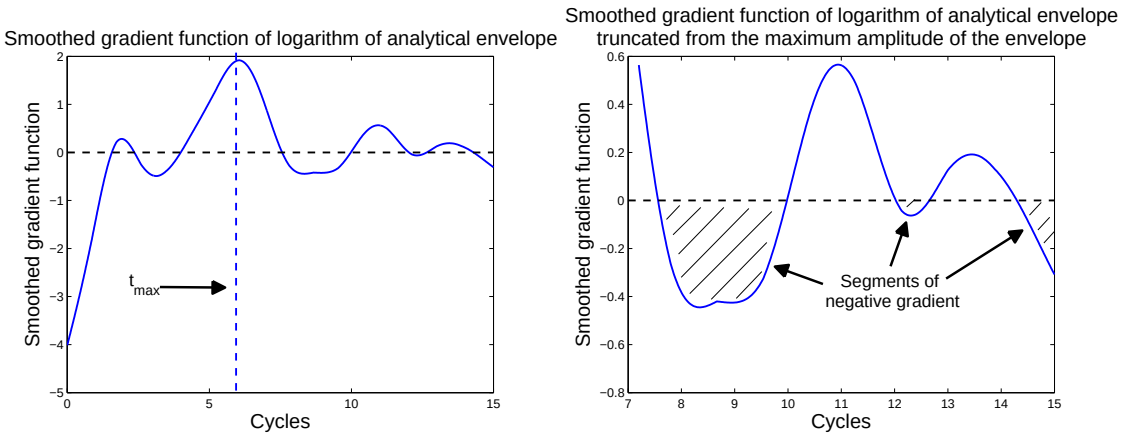

Figure 4.12: Smoothed gradient function of the logarithm of the signal envelope, for the bandpass filtered example shown in Figure 4.10. The right hand plot shows the function truncated from the time of the maximum amplitude, t_{max}, of the bandpass filtered signal. This produces three 'segments' where the gradient is negative, for each of which linear regression is performed.

The number of segments is controlled by the amount of smoothing applied to the gradient function. The smoothing is applied by calculating the gradient of the original function on a series of windows of length W (non-overlapped), and then interpolating back onto a time series the same length as the input signal. The window size was chosen to be:

$$W = \frac{2\pi T F_s}{k\omega_b} \tag{4.22}$$

which is then rounded to the nearest integer. T is length of the time-series (in seconds), F_s is the sampling frequency, ω_b is the centre frequency of the bandpass filtered signal and k is an integer parameter that controls the length of the window. Using a value of $k = 10$ was found to produce the appropriate balance between over and under-smoothing the gradient function (see Figures 4.13 & 4.14).

Once the gradient function has been calculated it is used to determine the segments of the data with negative gradient. At this stage tests are implemented, such as checking that there exists at least one segment with negative gradient before the inversion is performed. Furthermore, a minimum segment length is imposed by specifying that each segment must contain at least 5 cycles of signal.

Considering all segments, the gradient is calculated for each, thus resulting in a set of

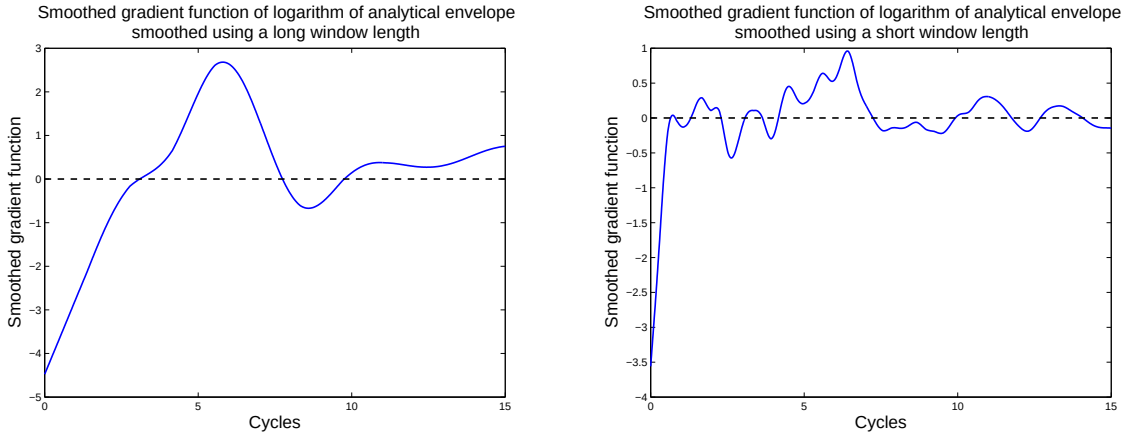

Figure 4.13: Dependence of the number of segments on the amount of smoothing of the gradient function. The left hand plot shows an over-smoothed function, with a long smoothing window ($k = 5$), resulting in a single segment. The right hand plot shows an under-smoothed function, using a short smoothing window ($k = 25$) resulting in a larger number of segments.

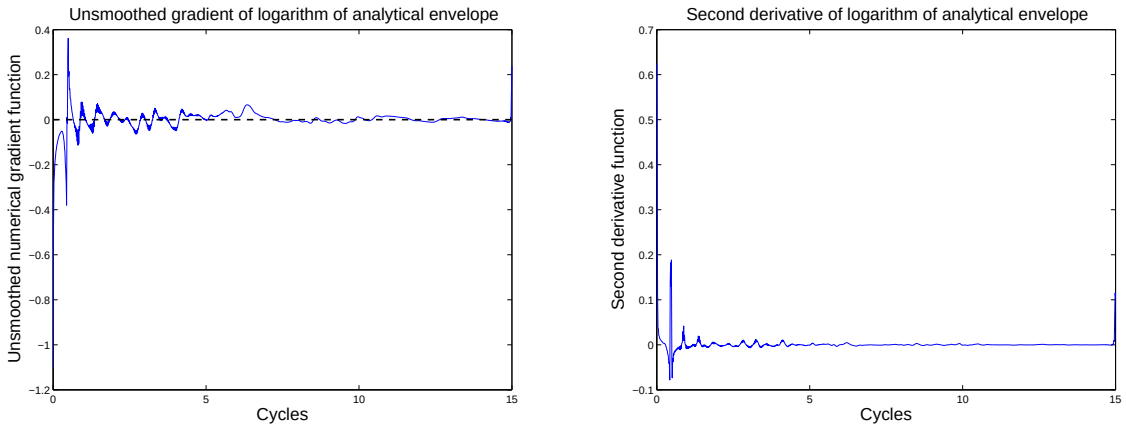

Figure 4.14: Unsmoothed gradient function and second derivative for the same example as Figures 4.12 & 4.13. Note the numerical wraparound effects at the beginning and end of the functions.

Q_{a} values, the number of which depends on the number of segments in the smoothed gradient function. From this set of values certain criteria can be used to choose the best value (e.g. lowest regression error), or combine all of them together in some way, using a weighted average. A weighted average was chosen, based on the square of the number of points in the segment, L_i^2, and also on the error in the regression ϵ_i (a proxy for the stability of the gradient). This choice of weighting ensures that the longest segments with the most stable gradient contribute the most to the average.

A problem to consider before calculating the weighted average is the choice of variable we should take the weighted average of. The measurement or result of the inversion is

actually the *gradient* or slope rather than the quality factor, Q_{a}, or attenuation Q_{a}^{-1}. This suggests we should take a weighted average of the gradients determined for each segment, and then use this weighted mean gradient to give the best overall estimate of the attenuation, Q_w^{-1}:

$$Q_w^{-1} = \frac{1 - e^{m_w}}{\pi} \tag{4.23}$$

for m_w the weighted average of the gradients calculated for each of the N segments, given by:

$$m_w = \frac{\sum_{i=1}^{N} m_i w_i}{\sum_{i=1}^{N} w_i} \tag{4.24}$$

where m_i is the gradient of the i^{th} segment and w_i is the set of weighting factors. The weighting factors chosen were $w_i = \epsilon_i L_i^2$, for regression error ϵ_i and segment length L_i.

Using the S-transform

A further development was to move away from using band-pass filters to isolate energy at a particular frequency. As discussed in Section 4.2 narrow filters in the frequency domain introduce "ringing" in the time domain which can affect the measurement of the amplitude decay. To estimate how the frequency content of a signal varies over time a time-frequency transform can be used. Taking a 'slice' at a given frequency provides information about how the amplitude or energy in the signal at that frequency varies over time, equivalent to looking at the analytical envelope of a narrow band-passed filtered signal. The S-transform (Stockwell et al., 1996) is an example of a time-frequency transform which, unlike the fixed-window short-time Fourier transform (STFT) or spectrogram, has a variable window size whose length is a function of the frequency being analysed (Reine, 2009). It uses shorter data segments as the frequency being analysed increases (Reine et al., 2009). Why use the S-transform in particular over other time-frequency transforms? Stockwell (2007) suggests that some of the unique advantages of the S-transform are that it absolutely references phase information and the time average of the S-transform is the same as the ordinary Fourier spectrum. Furthermore, it can provide simultaneous estimates of the local amplitude and phase spectra, unlike a wavelet transform approach, for example, which only gives information on the local amplitude or power spectrum. The S-transform can thus be considered a 'generalization of the Fourier transform to the case of nonstationary signals' (Stockwell, 2007), and for

a continuous signal, $x(t)$, it is defined as:

$$S(\tau, f) = \frac{|f|}{\sqrt{2\pi}} \int_{-\infty}^{\infty} x(t) e^{\frac{-(\tau-t)^2 f^2}{2}} e^{-i2\pi f t}\, dt \tag{4.25}$$

for time lag to the centre of the window, τ, and frequency, f. This can also be thought of as using a normalised Gaussian function of time and frequency

$$w_S(t, f) = \frac{|f|}{\sqrt{2\pi}} e^{-\frac{t^2 f^2}{2}} \tag{4.26}$$

as the windowing function and a set of sinusoidal basis functions of the form $e^{i2\pi f t}$.

The S-transform also has the advantage that it gives spectral estimates sampled at the discrete Fourier frequencies rather than arbitrary scale (Stockwell, 2007; Reine et al., 2009), making it a suitable choice for extracting the time decay of energy at a particular frequency from low-frequency events. This spectral method, of estimating the amplitude decay at a particular frequency with time, ensures that choosing the appropriate filter parameters and the effect that this will have on the measurement is no longer a concern. It is therefore a much more direct and natural way of analysing the energy at a certain frequency.

Another point to note is the increased phase shift that occurs with the steeper roll-off of narrow band-pass filters. Although we are only concerned with the relative amplitude decay and not the absolute time, shifting the energy to later times does reduce the maximum number of points that can be used in the linear regression, seen for example in the bottom two plots for a 2-pole Butterworth filter of 0.05Hz width in Figure 4.16. This leads to information being lost as the usable part of the coda becomes shorter. By contrast, using the S-transform to estimate the energy at a given frequency does not suffer from this effect, hence, this is another advantage of the method.

Although it can be computationally expensive to calculate the full S-transform for large datasets, the frequency range of interest is known beforehand and a modified version of the S-transform can therefore be used that truncates at a given frequency (T. Blanchard, pers. comm.). This can significantly reduce computation time as less effort is spent calculating redundant information in the spectrum. This, together with the fact that the length of most signals to be analysed is likely to be short (tens of seconds), means the computation time for the S-transform of each event is likely to be negligible.

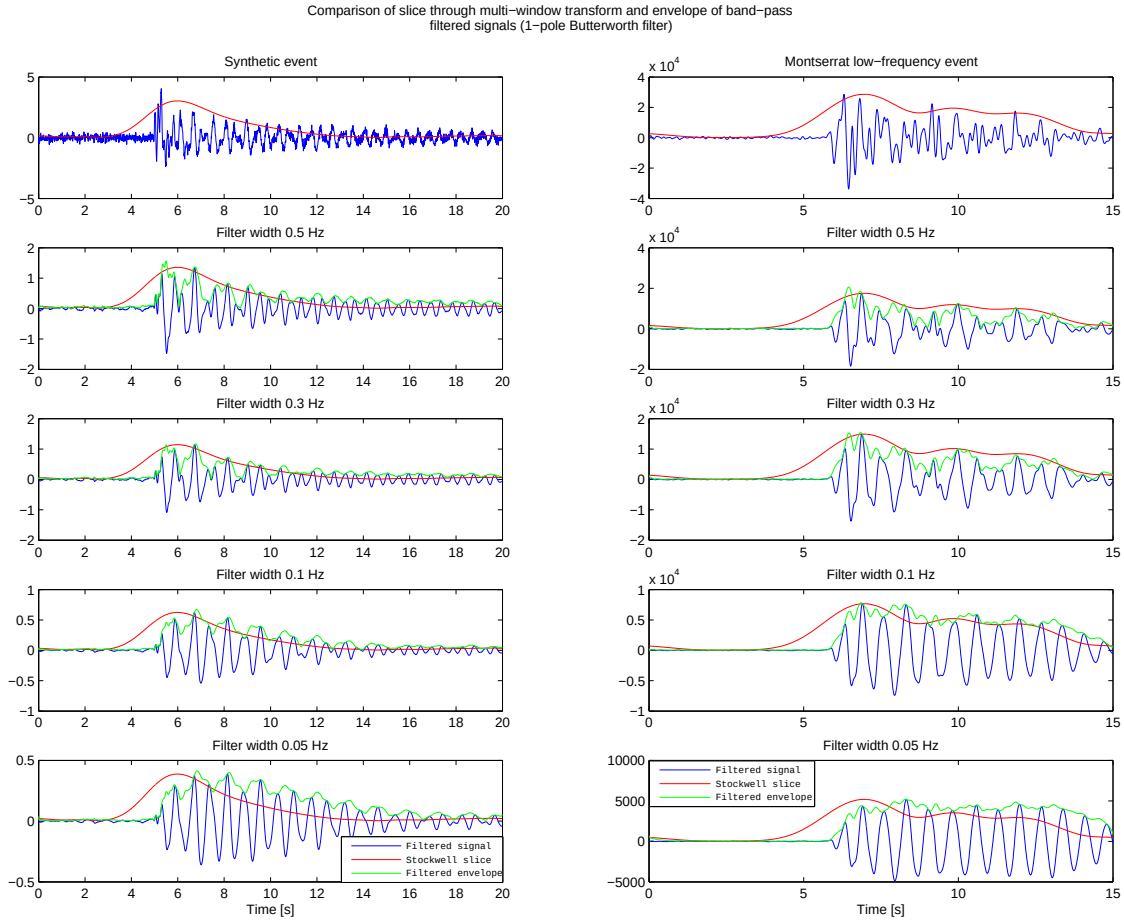

Figure 4.15: Comparison between a 'slice' through the S-transform at a given frequency and a series of analytical envelopes calculated for 1-pole Butterworth band-pass filters of increasingly narrow spectral bandwidths. The plots on the left show an example synthetic event composed of decaying sinusoids (see Section 4.3.2) and those on the right an example Montserrat low-frequency earthquake (vertical component). Both signals are filtered around the same dominant spectral peak at 1.39Hz.

4.3.2 Testing using synthetic signals

To test the robustness of these methods at measuring the apparent attenuation, several were tested on synthetic signals and the results compared. The synthetic signals were not produced by the finite-difference model but simply generated analytically by superimposing different damped sinusoids with known frequencies and damping factors. A variable percentage of Gaussian distributed white noise was also added to the synthetics in order to simulate the properties of real data better, and to test how well the methods cope with variable amounts of noise. This superposition of damped sinusoids can be described by:

$$s(t) = \sum_{j=1}^{N} A_j \sin(2\pi f_j t) \left(1 - \frac{\pi}{Q_j}\right)^{f_j t} + \tau_j + e \tag{4.27}$$

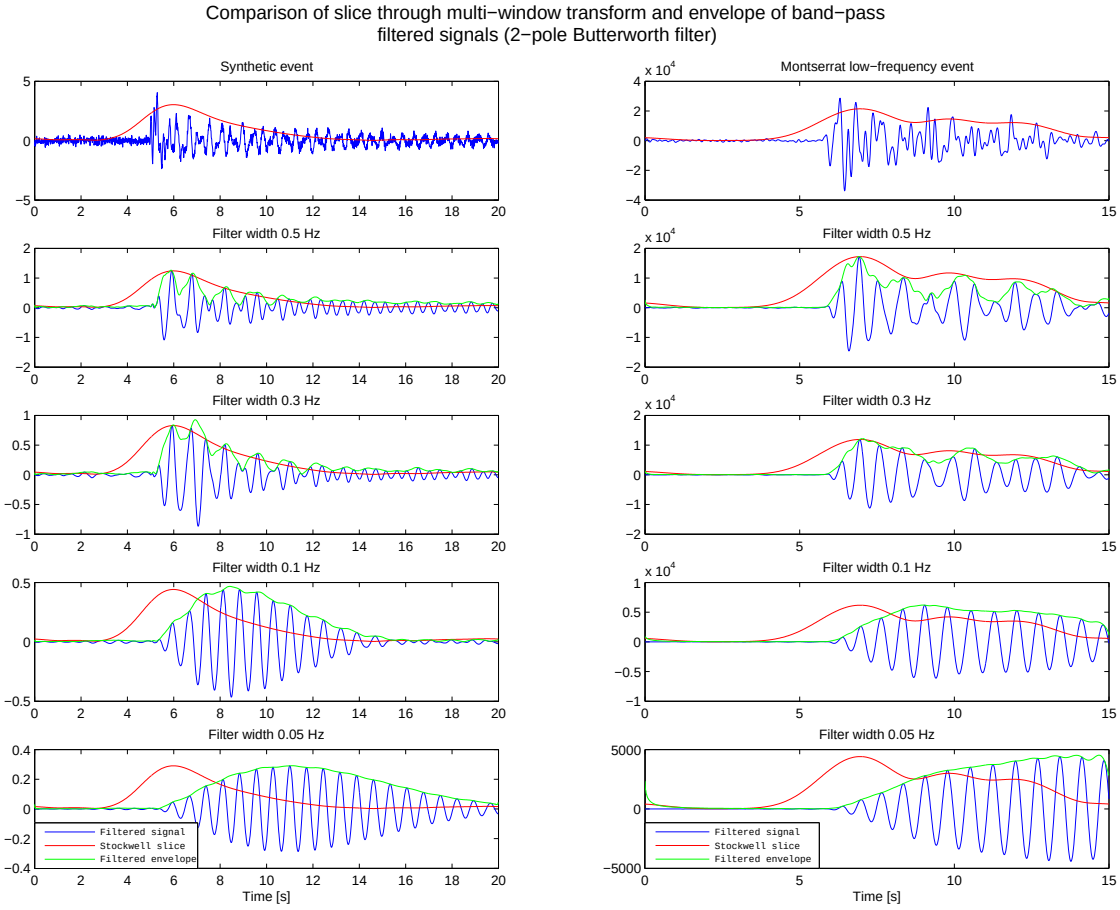

Figure 4.16: Comparison between energy isolated at a given frequency using the S-transform (in red) and a series of analytical envelopes calculated for 2-pole Butterworth band-pass filters of increasingly narrow spectral bandwidths (in green). The plots on the left show an example synthetic event composed of decaying sinusoids (plus some random noise) and those on the right an example Montserrat low-frequency earthquake (vertical component). Both signals are filtered around the same dominant spectral peak at 1.39Hz.

where $s(t)$ is the synthetic signal composed of N components. A value of $N = 3$ was chosen to match the three major spectral peaks identified from the spectra of low-frequency earthquakes at SHV. A_j is the amplitude of the j^{th} component, f_j the frequency, Q_j the quality factor, τ_j an optional time shift and e represents the added noise. An example of such a synthetic signal, showing how it is constructed as a linear combination of components, is depicted in Figure 4.17.

Whilst the use of Gaussian distributed white noise is adequate for a first order test of how the methods cope with noisy signals, it is perhaps not the most realistic simulation of background noise. Seismic background noise is not white and has a distinctive frequency distribution, with many contributing factors, although it is often dominated

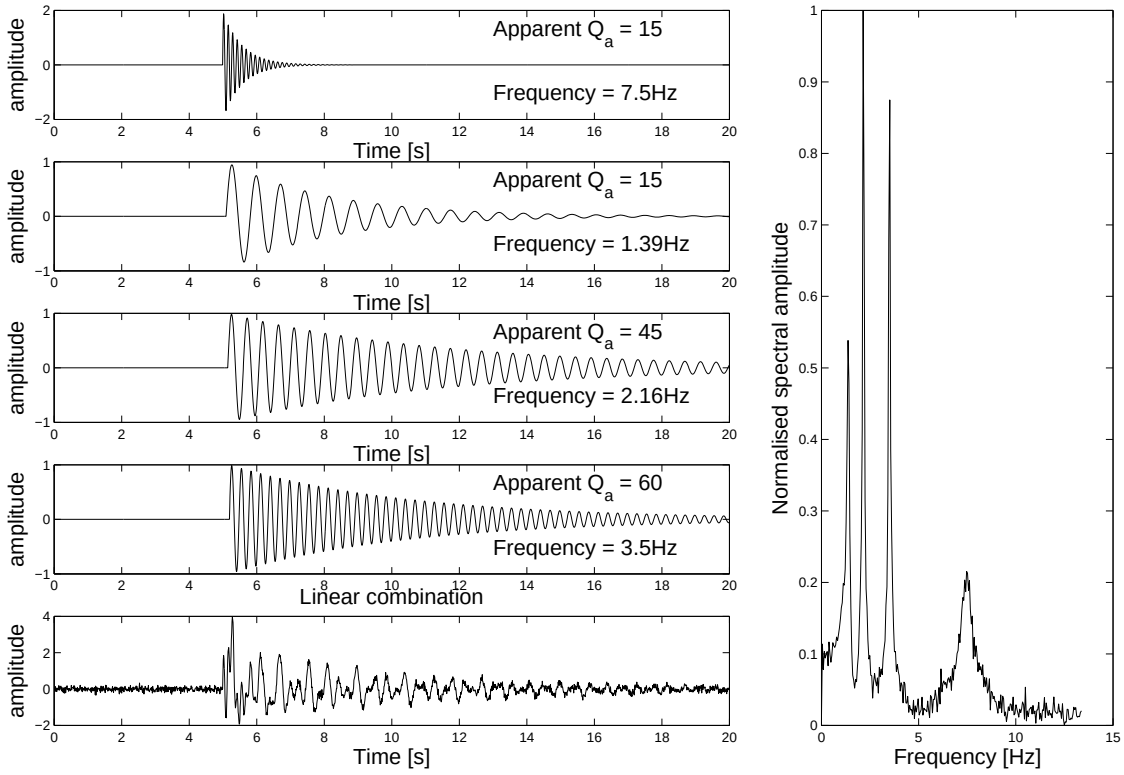

Figure 4.17: Example of a synthetic signal created by the superposition of damped sinusoids, showing the individual components and the resulting linear combination. 5% Gaussian distributed random white noise was added to the signal. The amplitude spectrum of the superposition, with peaks corresponding to the individual components, is shown in the right hand plot.

by *microseisms* with periods between 1 and 10 seconds (e.g. Stein & Wysession, 2003). This is a particularly relevant consideration at SHV where, due to its island nature, the oceanic microseism noise level is higher, and more variable, than elsewhere. Hence, a further development of the testing and comparison process in this section would be to compare the different methods using noise with a suitably realistic frequency distribution based on analysis of data from SHV.

Results: recovery of attenuation from synthetic signals

Several different methods were tested on sets of 100 synthetic events, and the results compared by calculating the residuals between the input and retrieved values of both Q_a and Q_a^{-1}. Each of the 100 synthetic signals contains components with the same frequencies, 1.39Hz, 2.16Hz and 3.5 Hz, which match the dominant spectral peaks from the real data (see Chapter 5). However, each component of each signal possessed a different damping factor. Differently weighted distributions of Q_a values were used to

examine whether the largest errors occur systematically at high or low attenuation levels for the different methods.

The different distributions tested, for $5 \leq Q_a \leq 100$, were: (1) a linear distribution (2) an exponentially increasing distribution (more low Q_a values), (3) a logarithmically increasing distribution (more high Q_a values), (4) a random distribution of values, and (5) a constant level of attenuation for all 100 events (with variation due to noise).

The residuals (the summed RMS misfit for all 100 values) between the input and recovered values were examined, and the errors calculated in terms of both the quality factor, Q_a, and the attenuation, Q_a^{-1}.

Comparison between the different methods

The tests were performed on the sets of synthetic signals using the following five methods to measure the apparent attenuation:

(i) Fixed length regression window

(ii) Fixed length regression window, with the data weighted using the 2^{nd} derivative (parameter, $\ell = 1$).

(iii) Segments of negative gradient, with the segment with the lowest regression error chosen.

(iv) Segments of negative gradient, calculating a weighted mean of the Q_a or Q_a^{-1} values.

(v) Segments of negative gradient, using a weighted mean of the gradients to calculate the attenuation.

The results of these tests are shown in Figures 4.18- 4.22 with the residuals listed in Table 4.1. The results show that, in general, the method of using the weighted mean of the gradients recovers the attenuation from the synthetic signals best. The limitations of the fixed regression window method are also highlighted, particularly in the linear and exponential Q_a distributions in Figures 4.18 and 4.19, which show that this method severely underestimates high attenuation (low Q_a) values. The results also demonstrate that the weighting of the inversion using the second derivative does not improve the

estimates, and should therefore be considered an unnecessary step in the measurement process.

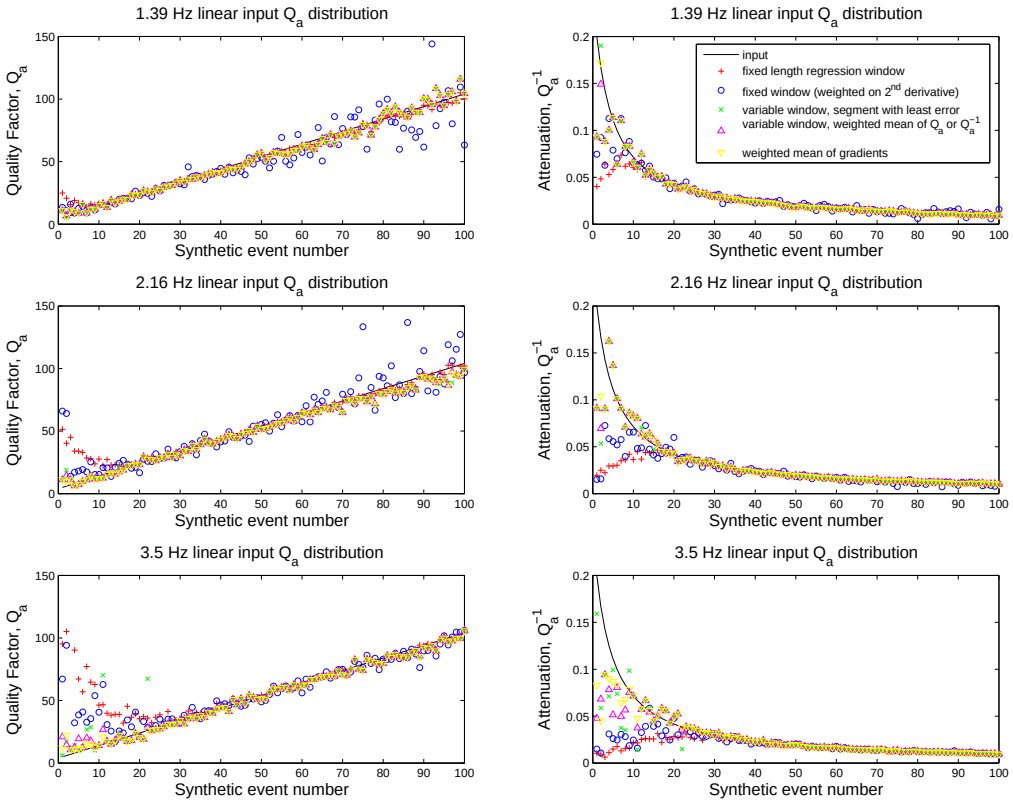

Figure 4.18: Recovery of attenuation from synthetic signals with a linear Q_a distribution. The plots show the Q_a and Q_a^{-1} values measured using each of the five methods, compared to the input distribution.

	RMS residual to input apparent Q value distribution															
	Frequency: 1.39Hz						**Frequency: 2.16Hz**						**Frequency: 3.50Hz**			
Method	**(i)**	**(ii)**	**(iii)**	**(iv)**	**(v)**		**(i)**	**(ii)**	**(iii)**	**(iv)**	**(v)**		**(i)**	**(ii)**	**(iii)**	**(iv)**	**(v)**
Lin.	3.66	15.70	**3.65**	**3.65**	**3.65**		9.03	13.24	4.20	3.95	**3.91**		26.20	14.82	7.85	3.75	**3.31**
Exp.	6.80	10.75	**3.29**	3.62	3.30		20.24	13.10	11.70	8.78	**5.64**		46.74	20.52	12.24	8.38	**4.61**
Log.	**3.75**	45.81	5.39	5.39	5.39		**5.95**	9.06	6.50	6.39	6.50		8.62	26.14	**2.96**	3.00	3.01
Rdm.	**2.77**	14.47	3.26	3.26	3.26		5.91	9.71	29.93	10.62	**3.76**		19.24	7.96	13.70	6.31	**2.96**
Cst.	**3.07**	25.94	4.97	4.97	4.97		**2.26**	302.84	6.18	5.66	5.71		**2.59**	6.06	2.93	3.01	3.05
	RMS residual to input apparent attenuation distribution															
	Frequency: 1.39Hz						**Frequency: 2.16Hz**						**Frequency: 3.50Hz**			
Method	**(i)**	**(ii)**	**(iii)**	**(iv)**	**(v)**		**(i)**	**(ii)**	**(iii)**	**(iv)**	**(v)**		**(i)**	**(ii)**	**(iii)**	**(iv)**	**(v)**
Lin.	0.0237	0.0177	0.0133	0.0132	**0.0131**		0.0312	0.0277	0.0174	0.0164	**0.0146**		0.0366	0.0313	**0.0171**	0.0213	0.0187
Exp.	0.0494	0.0389	**0.0267**	0.0297	0.0271		0.0635	0.0542	0.0352	0.0362	**0.0301**		0.0716	0.0591	0.0421	0.0405	**0.0363**
Log.	0.0161	0.0101	**0.0020**	**0.0020**	**0.0020**		0.0183	0.0147	**0.0056**	**0.0056**	**0.0056**		0.0190	0.0197	**0.0046**	**0.0045**	**0.0045**
Rdm.	0.0129	0.0131	**0.0055**	**0.0055**	**0.0055**		0.0193	0.0159	0.0114	0.0109	**0.0053**		0.0257	0.0205	0.0136	0.0112	**0.0069**
Cst.	**0.0004**	0.0025	0.0007	0.0007	0.0007		**0.0003**	0.0021	0.0010	0.0009	0.0009		**0.0004**	0.0010	**0.0004**	**0.0004**	**0.0004**
	RMS residual to input value for the gradient															
	Frequency: 1.39Hz						**Frequency: 2.16Hz**						**Frequency: 3.50Hz**			
Method	**(i)**	**(ii)**	**(iii)**	**(iv)**	**(v)**		**(i)**	**(ii)**	**(iii)**	**(iv)**	**(v)**		**(i)**	**(ii)**	**(iii)**	**(iv)**	**(v)**
Lin.	0.1182	0.0942	0.0755	0.0744	**0.0736**		0.1435	0.1317	0.0939	0.0903	**0.0831**		0.1600	0.1413	**0.0809**	0.1083	0.0977
Exp.	0.2412	0.1955	**0.1437**	0.1566	0.1454		0.2898	0.2571	0.1771	0.1827	**0.1568**		0.3148	0.2680	0.2071	0.2042	**0.1884**
Log.	0.0858	0.0605	**0.0137**	**0.0137**	**0.0137**		0.0936	0.0808	**0.0386**	**0.0386**	**0.0386**		0.0957	0.0980	0.0319	**0.0317**	**0.0317**
Rdm.	0.0575	0.0570	**0.0255**	**0.0255**	**0.0255**		0.0805	0.0684	0.0449	0.0431	**0.0233**		0.1013	0.0845	0.0572	0.0469	**0.0338**
Cst.	0.0014	0.0082	**0.0022**	**0.0022**	**0.0022**		**0.0010**	0.0067	0.0032	0.0028	0.0028		**0.0012**	0.0033	0.0014	0.0014	0.0014

Table 4.1: Comparison of the RMS residuals for the different methods. This table shows the residuals calculated in terms of the error in Q_a, Q_a^{-1} and the gradient for each of the five methods and Q_a distributions. The lowest residuals for each row are highlighted in bold.

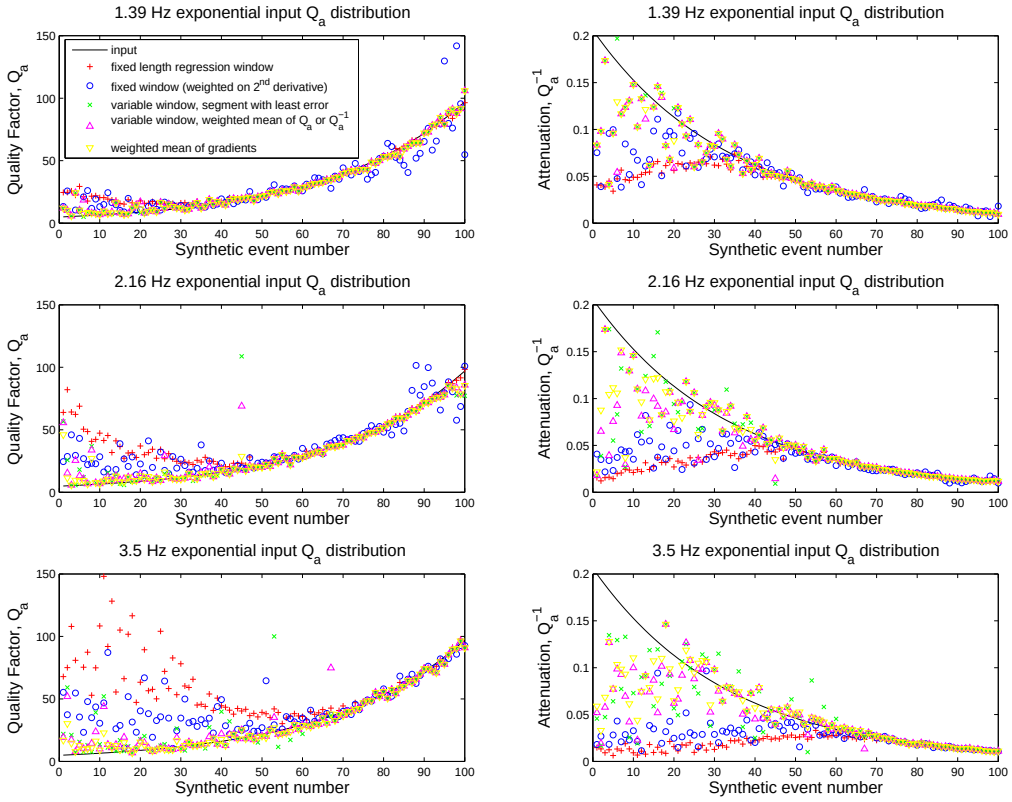

Figure 4.19: Recovery of attenuation from synthetic signals with a logarithmic Q_a distribution.

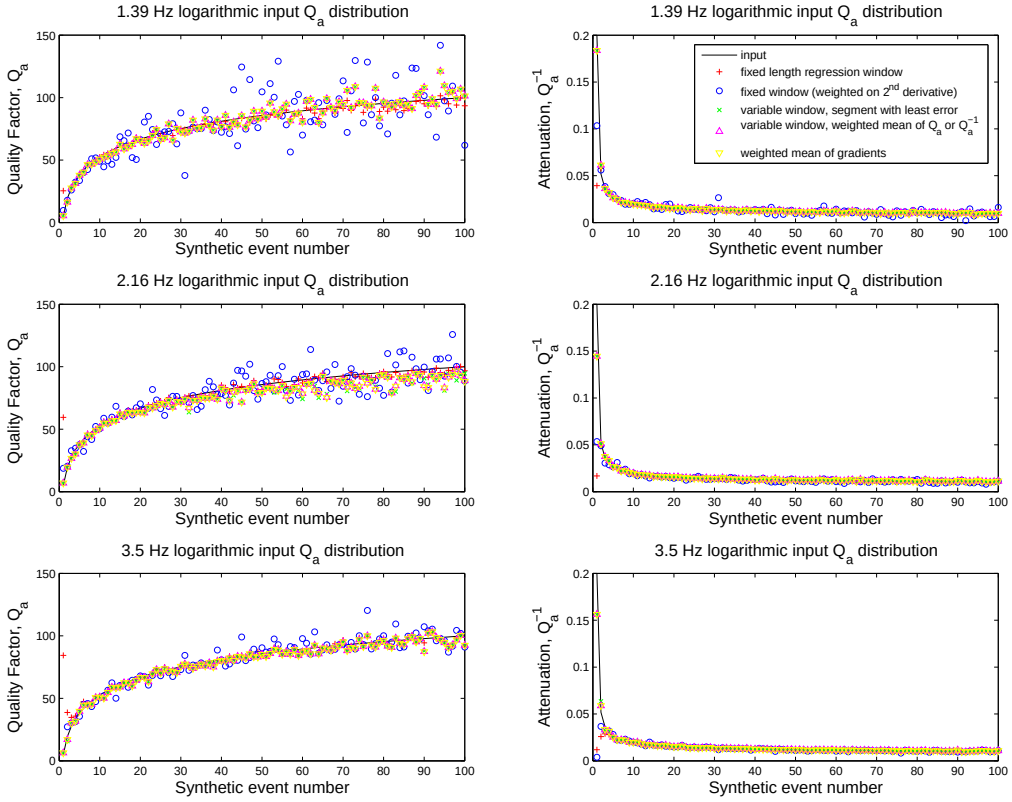

Figure 4.20: Recovery of attenuation from synthetic signals with an exponential Q_a distribution.

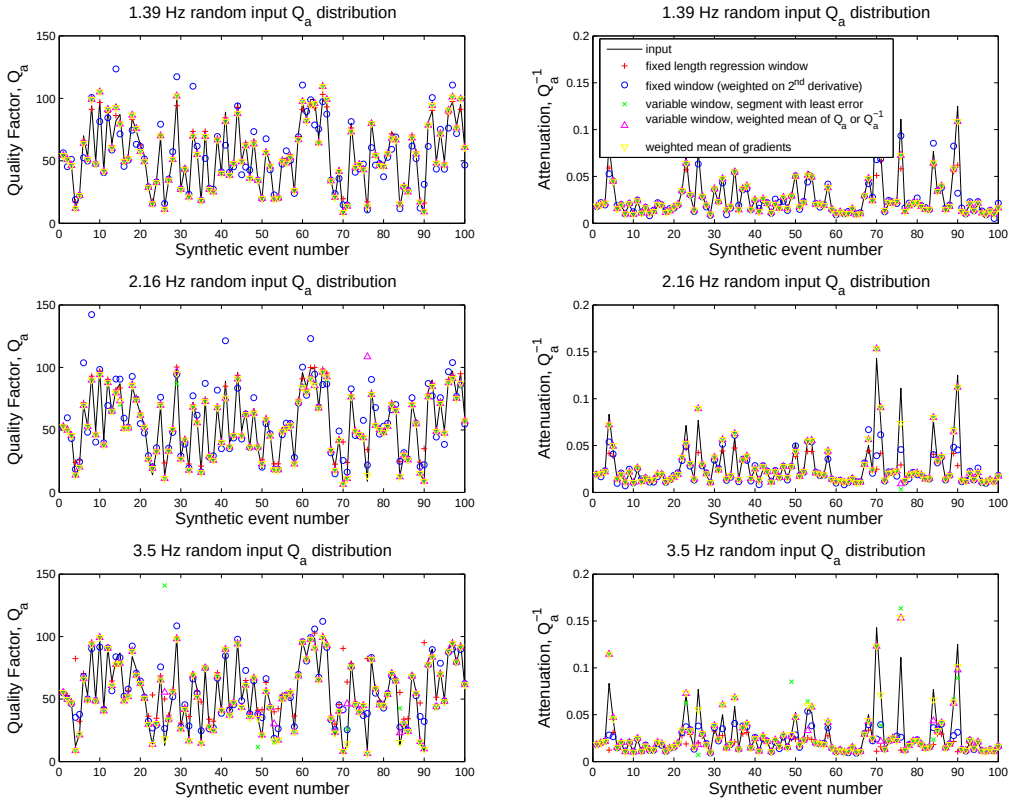

Figure 4.21: Recovery of attenuation from synthetic signals with a random Q_a distribution.

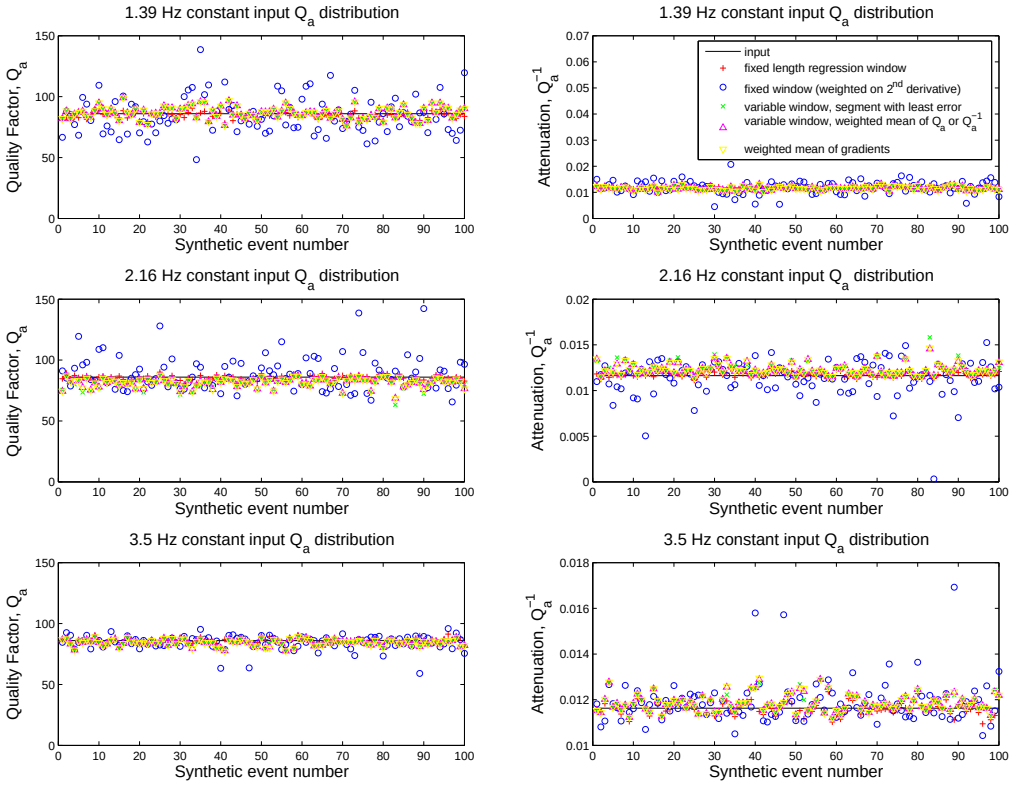

Figure 4.22: Recovery of attenuation from synthetic signals with a constant Q_a distribution.

Comparison between band-pass filters and the S-transform

The results in Figures 4.23- 4.27 and Table 4.3 show a comparison between using band-pass filtering and the S-transform method to isolate specific frequencies. The same five distributions of Q_{a} values as outlined previously were used in the comparison, to assess the systematic differences between the two approaches. The method used to determine the apparent attenuation was the same for both cases, method(v), with only the process of isolating the frequencies varied.

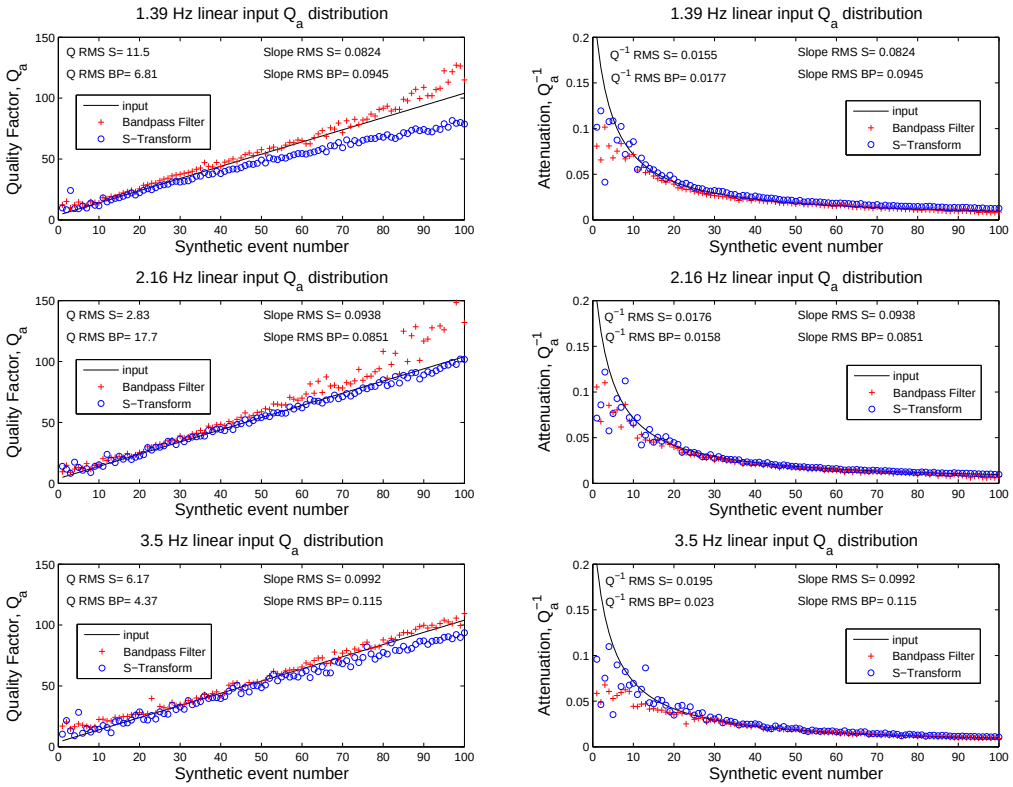

Figure 4.23: Comparison between band-pass filtering and the S-transform for a linear Q_{a} distribution. Shown in the plots are the RMS values in terms of Q_{a}, Q_{a}^{-1} and slope for both methods.

f, **frequency [Hz]**	ω_b, **filter half-width [Hz]**
1.39	0.1
2.16	0.125
3.5	0.15

Table 4.2: Filter parameters used in the comparison between band-pass filtering and the S-transform. Single pole Butterworth filters, with the half-widths shown in the table, were used in the comparison.

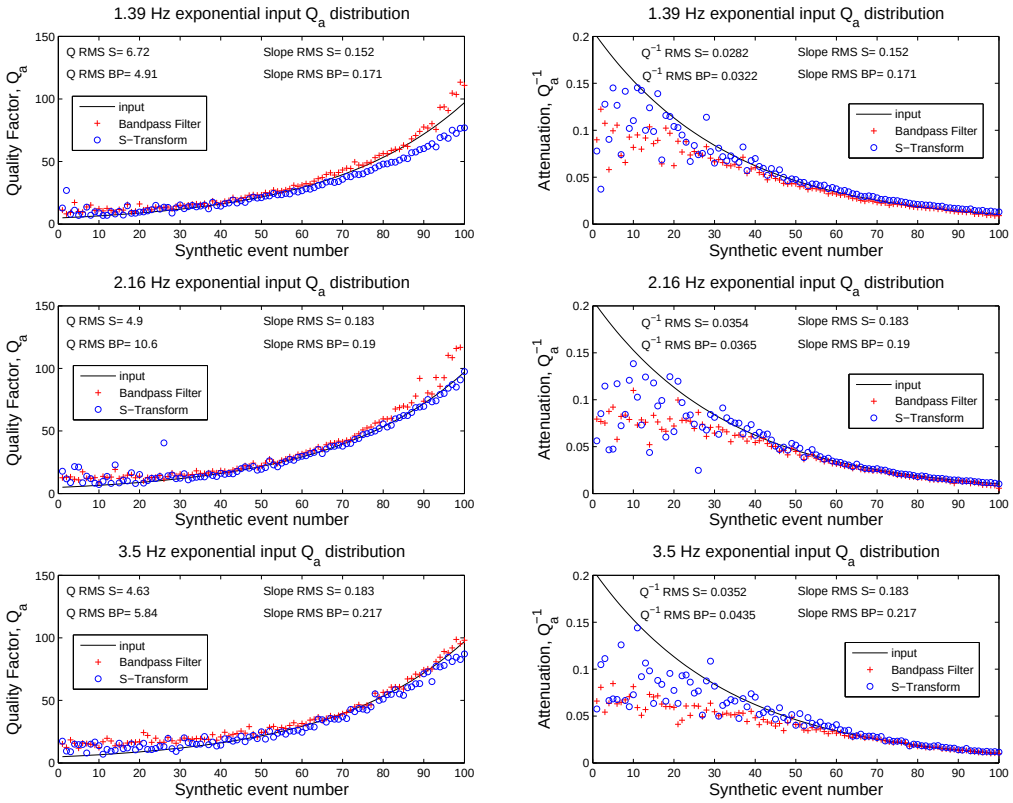

Figure 4.24: Comparison between band-pass filtering and the S-transform for an exponential Q_a distribution.

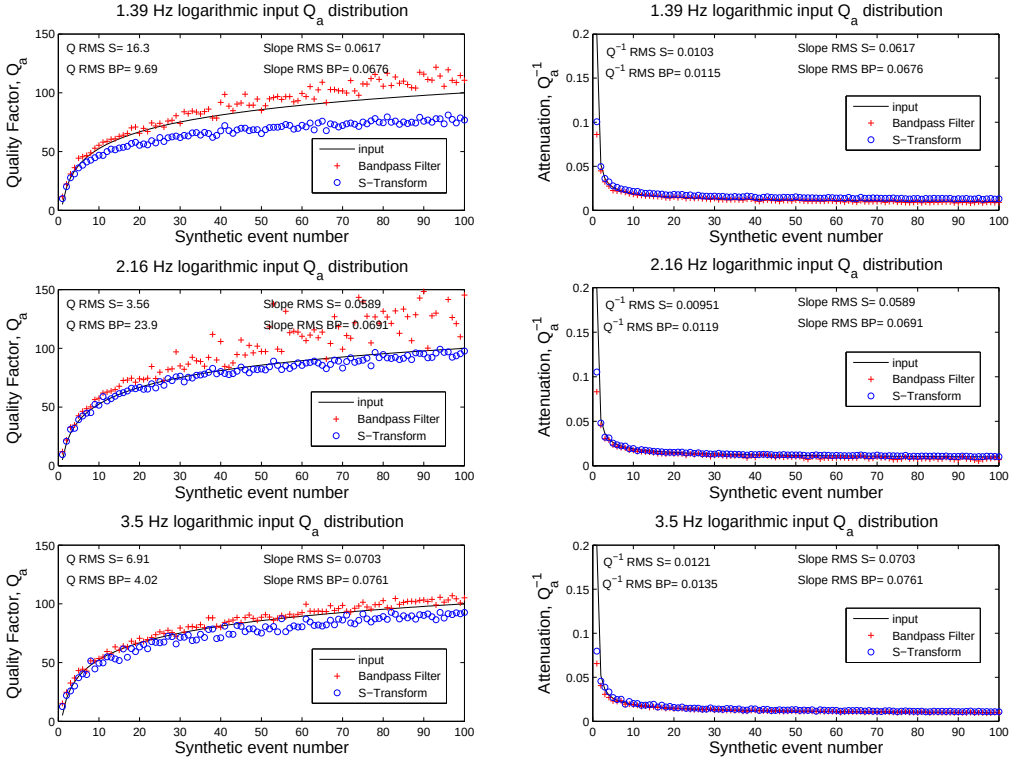

Figure 4.25: Comparison between band-pass filtering and the S-transform for a logarithmic Q_a distribution.

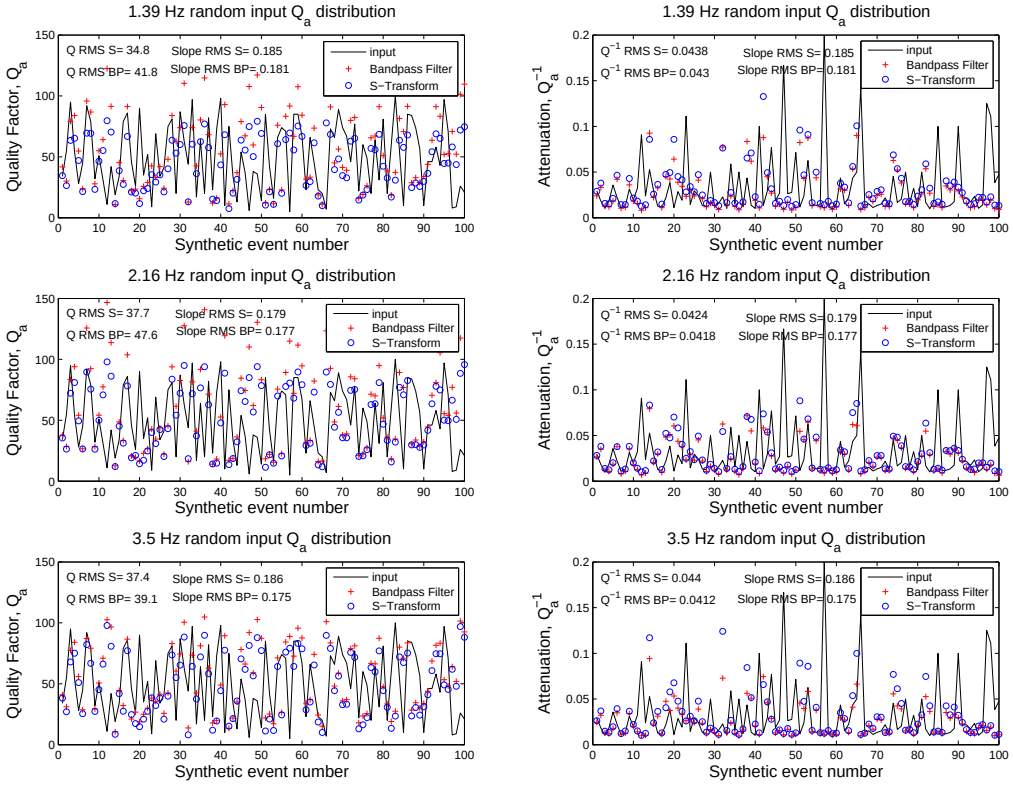

Figure 4.26: Comparison between band-pass filtering and the S-transform for a random Q_a distribution.

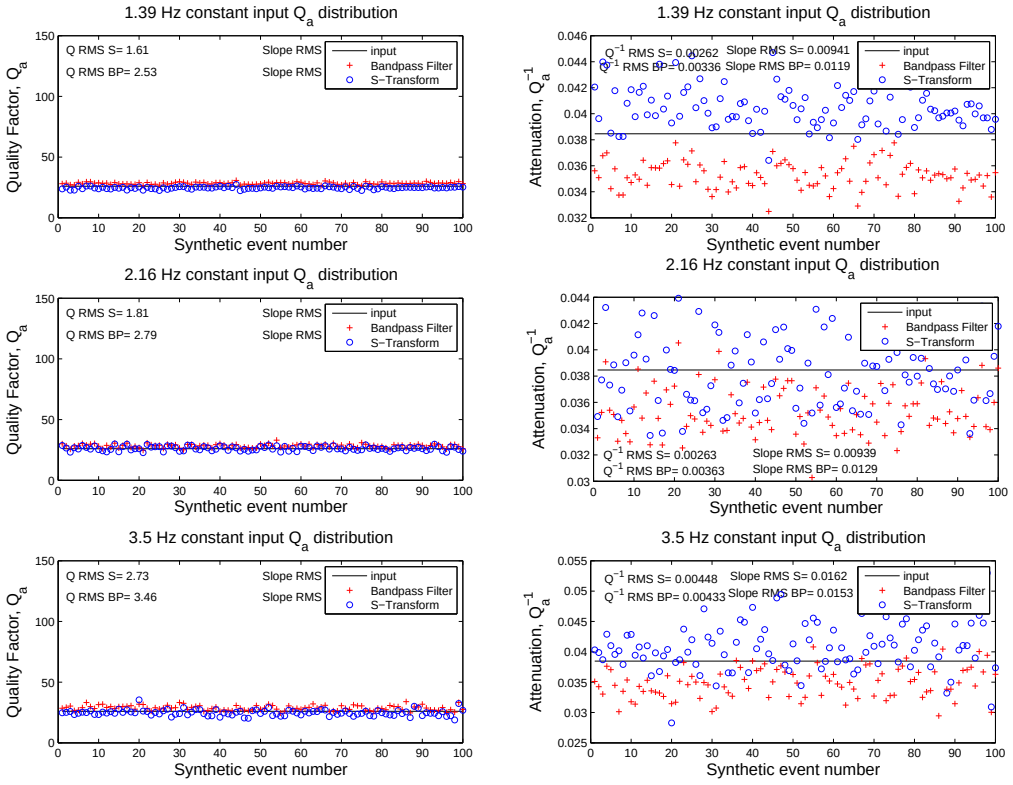

Figure 4.27: Comparison between band-pass filtering and the S-transform for a constant Q_a distribution.

	RMS residual to input apparent Q value distribution					
	Frequency: 1.39Hz		**Frequency: 2.16Hz**		**Frequency: 3.50Hz**	
	Band-pass	**S-Transform**	**Band-pass**	**S-Transform**	**Band-pass**	**S-Transform**
	filter		**filter**		**filter**	
Lin.	6.81	11.52	17.67	2.83	4.37	6.17
Exp.	4.91	6.72	10.60	4.90	5.84	4.63
Log.	9.69	16.28	23.88	3.56	4.02	6.91
Rdm.	46.46	38.65	52.15	42.44	43.75	41.64
Cst.	4.63	24.00	12.16	10.77	6.08	14.90
	RMS residual to input apparent attenuation value distribution					
	Frequency: 1.39Hz		**Frequency: 2.16Hz**		**Frequency: 3.50Hz**	
	Band-pass	**S-Transform**	**Band-pass**	**S-Transform**	**Band-pass**	**S-Transform**
	filter		**filter**		**filter**	
Lin.	0.0177	0.0155	0.0158	0.0176	0.0230	0.0195
Exp.	0.0322	0.0282	0.0365	0.0354	0.0435	0.0352
Log.	0.0115	0.0103	0.0119	0.0095	0.0135	0.0121
Rdm.	0.0500	0.0501	0.0484	0.0484	0.0481	0.0511
Cst.	0.0006	0.0039	0.0012	0.0015	0.0008	0.0021
	RMS residual to input value for the gradient					
	Frequency: 1.39Hz		**Frequency: 2.16Hz**		**Frequency: 3.50Hz**	
	Band-pass	**S-Transform**	**Band-pass**	**S-Transform**	**Band-pass**	**S-Transform**
	filter		**filter**		**filter**	
Lin.	0.0945	0.0824	0.0851	0.0938	0.1147	0.0992
Exp.	0.1708	0.1520	0.1903	0.1826	0.2168	0.1830
Log.	0.0676	0.0617	0.0691	0.0589	0.0761	0.0703
Rdm.	0.2119	0.2133	0.2059	0.2059	0.2054	0.2167
Cst.	0.0019	0.0126	0.0039	0.0047	0.0026	0.0069

Table 4.3: Comparison of the RMS residuals for the band-pass filtering and S-transform methods. This table lists the residuals in terms of error in Q_a, Q_a^{-1} and the gradient for each of the five Q_a distributions.

4.4 Discussion and Conclusions

This chapter detailed the development of several automated methods to measure the temporal amplitude decay or apparent attenuation of volcanic seismic signals. Numerical tests were carried out on synthetic signals, composed of superimposed damped sinusoids, to assess which of the methods performed best at recovering the input attenuation values.

By whichever way the error is defined, i.e. the RMS misfit to the set of Q_a, Q_a^{-1} or gradient values, the method using the weighted mean of the *gradients* of the segments gives the best results in terms of recovering the known damping factors from the synthetically generated signals. This method also copes significantly better with added random 'noise', suggesting it would be applicable to the analysis of low-frequency volcanic earthquakes. This can be seen by examining Figures 4.18 to 4.22 and the tabulated results in Table 4.1. As Figures 4.18 to 4.22 show, it depends on whether the results are plotted in terms of Q_a or Q_a^{-1} as to whether the residuals appear smaller at high or low attenuation, but the weighted mean of the *gradients* methods performs significantly better than other methods at both high and low values.

As an additional test averaging over 20 sets of 100 events was carried out, using the five Q_a distributions at three different frequencies, hence, $20 \times 100 \times 5 \times 3 = 30,000$ measurements of Q_a were performed. The results are displayed in Table 4.4. The weighted average of the gradients method, method (v), gives the lowest value for all ways of defining the error.

RMS residual to input apparent Q value distribution					
Method	**(i)**	**(ii)**	**(iii)**	**(iv)**	**(v)**
	23.39	42.83	16.87	23.44	9.51
RMS residual to input apparent attenuation distribution					
Method	**(i)**	**(ii)**	**(iii)**	**(iv)**	**(v)**
	0.0345	0.0300	0.0178	0.0174	0.0158
RMS residual to input value for the gradient					
Method	**(i)**	**(ii)**	**(iii)**	**(iv)**	**(v)**
	0.1573	0.1403	0.0889	0.0891	0.0830

Table 4.4: Comparison of the RMS residuals for the different methods. This table shows the RMS of the error in Q_a, Q_a^{-1} and the gradient for each of the five methods averaged over all Q_a distributions and frequencies. The weighted average of the gradients method, method (v), gives the lowest value for the residual, for all ways of defining the error.

Furthermore, it was demonstrated that using the S-transform rather than band-pass filters to isolate energy at a particular frequency is more reliable, easier to implement, and in this case, not much more computationally expensive than filtering. It also has the advantage of eliminating the potentially contaminatory effects of filtering, or the need to choose filter parameters, such as the order or half-width. Hence, this method of isolating the energy at discrete frequencies should be used in future studies.

In summary, the results of performing the tests on the synthetic signals demonstrate that a robust and automated method, combining the use of the S-transform and a weighted mean of coda segments with negative gradient, has been developed that is not too computationally expensive. In Chapter 5 this method is applied to real low-frequency earthquake datasets from SHV, Montserrat, as a viable method of measuring the apparent attenuation.

Chapter 5

Attenuation of low-frequency earthquakes at Soufrière Hills Volcano

Seismic attenuation can be related to the material properties of the medium through which a seismic wave propagates. This makes it a desirable attribute to measure, particularly in volcanic environments where understanding the properties of fluids within the volcanic system is important in terms of forecasting future behaviour. Low-frequency earthquakes are believed to originate from resonance of seismic energy within a fluid-filled body, and therefore present a unique opportunity to explore the internal workings of shallow volcanic plumbing systems.

As discussed in Section 1.6.3, measurements of the attenuation of low-frequency earthquakes have been made at various volcanoes (e.g. Mount Spurr volcano in Alaska (De Angelis & McNutt, 2005), Cotopaxi (Molina et al., 2004) and Tungurahua volcanoes (Molina et al., 2008) in Ecuador and Kusatsu-Shirane volcano, Japan (Nakano & Kumagai, 2005a)), with varying success. Despite extensive monitoring and a breadth of research on the current eruption of Soufrière Hills Volcano, Montserrat, attenuation has not been considered yet at this volcano.

This chapter presents analysis of the attenuation of low frequency earthquakes at Soufrière Hills Volcano, Montserrat. The motivation for the particular dataset used is first discussed in Section 5.1, before the results are presented in Section 5.2. Finally, the implications of the analysis in terms of magma properties and the wider context of the current eruption are then discussed in Section 5.3.

5.1 Choice of dataset

5.1.1 23rd to 28th June 1997

Precursory activity to the 25th June dome collapse event

Growth of the lava dome at SHV began in November 1995, initially with low extrusion rates of 0.1-0.5m^3s^{-1} (Watts et al., 2002). During the early part of 1997 the dome continued to grow, accelerating during May as a change in the direction of dome growth towards the north and northeastern face (Young et al., 1998) marked the onset of a period of rapid growth, with high extrusion rates of more than 5m^3s^{-1} (Watts et al., 2002). This acceleration in dome growth was accompanied by swarms of low-frequency seismicity as well as cyclic deformation of the edifice (Young et al., 1998). This cyclicity in seismicity and deformation waned from mid-May before picking up again from 22nd June and continuing for several days. At around 12:45pm local time on 25th June a significant dome collapse occurred, with *c.* 5×10^6 m^3 of material removed from the edifice (Young et al., 1998; Robertson et al., 2000). This event produced voluminous pyroclastic flows and associated surges which caused widespread devastation and lead to the only known fatalities of the eruption (Robertson et al., 2000). Despite the removal of this large mass of material during the collapse event, the cyclic activity continued during July.

The analysis in this chapter focuses on the seismic activity during the period between 23rd and 28th June, immediately preceding and following the 25th June collapse.

Seismicity and deformation cyclicity

This particular period of the current eruption (23rd to 28th June 1997) has been extensively studied previously, and this provides part of the motivation for the choice of this period for attenuation analysis. A series of seven swarms of hybrid earthquakes, each containing hundreds of events, occurred during the three days directly preceding the dome collapse event on 25th June, with a further 10 swarms recorded in the four days immediately following (Miller et al., 1998; Green, 2005; Green & Neuberg, 2006). These earthquake swarms, shown in Figures 5.2(b) and 5.4, were accompanied by remarkable cyclic deformation signals, measured close to the active dome by a tiltmeter at Chances Peak (Figure 5.1). The tilt data showed cycles with a period of 8-12 hours (Voight et al.,

1998), and correlate well with the cyclic swarms of seismicity (Figure 5.2(b)). Green & Neuberg (2006) analysed the low-frequency seismicity during this period and classified the events into several 'families' based on waveform similarity using cross-correlation techniques. The onset and cessation of specific waveform families was shown to coincide with the inflexion points of the tilt cycles, with the families of events evolving throughout the swarm (as the tilt increases) before ceasing to occur as the derivative of the tilt reaches a minimum (Figure 5.2(a)). If the derivative of the tilt is taken as a proxy for the rate of pressurisation in the volcano, Green & Neuberg (2006) concluded that low-frequency events are in some respect, either as a consequence or as a trigger, directly related to depressurisation or relaxation within the edifice or conduit system.

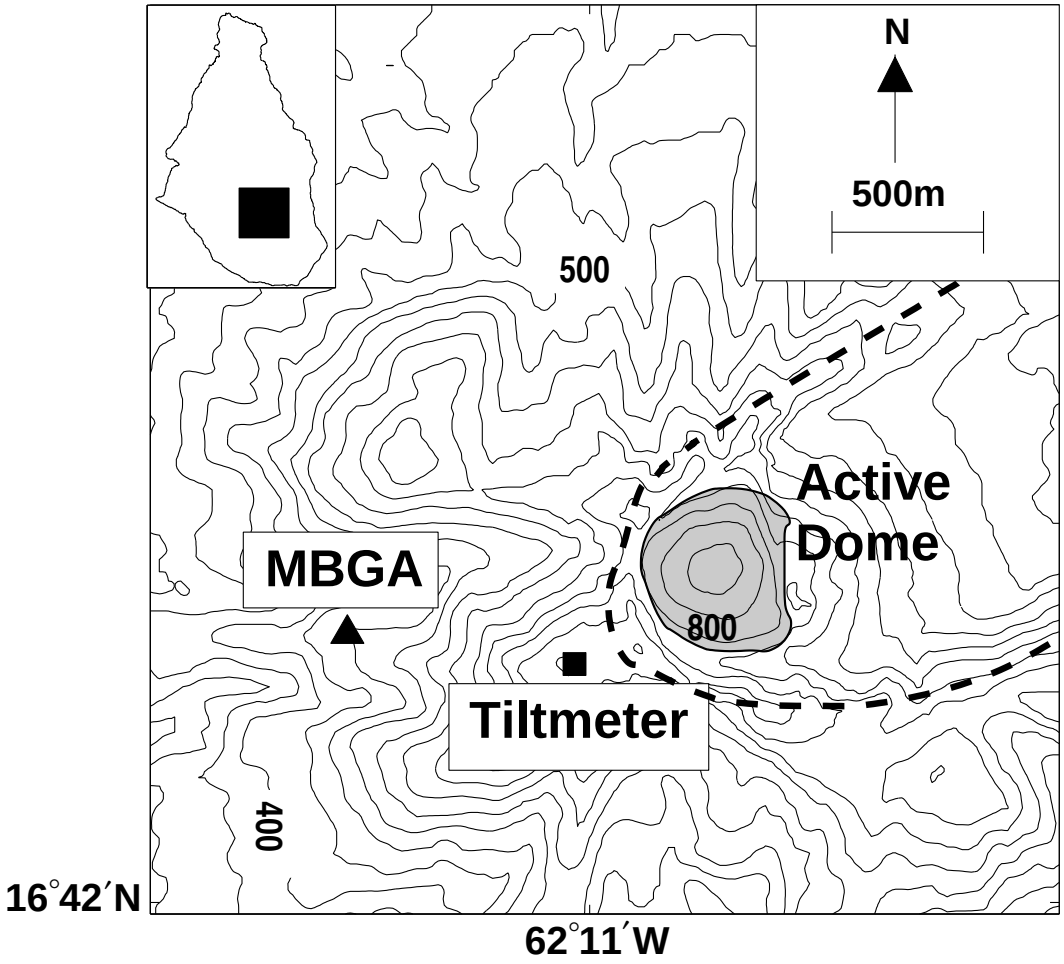

Figure 5.1: Map of the summit region of Soufrière Hills Volcano during 1997, showing the locations of the 3-component broadband seismometer at station MBGA (black triangle) and the tiltmeter installed at Chances Peak (black square). The contours are marked at 50m vertical intervals. The black dashed line indicates the edge of an old collapse scar, called English's Crater and the inset shows the position of the volcano and active dome relative to the island of Montserrat.

Amplitude and event rate variation

Systematic temporal changes in the amplitudes and event rate during this period preceding the collapse event were noted by Green (2005), and the dynamics of the earthquake swarms were further explored by Hammer & Neuberg (2009). A pattern of acceleration then deceleration can be seen *within* a single swarm, but across the seven swarms in the three day period preceding the dome collapse there is also an overall acceleration in the event rate, as shown in Figure 5.3. These observations were interpreted by Hammer & Neuberg (2009) as fluctuations in the ascent velocity of the magma through the conduit at depth. Hammer & Neuberg (2009) suggest the acceleration of the flow rate is due to progressive weakening and development of shear zones at the conduit walls, leading to a lowering of the bulk viscosity. Would this weakening of such shear zones, through repeated and accelerating failure, lead to changes in magma viscosity which could be measurable via the attenuation?

These studies suggest that this is an interesting period for analysis, with the dataset containing a lot of information about the processes linking seismicity and magma ascent rate during periods of rapid extrusion and dome growth. This motivates further study, to consider if similar temporal changes in the attenuation behaviour of the low-frequency events can be detected during this period, and makes the dataset a good choice for preliminary analysis of the attenuation of low-frequency events at SHV.

Waveform classification and availability of the data

The same classification scheme and nomenclature as that of Green (2005) and Green & Neuberg (2006), which classified the events into families based on waveform similarity, will be used throughout this chapter. The event onset times were picked from continuous waveform data using cross-correlation methods as this approach has a much better detection threshold than the MVO automated triggering routines, especially if the event rate is high.

The data for all events were obtained from the vertical component of station MBGA, recorded at MVO using a 3-component broadband seismometer with a sampling rate of 75Hz (see Appendix A). At the time, this station was the closest to the active dome and hence possessed the best signal-to-noise ratio. Its location relative to the volcano is shown in Figure 5.1.

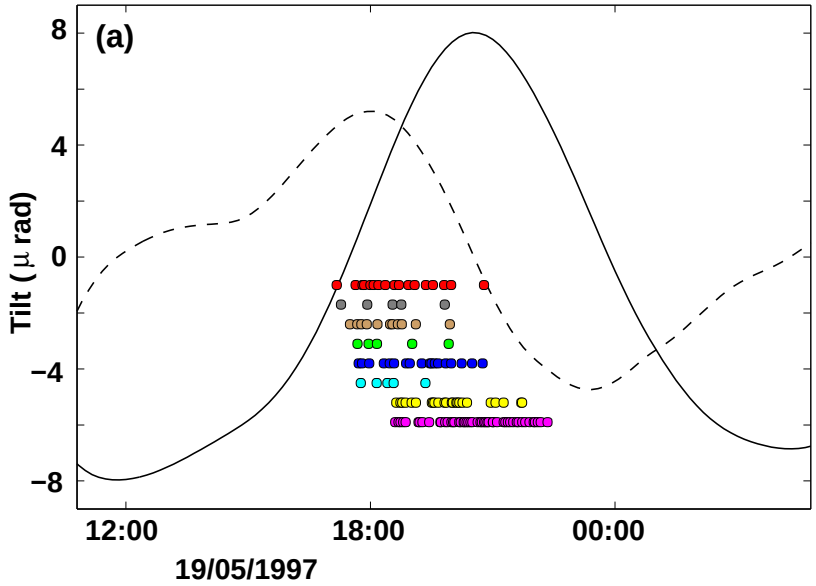

(a) Single tilt cycle and its derivative, together with waveform families.

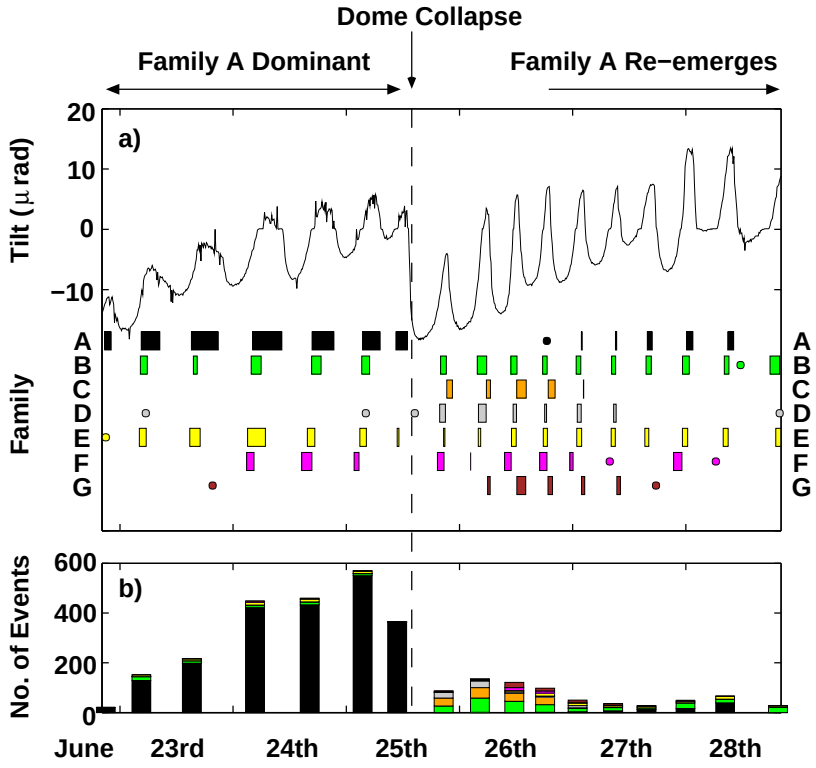

(b) Tilt cycles and seismicity over several days.

Figure 5.2: (a) Families of low-frequency earthquakes at SHV from 19th May 1997, shown together with tilt (solid line) and its time derivative (dashed line). Both tilt signals have been low pass filtered. Taken from Neuberg et al. (2006). (b) Waveform families and tilt at SHV during 23rd-28th June 1997. The coloured rectangles represent the different families (A-G), with their limits marking the first and last events. The time of the dome collapse on 25th June is indicated. The lower figure shows histograms indicating the number of events in each family, highlighting the dominance of family A (black) prior to the dome collapse. Taken from Green (2005).

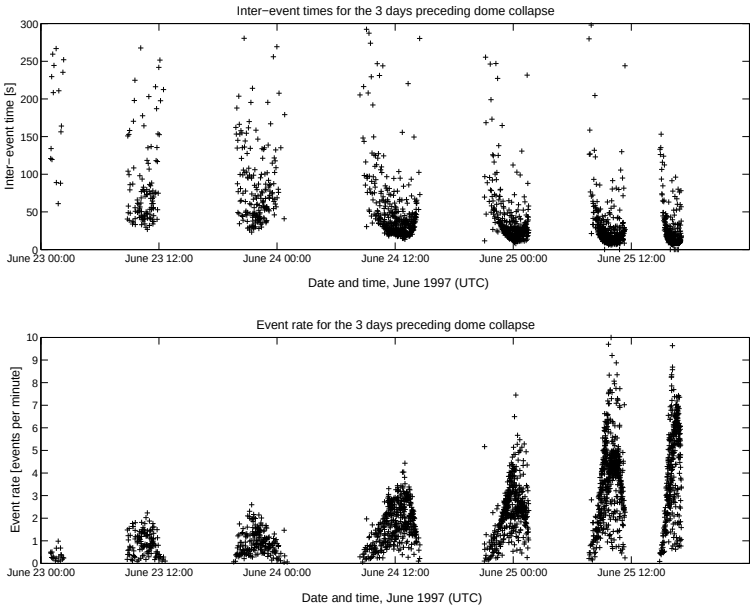

Figure 5.3: Inter-event times and event rate of earthquakes swarms preceding a dome collapse at SHV. Both plots were constructed using events from Family A identified by Green & Neuberg (2006). The top plot shows the time difference in seconds between temporally adjacent events for the seven swarms of earthquakes during the three days immediately preceding the dome collapse on the 25$^{\text{th}}$ June. The lower plot shows the inverse of the inter-event times, multiplied by 60 to give the event rate in numbers of earthquakes per minute.

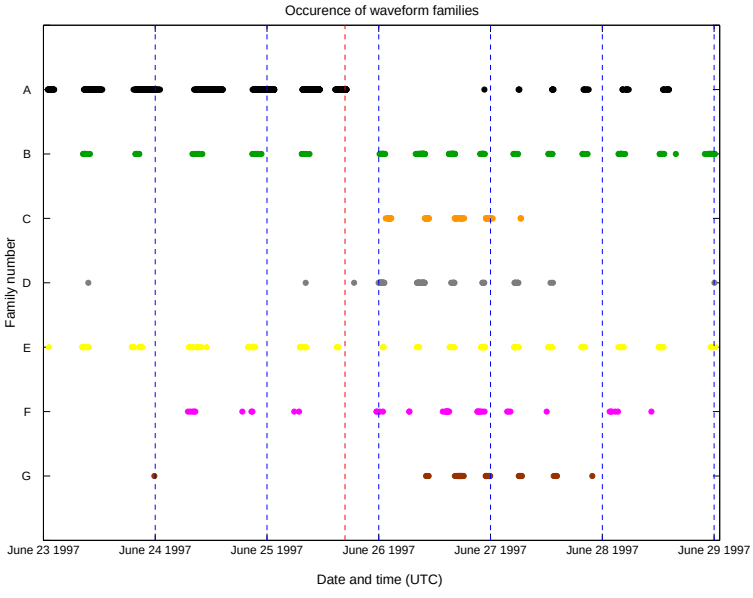

Figure 5.4: Occurrence of waveform families at SHV between 23$^{\text{rd}}$ and 28$^{\text{th}}$ June. The nine families of earthquakes (A-G) were identified by Green & Neuberg (2006) and are classified by waveform similarity. Family A dominates before the dome collapse with the largest number of events, containing 2124 events with unique onset times, identified from several sub-families. The time of the dome collapse is indicated by the vertical red dashed line.

5.1.2 Family A

The attenuation analysis will first focus on the events in Family A, as these are by far the most dominant waveform family, in terms of event numbers, during the period preceding the collapse (Green & Neuberg, 2006). This can be seen in the lower plot in Figure 5.2(b), which shows histograms of the number of events per swarm contained in each waveform family, with Family A (black) dominating the bars. In total across the seven swarms 2124 events with unique onset times were identified from the several sub-families of Family A of Green & Neuberg (2006). Stacked waveforms and their associated amplitude spectra for each of the seven swarms are shown in Figure 5.5, which also indicates the numbers of events within each swarm. There is a small but noticeable evolution in the stacked waveforms and spectra from swarm to swarm, particularly a reduction in the amount energy at around 3-4 Hz as time progresses. This can also be seen in Figures 5.6 and 5.7 which show the amplitude spectra of all family A events.

In general, however, the spectral content of the earthquakes is remarkably constant throughout the whole time period. To estimate the apparent attenuation of the low-frequency earthquakes, using the time-domain methods described in Chapter 4, certain discrete frequencies must be chosen for analysis. Figures 5.8 and 5.9 show the values of the three largest peaks identified from the amplitude spectrum of each event, again showing consistency and stability, both within each swarm and across all swarms. This in itself is perhaps not surprising, given that the events have already been classified together on the basis of a high degree of waveform similarity, but confirms the presence of a stable source body for this family throughout the duration of this time period.

These results, along with the amplitude spectra, suggest a choice of three frequencies for analysis: 1.39, 2.16 and 3.50 Hz. Of these, the peak at 1.39Hz is the most stable, present in nearly all of the events, whereas the peak at 2.16 Hz is perhaps a more tenuous choice, but becomes significant in the events in later swarms. These three frequencies will be used for the measurements of the attenuation of the events in Family A throughout this chapter.

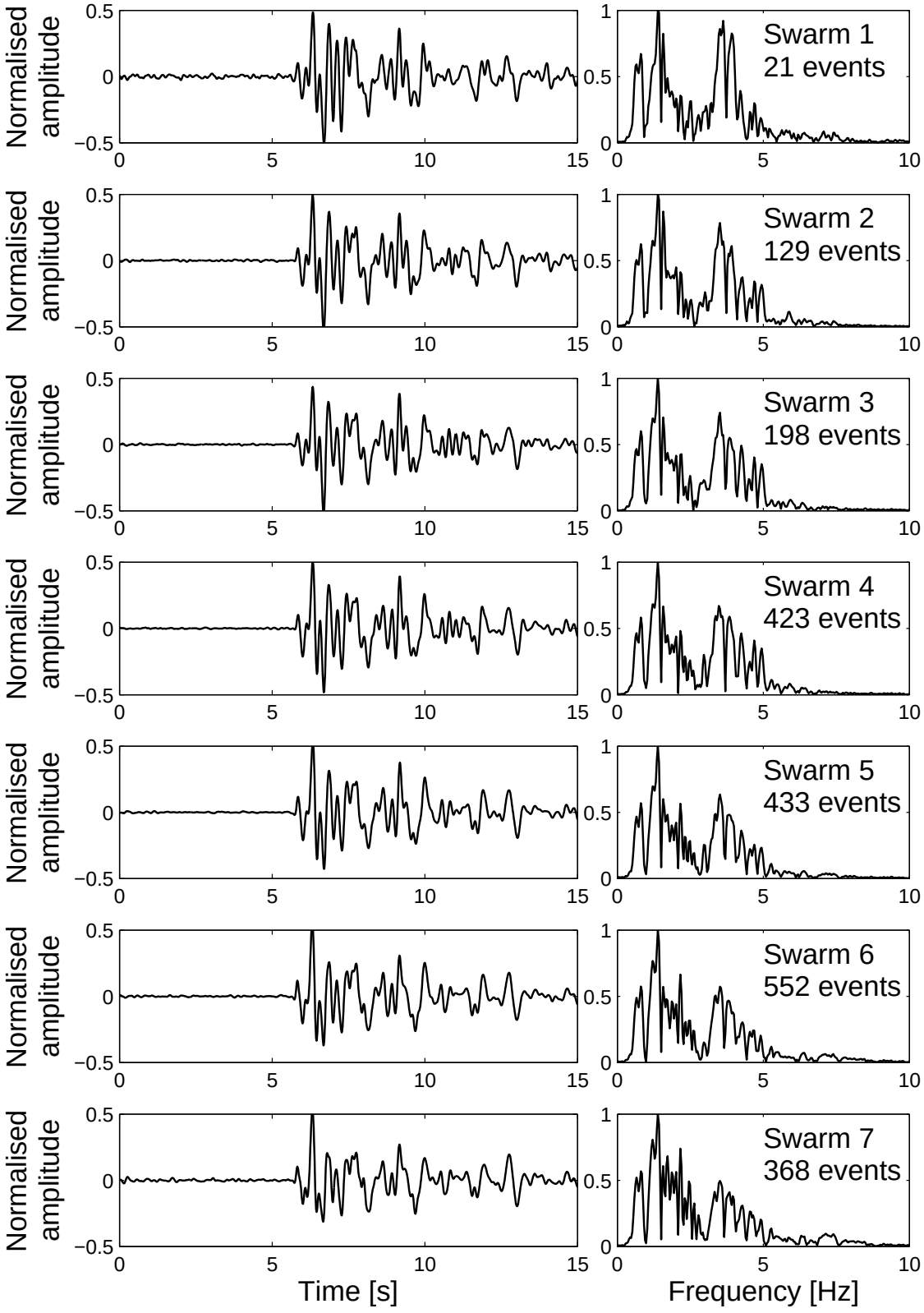

Figure 5.5: Stacked waveforms and associated spectra for the seven earthquake swarms preceding the 25$^{\text{th}}$ June dome collapse. Both velocity and spectral amplitudes have been normalised, and the velocity seismograms have been bandpass filtered between 0.5 and 5 Hz. The plot also indicates the number of events contained in each swarm.

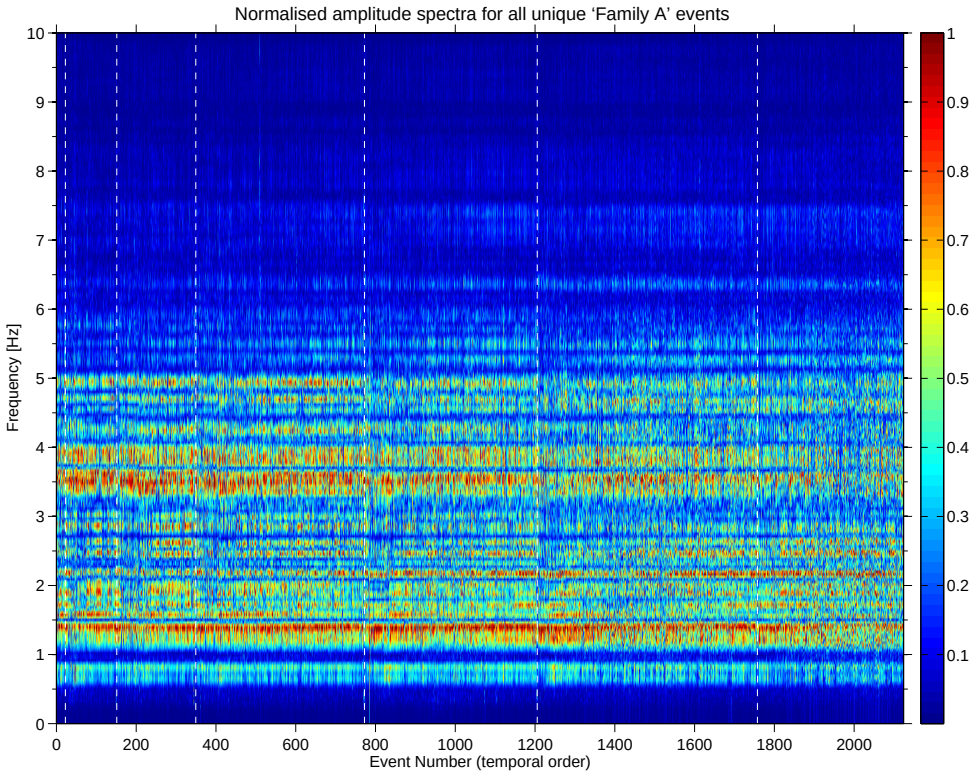

Figure 5.6: Amplitude spectra for all family A events preceding the dome collapse in temporal order, plotted as a function of the event number. This plot should not be confused with a typical spectrogram (calculated from continuous data) as it is constructed from the adjacent amplitude spectra of each discrete event. The vertical white dashed lines indicate discontinuities, and mark the boundaries between swarms.

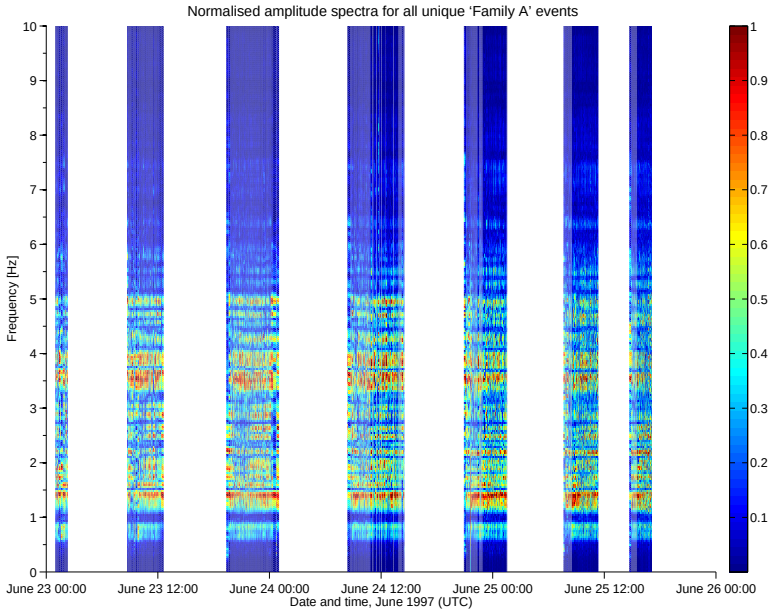

Figure 5.7: Amplitude spectra for all family A events, plotted as a function of the absolute time. This plot shows the same information as Figure 5.6, but with frequencies plotted as a function of the absolute times of the events, rather than event number.

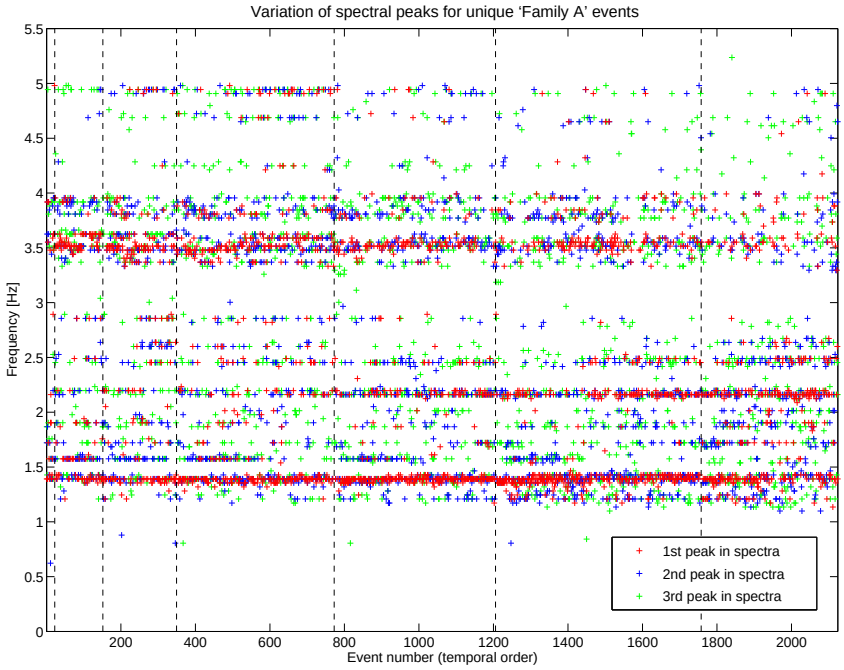

Figure 5.8: Variation of the spectral peaks of all family A events in temporal order, as a function of event number. The position of the three largest values of the amplitude spectrum was determined for each event, and is shown here as a function of the event number. The energy is concentrated in distinct bands at around 1.39, 2.16 and 3.50 Hz.

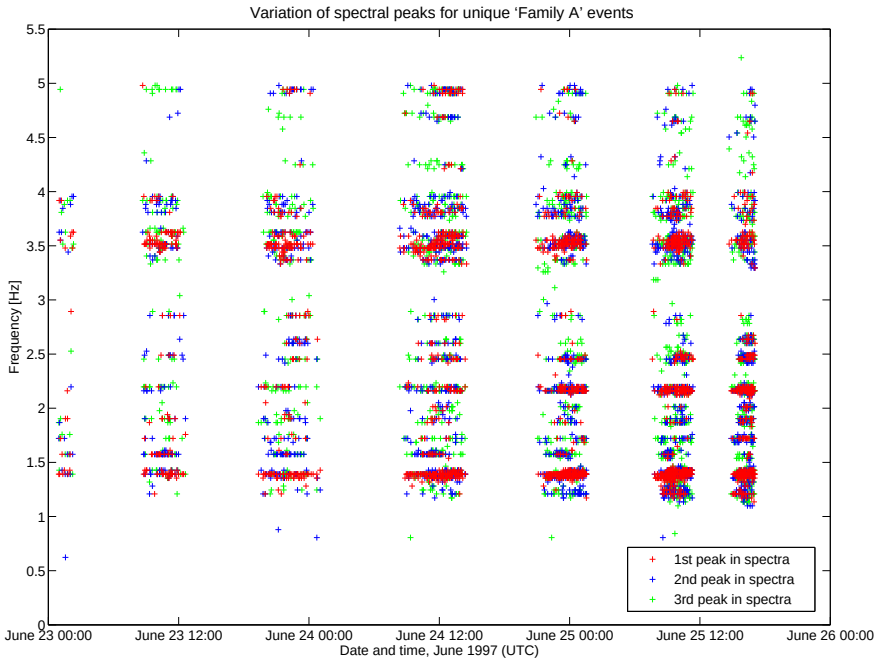

Figure 5.9: Variation of the spectral peaks of all family A events, as a function of absolute time. This plot shows the same information as Figure 5.6, but with frequencies plotted as a function of the absolute times of the events, rather than event number.

5.2 Measurements of attenuation

5.2.1 Pre-dome collapse: 23rd to 25th June

Measurement methods

The apparent attenuation was measured for each of the 2124 unique Family A events, at the three frequencies chosen from visual inspection of the spectra. To assess the robustness of both the methods and the measurements, the attenuation was initially measured using the following three methods:

1. The apparent attenuation was calculated from the slope of the logarithm of the analytical envelope, using the method outlined in Section 4.1.2. The portion of the signal coda used in the linear regression was determined using a fixed length window (see Section 4.3.1). The energy at each frequency was isolated using narrow 2-pole Butterworth bandpass filters, with fixed frequency bandwidths.

2. Again, the slope of the logarithm of the analytical envelope was used, but the limits of the regression window were chosen manually for each event. The energy at each frequency was isolated using narrow 2-pole Butterworth bandpass filters, with manually selected bandwidths.

3. The attenuation was calculated using the best of the automated methods described in Chapter 4, that employs a weighted mean of the slopes of sections of the coda with negative gradient and uses the S-transform to isolate energy at specific frequencies.

Initial results

Figures 5.10 to 5.13 show the results of the analysis in terms of both apparent Q_a and attenuation, respectively, as a function of the event number and the absolute event time. A comparison of the results for each of the three methods highlights two obvious features:

- The fixed window method shows the largest variability in Q_a values, with a high degree of scatter, particularly for the results at 2.16Hz (e.g. Figure 5.10).

- The automated method shows the least variability in terms of Q_a values, with much more clustered results. The measured Q_a values also appear to be lower using this

method, or higher when plotted in terms of the attenuation. An explanation may lie in the use of the S-transform rather than filtering to separate different frequencies. As discussed in Section 4.2, narrow bandpass filters introduce ringing, with the effect of increasing the Q_a or lowering the attenuation. The benefit of using the S-transform was demonstrated in Chapter 4, where this method was shown to recover the attenuation from synthetic signals better, particularly if the attenuation was high. Isolating the energy using filters may therefore lead to underestimation of the attenuation of the signals.

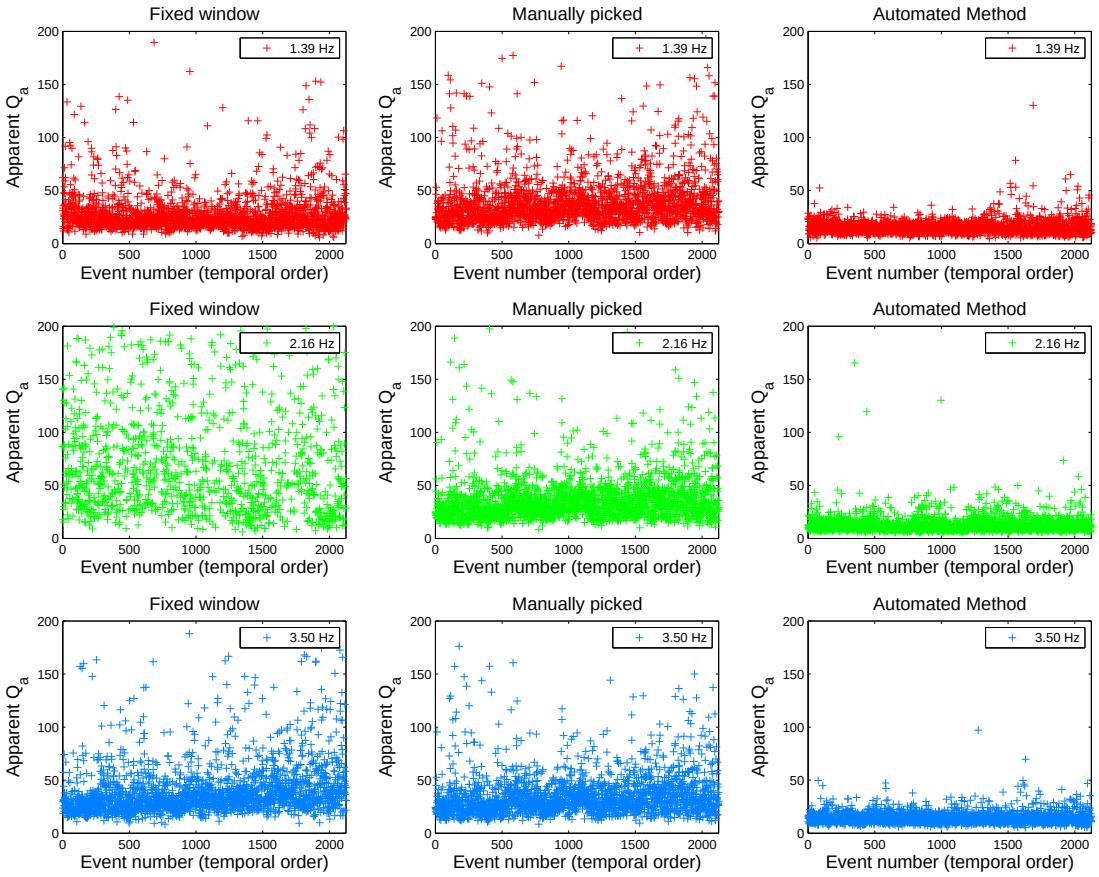

Figure 5.10: Apparent Q_a as a function of the event number, measured at three frequencies using three different methods. Each row (and therefore colour) represents a different frequency chosen from the spectra: 1.39, 2.16 and 3.50Hz. Each column represents one of the three methods used: (a) a fixed length of regression window, (b) manually chosen window lengths and (c) an automated method using a weighted average and the S-transform. The apparent Q_a values are sorted in temporal order and plotted as a function of the event number, with the discontinuities between swarms not marked in this diagram.

Figures 5.10 and 5.12 show the Q_a and attenuation of the events, plotted as a function of the event number in temporal order, to see if systematic temporal changes in attenuation

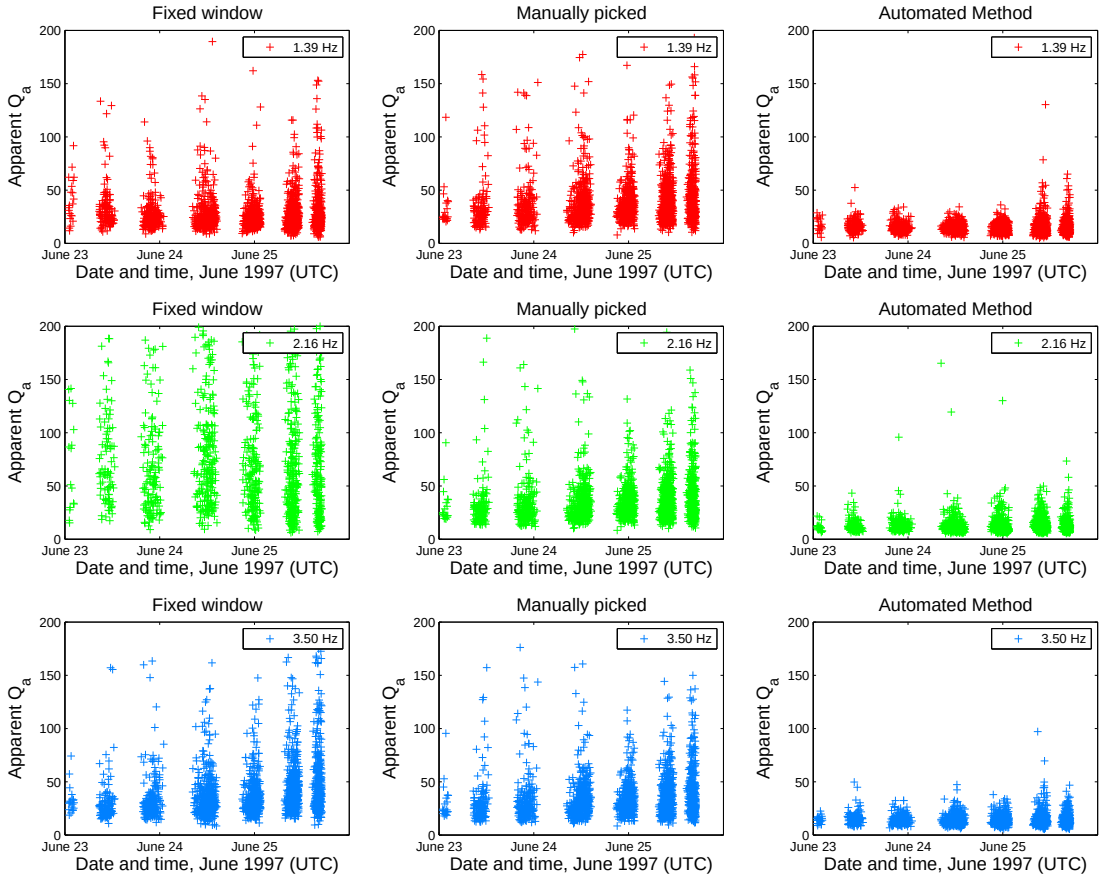

Figure 5.11: Apparent Q_a as a function of the absolute event time, measured at three frequencies using three different methods. This plot shows seven clusters of values, corresponding to the seven swarms of earthquakes preceding the 25th June dome collapse.

across the whole time period are visible within the measured values.

The results show no obvious or consistent temporal variation when displayed in this way. There is a suggestion of an increase in Q_a or decrease in attenuation with event number, particularly in the measurements made using the fixed window and manually selected parameters methods, although confident assertions are somewhat hampered by the high degree of scatter. To overcome this, temporally smoothed versions of these results were calculated, and these are discussed in the next section.

Figures 5.11 and 5.13 show the apparent Q_a and attenuation of the events plotted as a function of the absolute event times and the results again show no clear or obvious temporal trends between or within swarms, but there is a suggestion of an increase in scatter or variability for later swarms. To assess this quantitatively, the distribution of values in each of the swarms was statistically analysed and the results shown in the box plots in Figures 5.14 and 5.15. Values within the blue boxes lie between the 25% and

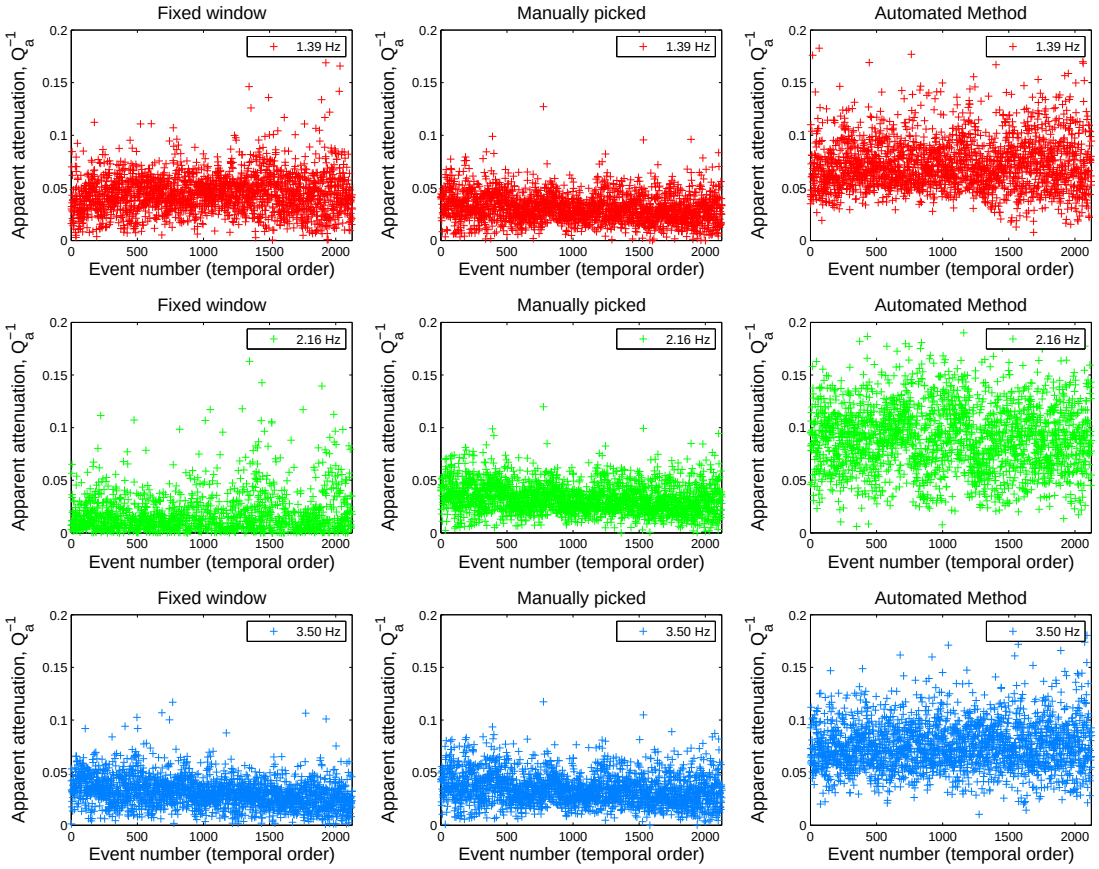

Figure 5.12: Apparent attenuation, Q_{a}^{-1}, as a function of the event number, measured at three frequencies using three different methods.

75% quartiles, with the red line inside each box showing the median or 50% percentile of the distribution. The upper and lower 'whiskers' represent the largest and smallest data values within 1.5 times the inter-quartile range. This corresponds to approximately $\pm 2.7\sigma$ or the 99.3% confidence interval for normally distributed data. Points outside this range, shown in red, are considered outliers. The box plots highlight several features of the data, confirming some of the earlier observations:

- The fixed window method shows the largest variation in Q_{a} values, particularly at 2.16Hz, and has the most outliers, including negative values of Q_{a}. This suggests a non-Gaussian distribution with some systematic bias in the results. This is shown by the higher kurtosis excess in Figure 5.16, and is further discussed in the comparison of the methods in the following section.

- The manual method shows an increase in Q_{a} across the swarms from a Q_{a} of around 20 for the first swarm to closer to 40 by the final swarm. There is also a pattern

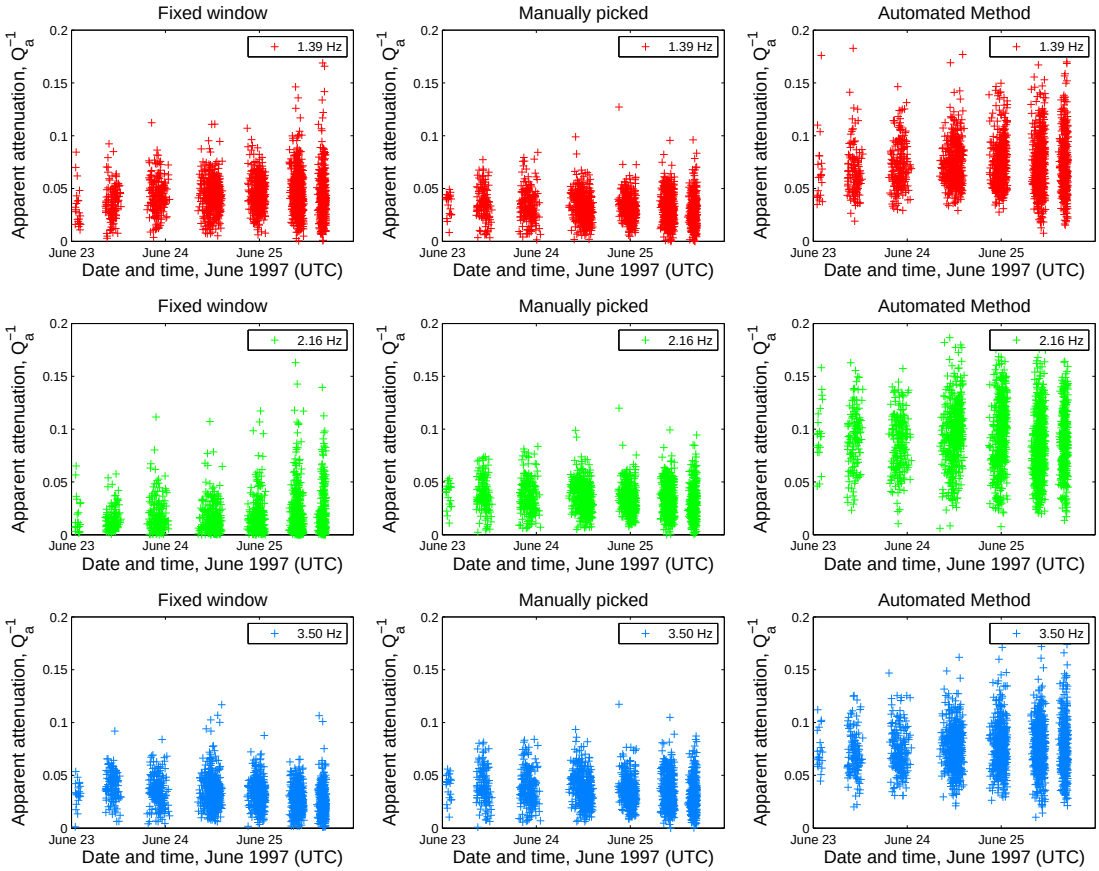

Figure 5.13: Apparent attenuation, Q_{a}^{-1}, as a function of the absolute event time, measured at three frequencies using three different methods.

of increasing scatter and variation in Q_{a} with time, shown by the increasing size of the boxes and lengthening of the 'whiskers' in Figure 5.14. All frequencies also show very similar behaviour using this method.

- This trend of increasing Q_{a} with time is not supported by the results using the automated method, which shows consistently lower Q_{a} values, with the interquartile range box falling between $10 \leq Q_{\mathrm{a}} \leq 20$ for nearly all frequencies and swarms. In fact, a trend of increasing attenuation could be argued, particularly in the 1.39Hz and 3.50Hz box plots in Figure 5.15.

Comparison of methods

The best of the automated measurement methods developed in Chapter 4, based on a weighted average of segments of negative gradient and using the S-transform to isolate frequencies, appears the most robust of the methods used. This method produced mea-

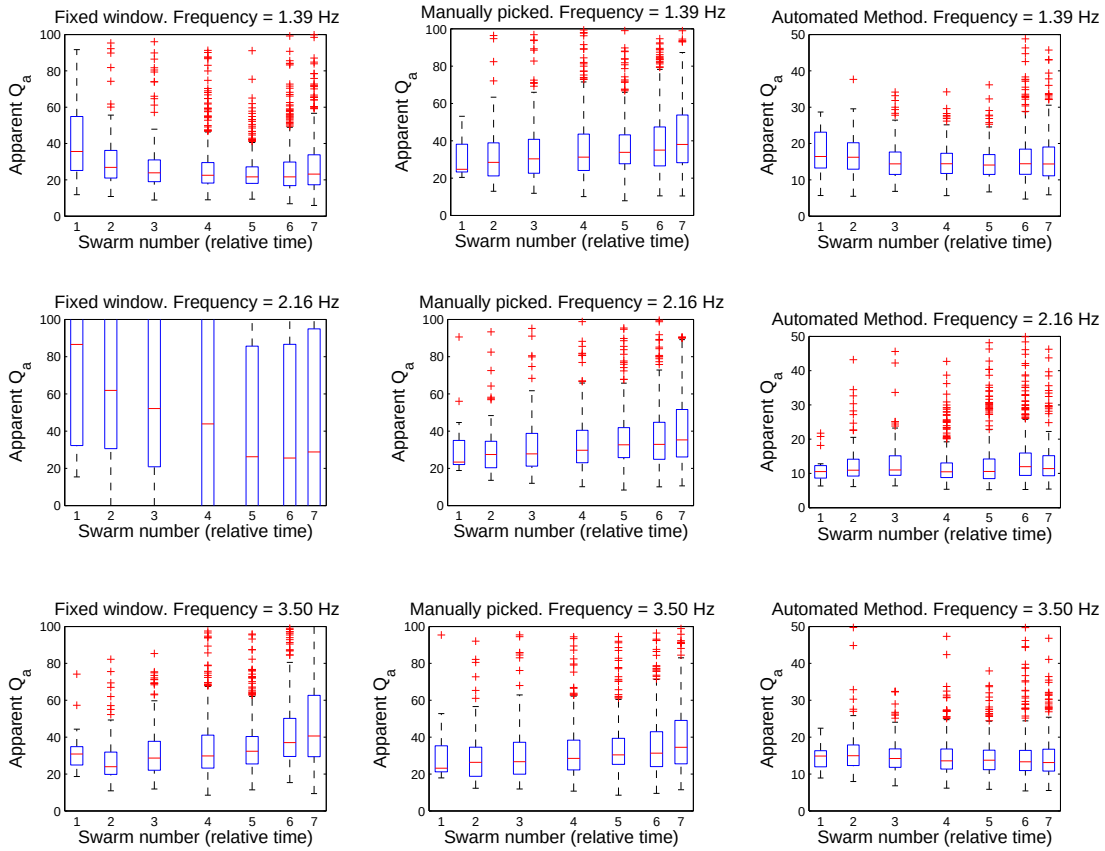

Figure 5.14: Box plot displaying the apparent Q_a distribution for each of the seven swarms, measured at three frequencies using three different methods. The blue box indicates the limits of the 25% and 75% quartiles, and the red line inside the box is the distribution median. The upper and lower 'whiskers' represent the largest and smallest data within 1.5 times the inter-quartile range. This corresponds to approximately $\pm 2.7\sigma$ or the 99.3% confidence interval for normally distributed data. Points outside this range, shown in red, are considered outliers. Note the different vertical scale, of $0 \leq Q_\mathrm{a} \leq 50$, for the automated method results in the third column of subplots.

surements with less scatter and variation in Q_a and gave consistently lower Q_a or higher Q_a^{-1} than the other methods. The results of calculating the kurtosis in Figure 5.16, show that the automated method also produces a more normally distributed range of attenuation values (kurtosis excess closer to zero), indicating less bias than the other two methods. This method has already been shown to be better at recovering the attenuation from synthetic signals in Chapter 4, particularly if the attenuation is high. The other advantages of this method are that it negates the possibility of user bias when using the manual method and the potentially contaminatory effects introduced by filtering. Therefore, only this method will be used to measure the attenuation in all subsequent analysis in this chapter.

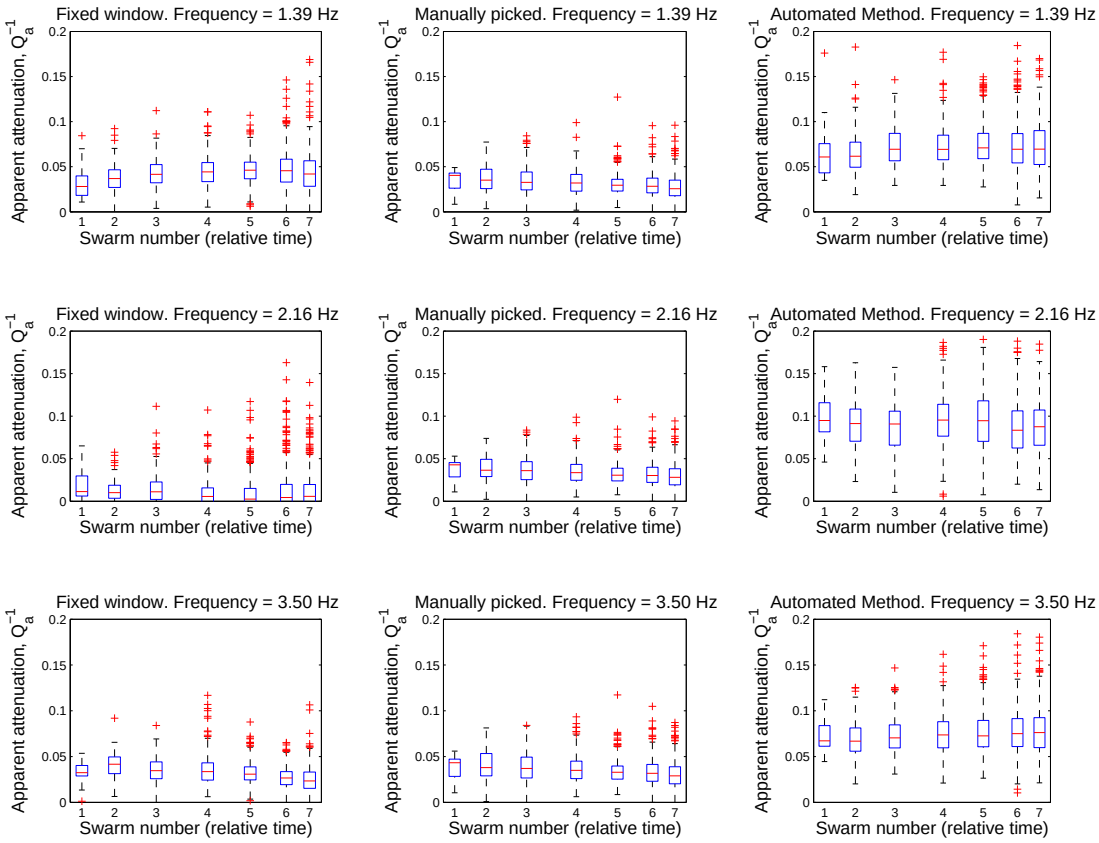

Figure 5.15: Box plot displaying the apparent attenuation, Q_{a}^{-1}, distribution for each swarm, measured at three frequencies using three different methods.

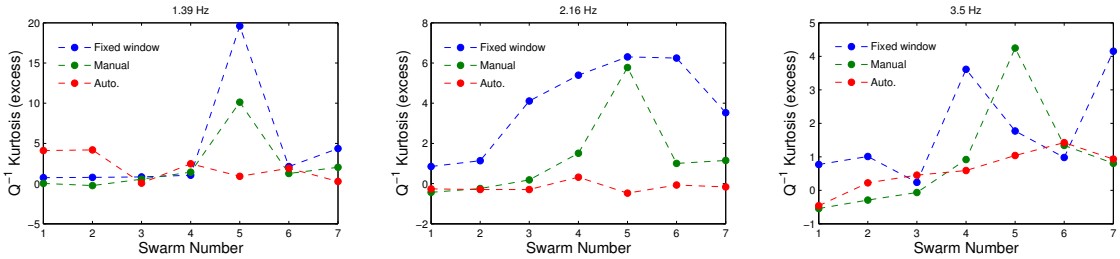

Figure 5.16: Q_{a}^{-1} kurtosis excess, calculated for each swarm. Shown is a comparison between the three methods at each of the three frequencies analysed. Values close to 0 indicate a normal distribution, with positive values indicating a more 'peaked', and negative values indicating a 'flatter', distribution respectively. In general, the fixed window and manual methods have positive values, particularly obvious at 2.16Hz. The automated method has values closest to zero for all three frequencies indicating that this method gives the most normally distributed measurements of attenuation.

Smoothed data using temporal bins

As discussed, the measured apparent Q_a and attenuation values show a high degree of scatter and variability, making it difficult to confidently interpret temporal variations. Therefore, to try and highlight trends and patterns within the distributions, the data were smoothed. Rather than using a moving average or a median filter over a fixed number of events, because the event rate varies both within and across the earthquake swarms (see Figure 5.3), the data were binned into temporal bins of fixed time length. A bin length of 20 minutes was chosen to give appropriate smoothing of the distribution of values. The mean values of the bins are plotted in black and the median values in red, along with error bars representing the standard deviation of values in each bin.

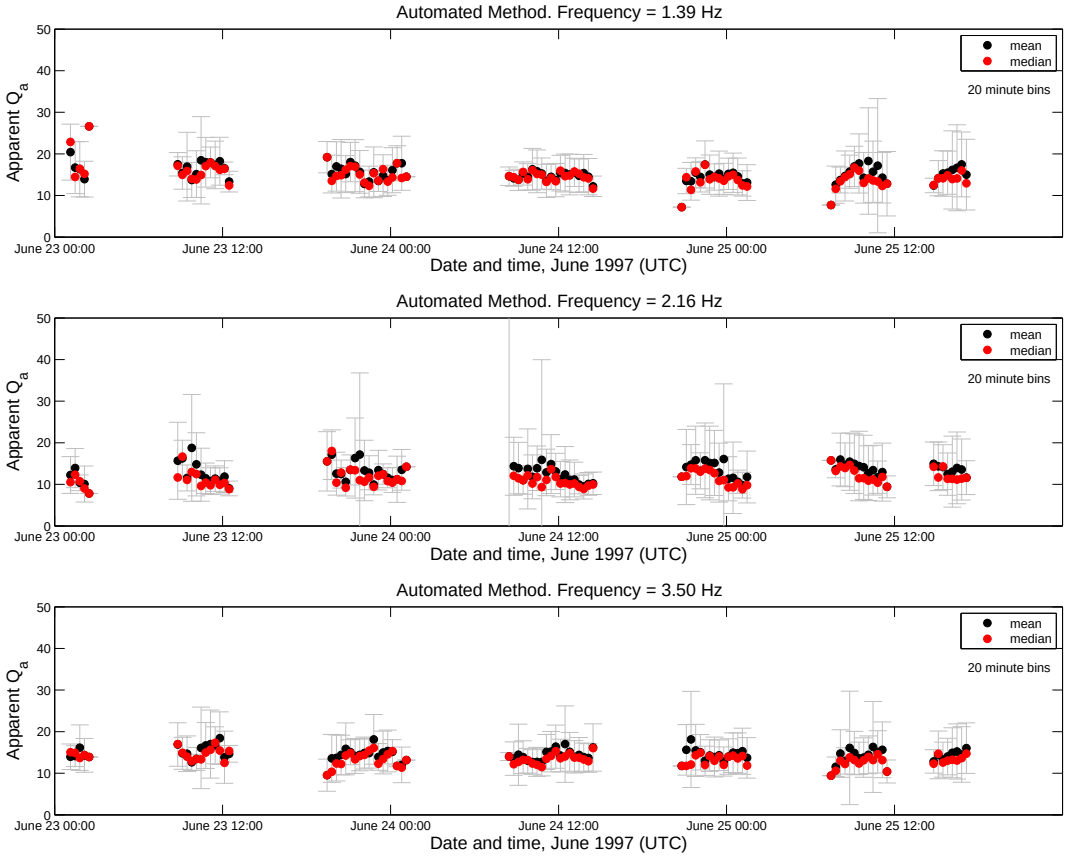

Figure 5.17: Apparent Q_a values calculated for 20 minute bins, using the automated method, measured at three different frequencies. As a way of smoothing the distribution, the data were placed into 20 minute long temporal bins. The black points are the mean values of the bins and the red points the median values, with the error bars representing $\pm 1\sigma$.

The results of temporally smoothing the data (measured using the automated method) into 20 minute bins show several interesting features. There is a noticeable difference

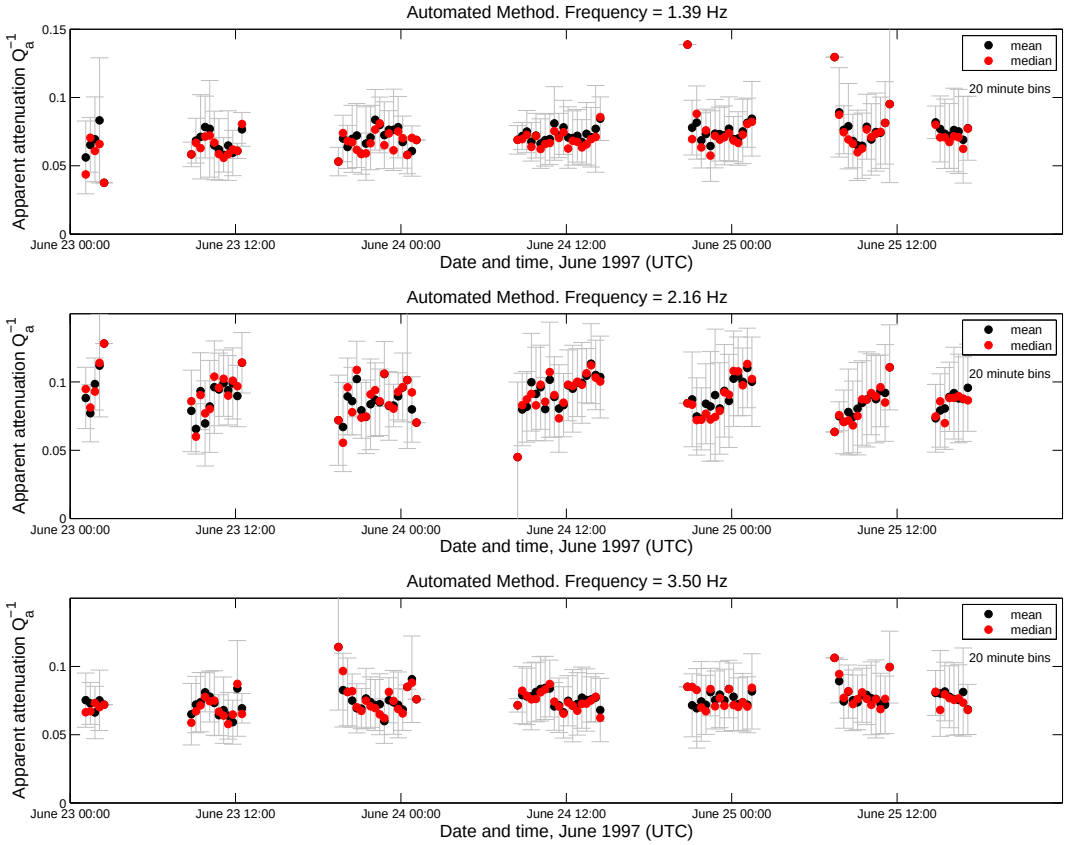

Figure 5.18: Apparent attenuation, Q_a^{-1}, calculated for 20 minute bins, using the automated method, measured at three different frequencies.

in behaviour between the results at different frequencies in the smoothed data. For the lowest spectral peak at 1.39Hz, there appears to be an increase followed by a decrease in Q_a (or vice versa for attenuation) within each swarm, a pattern which is particularly visible in the later swarms with greater numbers of events. For the spectral peak at 2.16Hz, there is a trend of increasing attenuation or decreasing Q_a within each swarm, again more strongly evident in the later swarms.

Frequency dependence

As discussed in Chapters 2 and 3, the intrinsic attenuation of a fluid such as magma is, in general, strongly frequency dependent, with the exact relationship depending on the rheology. The dependence of the apparent attenuation on the frequency at which it is measured, is now examined in more detail, as this relationship may help to reveal the rheological properties of the fluid within the resonator.

As a first order step, the mean attenuation values at each frequency were used to produce

a temporally averaged dependence of the attenuation on frequency, shown in Figure 5.19. The results show that, on average, the attenuation is higher at 2.16Hz with a mean of $\overline{Q}_a = 13.1 \pm 8.2$, compared to $\overline{Q}_a = 15.6 \pm 6.7$ for 1.39Hz and $\overline{Q}_a = 14.6 \pm 6.6$ for 3.50Hz. The results of performing t-tests, shown in Table 5.1, confirm that these differences between the mean Q_a values at different frequencies are significant at the 95% confidence level. The relationship in Figure 5.19 does not fit any simple interpretation or rheological model, however, it must be remembered that this apparent measurement also includes the radiative component which, as shown in Chapter 2, is also dependent on the frequency, making it difficult to separate the intrinsic and radiative effects.

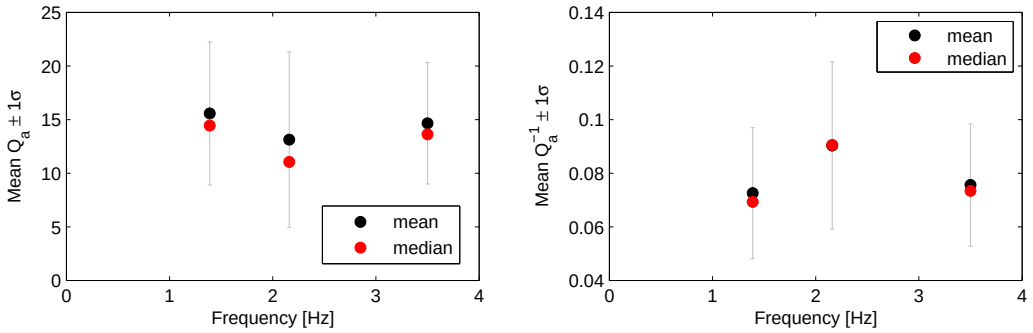

Figure 5.19: Temporally averaged frequency dependence of apparent Q_a and attenuation. The mean value for Q_a and Q_a^{-1} at each of the three frequencies was calculated, to obtain a temporally averaged estimate of the relationship between attenuation and frequency. The error bars represent $\pm 1\sigma$.

Freq. 1 [Hz]	**Freq. 2 [Hz]**	$\overline{Q}_a(f_1) \pm \sigma$	$\overline{Q}_a(f_2) \pm \sigma$	**t-value**	**df**	**p (<0.05)**
1.39	2.16	15.6 ± 6.7	13.1 ± 8.2	10.607	4201	5.87×10^{-26}
1.39	3.50	15.6 ± 6.7	14.6 ± 6.6	4.785	4215	1.77×10^{-6}
2.16	3.50	13.1 ± 8.2	14.6 ± 6.6	7.051	4204	2.06×10^{-12}

Table 5.1: Results of performing t-tests to compare the mean Q_a values at different frequencies. The t-values, degrees of freedom (df) and significance at the 95% confidence level (p), are shown. As can be seen from the low significance values, because of the large sample size and hence degrees of freedom, the differences between the mean Q_a values for each pair of frequencies are significant at the 95% confidence level. Note that the t-test assumes the Q_a values are normally distributed.

Since the absolute values of the apparent attenuation at each frequency show temporal variations, the dependence of attenuation on frequency may also change with time. To examine this, rather than averaging across all events, the ratio between values at different frequencies was calculated for each bin, with the results shown in Figures 5.20 and 5.21. These ratios show several features: (i) In general, the attenuation is higher at 2.16Hz compared to the other frequencies. (ii) There are systematic changes in the frequency

behaviour within each swarm, and the lower two plots in Figure 5.21 show the same general patterns as the absolute values of the individual frequencies in the top two plots of Figure 5.18. This suggests that the patterns observed in the 1.39Hz and 2.16Hz bands are the most dominant, with the 3.50Hz frequency changing the least by comparison. (iii) There is also a general trend of convergence for all three frequencies as time progresses, with the values of all three ratios becoming closer to unity for the later swarms.

These variations in Q_{a} at different frequencies also suggest that temporally averaging the frequency dependence of the attenuation, as in Figure 5.19, is not appropriate or justified, and that any quantitative interpretation of the attenuation must take account of these systematic temporal variations of the frequency dependence.

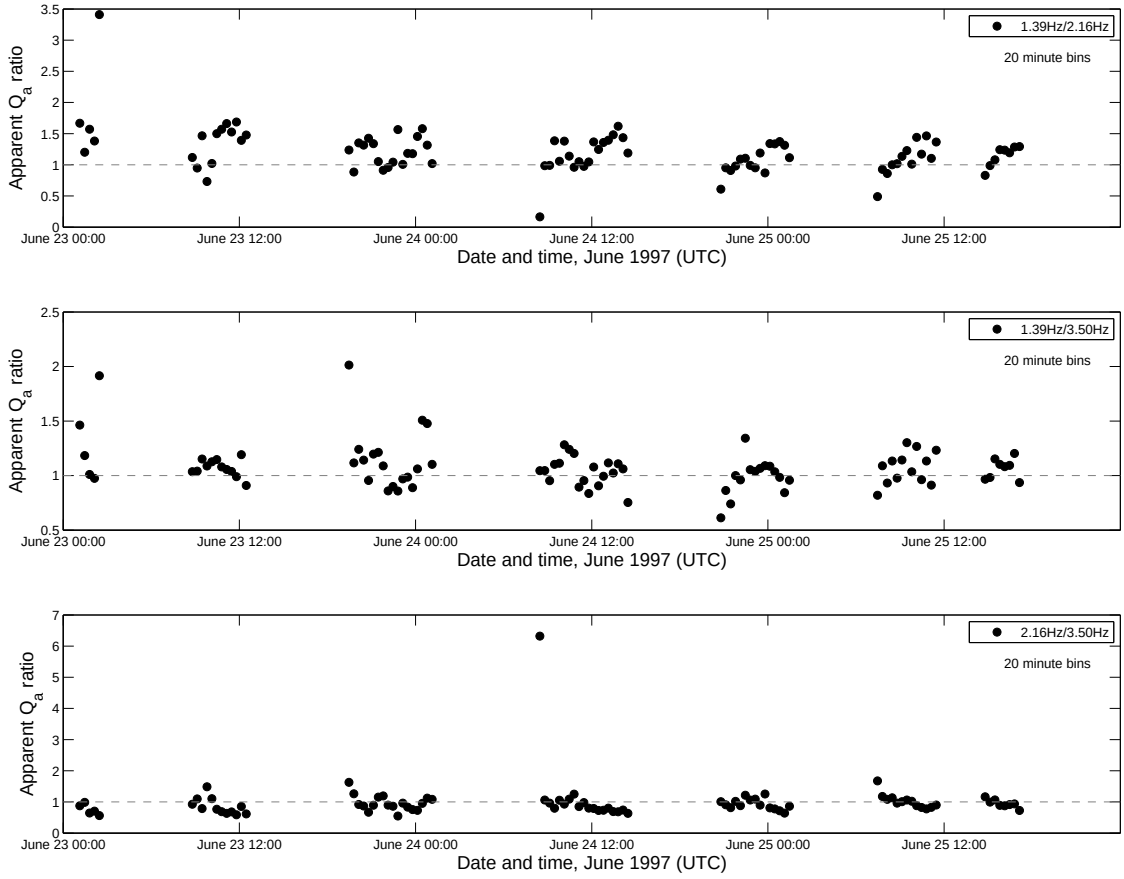

Figure 5.20: Ratio of apparent Q_{a} at different frequencies for family A events. The three subplots show the ratio between the mean apparent Q_{a} values in each bin for each unique pair of frequencies.

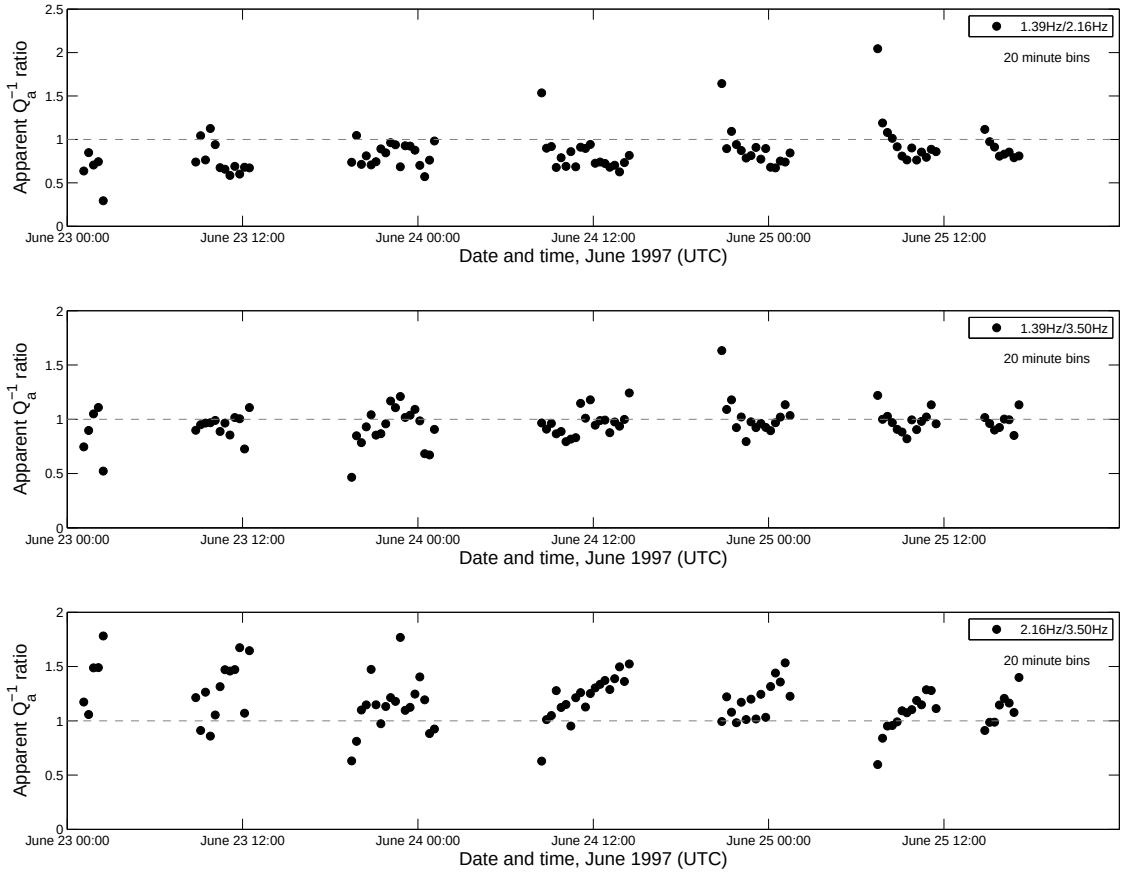

Figure 5.21: Ratio of apparent attenuation at different frequencies for family A events. The three subplots show the ratio between the mean apparent attenuation values in each bin for each unique pair of frequencies.

Correlation with event rate

The lowest spectral peak, at 1.39Hz, is the most stable and consistent of the frequencies analysed (see Figure 5.6) and the last four swarms preceding the dome collapse contain the largest number of events (see Figure 5.2(b)). This suggests the pattern seen in these results represents the most confident of the observed trends. Figure 5.22 focuses on the results for these swarms, at the lowest frequency of 1.39Hz, and highlights the observed trend of an increase and then decrease in Q_{a} (vice versa for attenuation), particularly evident for the last three swarms of events.

The event rate of the earthquakes show a pattern of acceleration and deceleration within each swarm (Figure 5.3), which Hammer & Neuberg (2009) attributed to fluctuations in the magma ascent velocity. Since a similar trend can be observed the attenuation data in Figure 5.22, a factor to consider is whether the variation in attenuation is related to these changes. To test this, the correlation between the apparent Q_{a} and attenuation values for each bin, respectively, and the event rate was calculated, using simple x-y scatter plots. The correlation was calculated using the linear correlation coefficient (Pearson product-moment correlation coefficient), defined for a series of n measurements of X and Y as

$$r_{xy} = \frac{\sum_{i=1}^{n} (x_i - \bar{x})\,(y_i - \bar{y})}{(n-1)\,s_x s_y} \tag{5.1}$$

where $\bar{x}$ and $\bar{y}$ are the means, and s_x and s_y are the standard deviations of X and Y respectively. In this case X corresponds to the mean apparent Q_{a} or attenuation for each bin and Y to the event rate, determined from the number of events in each bin, divided by the bin size.

The plots of the event rate against the measured attenuation values in Figure 5.23 show that for the four swarms analysed, there is a degree of correlation between the two. The results for the last two swarms in particular show a positive correlation between Q_{a} and event rate, and correspondingly, a negative correlation between attenuation and event rate. This indicates that the temporal amplitude decay of the earthquakes is reduced when the event rate is high, with some degree of linear dependence between the two, although this result does not necessarily imply a causal relationship. A quantitative interpretation of this result, in terms of magma viscosity, is discussed in Section 5.3.

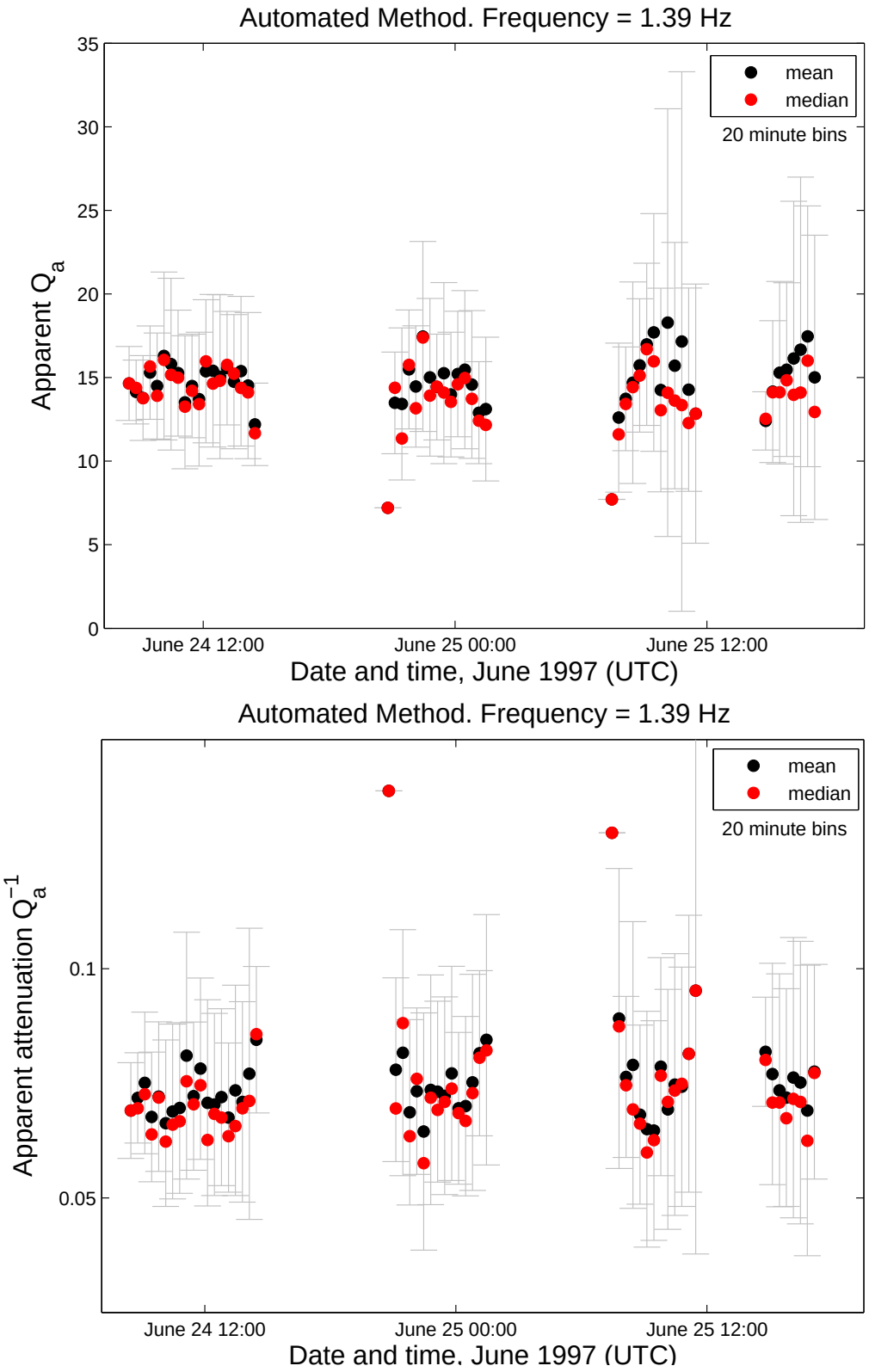

Figure 5.22: Temporal variation of apparent Q_a and attenuation at 1.39Hz for the final four swarms preceding the dome collapse. This plot zooms in on some of the trends in Figures 5.17 and 5.18, to highlight the pattern of an increase and then decrease in Q_a within each swarm at this frequency. Again, the black points are the mean values of the bins and the red points the median values, with the error bars representing $\pm 1\sigma$.

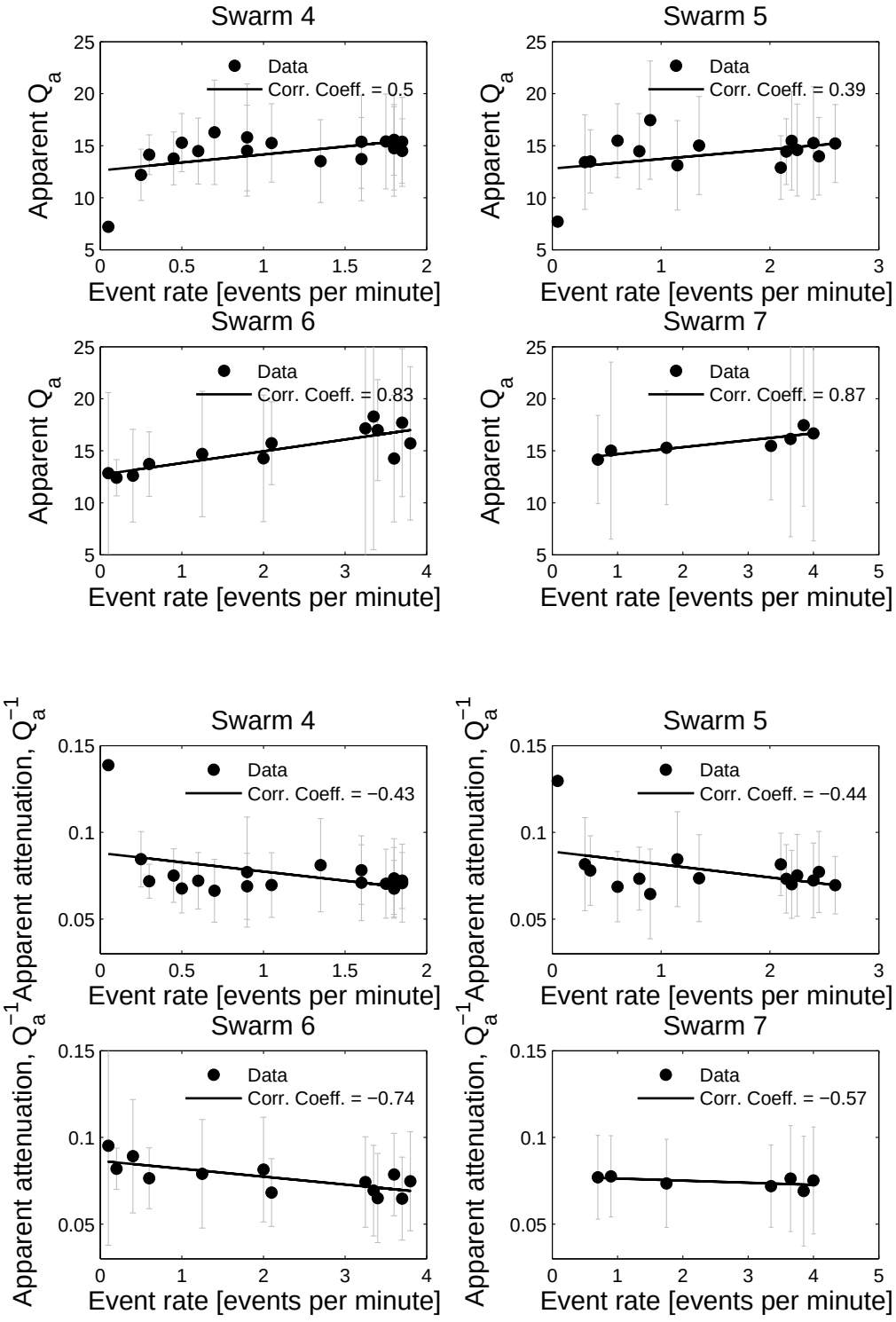

Figure 5.23: Correlation between mean apparent Q_a, attenuation and event rate for each bin. The linear correlation coefficients were determined using Equation 5.1, for the results at 1.39Hz from the last four swarms of earthquakes preceding the dome collapse on 25th June. Note the positive correlation between apparent Q_a and event rate, and the corresponding negative correlation between attenuation and event rate.

5.2.2 Post-dome collapse: 25$^{\text{th}}$ to 28$^{\text{th}}$ June

One remarkable observation of Green & Neuberg (2006) was the effect of the dome collapse on the waveform families. Certain waveform families, such as Family B, seem to continue to occur regardless, whilst others, such as Family C, *only* become active following the collapse (see Figure 5.2(b)). On the other hand, Family A, which was the most dominant before the collapse ceases immediately after but then slowly re-emerges, perhaps as similar pressure and viscosity conditions are achieved in order to trigger the seismicity at the same depth as previously (Green & Neuberg, 2006). This indicates that the removal of a significant mass of overburden that changes the internal pressure conditions (equivalent to a decompression of ∼3MPa (Green, 2005)), disrupts but does not permanently destroy the source of the low-frequency seismicity.

In this section, the attenuation values for the Family A events occurring *after* the dome collapse are calculated and compared to those beforehand to check if any changes can be seen. One factor to bear in mind is the greatly reduced sample size, as only 88 Family A events were recorded in the three days after the dome collapse, compared to more than 2000 in the three days preceding it.

Family A

Following the dome collapse on the 25$^{\text{th}}$ June, Family A slowly re-emerges, first appearing again after almost 24 hours, occurring in six swarms with 88 events recorded in total during this period. Figure 5.25 shows the stacked waveforms and their spectra for each of these six swarms. The waveforms and spectra are slightly noisier than previously, due to the smaller number of events in each swarm that are summed to produce the stacked waveforms. The individual amplitude spectra are displayed in Figure 5.24, showing the same dominant spectral peak at 1.39Hz, but with less coherent energy in discrete bands at higher frequencies, particularly around 2.16 Hz which was chosen previously. This again may be a function of the reduced number of events recorded.

The attenuation and Q_{a} values for these earthquakes are displayed, again as a function of the event number and absolute times, in Figures 5.26 and 5.27. The results show a similar pattern to the pre-dome collapse data with the automated method producing Q_{a} values clustered around $Q_{\text{a}} \approx 15$. Temporal smoothing was not applied due to the small number of events. Box plots were again calculated to examine the statistical distribution

of values within each swarm. Given the smaller numbers of events in these swarms, this approach is somewhat limited but does agree with the previous observations that the automated method gives values in the range $10 \leq Q_{\mathrm{a}} \leq 20$.

To highlight any differences or similarities between the pre- and post-dome collapse swarms of events, the results of all Family A events during the six day time period are displayed together on the same axes in Figure 5.29. The results show that for the third spectral peak at 3.5Hz, the attenuation is initially higher in the first swarm following the collapse before returning to the same level as previously, although given the small sample size this should be interpreted with caution. For the other two frequencies analysed there is no clear distinction that can confidently be made between swarms before and after the collapse.

In summary, the attenuation measured from the post-collapse swarms is consistent with that of the events preceding the dome collapse, indicating that once Family A has re-emerged and similar internal conditions are achieved to trigger the seismicity, the dome collapse has little impact on the attenuation of the earthquakes. This result is consistent with the occurrence of a particular waveform family of earthquakes requiring the *same set of internal conditions* triggering the *same resonator*.

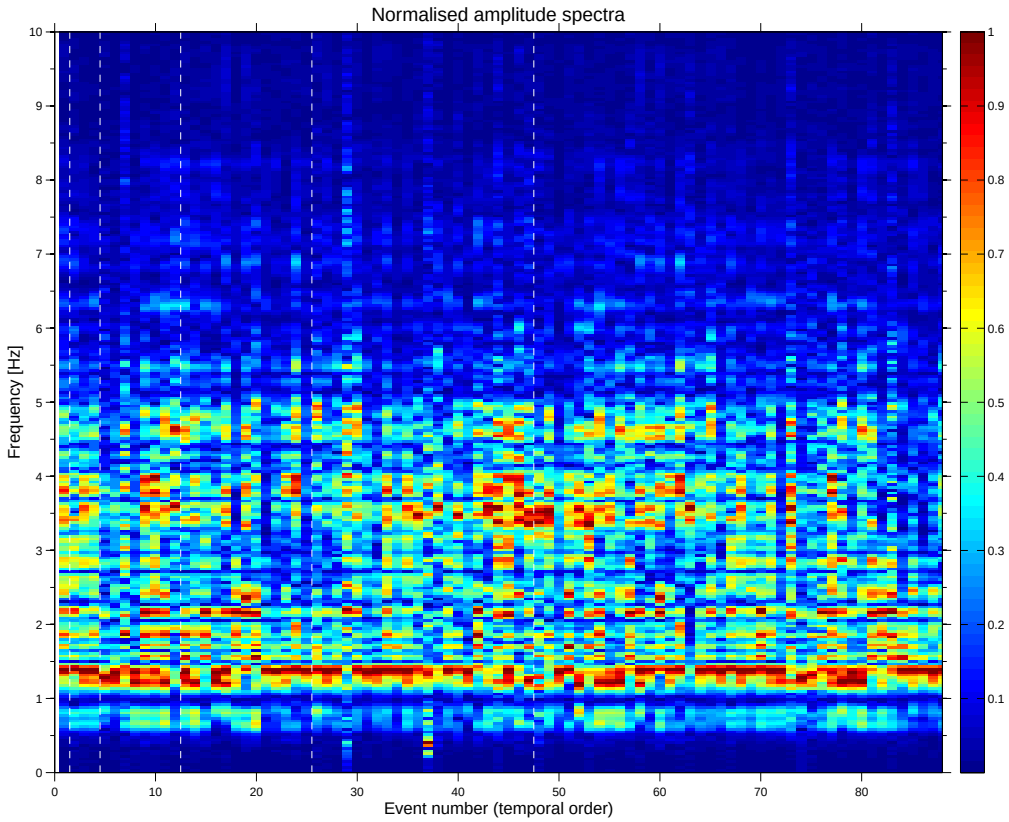

Figure 5.24: Amplitude spectra for post-dome collapse Family A events in temporal order, plotted as a function of the event number. The vertical white dashed lines indicate discontinuities, and mark the boundaries between swarms. Note the increasing number of events in each successive swarm as Family A re-emerges following the dome collapse.

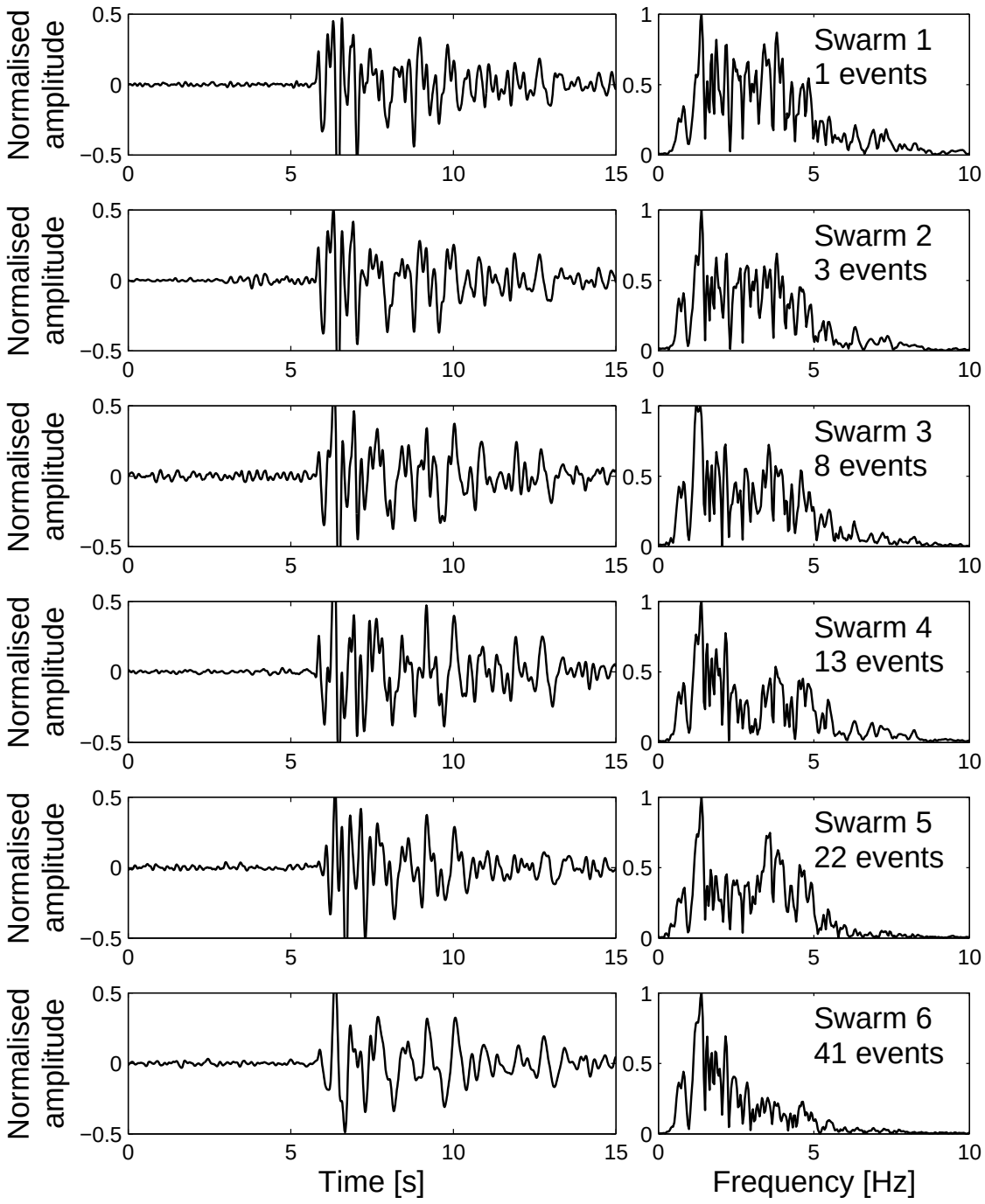

Figure 5.25: Stacked waveforms and associated spectra for the six swarms of Family A earthquakes following the 25th June dome collapse. Both velocity and spectral amplitudes have been normalised, and the velocity seismograms have been bandpass filtered between 0.5 and 5 Hz. The plot also indicates the number of events contained in each swarm, showing the reduced number of events, particularly in the earlier swarms.

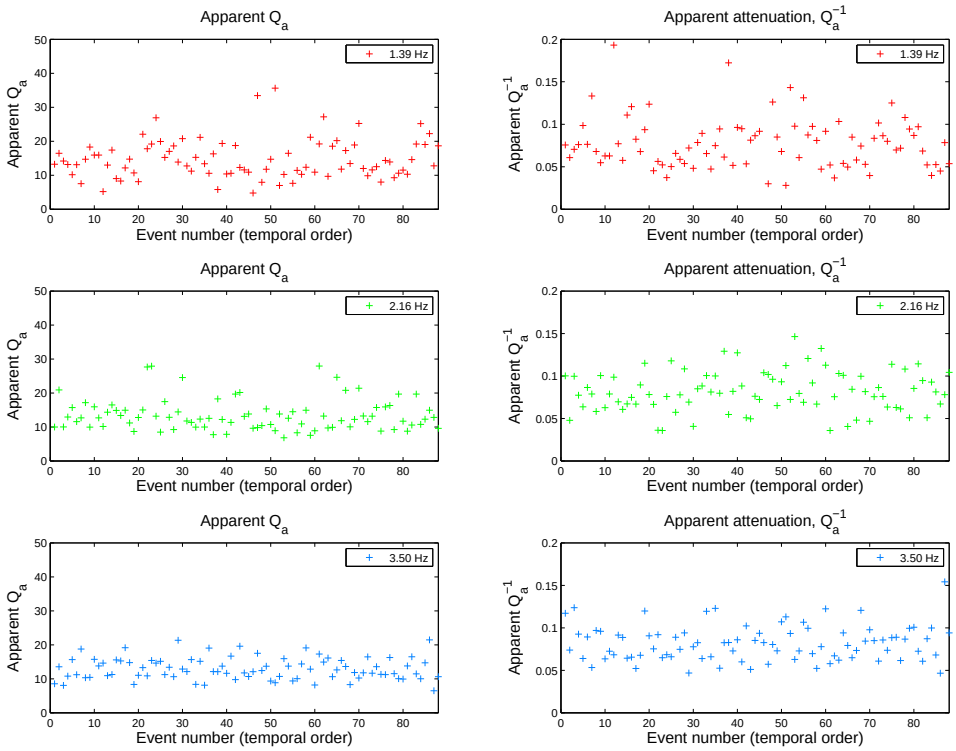

Figure 5.26: Apparent Q_a and attenuation as a function of the event number for post-dome collapse Family A events, measured at three frequencies.

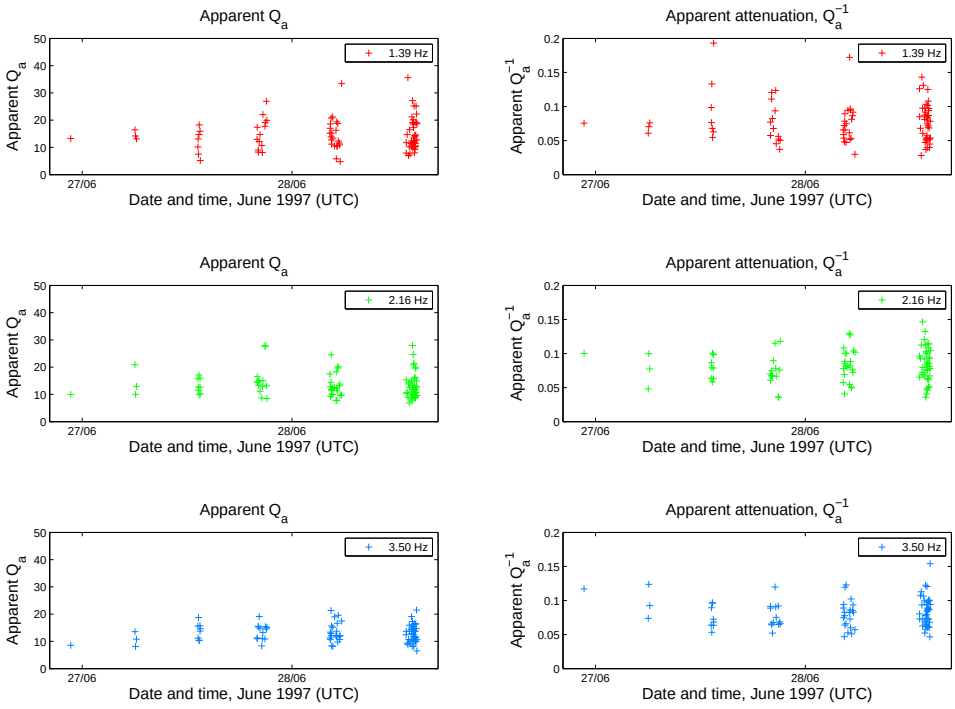

Figure 5.27: Apparent Q_a and attenuation as a function of the absolute event time for post-dome collapse Family A events, measured at three frequencies.

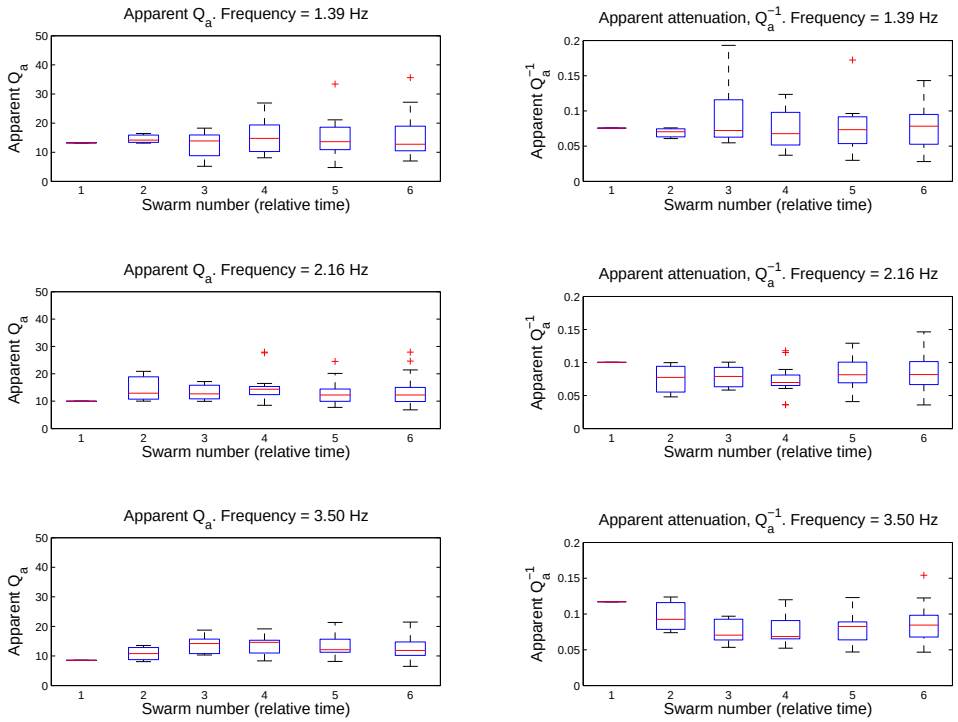

Figure 5.28: Box plots displaying the apparent Q_a and attenuation distributions for each post-dome collapse Family A swarm, measured at three frequencies.

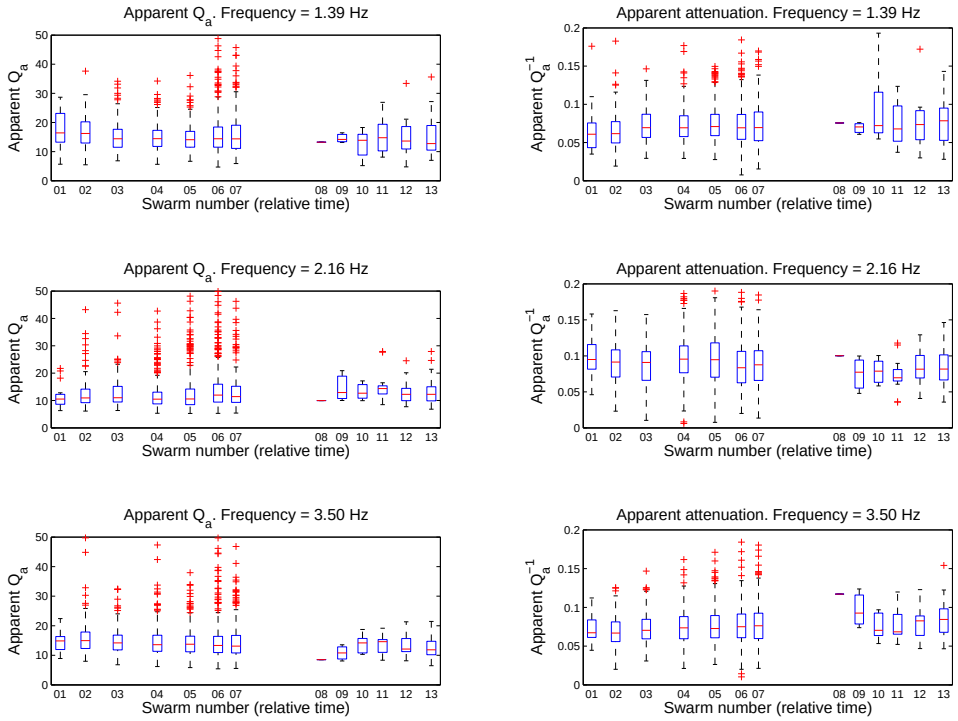

Figure 5.29: Box plot displaying the apparent Q_a and attenuation distributions for *all* Family A swarms, measured at three frequencies, to highlight any differences or similarities between the pre- and post-dome collapse swarms of events.

Family C

In the days immediately following the collapse Family A is no longer the dominant family, in terms of event numbers, of the recorded low-frequency seismicity. By analysing events from other waveform families, the attenuation of low-frequency earthquakes between different families can be compared. One of the families of events which only occurs *after* the dome collapse is Family C (see Figure 5.4), making it an appropriate choice for analysis here.

In total, 139 earthquakes were recorded and classified into waveform Family C by Green et al. (2006), occurring across five swarms. The stacked waveforms and their associated spectra for each of the swarms are shown in Figure 5.30. Note the difference between these earthquakes and Family A, as they show a more distinct higher frequency onset, reflected in a slightly broader spectral content and different dominant spectral peak. The individual amplitude spectra and their largest spectral peaks, shown in Figures 5.31 and 5.32, suggest a single spectral peak for analysis of 2.0Hz.

The attenuation and Q_{a} values, measured at 2.0Hz, are displayed in Figure 5.33, showing a lower Q_{a} or higher attenuation than for Family A. The box plots of the distributions of values within each swarm in Figure 5.33 show that the median value for each swarm lies between $10 \leq Q_{\mathrm{a}} \leq 15$, lower than for the Family A results. This indicates that there are measurable differences in attenuation between waveform families, as well as the differences in their waveforms and spectral content.

The presence of several co-existing waveform families of low-frequency earthquakes at SHV suggests that a number of different resonators may be active at any one time (Green et al., 2006), a hypothesis corroborated by the location analysis of Green (2005) which showed that the locations of events in different families are separated by the order of a few hundred metres. This conclusion makes the interpretation of differences in the attenuation between families more difficult, as a change in source location is likely to cause a change in the radiative component of the attenuation. Hence, any relative differences between different families cannot be wholly attributed to changes in the intrinsic component or, therefore, the fluid properties.

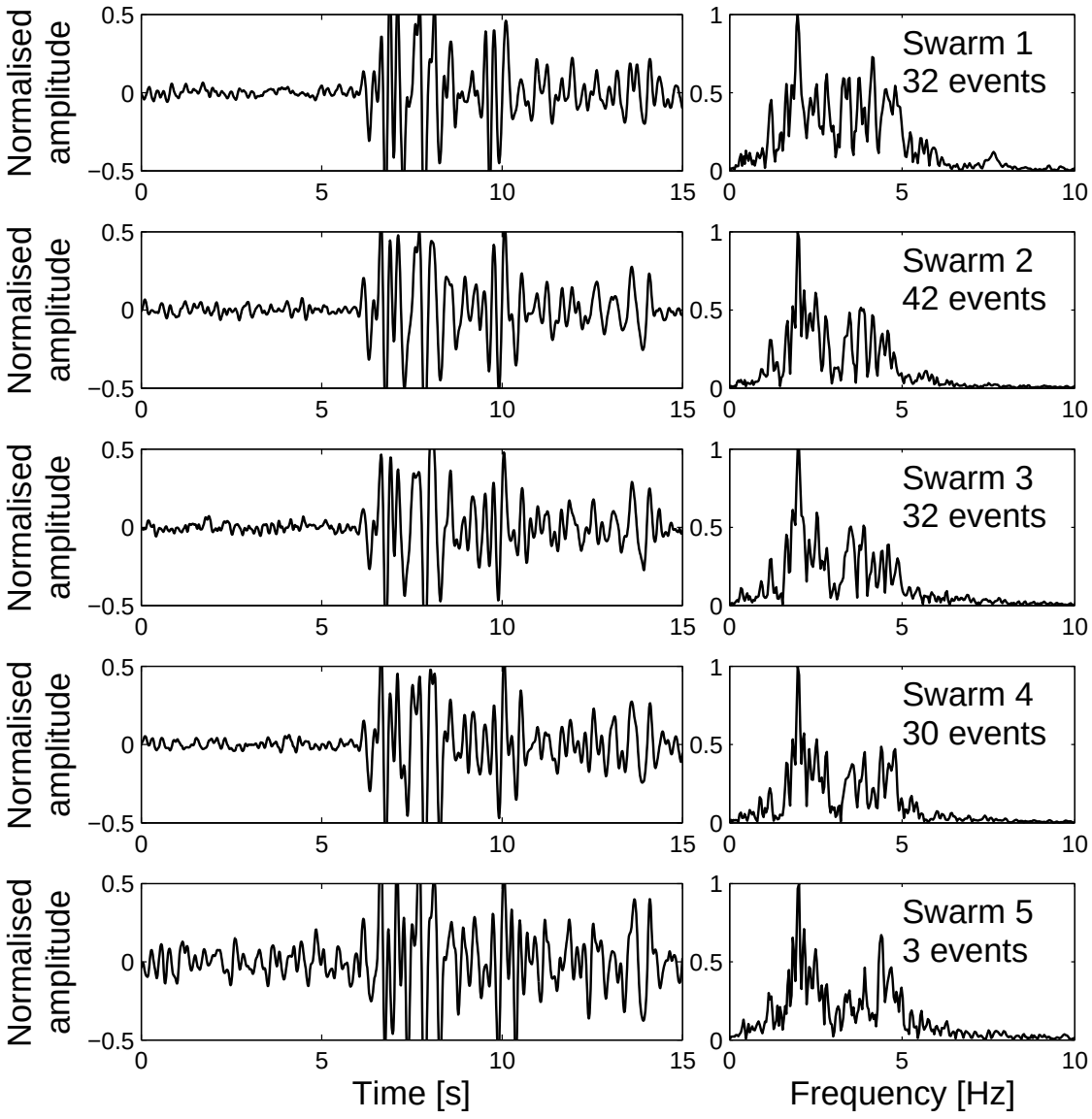

Figure 5.30: Stacked waveforms and associated spectra for the five swarms of Family C earthquakes following the 25th June dome collapse. Both velocity and spectral amplitudes have been normalised, and the velocity seismograms have been bandpass filtered between 0.5 and 5 Hz. The plot also indicates the number of events contained in each swarm.

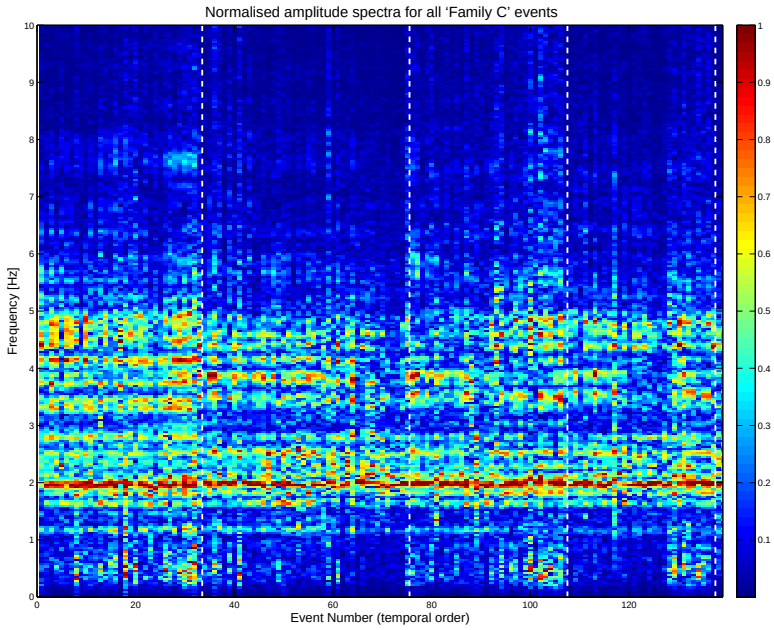

Figure 5.31: Amplitude spectra for post-dome collapse Family C events in temporal order, plotted as a function of the event number. The vertical white dashed lines indicate discontinuities, and mark the boundaries between swarms.

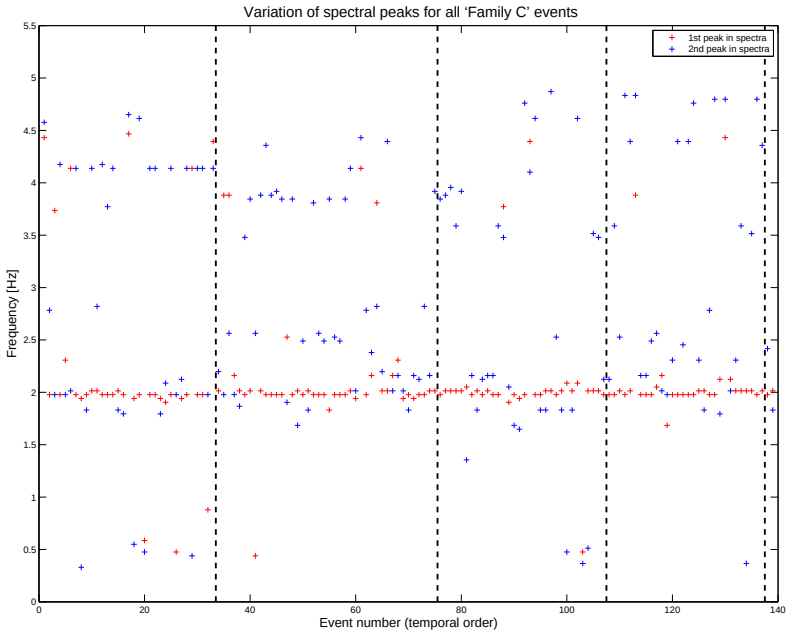

Figure 5.32: Variation of the spectral peaks of Family C events in temporal order, as a function of the event number. The position of the largest two values of the amplitude spectrum was determined for each event, and is shown here as a function of the event number. The energy is concentrated in one distinct energy band at almost exactly 2.0Hz.

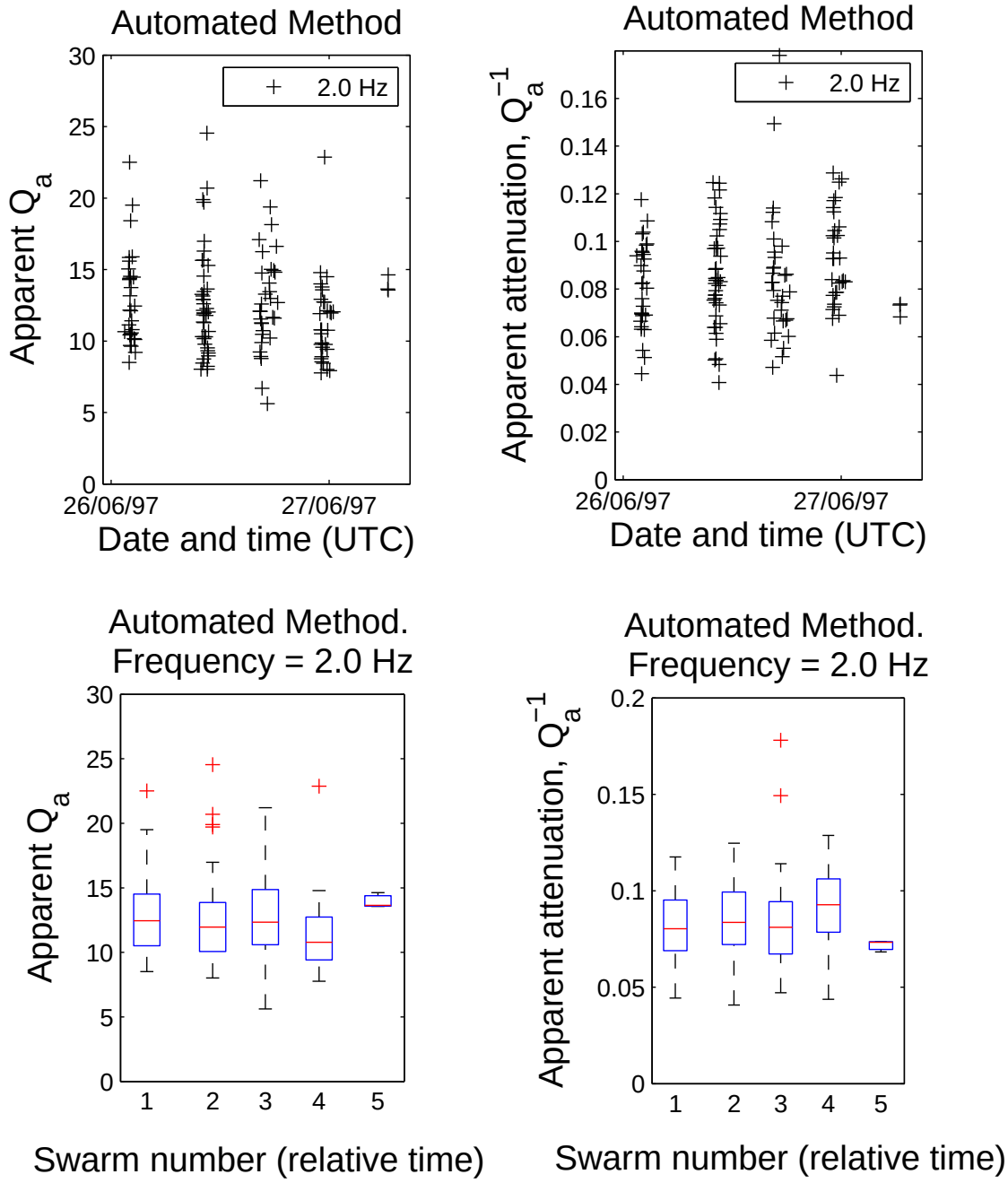

Figure 5.33: Apparent Q_a and attenuation as a function of time for Family C events, measured at 2.0Hz. The top two plots show the raw data values, whilst the lower two box plots indicate the distribution of values within each swarm of events.

5.3 Linking attenuation and viscosity

5.3.1 Interpreting temporal variations

The earthquakes used to measure the attenuation in this chapter were all recorded at the same station (MBGA) on the same component (vertical) and, because of the high degree of waveform similarity between events, the source must be stationary. Therefore, there can be no variation in the source-receiver geometry for all the events within a single waveform family. This implies that any observed temporal changes in the value of attenuation measured can be attributed purely to the intrinsic part, as significant changes in the resonator geometry seem unlikely on such timescales (hours to days) and can be confidently ruled out because, as shown in Figures 5.6 and 5.8, the spectral content remains remarkably consistent across all swarms. This leaves changes in the intrinsic properties of the magmatic fluid as the only viable source for any observed changes in the measured attenuation. This is an important point, as it allows direct interpretation of the temporal variations of the measurements in terms of the fluid properties, independent of the radiative component - something which cannot be done when comparing values between different families with different source locations.

5.3.2 Explaining the changes in intrinsic attenuation

Observations

In Section 5.2.1, the temporally smoothed measurements of attenuation at 1.39Hz showed a pattern of decreasing then increasing attenuation within singles swarms (Figure 5.22). This pattern was shown to correlate with the event rate (Figure 5.23), which exhibits a similar pattern of acceleration and deceleration within a single swarm (Figure 5.3).

As discussed, since these are temporal changes within a single family they can be attributed to the intrinsic part, as the radiative part cancels for relative measurements if we assume it is fixed with time:

$$\begin{aligned}\Delta Q_{\mathrm{a}}^{-1} = Q_{\mathrm{a}}^{-1}(t_2) - Q_{\mathrm{a}}^{-1}(t_1) &= \left(Q_{\mathrm{i}}^{-1}(t_2) + Q_{\mathrm{r}}^{-1}\right) - \left(Q_{\mathrm{i}}^{-1}(t_1) + Q_{\mathrm{r}}^{-1}\right) \\ &= Q_{\mathrm{i}}^{-1}(t_2) - Q_{\mathrm{i}}^{-1}(t_1) = \Delta Q_{\mathrm{i}}^{-1} \end{aligned} \tag{5.2}$$

where $\Delta Q_{\mathrm{a}}^{-1}$ is the measured change in apparent attenuation between two times t_1 and t_2, and $\Delta Q_{\mathrm{i}}^{-1}$ is the corresponding change in the intrinsic attenuation. What possible

physical changes in the shallow plumbing system could produce this pattern of attenuation within the swarms? In the next section a possible model or scenario to generate the observed changes in intrinsic attenuation is considered.

Model

To change the intrinsic attenuation of the fluid, Q_{i}^{-1}, requires a change in the viscosity. In Chapter 3 it was shown that the attenuation experienced by interface waves at the fluid-solid boundary is *only* dependent on the *shear* viscosity of the fluid. If it is assumed that low-frequency earthquakes are due to resonance of interface waves, and that the intrinsic attenuation considered is that experienced by interface waves, then a change in Q_{i}^{-1} requires a change in the (bulk) shear viscosity of the magma.

The data in Figure 5.22 first show a *decrease* in attenuation to a minimum, followed by an increase or recovery, within the swarm. To produce a decrease in the intrinsic attenuation, Q_{i}^{-1}, requires a decrease in the shear viscosity. Hammer & Neuberg (2009) suggest that the overall acceleration in event rate of seismicity across several swarms preceding the dome collapse can be attributed to an increase in the magma ascent velocity. A possible explanation offered for this increase in ascent velocity was that repeatedly triggering seismicity through brittle failure weakens the melt in shear zones at the conduit walls, making it progressively easier to fail.

A similar mechanism is proposed within a single swarm, with the initial acceleration in event rate and ascent velocity due to the development of shear zones. This, they suggest, would lead to a decrease in the bulk viscosity, which is exactly what is required to produce a decrease in attenuation. As the pressure gradient in the magma column falls, the corresponding decrease in flow rate would lead to a stiffening of the magma, thus increasing the viscosity again. This idea fits with the observed patterns in the data and is backed up by the correlation between attenuation and event rate for the binned data in the chosen swarms. The increase in event rate can be interpreted as an increase in the flux and therefore the shear stress. This observed dependence of the attenuation and hence the viscosity on the shear-stress could be indicative of non-Newtonian behaviour. Despite these subtle variations within swarms there is, however, no trend of decreasing attenuation visible across all the swarms preceding the dome collapse that would match the overall acceleration in event rate. Nevertheless, this represents a plausible physical model to explain the subtle variations within each swarm.

The ideas outlined are summarised in Figure 5.34:

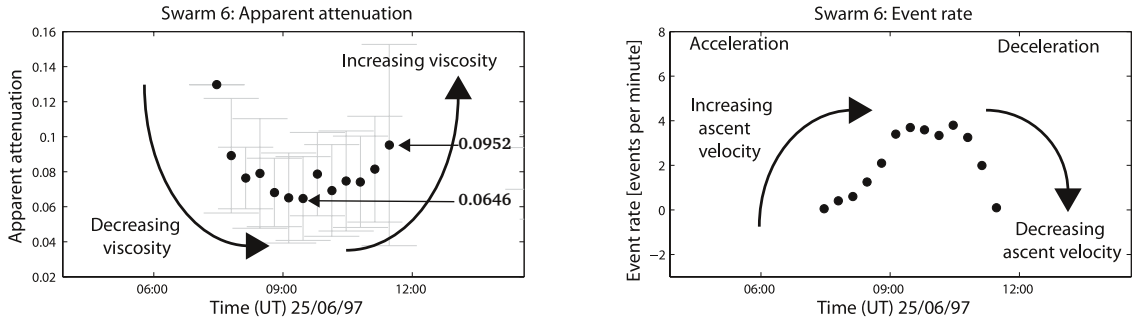

Figure 5.34: A possible physical model to explain the temporal changes in attenuation. Shown are the apparent attenuation values at 1.39Hz (left) and the event rate (right) for Swarm 6, for data in 20 minute bins. The acceleration and deceleration of the event rate, is due to fluctuations in the ascent rate, leading to changes in the shear viscosity. This in turn causes the decrease then increase in the measured apparent attenuation.

5.3.3 Seismological constraints on the magma

So far, the interpretation of the observed temporal changes in the attenuation has been qualitative, focusing on a physical model to explain the trends and patterns seen within a swarm of earthquakes. However, a major aim of this thesis was to explore the possibility of using seismology to place constraints on the physical properties of the fluid within the resonator. In this section the changes in intrinsic attenuation are quantitatively interpreted in terms of magma viscosity.

The results in Figures 5.22 and 5.34, showed a pattern of decrease then increase in attenuation at 1.39Hz within a single swarm. Focusing on the results of Swarm 6 in Figure 5.34, the magnitude of this change (from maximum to minimum) is given by:

$$\Delta Q_{\mathrm{a}}^{-1} = \Delta Q_{\mathrm{i}}^{-1} = Q_{\mathrm{i}}^{-1}(t_2) - Q_{\mathrm{i}}^{-1}(t_1) = 0.0646 - 0.0952 = -0.0306 \pm 0.0621 \qquad (5.3)$$

As previously discussed, for this case a temporal change in Q_{a}^{-1} can be attributed directly to a change in Q_{i}^{-1}. If it is assumed that this corresponds to the attenuation experienced by interface waves at the boundary between the magma and country rock, then the change in intrinsic attenuation can be quantitatively linked to the change in viscosity through the relationship derived in Chapter 3.

Figure 5.35 shows the interface wave Q_{i} and attenuation as a function of the shear viscosity, at frequencies of 1.39Hz and 2.16Hz, corresponding to those at which the apparent attenuation was measured. The curves were calculated using Equation 3.15,

with the parameters used typical of SHV (Collier & Neuberg, 2006), and listed in the box in the upper figure. However, despite having a measurement of the relative change in Q_{i}^{-1}, without an estimate of the radiative part, the absolute position on the curve cannot be fixed, and the change in Q_{i}^{-1} cannot be tied to a change in viscosity. Hence, an absolute estimate of viscosity cannot be directly obtained. If Q_{r}^{-1} is positive, the largest Q_{i}^{-1} can be is if Q_{r}^{-1} is negligible, meaning all the attenuation is due to the intrinsic component. Using the maximum absolute value for the apparent attenuation of the swarm of $Q_{\mathrm{a}}^{-1} = Q_{\mathrm{i}}^{-1} = 0.0952 \pm 0.0575$, would place an upper bound on the viscosity of $2.3 \pm 2 \times 10^5$ at 1.39Hz, using the curve shown in Figure 5.35.

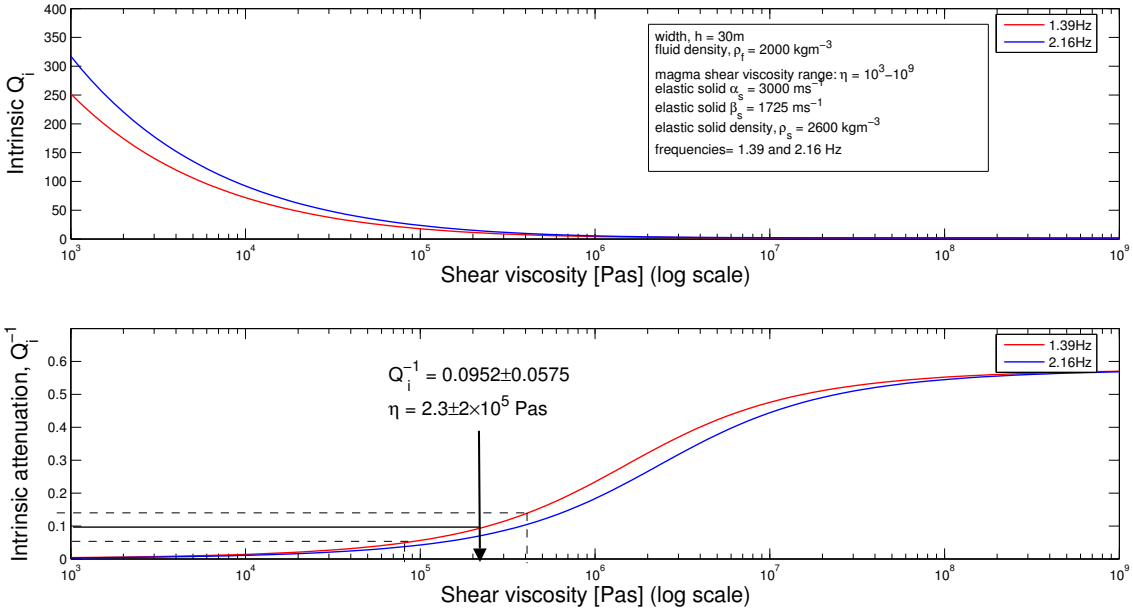

Figure 5.35: Interface wave Q_{i} and attenuation as a function of the shear viscosity, at frequencies of 1.39Hz and 2.16Hz, corresponding to those at which the apparent attenuation was measured. The curves were calculated using Equation 3.15, with the parameters used typical of SHV (Collier & Neuberg, 2006) and listed in the box in the upper figure. A pure melt, with equal shear and volume viscosities was also assumed. The maximum absolute value for the apparent attenuation in Swarm 6 (Figure 5.34) of $Q_{\mathrm{a}}^{-1} = 0.0952$, places an upper bound on the viscosity of $2.3 \pm 2 \times 10^5$Pas at 1.39Hz.

Frequency dependence

This analysis has, so far, focused on the measurements of attenuation using the most stable spectral peak at 1.39Hz. However, it is important to remember that measurements of the attenuation were made at two other frequencies, and this additional information can be used to constrain the viscosity further. The difference between measurements of

the attenuation at two frequencies cannot be used to estimate the intrinsic attenuation, because as shown in Chapter 2, the radiative component is not constant with frequency, so does not cancel out if relative measurements are made.

However, two sets of relative measurements with time, measured at two different frequencies, can be used to estimate the absolute viscosity, by considering their ratio. The attenuation as a function of viscosity can be evaluated at two different frequencies, using the expression in Equation 3.15. By considering the ratio of the gradient of these two functions with respect to viscosity, the absolute viscosity corresponding to this ratio can be found, since it is assumed that the same change in viscosity, $\Delta\eta$, must be responsible for the same change in attenuation at both frequencies:

$$\frac{\Delta Q_{\mathrm{i}}^{-1}(f_1,\eta)}{\Delta\eta} \Big/ \frac{\Delta Q_{\mathrm{i}}^{-1}(f_2,\eta)}{\Delta\eta} = \frac{\Delta Q_{\mathrm{i}}^{-1}(f_1)}{\Delta Q_{\mathrm{i}}^{-1}(f_2)}\,(\eta) \tag{5.4}$$

where the ratio of the gradients can be plotted as a function of the viscosity. The value of the absolute viscosity corresponding to the ratio determined from the data can be read off from the graph of this relationship. Still focusing on Swarm 6, the change in the attenuation at 2.16Hz is displayed alongside that at 1.39Hz in Figure 5.36. Taking the

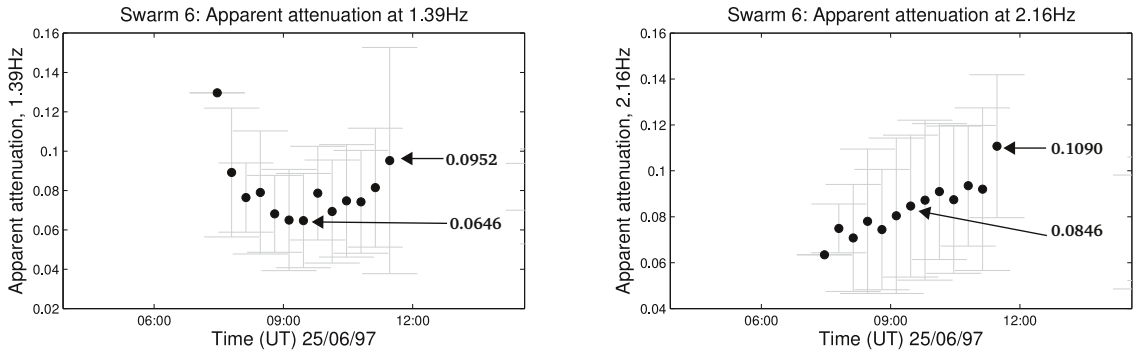

Figure 5.36: Apparent attenuation at 1.39 and 2.16Hz during the sixth swarm of earthquakes preceding the dome collapse, for the measurements binned into 20 minute bins.

second half of the swarm where attenuation increases at both frequencies, the change in attenuation at the two frequencies is given by

$$\begin{aligned}\Delta Q_{\mathrm{a}}^{-1}(f_1) &= 0.0952 - 0.0646 = 0.0306 \pm 0.0621 \\ \Delta Q_{\mathrm{a}}^{-1}(f_2) &= 0.1090 - 0.0846 = 0.0244 \pm 0.0438\end{aligned} \tag{5.5}$$

leading to a ratio of

$$\frac{\Delta Q_{\mathrm{i}}^{-1}(f_1)}{\Delta Q_{\mathrm{i}}^{-1}(f_2)} = \frac{0.0306 \pm 0.0621}{0.0244 \pm 0.0438} = 1.254 \pm 3.398 \tag{5.6}$$

The gradient, with respect to viscosity, was calculated numerically for the curves of attenuation against viscosity at the two different frequencies in Figure 5.35. The ratio of these curves is also plotted, showing that the maximum ratio of 1.348 occurs at a viscosity of 10^5 Pas. The value of the gradient obtained from the data was 1.254, which corresponds to a viscosity of $\approx 5 \times 10^5$ Pas from the analytical curve in Figure 5.37. This is close to, but still slightly larger than, the upper bound of $2.3 \pm 2 \times 10^5$ Pas given by assuming negligible radiative contribution. This estimate of the viscosity does not seem unreasonable, and is within the range of 10^3 to 10^6 Pas, given by Collier & Neuberg (2006) for the shear viscosity of the magma at SHV. However, given the large uncertainty bounds associated with both the changes in attenuation and the resulting ratio, this result should be interpreted with extreme care.

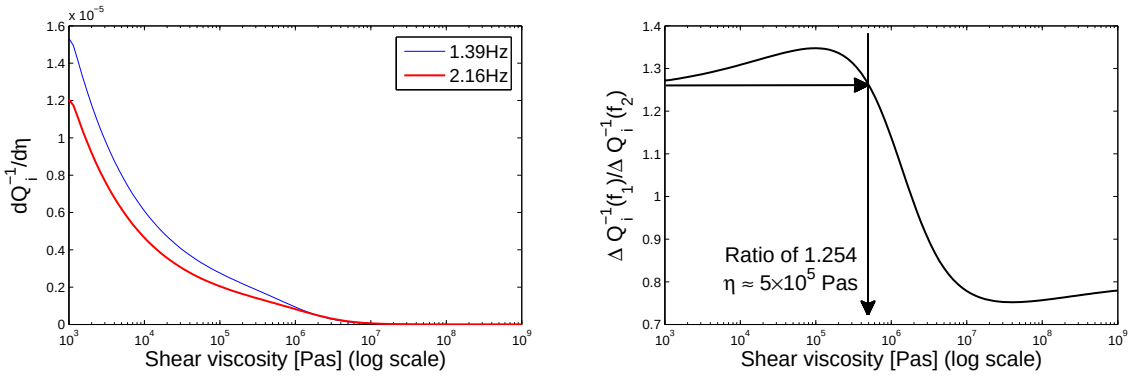

Figure 5.37: Gradient of intrinsic attenuation with respect to viscosity. The left hand plot shows the gradient (calculated numerically) of the attenuation with respect to viscosity for the two frequencies, 1.39Hz and 2.16Hz. The right hand plot shows the ratio of these two curves as a function of viscosity. The ratio between the relative measurements at the different frequencies measured from the data was 1.254. Using the curve in the right hand plot, this corresponds to an absolute value of the shear viscosity of $\approx 5 \times 10^5$Pas.

Discussion

The estimations of the shear viscosity given in the previous section should be approached with a degree of caution, as they are based on several underlying assumptions:

- The first assumption is that the radiative part of the attenuation is constant with time, for a given waveform family, at a given frequency, allowing it to cancel out for relative measurements.
- The second assumption is that the intrinsic part of the attenuation corresponds

directly to that experienced by interface waves, $Q^{-1}_{\text{interface}}$.

- The relationship between the interface wave attenuation and viscosity, derived in Chapter 3, assumes a Kelvin-Voight rheology for fluid. The magma is also assumed to be a pure melt, with equal shear and volume viscosities, and takes no account of other physical processes, such as bubble growth, that strongly affect the attenuation in a three-phase magma.

- The relationship between the interface wave attenuation and viscosity also depends on the choice of parameters, such as the width of the fluid layer, the fluid density, and the density and seismic velocities of the surrounding elastic medium. Only one set of parameters, albeit thought to be appropriate for SHV, was used in the evaluation of the relationship in this analysis.

- The large uncertainties associated with the attenuation measurements must also be considered, and suggests that the viscosity estimates cannot be taken with a high degree of confidence, particularly the estimate derived from changes in attenuation at two different frequencies. The differences between the mean and median of attenuation value distributions within the swarms (e.g. Figure 5.22) suggest the need for more robust statistical analysis, such as skewness, to improve confidence in the observed temporal patterns of attenuation.

Nevertheless, despite these limitations, assumptions and uncertainties, a valid methodology has been outlined which does allow the seismological data to place constraints on the magma and gives quantitative estimates of the shear viscosity of the magma at SHV.

5.4 Discussion and Conclusions

5.4.1 Comparison with Q_{a} at other volcanoes

Since the analysis in Section 5.2 is the first to measure the attenuation of low-frequency events at SHV, a useful exercise is to compare the values of Q_{a} determined for SHV with those measured at other volcanoes, since this provides an additional check on the validity of the measurements. Table 5.4.1 shows the range of measured apparent Q_{a} values from various volcanoes worldwide. The data in the table were compiled from several studies, all of which measured the complex frequencies to determine the apparent quality factor. Comparing the results of the analysis at SHV with the values in Table 5.4.1 suggests

Author	Volcano	Range of Q values
Kumagai & Chouet (1999)	Redoubt, Alaska.	20-50
Kumagai & Chouet (1999)	Kilauea, Hawaii.	20-50
Kumagai & Chouet (1999)	Kusatsu-Shirane, Japan.	>100 (up to 500)
Kumagai & Chouet (1999)	Galeras, Colombia.	>100 (up to 500)
Kumagai et al. (2002)	Kusatsu-Shirane, Japan.	10-160 (average 100)
Nakano & Kumagai (2005b)	Kusatsu-Shirane, Japan.	20-100
De Angelis & McNutt (2005)	Mt. Spurr, Alaska.	25-105
Molina et al. (2004)	Tungurahua, Ecuador.	100-400
Molina et al. (2008)	Cotopaxi, Ecuador.	Scatter of values >100

Table 5.2: Measured apparent Q_a values from various volcanoes. The data in this table were compiled from several studies, all of which measured the complex frequencies to determine the apparent quality factor.

that SHV is certainly not atypical, as an intrinsic Q_a of between 20-50 is typical of the range recorded for several other silicic or andesitic volcanoes. If the results of only the automated method are considered, the range of Q_a values determined for the Family A events is $10 \leq Q_a \leq 20$, and even lower for the Family C events. This puts the SHV results on the lower end of any of the ranges given in the table. This observation suggests that, based on this preliminary analysis, the conduit system responsible for generating the low-frequency seismicity at SHV may be more attenuating than other volcanoes.

5.4.2 Conclusions

In this chapter attenuation analysis was carried out for a dataset of low-frequency earthquakes recorded at Soufrière Hills Volcano, Montserrat. The dataset comprised of earthquakes between 23rd and 28th June 1997 classified into families, on the basis of waveform similarity, by Green & Neuberg (2006). These earthquakes were analysed and the temporal variation of the measured attenuation was examined. The attenuation measured from earthquakes preceding and following a significant collapse of the lava dome were compared, as was the attenuation of earthquakes from different waveform families. From the results of the analysis the following conclusions can be drawn:

- Attenuation values were initially calculated using three different methods. The best of the automated measurement methods developed in Chapter 4, based on a weighted average of segments of negative gradient and using the S-transform to isolate frequencies, was the most robust of the methods tested, and hence was chosen for analysis in the remainder of the chapter.

- Analysis of Family A events occurring before and after the dome collapse suggested that the collapse did not significantly affect the attenuation, consistent with the occurrence of a particular family of earthquakes requiring the *same set of internal conditions* triggering the *same resonator*. However, subtle variations *within* earthquake swarms were observed.

- Analysis of Family C events showed that there are measurable differences in attenuation between waveform families, as well as differences in their waveforms and spectral content. The presence of several co-existing waveform families of low-frequency earthquakes at SHV suggests that a number of different resonators may be active at any one time, a conclusion which makes the interpretation of differences in the attenuation between families more difficult, as a change in source location is likely to cause a change in the radiative component of the attenuation.

- Temporal smoothing of the results for the swarms of earthquakes preceding the dome collapse revealed temporal trends in the attenuation behaviour within swarms. For temporal variations within a given waveform family, at a given frequency, the changes in apparent attenuation can be mapped to changes in intrinsic attenuation. A decrease then increase in attenuation was observed that correlated with the acceleration then deceleration in event rate seen within each swarm. A physical model was proposed to explain these variations, where fluctuations in magma ascent rate explain both the changes in event rate and the changes in viscosity required to produce the observed changes in attenuation. This model also hints at non-Newtonian flow behaviour. However, large uncertainties in these measurements suggest the need for more robust statistical analysis to improve confidence in the observed temporal trends.

- A methodology was proposed to give a quantitative interpretation of these temporal changes in the apparent attenuation, based on the assumption that they map to the intrinsic attenuation of interface waves. This gave estimates of the magma shear viscosity of $2.3 \pm 2 \times 10^5$ Pas, consistent with the range of values previously proposed by Collier & Neuberg (2006) for SHV of 10^3-10^6 Pas, although again there are large uncertainties associated with this estimate.

- The absolute values of measured Q_a for SHV are on the low end of the scale, when compared to typical values for the apparent Q_a determined at other volcanoes in

other studies, suggesting that the conduit system responsible for generating the low-frequency seismicity at SHV may be more attenuating than elsewhere.

- Temporal changes of the apparent attenuation have been observed at SHV, and these were interpreted in terms of intrinsic changes in the properties of the magma. Comparing the attenuation at different time periods during the eruption could test if there are observable changes in attenuation during different eruptive phases. Further data analysis would also allow a catalogue and baseline level of attenuation to be compiled, which may prove useful as a monitoring and forecasting tool.

Chapter 6

Discussion

In this chapter the wider volcanological implications, along with some of the limitations, of the key results of this research are discussed. The significance of the results presented in the previous chapters of this thesis are placed in context, with a discussion based on the aims and key questions identified in Section 1.7.2.

6.1 Interface and acoustic waves

Acoustic waves are longitudinal compressional waves that can propagate within a fluid such as magma. The speed of propagation of these waves is termed the acoustic velocity of the fluid. At the boundary between a fluid and an elastic solid a different type of wave can propagate, which exists only at the interface between the two media. Interface waves have been recognised as important in volcano-seismology, and resonance of these waves in fluid-filled bodies has become a well established model for the generation of low-frequency earthquakes. Such interface waves exhibit very different behaviour in terms of their amplitude and velocity to acoustic waves. A key feature is that they are *dispersive*, that is their velocity varies with frequency, and one particular type or mode of these waves travels with a phase velocity that is slower than the acoustic velocity of the fluid. A consequence of this dispersion and slow velocity is that they can explain the low-frequency content of observed seismic signals through resonance in a comparatively small source body, compared to that which would be required for similar 'organ-pipe' modes of standing acoustic waves.

This study has focused on the attenuation of low-frequency earthquakes, and understanding how interface waves are attenuated has proved to be a key part of the quantitative

analysis. Since their amplitude and dispersion characteristics are clearly different to those of acoustic waves, it should not be assumed that acoustic and interface waves are attenuated in the same way, something which has not seriously been considered before by authors analysing attenuation on volcanoes, as Collier et al. (2006) point out. In Chapters 2 and 3 of this thesis, it was shown that interface waves are less attenuated than acoustic waves for a given set of parameters, with particular conditions placed on the fluid shear and volume viscosities.

If the attenuative effects of viscosity are less for interface waves than for acoustic waves, then this widens the set of possible resonators, as a higher viscosity fluid can be employed to produce the same level of damping of the seismic energy as acoustic waves would experience. As discussed in Section 1.4, many authors have favoured narrow, crack-like geometries, filled with low viscosity, low attenuating fluids, with a high impedance contrast required to explain the extended signal duration. Such models may well be appropriate for certain volcanoes, such as Kusatsu-Shirane, Japan, where low-frequency earthquakes with apparent quality factors of higher than 100 have been observed, and explained by ash-gas mixtures (Kumagai & Chouet, 1999). What this research has shown, however, is that this does not necessarily have to be the case. The conduit resonance model, with a lower aspect ratio and higher fluid viscosity can also act as a viable source resonator for low-frequency earthquakes.

One caveat that should be issued with this interpretation is that the analytical derivation in Chapter 3 was based on the assumption that the fluid behaves like a Kelvin-Voight material. Dingwell (1995) suggested that a bubble and crystal free melt behaves more like a Maxwell body, even during glass transition (Dingwell & Webb, 1990), while a three-phase magma can exhibit various rheological behaviours, depending on the gas and crystal contents (e.g. Prud'Homme & Bird, 1978; Hess & Dingwell, 1996). These studies suggest that the impact of different rheological models of the fluid on the analytical expression for interface wave attenuation is something which should be considered in future studies.

6.2 Resonance, attenuation, and low-frequency earthquakes

A number of authors (Neuberg et al., 2000; Jousset et al., 2003; 2004; Neuberg et al., 2006; Sturton & Neuberg, 2006) have proposed resonance of a magma-filled conduit or dyke as a source of low-frequency seismicity on volcanoes, particularly at Soufrière Hills Volcano, Montserrat. One of the criticisms of this model has been that if the source body contains high viscosity, bubble-rich silicic magma such as andesite, then the attenuation of the fluid would be too high to support resonance as seismic energy would be too rapidly damped (Chouet, 1996b). The question of whether such a viscous magma can support resonance has yet to be fully answered.

In a study which used numerical models of bubble growth to quantify the attenuation in a gas-charged magma, Collier et al. (2006) calculated how far a seismic wave could propagate in such a magma before its amplitude was damped below the background noise level (Figure 6.1). They concluded that the maximum distance a 1-3Hz wave could propagate was around 1000m, and because the energy must be able to travel up and down multiple times within the resonator, this constrained the maximum size of the source body to be ∼200m, although this depended on several parameters notably the bubble number density.

However, this analysis was based only on acoustic attenuation, i.e. that experienced by acoustic waves propagating within the fluid, and assumed a simple exponential decay of the amplitude with distance based on the modelled quality factors. As shown both numerically and analytically in Chapters 2 and 3, interface waves do not experience the same level of attenuation as acoustic waves. In fact, it was shown by the gradients estimated in Chapter 2 that interface waves can be attenuated less than acoustic waves by a factor of up to 5. This result suggests the maximum propagation distances given by Collier et al. (2006) could be extended by this factor. Hence, if the distance an interface wave can propagate before being damped is 5 times larger, as energy is more efficiently trapped by interface waves, then this implies conduit sections several times longer than 200m would be able to sustain or support resonance.

This suggests models of resonance with conduit lengths of up to 1000m or longer (e.g. Jousset et al., 2003; 2004; Sturton & Neuberg, 2006) proposed for SHV may indeed represent feasible and realistic sources of low-frequency earthquakes.

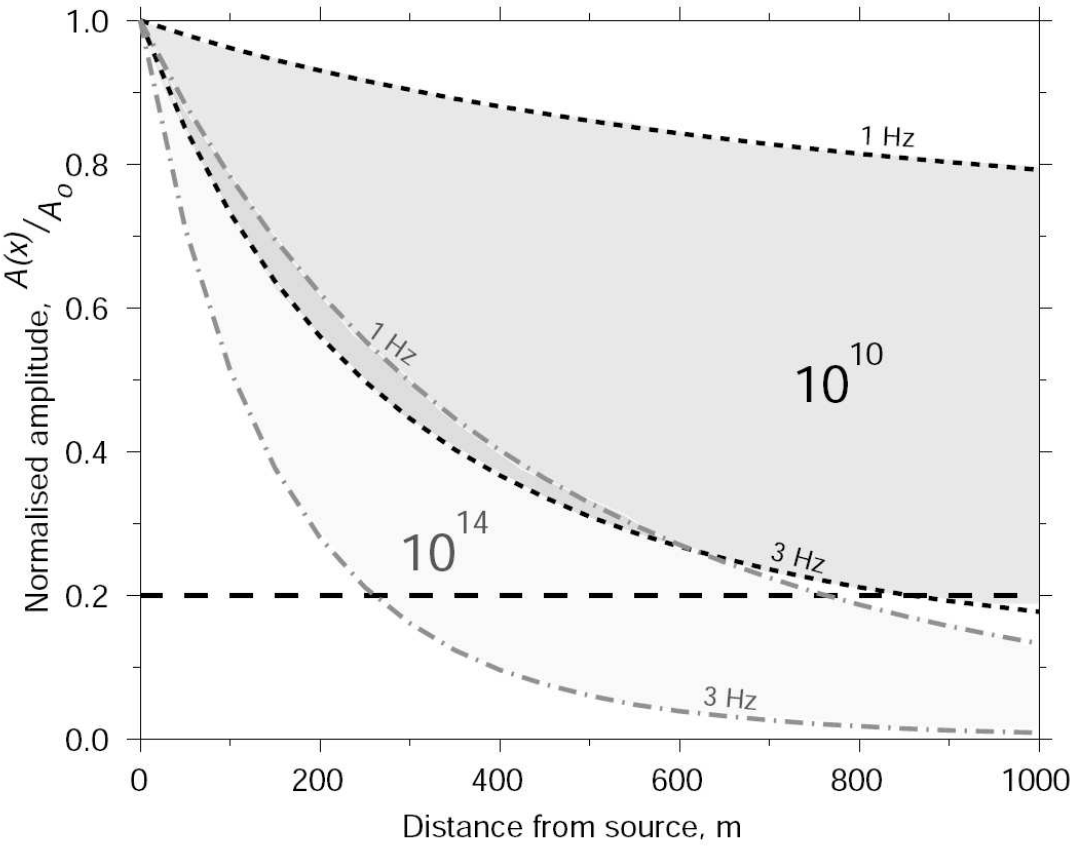

Figure 6.1: Distance a 1-3 Hz acoustic wave could travel within a conduit filled with gas-charged magma. Two different bubble number densities were considered: $n = 10^{10}\mathrm{m}^{-3}$ (dark shaded area) and $n = 10^{14}\mathrm{m}^{-3}$ (light shaded area). For the lower bubble number density the wave could travel approximately 1000m before becoming lost in the noise. The background noise threshold was chosen to be 20% of the initial amplitude. Taken from Collier et al. (2006).

6.3 Decomposing the attenuation

As discussed in Chapter 1, Aki (1984) was the first to propose that the energy loss from a vibrating fluid body could be decomposed. He put forward the idea that the total seismic amplitude loss could be represented as a sum of the radiation and intrinsic losses:

$$Q_{\mathrm{a}}^{-1} = Q_{\mathrm{i}}^{-1} + Q_{\mathrm{r}}^{-1} \tag{6.1}$$

where Q_{r}^{-1} is the attenuation corresponding to radiation loss, and Q_{i}^{-1} is the intrinsic or viscous attenuation which Aki (1984) attributed to magma viscosity.

This relationship has been assumed and applied to volcanic signals by several authors, without consideration of both components simultaneously. Previous studies that used the

attenuation of low-frequency volcanic earthquakes as a probe for the fluid composition either, (i) ignored Q_i completely (Morrissey & Chouet, 2001) or, (ii) treated it separately to the radiative part (Kumagai & Chouet, 2000). The research in Chapter 2 showed that the simple relationship in Equation 6.1 is not valid, if the intrinsic part is simply assumed to be the attenuation experienced by an acoustic wave propagating within the fluid. What in fact should be considered is that the Q_i^{-1} corresponds to the attenuation experienced by interface waves and not acoustic waves, and as shown in Chapter 3 these are, in general, not the same. The results of the modelling in Chapter 2 showed that a more appropriate relationship is

$$Q_\mathrm{a}^{-1} = \kappa Q_\mathrm{acoustic}^{-1} + Q_r^{-1}, \tag{6.2}$$

with the total intrinsic contribution coming from interface waves

$$Q_\mathrm{interface}^{-1} = \kappa Q_\mathrm{acoustic}^{-1}, \tag{6.3}$$

where κ is a scale factor that was shown to be less than 1, implying interface waves are less attenuated than acoustic waves, with values between 0.15 and 0.4.

This difference between interface and acoustic wave attenuation is important when it comes to quantitatively interpreting measured attenuation values and making inferences about the composition or properties of the fluid responsible for the resonance. For example, Kumagai & Chouet (2000) employed the crack model of Chouet (1986; 1988; 1992) to determine the radiative Q_r for various fluids - based on interface wave resonance (they use the term 'crack waves') - but then went on to calculate the intrinsic attenuation of these fluids based on *acoustic* wave propagation. This suggests that their comparison between Q_i and Q_r should be adjusted to take account of this, as the attenuative effects of the fluid on the resonance may have been overestimated. It is not clear, however, that interface waves necessarily propagate or are attenuated in the same way if the resonator is filled with a purely gas phase, such as the ash and gas mixtures of Morrissey & Chouet (2001), rather than a liquid (melt) or three-phase fluid.

In Chapter 2, it was shown that the radiative component of the attenuation is highly geometrically dependent, and this has consequences, especially for obtaining absolute measurements of the intrinsic attenuation from the measured apparent attenuation. This suggests there are strong advantages in using *relative* measurements of attenuation. For a stationary source, with no change in source-receiver geometry, the radiative part can be assumed to be constant over short timescales. This means that it will cancel if relative

measurements at different times are compared, allowing the apparent attenuation to be mapped directly to changes in the intrinsic component, some applications of which are discussed in the final section.

6.4 Seismological constraints on the magma properties

Low frequency earthquakes have been observed on many volcanoes worldwide and are considered key tools in volcanic monitoring and eruption forecasting. A model to explain the occurrence of low-frequency earthquakes such as those observed on Soufrière Hills Volcano, Montserrat, is conduit resonance, where seismic energy generated by brittle failure of the melt is trapped in a resonating system (Neuberg et al., 2006). The seismic parameters in such a volcanic environment are strongly dependent on the properties of the magma, which control the character of this resonance and hence in turn the characteristics of the low frequency seismicity. Crucially therefore, low-frequency earthquakes provide volcano monitoring organisations with one of the few direct links between surface observations and internal magma processes, and the ability of seismic attenuation as an attribute to place constraints on these fluid properties will now be discussed.

Intrinsic attenuation is controlled by the properties of the material through which a seismic wave propagates, hence measuring the attenuation of seismic waves can constrain these properties. In particular, studying the temporal amplitude decay of low-frequency earthquakes can be used to examine the intrinsic attenuation of the fluid within the resonator. In Chapter 2 it was shown that the effective intrinsic attenuation that should be considered for this resonance is that of interface waves, and not that corresponding to acoustic waves within the fluid. In Chapter 3 it was shown that interface wave attenuation and viscosity can be linked through an analytical relationship, with the attenuation depending on the shear viscosity of the fluid.

However, as discussed in the previous section, the measured apparent attenuation is a combination of both intrinsic and radiative effects. Therefore, to estimate and constrain magma properties, the intrinsic part must somehow be isolated or separated. A possible methodology to estimate the magma viscosity from seismic signals is as follows:

1. Measure the apparent Q_{a}^{-1} from the seismic data, at specific frequencies chosen from the resonant peaks in the spectra.

2. Use the finite-difference model with no intrinsic attenuation to obtain Q_{r}^{-1} as accurately as possible for the specific source-receiver geometry, including if possible realistic topography and an appropriate source geometry.

3. Subtract Q_{r}^{-1} from Q_{a}^{-1}, remembering to consider that the remainder, Q_{i}^{-1}, is not the same as the attenuation experienced by an acoustic wave in the fluid.

4. Relate the measurement of Q_{i}^{-1} to viscosity through the analytical expression for interface wave attenuation.

Clearly, this process relies on several assumptions, but step (2) is the most problematic as it requires careful and specific modelling for each source location and station pair, and some prior knowledge of the possible geometry of the resonator. An alternative to this is to use relative rather than absolute measurements since, as discussed in Chapter 5, the radiative part will cancel out if it can be assumed to be constant over short timescales for a constant source-receiver geometry. Such an approach allows temporal changes in apparent attenuation to be directly mapped to changes in the intrinsic attenuation. This method was applied to SHV in Chapter 5, with promising results, resulting in an estimate of the magma shear viscosity of $2.3 \pm 2 \times 10^5$ Pas. This demonstrates the viability of the approach, and that quantifying the attenuation of low-frequency earthquakes can give useful information about the properties of the magma in the shallow plumbing system. From a monitoring perspective, the temporal evolution of parameters can still be very useful as an indicator of behaviour, even if absolute numbers are not attached to these measurements. The method could be refined and improved by using several frequencies and/or several stations together to constrain the viscosity better, or changes in the viscosity, during periods of rapid extrusion and high magma ascent rates.

Chapter 7

Conclusions

This thesis presents a study of the attenuation of low-frequency volcanic earthquakes, with particular emphasis on quantitatively linking seismic signals to magmatic processes and properties. Low frequency volcanic earthquakes are believed to originate from resonance of seismic energy within subsurface fluid-filled bodies, and through a combination of modelling work, theory and data analysis, the use of seismic attenuation as a tool for probing and understanding the internal structure and workings of volcanoes was explored. In this chapter the main results and contributions of the thesis are summarised, followed by suggestions for future work to extend and complement this study.

7.1 Summary of conclusions and contributions

Modelling the attenuation of low-frequency volcanic earthquakes

In Chapter 2 both elastic and viscoelastic models of seismic wave propagation were used to examine the amplitude decay of low frequency earthquakes. In Section 2.3 analysis of the radiative part of the amplitude decay suggested that there is significant variation in the radiative attenuation, Q_{r}^{-1}, with frequency and source-receiver geometry, even without the additional effects of topographic scattering. In Section 2.4 it was shown that the intrinsic part of the attenuation, attributed to the fluid properties, does not contribute as much as expected to the apparent amplitude decay, based on the assumption of Aki (1984) that the apparent attenuation is simply the sum of the intrinsic attenuation experienced by acoustic waves and the radiative attenuation.

The attenuation of interface waves

In Chapter 3 an explicit analytical expression was derived for the attenuation of interface waves in a viscoelastic fluid layer sandwiched between two elastic half-spaces. The interface wave attenuation was compared to the attenuation of acoustic waves propagating within the fluid and it was shown that, for a particular set of parameters, interface waves are attenuated less than acoustic waves for frequencies within the seismic bandwidth of low-frequency earthquakes. It was demonstrated that the relationship between the volume and shear viscosities of the fluid greatly influences the attenuative behaviour. The finite-difference model was modified to implement a Kelvin-Voight rheology to allow comparison with the results of the modelling in Chapter 2. The ratio of interface wave to acoustic attenuation derived from the model failed to match the analytical results, due to the strong geometric dependence of the radiative part, which may also prevent easy separation of the intrinsic attenuation from the measured apparent values.

Measuring the attenuation

Several automated methods to quantify the temporal amplitude decay or apparent attenuation of seismic signals were developed in Chapter 4. The method employing a weighted average of segments of the signal coda with negative gradient performed the best, in terms of recovering attenuation, when tests were carried out on synthetic signals. It was also shown that using the S-transform to isolate energy at specific frequencies has several advantages over bandpass filtering, and lead to reduced errors in the estimates of the attenuation measured from synthetic signals. This method was therefore applied to low-frequency earthquake datasets from SHV, Montserrat in Chapter 5.

Attenuation at Soufrière Hills Volcano, Montserrat

In Chapter 5, the attenuation was measured for a dataset of low-frequency earthquakes recorded at Soufrière Hills Volcano, Montserrat. Analysis of earthquakes occurring before and after a major collapse of the lava dome suggested that this did not significantly affect the attenuation, consistent with the occurrence of a particular waveform family of earthquakes requiring the *same set of internal conditions* triggering the *same resonator*. The presence of several co-existing waveform families of low-frequency earthquakes at SHV suggests that a number of different resonators may be active at any one time,

and different waveform families of earthquakes showed measurable differences in attenuation, as well as differences in their waveforms and spectral content. A decrease then increase in attenuation was observed within earthquake swarms that correlated with the acceleration then deceleration in event rate. A physical model was proposed to explain these variations, where fluctuations in magma ascent rate explain both the changes in event rate and the changes in viscosity required to produce the observed changes in attenuation. A methodology was proposed to give a quantitative interpretation of these temporal changes in the apparent attenuation, based on the assumption that they map to the intrinsic attenuation of interface waves. This gave estimates of the magma shear viscosity of $2.3 \pm 2 \times 10^5$ Pas, consistent with the range of values previously proposed by Collier & Neuberg (2006) for SHV of 10^3-10^6 Pas.

7.2 Future work

This thesis focused on the attenuation of low-frequency volcanic earthquakes, and the results provide a good basis for future development of methods to quantitatively link low-frequency seismic signals on volcanoes to internal magma processes and properties. Several potential directions for future work to extend and improve the research undertaken in this thesis are discussed below.

Interface wave attenuation and magma rheology

A limitation of the analytical expression for the interface wave attenuation derived in Chapter 3 is that it is based on a Kelvin-Voight fluid rheology. A further study could implement other simple rheologies, such as a Maxwell body, and repeat the analytical derivation. This could confirm whether interface wave and acoustic wave attenuation differs in the same way for a more appropriate magma rheology, and hence improve confidence in the link between measured attenuation values and inferred viscosities. Along similar lines, as discussed in Section 2.5, different rheological models for the magma that offer a more realistic frequency and spatial dependence could be incorporated into the finite-difference model.

Further analysis of attenuation at SHV

Further analysis of the attenuation of low-frequency earthquakes at SHV would bring several benefits. Comparison between values of attenuation at different seismic stations would allow some estimation and quantification of the geometrical variations in radiative component, and possibly place some constraints on the resonator geometry through comparison with numerical models. Comparing values of attenuation from different stations for the same time period would also provide additional independent constraints on the fluid properties. A comparison of attenuation during different eruptive periods would test if the attenuation can be linked to ascent rate at times other than during rapid dome growth, and also whether longer-term trends in parameters can be detected.

Combining magma flow modelling and seismicity

A further step in the modelling work described in this thesis would be to develop the link between the finite-difference models of seismic wave propagation and finite-element models of magma flow within conduits, such as that of Collier & Neuberg (2006). Linking low-frequency seismicity and magma properties is a two way process, and combining information between the two models would help to gain information and constraints on the magma properties from the seismicity (and vice versa). Attenuation is an important part of this process, and implementation of realistic Q distributions within the finite-difference models was started by Collier (2005), but requires a full treatment of degassing and gas loss to produce realistic gas volume fractions in upper conduit sections, something which has yet to be achieved. Implementing 2-D dependence of Q within the fluid, using realistic distributions based on the flow model approach of Collier et al. (2006), would allow an appropriate frequency dependence to be modelled, rather than a constant Q.

Magma flow meter

All of the ideas discussed above are important in understanding the properties of the magma and their temporal evolution. The flow dynamics within the conduit system impact directly on the brittle failure criterion for the earthquake trigger mechanism, and hence affect its relationship with the ascent rate of the magma. This is something which needs further study before low-frequency earthquakes can be used a quantitative magma 'flow meter'. Attenuation is an important factor to consider in this context too,

since quantifying the magma ascent rate via the earthquake source mechanisms requires a full treatment of amplitudes, including any losses due to attenuation. Any further investigation into the seismic source mechanism of low-frequency earthquakes, such as examining a superposition of double couple mechanisms or moment tensor analysis, must include the effects of attenuation if the amplitudes or seismic moment are to be quantitatively linked to slip and hence magma movement.

Appendix A

Seismic station information

Seismometer location and instrument type

The seismic data used in the attenuation analysis in Chapter 5 were recorded at station MBGA, which formed part of the MVO digital broadband seismic network in 1997. The station coordinates and instrument details are given in Table A.1 below.

Table A.1: MBGA: seismometer location and instrument type.

Station	Instrument	Lat. [°N]	Long. [°W]	Elevation [m]	Gain [$vm^{-1}s$]	Digitiser Rate [count μv^{-1}]
MBGA	Güralp CMG-40T	16.7102	62.1886	478	800	1.00

References

Aki, K., 1980. Attenuation of shear-waves in the lithosphere for frequencies from 0.05 to 25 Hz, *Phys. Earth Planet. Int.*, **21**, 50–60.

Aki, K., 1984. Magma intrusion during the Mammoth Lakes earthquake., *J. Geophys. Res.*, **89**, 7689–7696.

Aki, K. & Richards, P., 2002. *Quantitative Seismology*, 2nd Edition, University Science Books, Sausalito, California.

Aki, K., Fehler, M., & Das, S., 1977. Source mechanism of volcanic tremor: fluid-driven crack models and their application to the 1963 Kilauea eruption, *J. Volcanol. Geotherm. Res.*, **2**, 259–287.

Bagdassarov, N., Dingwell, D., & Webb, S., 1994. Viscoelasticity of crystal- and bubble-bearing rhyolite melts, *Phys. Earth Planet. Int.*, **83**, 83–99.

Barazangi, M., Isacks, B., Dubois, J., & Pascal, G., 1974. Seismic wave attenuation in the upper mantle beneath the southwest Pacific, *Tectonophysics*, **24**(1-2), 1 – 12.

Barnes, H., Hutton, J., & Walters, K., 1989. *An Introduction to Rheology*, vol. 3 of **Rheology Series**, Elsevier.

Battaglia, J., Aki, K., & Ferrazzini, V., 2005. Location of tremor sources and estimation of lava output using tremor source amplitude on the Piton de la Fournaise volcano: 1. Location of tremor sources, *J. Volcanol. Geotherm. Res.*, **147**(3-4), 268–290.

Ben-Menahem, A. & Singh, S. J., 2000. *Seismic waves and sources*, 2nd Ed., Dover Publications Inc., Mineloa, New York.

Benoit, J. & McNutt, S., 1997. New constraints on source processes of volcanic tremor at Arenal Volcano, Costa Rica, using broadband seismic data, *Geophys. Res. Lett.*, **24**, 449–452.

Best, A. I., McCann, C., & Sothcott, J., 1994. The relationships between the velocities, attenuations and petrophysical properties of reservoir sedimentary rocks, *Geophys. Prosp.*, **42**(2), 151–178.

Biot, M. A., 1952. Propagation of elastic waves in a cylindrical bore, *J. Appl. Phys.*, **42**, 82–92.

Blanch, J., Robertsson, J., & Symes, W., 1995. Modelling of a constant Q: methodology and algorithm for an efficient and optimally inexpensive viscoelastic technique, *Geophysics*, **60**(1), 176–184.

Cagniard, L., 1939. *Reflexion et refraction des ondes seismiques progressives*, Gauthier-Villars, Paris., English translation by Flinn, E. A. and Dix, C. J. (McGraw-Hill, International Series in the Earth Sciences, 1962).

Calder, E. S., Luckett, R., Sparks, R. S. J., & Voight, B., 2002. Mechanisms of lava dome instability and generation of rockfalls and pyroclastic flows at Soufrière Hills Volcano, Montserrat, in *The eruption of Soufrière Hills Volcano, Montserrat, from 1995 to 1999*, vol. 21, pp. 173–190, eds Druitt, T. & Kokelaar, B., Geological Society of London Memoir.

Calder, E. S., Cortés, J. A., Palma, J. L., & Luckett, R., 2005. Probabilistic analysis of rockfall frequencies during an andesite lava dome eruption: The Soufrière Hills Volcano, Montserrat, *Geophys. Res. Lett.*, **32**(16), L16309.

Carcione, J., 2001. *Wave Fields in Real Media - Wave Propagation in Anisotropic, Anelastic and Porous Media*, Elsevier.

Carcione, J. M., Herman, G. C., & ten Kroode, A. P. E., 2002. Seismic modelling, *Geophysics*, **67**(4), 1304–1325.

Carn, S., Watts, R., Thompson, G., & Norton, G., 2004. Anatomy of a lava dome collapse: the 20 March 2000 event at Soufrière Hills Volcano, Montserrat, *J. Volcanol. Geotherm. Res.*, **131**(3-4), 241 – 264.

Cerjan, C., Kosloff, D., Kosloff, R., & Reshef, M., 1985. A nonreflecting boundary condition for discrete acoustic and elastic wave equations, *Geophysics*, **50**, 705–708.

Chouet, B. A., 1986. Dynamics of a fluid-driven crack in three dimensions by the finite difference method, *J. Geophys. Res.*, **91**, 13967–13992.

Chouet, B. A., 1988. Resonance of a fluid-driven crack: Radiation properties and implications for the source of long-period events and harmonic tremor, *J. Geophys. Res.*, **93**(B5), 4375–4400.

Chouet, B. A., 1992. Volcano seismology, in *IAVCEI Proceedings in Volcanology, Vol. 3*, pp. 133–156, eds P. Gasparini, R. S. & Aki, K., Springer-Verlag, Berlin.

Chouet, B. A., 1996a. Long-period volcano seismicity: its source and use in eruption forcasting, *Nature*, **380**, 309–316.

Chouet, B. A., 1996b. New Methods and Future Trends in Seismological Volcano Monitoring, in *Monitoring and Mitigation of Volcano Hazards*, pp. 23–97, eds Scarpa, R. & Tilling, R. I., Springer.

Chouet, B. A., 2003. Volcano Seismology, *Pure Appl. Geophys.*, **160**, 739–788.

Chouet, B. A. & Julian, B., 1985. Dynamics of an Expanding Fluid-Filled Crack, *J. Geophys. Res.*, **90**(B13), 11187–11198.

Chouet, B. A., Page, R., Stephens, C., Lahr, J., & Power, J., 1994. Precursory swarms of long-period events at Redoubt volcano (1989-1990), Alaska: Their origin and use as a forecasting tool, *J. Volcanol. Geotherm. Res.*, **62**, 95–135.

Clayton, R. W. & Engquist, B., 1977. Absorbing boundary conditions for accoustic and elastic wave equations, *Bull. Seism. Soc. Am.*, **67**(6), 1529–1540.

Cole, P., Bass, V., Christopher, T., Eligon, C., Fergus, M., Gunn, L., Odbert, H., Robertson, R., Simpson, R., Stewart, R., Stinton, A., Stone, J., Syers, R., Watts, R., & Williams, P., 2010. Report to the Scientific Advisory Committee on Montserrat Volcanic Activity, Open-file Report 10/01, Montserrat Volcano Observatory.

Collier, L., 2005. *The interaction of gas-charged magma and seismic waves*, Ph.D. thesis, The University of Leeds.

Collier, L. & Neuberg, J., 2006. Incorporating seismic observations into 2D conduit flow modelling, *J. Volcanol. Geotherm. Res.*, **152**, 331–346.

Collier, L., Neuberg, J., Lensky, N., & Lyakhovsky, V., 2006. Attenuation in gas-charged magma, *J. Volcanol. Geotherm. Res.*, **153**, 21–36.

Commander, K. & Prosperetti, A., 1989. Linear pressure waves in bubbly liquids: Comparison between theory and experiments, *J. Acoust. Soc. Am.*, **85**(2), 732–746.

Courant, R., Friedrichs, K., & Lewy, H., 1928. On the Partial Difference Equations of Mathematical Physics, *Math. Ann.*, **100**, 32–74.

Dasgupta, R. & Clark, R. A., 1998. Estimation of Q from surface seismic reflection data, *Geophysics*, **63**(6), 2120–2128.

De Angelis, S. & McNutt, S. R., 2005. Degassing and hydrothermal activity at Mt. Spurr, Alaska during the summer of 2004 inferred from the complex frequencies of long-period events, *Geophys. Res. Lett.*, **32**(12), L12312.

Dingwell, D., 1995. *Relaxation in silicate melts: some applications*, vol. 32, chap. 2, pp. 21–66, Mineral Society of America; J.F. Stebbins, P.F. McMillan and D.B. Dingwell Editors, Series Editor: Paul. H. Ribbe.

Dingwell, D. & Webb, S., 1989. Structural Relaxation in Silicate melts and non-Newtonian melt rheology in geologic processes, *Physics and Chemistry of Minerals*, **16**(5), 508–516.

Dingwell, D. & Webb, S., 1990. Relaxation in silicate melts, *Euro. J. Mineral*, **2**, 427–449.

Dvorkin, J. P. & Mavko, G., 2006. Modeling attenuation in reservoir and nonreservoir rock, *The Leading Edge*, **25**(2), 194–197.

Eichelberger, J. C., 1995. Silicic volcanism: Ascent of viscous magmas from crustal reservoirs, *Ann. Rev. Earth Planet. Sci.*, **23**(1), 41–63.

Fehler, M. & Chouet, B. A., 1982. Operation of a digital seismic network on Mount St. Helens Volcano and observations of long-period seismic events that originate under the volcano, *Geophys. Res. Lett.*, **9**, 1017–1020.

Ferrazzini, V. & Aki, K., 1987. Slow waves trapped in a fluid-filled crack: implications for volcanic tremor, *J. Geophys. Res.*, **92**, 9215–9223.

Fischer, T., Morrissey, M., Calvache, M., Gómez, D., Torres, R., Stix, J., & Williams, S., 1994. Correlations between SO_2 flux and long-period seismicity at Galeras volcano, *Nature*, **368**, 135–137.

Fuchs, K. & Müller, G., 1971. Computation of Synthetic Seismograms with Reflectivity Method and Comparison with Observations, *Geophys. J. R. Astr. Soc.*, **23**(4), 417–&.

Garvin, W., W., 1956. Exact Transient Solution of the Buried Line Source Problem, *Proc. R. Soc. Lond. A*, **234**, 528–541.

Gil Cruz, F. & Chouet, B. A., 1997. Long-period events, the most characteristic seismicity accompanying the emplacement and extrusion of a lava dome in Galeras Volcano, Colombia, 1991, *J. Volcanol. Geotherm. Res.*, **77**, 121–158.

Goldstein, P. & Chouet, B. A., 1994. Array measurements and modeling of sources of shallow volcanic tremor at Kilauea Volcano, Hawaii, *J. Geophys. Res.*, **99**(B2), 2637–2652.

Gómez, M. & Torres, C., 1997. Unusual low-frequency volcanic seismic events with slowly decaying coda waves observed at Galeras and other volcanoes, *J. Volcanol. Geotherm. Res.*, **77**, 173–193.

Got, J.-L., Frechet, J., & Klein, F. W., 1994. Deep fault plane geometry infered from multiplet relative relocation beneath the south flank of Kilauea, *J. Geophys. Res.*, **99**(B8), 15375–15386.

Green, D., 2005. *Multi-parameter monitoring and modelling of cyclic volcanic activity*, Ph.D. thesis, The University of Leeds.

Green, D. & Neuberg, J., 2006. Waveform classification of volcanic low-frequency earthquake swarms and its implication at Soufrière Hills Volcano, Montserrat., *J. Volcanol. Geotherm. Res.*, **153**, 51–63.

Green, D. N. & Neuberg, J., 2005. Seismic and infrasonic signals associated with an unusual collapse event at the Soufrière Hills volcano, Montserrat, *Geophys. Res. Lett.*, **32**(7), L07308.

Green, D. N., Neuberg, J., & Cayol, V., 2006. Shear stress along the conduit wall as a plausible source of tilt at Soufrière Hills volcano, Montserrat, *Geophys. Res. Lett.*, **33**(10), L10306.

Gubbins, D., 2004. *Time series analysis and inverse theory for geophysicists*, Cambridge University Press.

Hagerty, M. T., Schwartz, S. Y., A., G. M., & Protti, M., 2000. Analysis of seismic and acoustic observations at Arenal Volcano, Costa Rica, 1995-1997, *J. Volcanol. Geotherm. Res.*, **101**, 27–65.

Hale, A., Calder, E., Loughlin, S., Wadge, G., & Ryan, G., 2009. Modelling the lava dome extruded at Soufrière Hills Volcano, Montserrat, August 2005-May 2006: Part II: Rockfall activity and talus deformation, *J. Volcanol. Geotherm. Res.*, **187**(1-2), 69 – 84.

Hammer, C. & Neuberg, J., 2009. On the dynamical behaviour of low-frequency earthquake swarms prior to a dome collapse of Soufrière Hills Volcano, Montserrat, *Geophys. Res. Lett.*, **36**.

Harford, C. L., Pringle, M. S., Sparks, R. S. J., & Young, S. R., 2002. The volcanic evolution of Montserrat using $^{40}Ar/^{39}Ar$ geochronology, in *The eruption of Soufrière Hills Volcano, Montserrat, from 1995 to 1999*, vol. 21, pp. 93–113, eds Druitt, T. & Kokelaar, B., Geological Society of London Memoir.

Harrington, R. M. & Brodsky, E. E., 2007. Volcanic hybrid earthquakes that are brittle-failure events, *Geophys. Res. Lett.*, **34**(6).

Hautmann, S., Gottsmann, J., Sparks, R. S. J., Costa, A., Melnik, O., & Voight, B., 2009. Modelling ground deformation caused by oscillating overpressure in a dyke conduit at Soufrière Hills Volcano, Montserrat, *Tectonophysics*, **471**(1-2), 87 – 95.

Herd, R. A., Edmonds, M., & Bass, V. A., 2005. Catastrophic lava dome failure at Soufrière Hills Volcano, Montserrat, 12-13 July 2003, *J. Volcanol. Geotherm. Res.*, **148**(3-4), 234 – 252.

Hess, K.-U. & Dingwell, D. B., 1996. Viscosities of hydrous leucogranitic melts: a non-Arrhenian model, *American Mineralogist*, **81**, 1297–1300.

Hestholm, S. & Ruud, B., 2000. 2D finite-difference viscoelastic wave modelling including surface topography, *Geophysical Prospecting*, **48**, 341–373.

Iverson, R. M., Dzurisin, D., Gardner, C. A., Gerlach, T. M., LaHusen, R. G., Lisowski, M., Major, J. J., Malone, S. D., Messerich, J. A., Moran, S. C., Pallister, J. S., Qamar, A. I., Schilling, S. P., & Vallance, J. W., 2006. Dynamics of seismogenic volcanic extrusion at Mount St Helens in 2004-05, *Nature*, **444**(7118), 439–443.

Jeng, Y., Tsai, J., & Chen, S., 1999. An improved method of determining near-surface Q, *Geophysics*, **64**(5), 1608–1617.

Jolly, A., Thompson, G., & Norton, G., 2002. Locating pyroclastic flows on Soufrière Hills Volcano, Montserrat, West Indies, using amplitude signals from high dynamic range instruments, *J. Volcanol. Geotherm. Res.*, **118**(3-4), 299 – 317.

Jousset, P., Neuberg, J., & Sturton, S., 2003. Modelling the time-dependent frequency content of low-frequency volcanic earthquakes, *J. Volcanol. Geotherm. Res.*, **128**, 201–223.

Jousset, P., Jolly, A., & Neuberg, J., 2004. Modelling low-frequency earthquakes in a viscoelastic medium with topography, *Geophys. J. Int.*, **159**, 776–802.

Julian, B. R., 1994. Volcanic tremor: Nonlinear excitation by fluid flow, *J. Geophys. Res.*, **99**(B6), 11859–11877.

Key, A. J., 2007. *Conduit flow modelling to investigate possible sources of low-frequency earthquakes.*, Master's thesis, The University of Leeds.

Kjartansson, E., 1979. Constant Q-wave propagation and attenuation, *J. Geophys. Res.*, **84**(B9), 4737–4748.

Klimentos, T. & McCann, C., 1990. Relationships among compressional wave attenuation, porosity, clay content, and permeability in sandstones, *Geophysics*, **55**(8), 998–1014.

Knopoff, L. & Randall, M. J., 1970. The Compensated Linear-Vector Dipole: A Possible Mechanism for Deep Earthquakes, *J. Geophys. Res.*, **75**(26), 4957–4963.

Korneev, V., 2008. Slow waves in fractures filled with viscous fluid, *Geophysics*, **73**(1), N1–N7.

Kumagai, H. & Chouet, B. A., 1999. The complex frequencies of long-period seismic events as probes of fluid composition beneath volcanoes, *Geophys. J. Int.*, **138**, F7–F12.

Kumagai, H. & Chouet, B. A., 2000. Acoustic properties of a crack containing magmatic or hydrothermal fluids, *J. Geophys. Res.*, **105**(B11), 25493–25512.

Kumagai, H. & Chouet, B. A., 2001. The dependence of acoustic properties of a crack on the resonance mode and geometry, *Geophys. Res. Lett.*, **28**(17), 3325–3328.

Kumagai, H., Chouet, B. A., & Nakano, M., 2002. Waveform inversion of oscillatory signatures in long-period events beneath volcanoes, *J. Geophys. Res.*, **107**(B11), 2301.

Kumagai, H., Chouet, B. A., & Dawson, P. B., 2005. Source process of a long-period event at Kilauea volcano, Hawaii, *Geophys. J. Int.*, **161**(1), 243–254.

Kumagai, H., Chouet, B., & Nakano, M., 2002. Temporal evolution of a hydrothermal system in Kusatsu-Shirane Volcano, Japan, inferred from the complex frequencies of long-period events, *J. Geophys. Res.*, **107**(B10).

Kumazawa, M., Imanishi, Y., Fukao, Y., Furumoto, M., & Yamamoto, A., 1990. A theory of spectral analysis based on the characteristic property of a linear dynamic system, *Geophys. J. Int.*, **101**(3), 613–630.

Küpper, F. J., 1958. Theoretische Untersuchung Über die Mehrfachaufstellung von Geophonen, *Geophys. Prosp.*, **6**(3), 194–256.

Lahr, J. C., Chouet, B. A., Stephens, C. D., Power, J. A., & Page, R. A., 1994. Earthquake classification, location and error analysis in a volcanic environment, *J. Volcanol. Geotherm. Res.*, **62**, 137–151.

Le Friant, A., Harford, C., Deplus, C., Boudon, G., Sparks, R., Herd, R., & Komorowski, J.-C., 2004. Geomorphological evolution of Montserrat (West Indies): importance of flank collapse and erosional processes, *J. Geol. Soc. London*, **161**(1), 147–160.

Levander, A. R., 1988. Fourth-order finite-difference P–SV seismograms, *Geophysics*, **53**, 1425–1436.

Loughlin, S., Christopher, T., Luckett, R., Jones, L., & Baptie, B., 2007. Large volume dome collapse at the Soufrière Hills Volcano, Montserrat, 20 May 2006, in *Geophysical Research Abstracts*, vol. 9, p. 11090, (European Geosciences Union, General Assembly 2007).

Luckett, R., Loughlin, S., De Angelis, S., & Ryan, G., 2008. Volcanic seismicity at Montserrat, a comparison between the 2005 dome growth episode and earlier dome growth, *J. Volcanol. Geotherm. Res.*, **177**, 894–202.

McDonal, F., Angona, F., & Mills, A., 1958. Attenuation of shear and compressional waves in Pierre shale, *Geophysics*, **23**, 421–439.

McNutt, S. R., 2002. Volcano seismology and monitoring for eruptions, in *International Handbook of Earthquake and Engineering Seismology, Int. Geophys. Ser.*, vol. 81, pp. 383–406, eds Lee, W. H. K., Kanamori, H., Jennings, P. C., & Kisslinger, C., Elsevier, New York.

McNutt, S. R., 2005. Volcanic seismology, *Ann. Rev. Earth Planet. Sci.*, **33**(1), 461–491.

Miller, A., Stewart, R., White, R., Luckett, R., Baptie, B., Aspinall, W., Latchman, J., Lynch, L., & Voight, B., 1998. Seismicity associated with dome growth and collapse at the Soufrière Hills Volcano, Montserrat, *Geophys. Res. Lett.*, **25**, 3401–3404.

Miller, A., Foulger, G., & Julian, B., 1998a. Non-double-couple earthquakes 2. Observations, *Rev. Geophys.*, **36**(4), 551–568.

Miller, A., Julian, B., & Foulger, G., 1998b. Three-dimensional seismic structure and moment tensors of non-double-couple earthquakes at the Hengill-Grensdalur volcanic complex, Iceland, *Geophys. J. Int.*, **133**(2), 309–325.

Minakami, T., 1974. Seismology of Volcanoes in Japan, in *Physical Volcanology*, eds Civetta, L., Gasparini, P., Luongo, G., & Rapolla, A., Elsevier, Amsterdam.

Molina, I., Kumagai, H., Garca-Aristizbal, A., Nakano, M., & Mothes, P., 2008. Source process of very-long-period events accompanying long-period signals at Cotopaxi Volcano, Ecuador, *J. Volcanol. Geotherm. Res.*, **176**(1), 119 – 133.

Molina, I., Kumagai, H., & Yepes, H., 2004. Resonances of a volcanic conduit triggered by repetitive injections of an ash-laden gas, *Geophys. Res. Lett.*, **31**(3).

Moran, S. C., 2003. Multiple Seismogenic Processes for High-Frequency Earthquakes at Katmai National Park, Alaska: Evidence from Stress Tensor Inversions of Fault-Plane Solutions, *Bull. Seism. Soc. Am.*, **93**(1), 94–108.

Morrissey, M. M. & Chouet, B. A., 2001. Trends in long-period seismicity related to magmatic fluid compositions, *J. Volcanol. Geotherm. Res.*, **108**, 265–281.

Müller, G., 1970. Exact Ray Theory and its Application to Reflection of Elastic Waves from Vertically Inhomogeneous Media, *Geophys. J. R. Astr. Soc.*, **21**(3-4), 261–&.

Nakano, M. & Kumagai, H., 2005a. Waveform inversion of volcano-seismic signals assuming possible source geometries, *Geophys. Res. Lett.*, **32**(12), L12302.

Nakano, M. & Kumagai, H., 2005b. Response of a hydrothermal system to magmatic heat inferred from temporal variations in the complex frequencies of long-period events at Kusatsu-Shirane Volcano, Japan, *J. Volcanol. Geotherm. Res.*, **147**(3-4), 233–244.

Nakano, M., Kumagai, H., & Chouet, B. A., 2003. Source mechanism of long-period events at Kusatsu-Shirane Volcano, Japan, inferred from waveform inversion of the effective excitation functions, *J. Volcanol. Geotherm. Res.*, **122**(3-4), 149 – 164.

Nakano, M., Kumagai, H., Chouet, B., & Dawson, P., 2007. Waveform inversion of volcano-seismic signals for an extended source, *J. Geophys. Res.*, **112**(B2), B02306.

Nakano, M., Kumagai, H., Kumazawa, M., Yamaoka, K., & Chouet, B., 1998. The excitation and characteristic frequency of the long-period volcanic event: An approach based on an inhomogeneous autoregressive model of a linear dynamic system, *J. Geophys. Res.*, **103**(B5), 10031–10046.

Navon, O., Chekhmir, A., & Lykhovsky, V., 1998. Bubble growth in highly viscous melts: theory, experiments, and autoexplosivity of dome lavas, *Earth Planet. Sci. Lett.*, **160**, 763–776.

Neuberg, J., 2000. Characteristics and causes of shallow seismicity in andesite volcanoes, *Phil. Trans. R. Soc. Lond. A*, **358**, 1533–1546.

Neuberg, J. & O'Gorman, C., 2002. A model of the seismic wavefield in gas-charged magma: application to Soufrière Hills volcano, Montserrat, in *The eruption of Soufrière Hills Volcano, Montserrat, from 1995 to 1999*, vol. 21, pp. 603–609, eds Druitt, T. & Kokelaar, B., Geological Society of London Memoir.

Neuberg, J. & Pointer, T., 2000. Effects of volcano-topography on seismic broadband waveforms, *Geophys. J. Int.*, **143**, 239–248.

Neuberg, J., Luckett, R., Ripepe, M., & Braun, T., 1994. Highlights from a seismic broadband array on Stromboli Volcano, *Geophys. Res. Lett.*, **21**(9), 749–752.

Neuberg, J., Baptie, B., Luckett, R., & Stewart, R., 1998. Results from the broadband seismic network on Montserrat., *Geophys. Res. Lett.*, **25**, 3661–3664.

Neuberg, J., Luckett, R., Baptie, B., & Olsen, K., 2000. Models of tremor and low–frequency earthquake swarms on Montserrat, *J. Volcanol. Geotherm. Res.*, **101**, 83–104.

Neuberg, J., Tuffen, H., Collier, L., Green, D., Powell, T., & Dingwell, D., 2006. The trigger mechanism of low-frequency earthquakes on Montserrat., *J. Volcanol. Geotherm. Res.*, **153**, 37–50.

O'Connell, R. & Budiansky, B., 1978. Measures of dissipation in viscoelastic media, *Geophys. Res. Lett.*, **5**(1), 5–8.

Ohminato, T. & Chouet, B., 1997. A free-surface boundary condition for including 3D topography in the finite-difference method, *Bull. Seism. Soc. Am.*, **87**(2), 494–515.

Ottemöller, L., 2008. Seismic hybrid swarm precursory to a major lava dome collapse: 9-12 july 2003, Soufrière Hills volcano, Montserrat, *J. Volcanol. Geotherm. Res.*, **177**, 903–910.

Petersen, T., Caplan-Auerbach, J., & McNutt, S. R., 2006. Sustained long-period seismicity at Shishaldin Volcano, Alaska, *J. Volcanol. Geotherm. Res.*, **151**(4), 365 – 381.

Powell, T. & Neuberg, J., 2003. Time dependent features in tremor spectra, *J. Volcanol. Geotherm. Res.*, **128**, 177–185.

Power, J. A., Lahr, J., Page, R., Chouet, B., Stephens, C., Stephens, D., Harlow, D., Murray, T., & Davies, J., 1994. Seismic evolution of the 1989-1990 eruption sequence of Redoubt Volcano, Alaska, *J. Volcanol. Geotherm. Res.*, **62**, 69–94.

Prud'Homme, R. & Bird, R., 1978. The dilational properties of suspensions of gas bubbles in incompressible Newtonian and non-Newtonian fluids., *J. Non-Newtonian Fluid Mech.*, **3**, 261–279.

Raikes, S. A. & White, R. E., 1984. Measurements of Earth Attenuation from Downhole and Surface Seismic Recordings, *Geophys. Prosp.*, **32**(5), 892–919.

Ramos, E. G., Hamburger, M. W., Paulis, G. L., & Laguerta, E. P., 1999. The low-frequency earthquake swarms at Mount Pinatubo, Philippines: implications for magma dynamics, *J. Volcanol. Geotherm. Res.*, **92**, 295–320.

Rea, W. J., 1974. The volcanic geology and petrology of Montserrat, West Indies, *J. Geol. Soc. London*, **130**, 341–366.

Reine, C., van der Baan, M., & Clark, R., 2009. The robustness of seismic attenuation measurements using fixed- and variable-window time-frequency transforms, *Geophysics*, **74**(2), WA123–WA135.

Reine, C. A., 2009. *A Robust Prestack Q-Inversion In The τ-p Domain Using Variable-Window Spectral Estimates*, Ph.D. thesis, The University of Leeds.

Ricker, N., 1943. Further developments in the wavelet theory of seismogram structure, *Bull. Seism. Soc. Am.*, **33**(3), 197–228.

Ricker, N., 1944. Wavelet functions and their polynomials, *Geophysics*, **9**(3), 314–323.

Ricker, N., 1953. The forms and laws of propagation seismic wavelets, *Geophysics*, **18**(1), 10–40.

Robertson, R. E. A., Aspinall, W. P., Herd, R. A., Norton, G. E., Sparks, R. S. J., & Young, S. R., 2000. The 1995-1998 eruption of the Soufrière Hills Volcano, Montserrat, WI., *Phil. Trans. R. Soc. Lond. A*, **358**, 1619–1637.

Robertsson, J., Blanch, J., & Symes, W., 1994. Viscoelastic finite-difference modelling, *Geophysics*, **59**(9), 1444–1456.

Roman, D., Neuberg, J., & Luckett, R., 2006. Assessing the likelihood of volcanic eruption through analysis of volcanotectonic earthquake fault-plane solutions, *Earth Planet. Sci. Lett.*, **248**, 244–252.

Roman, D., De Angelis, S., Latchman, J., & White, R., 2008. Patterns of volcanotectonic seismicity and stress during the ongoing eruption of the Soufrière Hills Volcano Montserrat (1995-2007), *J. Volcanol. Geotherm. Res.*, **173**, 230–244.

Roman, D. C. & Cashman, K. V., 2006. The origin of volcano-tectonic earthquake swarms, *Geology*, **34**(6), 457–460.

Romanowicz, B., 1998. Attenuation tomography of the earth's mantle: A review of current status, *Pure Appl. Geophys.*, **153**(2-4), 257–272.

Roth, E. G., Wiens, D. A., & Zhao, D., 2000. An empirical relationship between seismic attenuation and velocity anomalies in the upper mantle, *Geophys. Res. Lett.*, **27**(5), 601–604.

Rowe, C., Thurber, C., & White, R., 2004. Dome growth behavior at Soufriere Hills Volcano, Montserrat, revealed by relocation of volcanic event swarms, 1995-1996, *J. Volcanol. Geotherm. Res.*, **134**(3), 199–221.

Sánchez, J. J., Wyss, M., & McNutt, S. R., 2004. Temporal-spatial variations of stress at Redoubt volcano, Alaska, inferred from inversion of fault plane solutions, *J. Volcanol. Geotherm. Res.*, **130**(1-2), 1 – 30.

Sawada, M., 1994. B-type and explosion earthquakes observed at Asama volcano, central Japan, *J. Volcanol. Geotherm. Res.*, **63**(3-4), 111 – 128.

Scarpa, R. & Gasparini, P., 1996. A Review of Volcano Geophysics and Volcano-Monitoring Methods, in *Monitoring and Mitigation of Volcano Hazards*, pp. 3–22, eds Scarpa, R. & Tilling, R. I., Springer.

Schurr, B., Asch, G., Rietbrock, A., Trumbull, R., & Haberland, C., 2003. Complex patterns of fluid and melt transport in the central Andean subduction zone revealed by attenuation tomography, *Earth Planet. Sci. Lett.*, **215**(1-2), 105 – 119.

Seidl, D. & Hellweg, M., 2003. Parameterization of multichromatic tornillo signals observed at Galeras Volcano (Columbia), *J. Volcanol. Geotherm. Res.*, **125**, 171–189.

Seidl, D., Hellweg, M., Rademacher, H., Gomez, D., & Torres, R., 1999. The anatomy of a tornillo: puzzles from three-component measurements at Galeras volcano (Colombia), *Ann. Geo.*, **42**(3), 355–364.

Smith, P. & Neuberg, J., 2007a. Using the Seismic Amplitude Decay of Low-Frequency Events to Constrain Magma Properties., *EOS Trans. AGU*, **88**(52), Fall Meet Suppl., Abstract V51D-0782.

Smith, P. & Neuberg, J., 2007b. An amplitude battle: attenuation in bubbly magma versus conduit resonance, in *Earth: Our Changing Planet. Proceedings of IUGG XXIV General Assembly Perugia, Italy 2007.*, eds Ubertini, L., Manciola, P., Casadei, S., & Grimaldi, S., ISBN: 978-88-95852-25-4, Abstract JVS004-2444.

Smith, P. & Neuberg, J., 2008. Constraining magma properties by estimation of Q from low-frequency seismicity., in *Understanding Volcanoes, IAVCEI 2008 General Assembly, 17-22 August, Reykjavik, Iceland*, Abstract No. 233.

Smith, P. & Neuberg, J., 2010. The attenuation of interface waves: implications for low-frequency volcanic earthquakes., in *Geophysical Research Abstracts*, vol. 12, p. 11329, (European Geosciences Union, General Assembly 2010).

Smith, P. J., 2006. *Combining magma flow models with seismic signals*, Master's thesis, The University of Leeds.

Souriau, A. & Romanowicz, B., 1996. Anisotropy in inner core attenuation: A new type of data to constrain the nature of the solid core, *Geophys. Res. Lett.*, **23**(1), 1–4.

Stein, S. & Wysession, M., 2003. *An Introduction to Seismology, Earthquakes and Earth Structure*, Blackwell Publishing Ltd., Oxford, U.K.

Stephens, C., Chouet, B., Page, R., Lahr, J., & Power, J., 1994. Seismological aspects of the 1989-1990 eruptions at Redoubt Volcano, Alaska: the SSAM perspective., *J. Volcanol. Geotherm. Res.*, **62**, 153–182.

Stewart, R., Bass, V., Christopher, T., Clouard, V., De Angelis, S., Dondin, F., Fournier, N., Joseph, E., Komorowski, J.-C., Robertson, R., & Syers, R., 2008. Report for the Scientific Advisory Committee on Montserrat Volcanic Activity, Open-file Report 08/02, Montserrat Volcano Observatory.

Stewart, R., Bass, V., Chardot, L., Christopher, T., Dondin, F., Finizola, A., Fournier, N., Joseph, E., Komorowski, J.-C., Legendre, Y., Peltier, A., Robertson, R., Syers, R., & Williams, P., 2009. Report for the Scientific Advisory Committee on Montserrat Volcanic Activity, Open-file Report 09/01, Montserrat Volcano Observatory.

Stockwell, R., 2007. A basis for efficient representation of the S-transform, *Digit. Signal Prog.*, **17**(1), 371 – 393.

Stockwell, R., Mansinha, L., & Lowe, R., 1996. Localization of the complex spectrum: The S transform, *IEEE Trans. Signal Process.*, **44**(4), 998–1001.

Stoneley, R., 1924. Elastic waves at the surface of separation of two solids, *Proc. R. Soc. Lond. A*, **106**(738), 416–428.

Stoneley, R., 1926. The Effect of the Ocean on Rayleigh Waves, *Geophys. J. Int.*, **1**(s7), 349–356.

Sturton, S. & Neuberg, J., 2003. The effect of a decompression on seismic parameter profiles in a gas-charged magma, *J. Volcanol. Geotherm. Res.*, **128**, 187–199.

Sturton, S. & Neuberg, J., 2006. The effects of conduit length and acoustic velocity on conduit resonance: implications for low-frequency events, *J. Volcanol. Geotherm. Res.*, **151**, 319–339.

Tessmer, E., Kosloff, D., & Behle, A., 1992. Elastic wave propagation simulation in the presence of surface topography, *Geophys. J. Int.*, **108**, 621–632.

Thomas, M. & Neuberg, J., 2010. Linking observations at active volcanoes to physical processes through conduit flow modelling, in *Geophysical Research Abstracts*, vol. 12, p. 11147, (European Geosciences Union, General Assembly 2010).

Tilling, R. I., 2005. Volcano hazards, in *Volcanoes and the Environmemt*, chap. 2, p. 72, eds Martí, J. & Ernst, G. G. J., Cambridge University Press.

Tonn, R., 1991. The Determination of the Seismic Qaulity Factor-Q from VSP data - A Comparison of Different Computational Methods, *Geophys. Prosp.*, **39**(1), 1–27.

Tuffen, H., Smith, R., & Sammonds, P. R., 2008. Evidence for seismogenic fracture of silicic magma, *Nature*, **453**(7194), 511–514.

Umakoshi, K., Takamura, N., Shinzato, N., Uchida, K., Matsuwo, N., & Shimizu, H., 2008. Seismicity associated with the 1991-1995 dome growth at Unzen Volcano, Japan, *J. Volcanol. Geotherm. Res.*, **175**(1-2), 91 – 99.

Varley, N., Arámbula-Mendoza, R., ReyesDávilla, G., Stevenson, J., & Harwood, R., 2010. Long-period seismicity during magma movement at Volcán de Colima, *Bull. Volcanol.*, pp. 1–15.

Varley, N., Arámbula-Mendoza, R., Reyes-Dávilla, G., Sanderson, R., & Stevenson, J., in press. Generation of Vulcanian activity and long-period seismicity at Volcán de Colima, Mexico., *J. Volcanol. Geotherm. Res.*.

Virieux, J., 1986. $P - SV$ wave-propagation in heterogeneous media: velocity-stress finite-difference method, *Geophysics*, **51**, 889–901.

Voight, B., Hoblitt, R., Clarke, A., Lockhart, A., Miller, A., Lynch, L., & McMahon, J., 1998. Remarkable cyclic ground defomation monitored in real-time on Montserrat, and its use in eruption forcasting, *Geophys. Res. Lett.*, **18**(25), 3405–3408.

Voight, B., Komorowski, J.-C., Norton, G. E., Belousov, A. B., Belousova, M., Boudon, G., Francis, P. W., Franz, W., Heinrich, P., Sparks, R. S. J., & Young, S. R., 2002. The 26 December (Boxing Day) 1997 sector collapse and debris avalanche at Soufrière Hills Volcano, Montserrat, *Geological Society, London, Memoirs*, **21**(1), 363–407.

Wadge, G., Herd, R., Ryan, G., Calder, E., & Komorowski, J.-C., 2010. Lava production at Soufrière Hills Volcano, Montserrat: 1995-2009, *Geophys. Res. Lett.*, **37**.

Waite, G., Chouet, B., & Dawson, P., 2008. Eruption dynamics at Mount St. Helens imaged from inversion of broadband waveforms: interaction of the shallow magmatic and hydrothermal system, *J. Geophys. Res.*, **113**(B02305).

Watts, R. B., Herd, R. A., Sparks, R. S. J., & Young, S. R., 2002. Growth patterns and emplacement of the andesitic lava dome at Soufrière Hills Volcano, Montserrat, in *The Eruption of Soufrière Hills Volcano, Montserrat from 1995 to 1999*, vol. 21, pp. 115–152, eds Druitt, T. H. & Kokelaar, B. P., Geological Society Memoirs, London.

White, R., 1992. The accuracy of Estimating Q from Seismic Data, *Geophysics*, **57**(11), 1508–1511.

White, R., Miller, A., Lynch, L., & Power, J., 1998. Observations of hybrid seismic events at Soufrière Hills Volcano, Montserrat: July 1995 to September 1996, *Geophys. Res. Lett.*, **25**(19), 3657–3660.

Xu, J., 1995. *Implementation of free-surface boundary conditions for finite-difference solutions to the wave equation.*, Master's thesis, University of Utah, Salt Lake City, UT.

Yamamoto, M., Kawakatsu, H., Kaneshima, S., Mori, T., Tsutsui, T., Sudo, Y., & Morita, Y., 1999. Detection of a crack-like conduit beneath the active crater at Aso Volcano Japan, *Geophys. Res. Lett.*, **26**(24), 3677–3680.

Young, S. R., Sparks, R. S. J., Aspinall, W., Lynch, L., Miller, A., Robertson, T., & Shepherd, J., 1998. Overview of the eruption of Soufrière Hills Volcano, Montserrat, 18 July 1995 to December 1997, *Geophys. Res. Lett.*, **25**, 3389–3392.

Zener, C., 1948. *Elasticity and anelasticity of metals*, The University of Chicago Press.

Zimanowski, B., 1998. Phreatomagmatic explosions, in *From Magma to Tephra.*, pp. 25–53, eds Freundt, A. & Rosi, M., Elsevier.